THE MODEL K-16B
V/STOL RESEARCH
AMPHIBIOUS AIRCRAFT:

Research and Development
(February 1956 - September 1962)

Summary Report
March, 1967

Distribution of this document is
unlimited.

Harry S. Egerton
James E. Fitzpatrick

SEP

186

NOTICES

This report has been reviewed by the Naval Air
Systems Command. The findings in this report are those
of the contractor, and not those of the Naval Air Systems Com-
mand or the Department of the Navy.

When Government drawings, specifications, or other
data are used for any purpose other than in connection with
a definitely related Government procurement operation, the
United States Government thereby incurs no responsibility
nor any obligation whatsoever; and the fact that the Govern-
ment may have formulated, furnished, or in any way supplied
the said drawings, specifications, or other data, is not to
be regarded by implication or otherwise as in any manner li-
censing the holder or any other person or corporation, or
conveying any rights or permission to manufacture, use, or
sell any patented invention that may in any way be related
thereto.
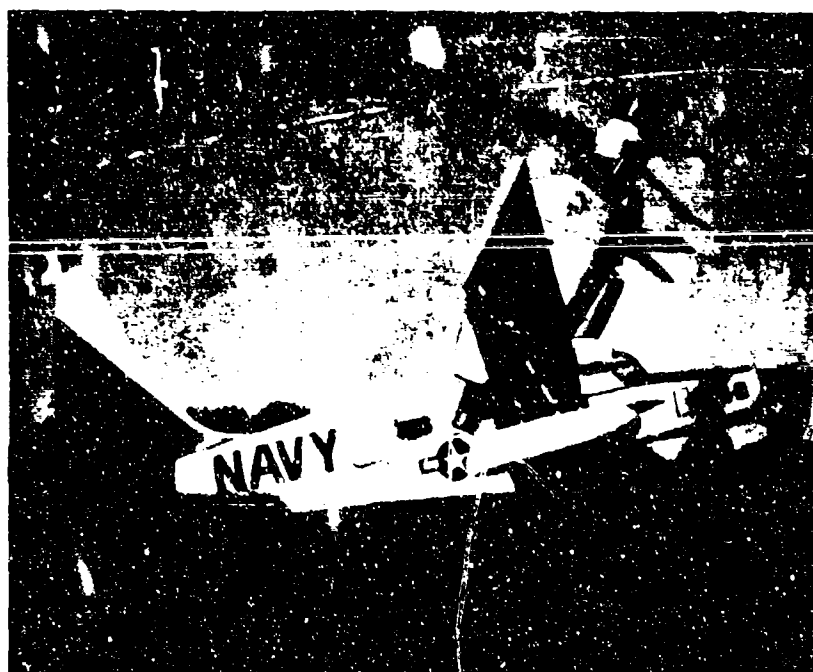
THE MODEL K-16B
V/STOL RESEARCH
AMPHIBIOUS AIRCRAFT:

Research and Development
(February 1956 - September 1962)

Summary Report
March, 1967

Harry S. Egerton
James E. Fitzpatrick

ABSTRACT

        Analytical and experimental research was conducted
to investigate the use of a variable camber, cyclic controlled
propeller, in combination with a partially-tilting wing with
full-span flaps, to permit V/STOL aircraft operation. These
features were incorporated in a full scale experimental air-
craft designated the K-16B. This aircraft was used to explore
the feasibility of a unified propulsion-control system designed
to reconcile the conflict between the requirements of static
thrust in hover and high-speed propeller efficiency, and to pro-
vide helicopter-type control in hover without the need for auxi-
liary control devices. This is accomplished by trailing edge
flaps in the blades of the propeller. Collective deflection
of these flaps increases blade camber for high static thrust.
They are retracted in forward flight for a clean cruising-blade
profile. Cyclic deflection of the flaps furnishes control mo-
ments in hover. The system was investigated on ground bench
stands and in full-scale powered model tests of the K-16B in
the NASA, Ames Research Center, 20 x 80 foot wind tunnel.

        The configuration tested proved to have insufficient
thrust for vertical flight as its instrumented test gross weight;
lateral and directional control power was deficient; severe wing
and horizontal tail stall were encountered in portions of the
transition region; and a number of detail design deficiencies
became evident. For these reasons, flight tests were not con-
ducted. Data from the wind-tunnel tests, however, served to
validate methods of analysis developed during the program, and
the final methods show good correlation.

        This report presents the data and the methods and
correlations; describes the testing performed and the problems
encounteres; and shows the probable solutions to the problems
encountered.

        It is concluded that the propulsive rotor is a fea-
sible concept for propeller-driver V/STOL aircraft, offering
a unique combination of advantages for propulsion and control,
of such aircraft; that a practical and effective rotor could
probable be developed using the research data and methods of
analysis developed in this program.

i

FOREWORD

Donald W. Robinson, Jr.

CONTENTS

INTRODUCTION

Information about the hover and transition stability and control characteristics of V/STOL aircraft that have flown is sparse and closely guarded. But, it has been officially acknowledged that all V/STOL's that have flown have exhibited control and stability deficiencies, and that propeller driven V/STOL's have also been wanting in static thrust. A description is presented of a V/STOL aircraft research program that demonstrates a unified propulsion-control system that resolves many of the difficulties.

A propeller can be an efficient, unified propulsion-control unit. But success using a conventional propeller is illusory. V/STOL experience has shown the conventional propeller to be an inefficient static thrust producer. When the propeller is designed for static thrust requirements, the same experience shows that cruise efficiency suffers. Adding blade-pitch cyclic control makes matters worse. Hover cyclic control requires cyclic lift, but control is limited by blade stall if conventional propellers are used. This becomes apparent if a blade-section lift curve is pictured. In hover, the blade will be very highly loaded, and the mean lift coefficient will be at a point on the curve that is very near stall. Cyclic control will call for additional lift, which will cause the blades to stall. Of course, the mean lift coefficient can be backed down the curve to provide a margin for cyclic lift, but there will be an accompanying decrease in static thrust capacity.

A high-lift device in a propeller will give additional mean lift coefficient in hover and reduced coefficient in cruise, permitting the propeller to satisfy both ends of the speed spectrum. But this is only a partial solution. For example, it is desirable to eliminate a tail rotor and its recognized disadvantages of lift/pitch coupling, high-frequency vibration induced in the structure, and the high maintenance cost of the drive. The high-lift device, then, must also provide for control analogous to helicopter control. It can provide this control without stall because of its ability to furnish increased lift coefficient.

1

Our approach to a high-lift device is trailing
edge flaps in the blades. Collective deflection of them
provides variable camber, resolving the conflict between
static thrust in hover and propeller efficiency in fixed-
wing flight. Cyclic deflection of the flaps results in cy-
clic lift control in a manner duplicating the hovering con-
trol of a helicopter. For cruising flight, the propeller
provides thrust in a conventional manner with the blade
flaps undeflected.

The concept has been incorporated in a twin pro-
pulsive-rotor (cyclic propeller), partial-tilting-wing,
V/STOL amphibious airplane designed to applicable Military
specifications for both Class VU and helicopter structural
and flying qualities. Under Bureau of Naval Weapon Con-
tract NOa(s)56-549c, we conducted intensive research of the
approach, using a modified JRF-5 airframe which was redesig-
nated as the Model K-16B. The tilt-wing accommodates sym-
metrically disposed powerplants, each driving a propulsive-
rotor. The rotors are interconnected to prevent asymmetric
thrust in the event of a one-engine failure.

Correlation of data from ground stand and full
scale wind tunnel testing confirms the propulsive-rotor to
be an efficient propulsion-control assembly. The testing
illuminated several mechanical problems, principally with
oscillating bearings in the blade-flap control system. But
the solutions are in hand with a redesign of the control
system geometry, and with the development of high-capacity
self-lubricating bearings and elastomeric bearings. Though
the answers to many questions are now known, the develop-
mental implementation of second generation V/STOL aircraft
such as the XC142 and the X22 caused funding limitations
that prevented flight research with the K-16B.

This report presents details of conception, re-
search, and evaluation of this V/STOL design, along with
actual or recommended solutions of problems that arose.

2

HISTORY AND PHILOSOPHY
OF DEVELOPMENT

CONCEPTION

Controllability of the VTOL at low speeds must be comparable to the helicopter if it is to maneuver effectively near the ground. Precise spot-hovering, particularly in gusts and winds up to 30 knots, compounds the problems of adequate hover control. Further, the conflict between propeller performance requirements for hover and for fixed-wing cruise must be resolved.

Our V/STOL studies began in 1954 and were concerned with the area of propulsion. But, very early in the study it was recognized that operational feasibility could not be obtained until effective controllability in the hover and low-speed regime could be demonstrated - an area in which little or no effort was being applied at that time.

It was necessary to make the first attempt to derive controllability criteria for the low-speed regime of V/STOL aircraft. Because the helicopter was the only aircraft type that had achieved satisfactory VTOL control, it was logical to base a set of working criteria on the type.

Discussions with company test pilots indicated that maximum acceleration about the three body axes was a good measure of helicopter controllability in hover. This appeared to be a reasonable approach because angular accelerations of the aircraft produce proportional translational accelerations at the pilot's seat - an important item of sensory information used by the pilot for controlling the vehicle. By plotting maximum angular acceleration in pitch, roll, and yaw for known successful helicopters against gross weight, a set of working criteria was established.

For representative V/STOL configurations a good "rule-of-thumb" was found: A maximum pitching moment equivalent to that produced by a vertical thrust at the tail of approximately 20 percent of gross weight is required in pitch; 10 percent of gross weight at each wing tip in roll; and 6 percent of gross weight at the tail in yaw. Obtaining these amounts of thrust with auxiliary devices such as blowers, engine bleed, jet engines, or tail rotors appeared either impractical or costly in terms of fuel consumption, weight penalty, or complexity.

3

It was decided that the best compromise for a subsonic configuration would be a propeller-driven vehicle with a disc loading between that of a normal helicopter rotor and a conventional propel'ır. If range and speed requirements are relatively modes and if extensive hovering is required, then the natural choice is the helicopter. On the other hand, if long range and high speed are primary considerations, the normal approach would be to impart VTOL capability to the conventional high-efficiency airplane. Where speeds greater than 400 knots are not required, an efficient approach is the tilt-wing, propeller-driven configuration.

It is apparent that the design of a control system concerns first, the selection of methods to produce control forces in their proper locations; second, the design of a system that transforms pilot commands into properly proportioned actuation of the control force producers.

A less obvious aspect of hovering control is that of providing translational forces along the three body axes. To hover the aircraft over a precise spot, the pilot must be able to maneuver the aircraft fore and aft, from side to side, and up and down, not only in still air but also in gusts and winds up to 30 knots. It is desirable that the aircraft be able to provide these translational forces with a minimum of angular rotation because the time response, particularly for large aircraft, and the relative disorientation introduced by using only angular rotation to produce translationa. forces increases piloting difficulties. Hence, there is a desirable relationship between the translational forces and the control moments, in terms of magnitude and time response, for the aircraft to provide easy piloting technique.

Roll control can be attained by differential pitch of the right- and left-hand propellers.

An apparently straightforward way for obtaining yaw control is by differential aileron. But in ground effect the ailerons tend to lose some of their effectiveness - as much as 50 percent. Now, from theory based on a 25 percent-chord aileron, the value for aileron effectiveness ($d\alpha/d\delta$) is 0.5. This value can be affected by

nacelle shape, slipstream rotation, or ground effect, and might be reduced to as little as 0.2. To get the value of 0.5 in ground effect the ailerons would have to be relatively very large. Tail fans also have been used for directional control but have disadvantages both mechanical and aerodynamic, the latter in particular in high-speed flight.

4

Pitch control might be attained with a wing flap on a low-wing configuration that might give the flap an appreciable moment arm, but it will result in an ungainly configuration. A tail rotor adds mechanical complications, requires an appreciable amount of power, introduces vertical acceleration coupling, does not provide fore-and-aft translational forces, and gives drag in forward flight. A jet engine or a blower is impractical from a fuel consumption standpoint.

A cyclic control system has the advantage of providing control moments about, and translational forces along all the aircraft axes in a manner similar to that of a helicopter. Because the thrust vector is tilted with cyclic control, a translational force that anticipates angular rotation is produced.

Hover cyclic control is limited by blade stall if simply added to conventional propellers. V/STOL propeller blades are highly loaded in hover (very near stall), and it

is desirable to carry even higher $\bar{C}_L$. Cyclic control means

cyclic C_L, imposing additional burdens on blade loading.

According to Fay (41), an invariant-camber propeller blade will generate appreciable control power within the capability of the blade without stall provided that $\bar{C}_L$ is compara-

ble to helicopter rotor design practice. But such a blade will have unacceptably poor efficiency at the low thrust coefficients required for cruise. Blade trailing edge flaps,

being high lift devices, give additional cyclic C_L; addi-

tional $\bar{C}_L$ in hover and reduced $\bar{C}_L$ in cruise by retraction -

nearer to best L/D - and therefore better efficiency. The incorporation of a blade flap allows the selection of a blade profile and activity factor compatible with the high-speed propeller requirements, but by collective flap deflection attain the higher lift coefficients (because of the greater virtual camber) required for hover performance, with ample margin for necessary cyclic control and trim inputs without stall.

To minimize the cruising efficiency penalty that a high-activity-factor static thrusting propeller entails, it is advantageous to operate the hovering propeller at as high a blade loading as is possible. For example, to satisfy

5

hovering requirements a highly cambered airfoil is necessary
to obtain a high blade loading. The rapid drop in required
thrust from hovering to forward flight, however, forces the
propeller to operate at low thrust coefficients in cruise.
To operate efficiently at these low coefficients, a low
solidity is needed to keep the blade loading near the maxi-
mum lift/drag ratio on the blade section. Variable camber
blades will resolve these conflicting requirements.

The beauty of the concept can be shown by an il-
lustrative blade-section lift curve. In hover, an invari-
ant camber blade, designed for
a reasonable cruise efficiency,
would be operating at Point A
on Line 1. Cyclic control

requires additional C_L. A cy-

clic control input then would
move the blade over the peak
into stall. The mean lift
coefficient will have to be
backed off to Point A' to pro-
vide a margin for cyclic con-
trol, but there will be an ac-
companying decay in propeller
hover performance. A propul-
sive rotor, designed for the
same cruise efficiency, could
have a curve represented by
Line 2 because of its vari-
able camber capability. It
would operate at Point B.
The trailing edge flap of the
propulsive-rotor blade is a
high-lift device; so, a flap

deflection for cyclic control would result in Line 3. There
is no decay in hover performance, and there is an incremental
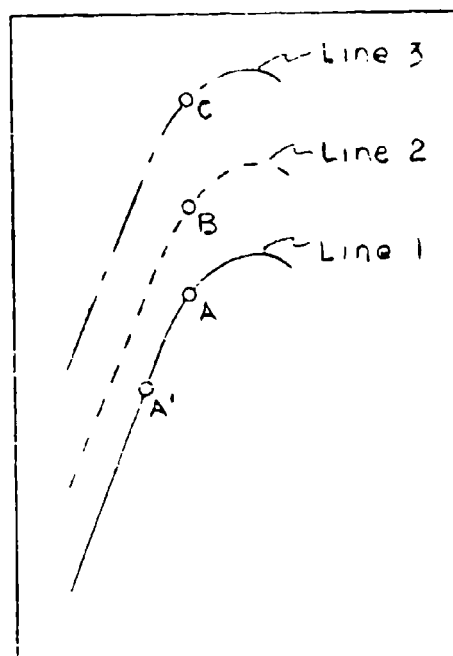
increase in C_L for cyclic control to Point C, without blade

stall. For fixed-wing flight, a propulsive-rotor with flap
retracted would be equivalent to a conventional propeller
in terms of geometry, twist, camber, and efficiency.

Kaman helicopters have been hallmarked by their
servo-flap system. A so-called "buried" flap had been ex-
tensively analyzed and flight-tested under Bureau of Naval
Weapons Contract NOa(s)52-622 and reported in KAC Reports
T-86(42); G-43(43); and G-51(44).

Drawing on this background, a propulsive-rotor was
designed with a twist distribution for reasonably-high-speed
cruise efficiency, but reconciling the conflicting require-
ments for cruise efficiency and high static thrust in hover
by using a trailing edge flap to provide a variable camber
blade. The introduction of cyclic lift control by cyclic
deflection of the flap presented an economical system for
attaining the control forces and moments. A flapping blade
was adopted to reduce the root bending stresses caused not
only by the thrust offset, but also by the one-per-rev vibra-
tory stresses characteristic of the high angle-of-attack
condition of VTOL and STOL aircraft in transition flight.

The strip analysis method (Appendix D) used for
hovering flight is conservative when compared with a propel-
ler of similar thrusting characteristics. The reasons are
twofold. The strip analysis method makes use of two-dimen-
sional data which includes the effect of stall. In forward
cruising flight the method is good because the sections are
operating far below the stall. In hovering flight, because
of high compromise twists, the inboard sections are operat-
ing at an angle-of-attack beyond which stall would occur in
two-dimensional flow. But on an operating propeller a
strong radial pressure gradient exists due to higher veloc-
ities at the outboard stations. The spanwise pressure gra-
dient produced by rotation has the effect of sweeping the
boundary layer outboard toward the tip. It thus postpones
the stall at more inboard stations. On a model propeller,
the maximum lift at the 80 percent radius station was in-
creased by approximately 30 percent as a result of this
boundary layer thinning (Himmelskamp - 45). In addition,
when blade stall proceeds toward the tip, a tip vortex
sheet is produced which increases blade lift and drag
(Kucheman - 46).

No method has been found for relating the strength
of these vortex sheets to the tip angle-of-attack and load
distribution; therefore they are not accounted for in the
two-dimensional strip analysis. Because the effect of the
natural boundary layer control on the inboard sections is
not taken into account in the present analytical method, the
calculated results are conservative.

The analytical predictions were so encouraging the
Bureau of Naval Weapons awarded Contract NOa(s)56-549c
(February 1956) to continue the research. In view of the
unique nature of the concept, the Bureau elected to design
the program in phases.

GROUND RESEARCH STANDS

The first phase was designed to substantiate the predictions with a feasibility model. A prototype 3-bladed rotor of 14-foot diameter with buried flaps of approximately 50 percent chord and 50 percent blade span was tested on a helicopter whirl-test stand. The investigation covered ranges of collective flap deflection to increase static thrust, and cyclic flap deflection to obtain control forces and moments. The results of the test concurred with the analytical methods developed for predicting aerodynamic and aeroelastic characteristics of a propulsive-rotor.

This feasibility test experimentally established the validity of the hypothesis, but at relatively low levels of power and speed. Consequently, the contract was amended (January 1957) to authorize a more sophisticated ground test stand evaluation.

Obtaining a balance between the power-installed requirements for cruise and those for hovering is an important function of V/STOL design. Amongst the various V/STOL configurations, the tilt-wing presents a unique opportunity for obtaining the desired balance by virtue of its freedom to select a wing of nearly or actually optimum loading.

If the vertical lift at zero forward speed is provided by slipstream turning the resultant force is less than the thrust of the propeller; that is, there is a turning loss and the loss must be made up with more thrust from the propeller. On the other hand, if the vertical lift is obtained by tilting the wing-propeller combination through a right-angle, wing stall problems in transition can become acute. From parametric studies, it appeared that a combination of the two principles should be adopted.

In the K-16B, a Fowler flap is deflected 40 degrees to deflect the slipstream 20 degrees. Consequently, the wing need be tilted only enough to make up the remaining 70 degrees. Fuselage angle, both on the ground and in flight, can be a portion of this latter angle. The 20 degrees of slipstream turning can be accomplished with a minimum of turning loss. Because the wing flap deflects the slipstream, the wing attitude angle required to sustain the aircraft in equilibrium at a particular speed is lower than without flaps. The wing resultant angle-of-attack consequently is lower, which reduces transition stall problems.

Another factor influencing the choice of tilt-wing and flap configuration is the longitudinal trim characteristics. The large flaps of a deflected slipstream vehicle

8

cause a large nose-down pitching moment. The propeller normal force of a tilt-wing configuration results in large nose-up pitching moments. The K-16B combines both to minimize the out-of-trim moments to be overcome by the controls.

Finally, the flapped wing affords reasonable power-off stalling speeds in conventional airplane configuration.

A twin-engine utility airplane in the 9000 pound class was blocked out. Turbine engines in the 1000-hp range being required, suitable rotor and drive systems were designed and fabricated. In addition, a half-span wing fitted with 40 percent Fowler flaps, nacelle, and cowling, designed to Specification MIL-A-8629 Class VU, was built.

These components were installed on a test stand that was appropriately floated on loadcells to permit measurement of the six components of force and moment for the determination of controllability, thrust, and lift performance. Additional instrumentation permitted a strain survey of the blades and hub, and measurements of blade motions, blade/flap hinge moments, and control inputs. The program also evaluated the degree of slipstream deflection by the wing-flap, rotor/wing slipstream interference, wing straightening effect, and effect of ground proximity.

Again results were in general accord with the hypothesis, although they did disclose areas, both in analysis and design, that required modification. These problems and their solutions are discussed in the "Test Article Development" section.

During the closing stages of the test program, analysis of data indicated that either further experimental results would continue to agree with theory, or the required modifications to analytical techniques were known. With the successful conclusion of testing expected in the near future, the contract was again amended (June 1958) authorizing a flight research vehicle.

FLIGHT RESEARCH AIRCRAFT

The purpose of this aircraft, known as the K-16B, was to provide a vehicle that would assist the Bureau of Naval Weapons in the establishment of both flying qualities and structural specifications for the coming generations of V/STOL aircraft. To provide for a reasonably thorough assessment, a considerable degree of flexibility must be incorporated into the various systems. A structural flight

envelope approaching that of operational aircraft must also be provided. Both objectives have been met in the K-16B.

In the interest of economy, the Bureau furnished a surplus JRF-5 fuselage to be modified for V/STOL operation. Because this is an amphibious fuselage with known hull characteristics, an additional advantage accrued to the overall program in that a qualitative assessment of V/STOL open-ocean operation could be made.

A description of the structure and systems, and a summary of the principle design dimensions will be found in Appendix B. The general arrangement is shown in Figure 1.

The authorization to proceed with the K-16B also called for dynamic substantiation of the rotor and of the power-and-drive system. Normally, the analytical treatment is substantiated by separate bench stand testing of the components before they are brought together for systems dynamic substantiation. Considerable economies can be realized by moving immediately to a qualification test of the complete system without prior component testing. But this entails a calculated risk - if one component fails the failure may be catastrophic, and at the least will delay work on the entire system. However, in view of the limited funding, the endurance stand was designed to qualify both the components and the complete system at the same time.

Subsequent to the authorization of the flight vehicle the decision was made to perform a full-scale wind tunnel evaluation. After functional tie-down testing, the airplane was shipped to NASA, Ames Research Center, for testing in the 40 x 80 foot wind tunnel.

In the next section are briefly discussed the analyses and tests that evaluate the ability of the K-16B to safely perform within the prescribed flight envelope. An analysis of the full-scale wind tunnel data will be found in a later section. In the section "Test Article Development" are reviewed a number of problems that arose and their solutions, and problems that remain and their probable solutions.

10

Figure 1

General Arrangement
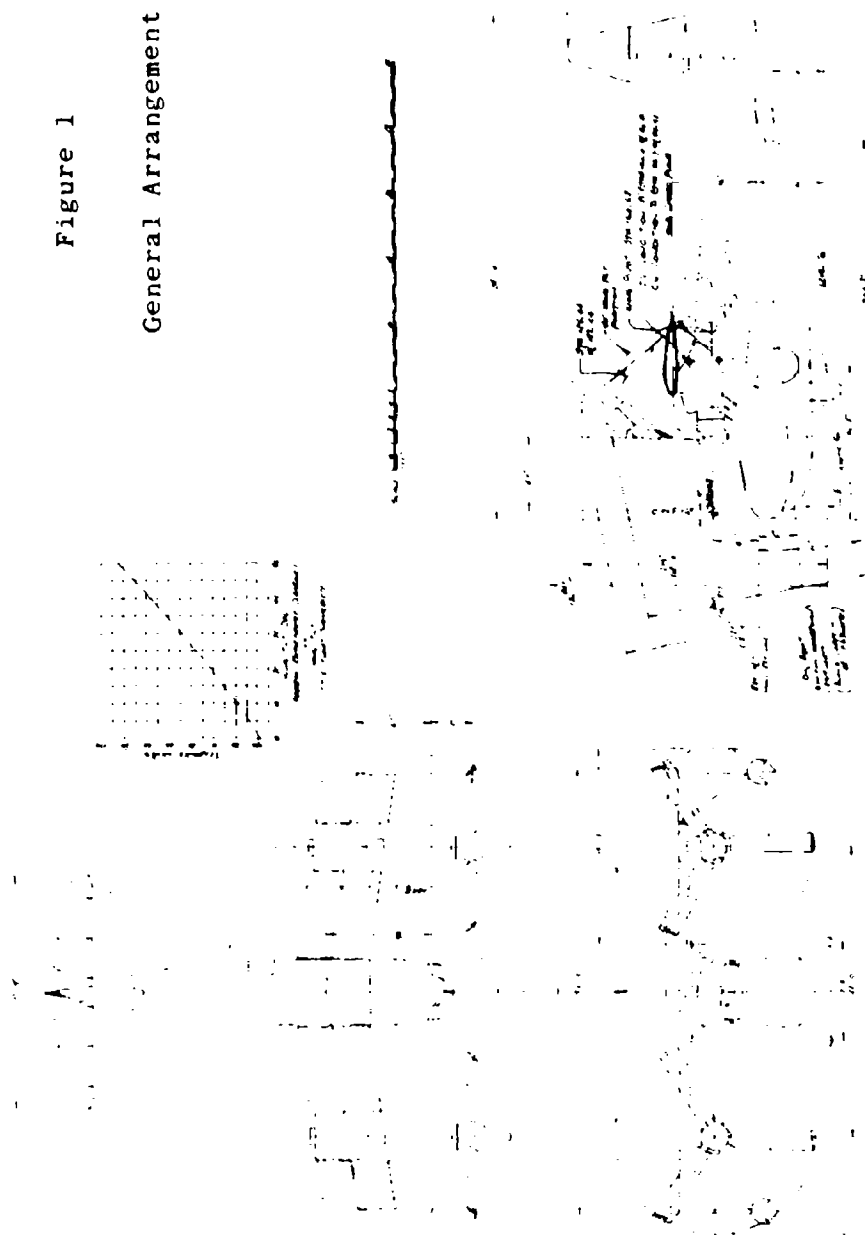
ANALYSES AND TESTS_____

The first phase of the propulsive-rotor research was designed to correlate analytical predictions with tests of a feasibility model. A prototype 3-bladed rotor of 14-foot diameter with 50 percent chord and 50 percent blade-span buried flaps was tested on a helicopter rotor whirl-test stand. This test set-up is shown in Figure 2. The investigation covered ranges of collective flap deflection to increase static thrust, and cyclic flap deflection to obtain control forces and moments.

The results of the test, presented in KAC Report G-90(1), concurred with the preliminary estimates of aerodynamic and aeroelastic characteristics of a propulsive-rotor. It was concluded:

- the hover controllability of present-day helicopters represents a reasonable criterion for design of V/STOL control systems;
- in terms of additional power and weight requirements, the most economical way of achieving this degree of control in propeller-driven V/STOL aircraft is by means of cyclic lift control of the propeller;
- trailing-edge flaps on the propeller blades provide a satisfactory degree of cyclic control;
- steady, positive, trailing-edge flap deflections provide increased propeller maximum lift coefficients.

This feasibility test stand experimentally established the validity of the concept at relatively low levels of power and speed. Consequently, the contract was amended to authorize a more sophisticated ground stand evaluation of the concept.

This phase of the program was accomplished on a test stand floated on Baldwin-Hamilton Type U-1 loadcells, permitting the determination of lift, thrust, and side forces, and of pitching, yawing, and rolling moments. On this stand were mounted a half-span wing fitted with Fowler-type flaps, a nacelle, and one rotor and drive system.
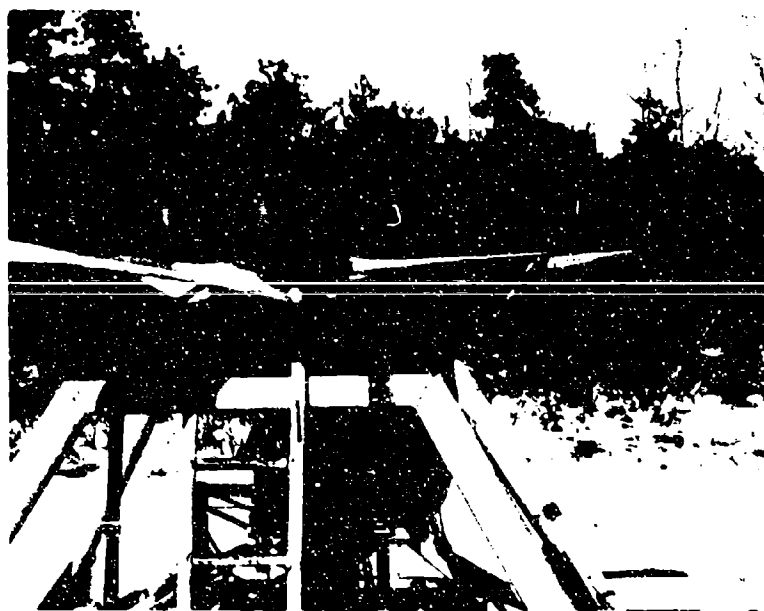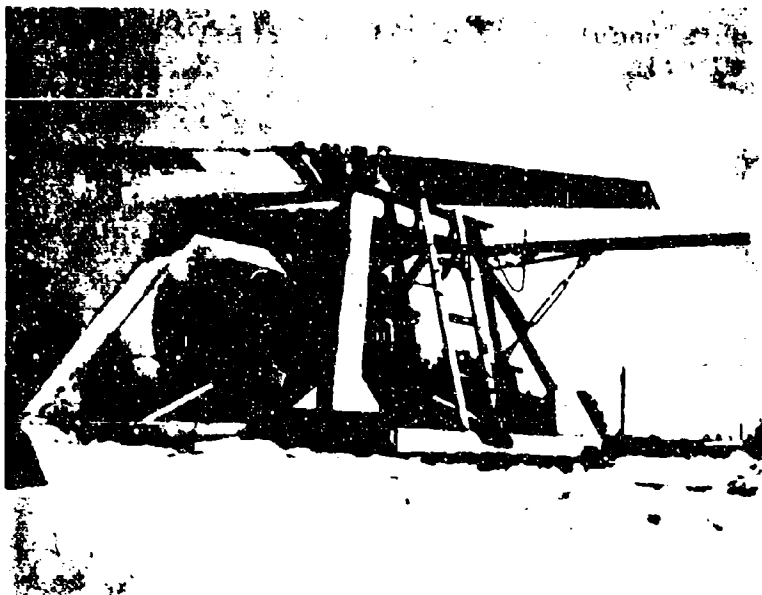
12

Figure 2

Feasibility Test Stand

13

Structural components peculiar to a flight article were designed to the criteria for Class VU aircraft of Specification MIL-A-8629, that the test results might reflect the compromises normally encountered when designing an operational military aircraft.

The test stand as described (Figure 3) permitted a performance assessment out of ground effect. To investigate the influence of ground proximity on performance, a plane was constructed to simulate the ground (Figure 4).

The results of this testing were again in general accord with the developed procedures, (KAC Reports G-111-1 through -4)(2/5), although the program did disclose areas in the particular hardware, both in analysis and design, that required modification. They were:

- variable inflow theory must be considered in the rotor analysis;
- to increase flapping sensitivity requires the introduction of negative δ_3;
- lead-lag freedom is not a necessity;
- flap hinge moment must be reduced.

During the closing stages of this testing it was apparent that procedure had been substantiated, so the contract was again amended to provide for a V/STOL flight research aircraft. A surplus JRF-5 to be modified to the V/STOL configuration was supplied by the Bureau.

This vehicle was to furnish a platform that would permit the safe accomplishment of flight research within a meaningful envelope to assist in the establishment of realistic flying qualities specifications for V/STOL aircraft. To meet this requirement it obviously could not be a limited-envelope test-bed; there must be adequate engineering justification supported by ground test in areas of question. But funding limitations affected planning. Initial judgement indicated that the engineering justification could be substantiated by the following tests:

- powered 1/8-scale wind-tunnel model;
- wing proof-load;
- controls proof-load;
- mechanical instability and flutter;
- dynamic component endurance;
- functional tie-down.

14

Figure 3

Aerodynamic Research Test Stand
without Groundboard

Figure 4

Aerodynamic Research Test Stand
with Groundboard

15

Subsequently, the test program was expanded to include:

- additional 1/8-scale model wind-tunnel tests;
- blade flap and flap-retention fatigue test;
- blade flap-control fatigue test;
- simulator flight evaluation;
- 1/8-scale wind-tunnel tests of blade flapping and damping in high-speed flight;
- full-scale wind-tunnel test.

AERODYNAMICS

Aerodynamic analysis followed a normal pattern, the only deviation being the need to consider two flight regimes for the same airplane - airplane in fixed-wing, high-speed flight, and helicopter in low-speed flight. Analyses covered methods of analysis, airloads, and estimated flying qualities, and are reported in KAC Reports G-113-2(7); -4(9); -5(10); -7(12); and -31(36). Applicable reports were modified as results of testing became available.

Estimating stability and controllability of the aircraft at all flight speeds was complicated by the unusual trimming and control devices available. The steady level flight of an aircraft requires a balance of forces in the vertical and horizontal directions. In any airplane this is brought about by a combination of propeller thrust and wing lift that balances the aircraft weight and drag. In the K-16B, because of the high thrust available, this balance can be achieved at any flight speed. As the speed is reduced below the flaps-down stalling speed, more of the lifting force must come from a component of the rotor thrust, and the attitude of the wing-propeller combination in space must move toward the vertical. If the wing and fuselage were fixed with respect to each other, rather inconvenient attitudes would result. The pilot of the K-16B can, however, tilt the fuselage down with respect to the wing as speed is reduced. Fuselage attitude, therefore, can be considered a trimming device. In addition, the regular aerodynamic control surfaces become inadequate at these low speeds, and full control is obtained by the cyclic and differential-collective control of the rotor's articulated blades.

The detail design specification for the 1/8-scale wind-tunnel model is found in KAC Report G-113-1(6). Each model rotor was driven by a 30-hp electric motor through a 2.17:1 reduction gearbox, and run at an rpm that was varied from 8000 to 12,000 rpm. To match T''_c with available power and speed, the rotors were four-bladed but otherwise scaled dimensionally. The blades did not have trailing-edge flaps but did have flapping hinges. A strain-gage balance within each nacelle measured rotor thrust, torque, normal force, and pitching moment about the hub.

The tests were conducted in the DTMB 3 x 10 foot Atmospheric Wind Tunnel No. 1. Figure 5 shows the model during test operations. These tests were completed by February 1960 and are reported in DTMB Aero Report 998(47), and KAC Report G-113-7 Appendix A(12). Aerodynamic predictions of suitable stability were generally substantiated, except for directional instability in the airplane "clean" configuration. Additional area added to the vertical fin corrected this.

As a result of these tests however, the possibility of stall was indicated on the model under conditions simulating level flight at speeds between 20 and 60 knots (Ibid). "Fallout" from NASA research then in progress also indicated that transition stall might be more serious than originally believed. Hence, the model was retested with several configuration changes to assess their effect on transition stall.

The leading-edge was modified in a manner similar to that shown in NACA TN2228, Figure 2(48). A leading-edge slat, a modification of that reported in NACA TR732(49), was also tested. Further, a center section slat was empirically designed.

All the configuration changes resulted in improvement in the model aerodynamic characteristics. In view of the good results obtained with the leading-edge modification (a glide-path angle of 10 degrees could be maintained throughout the transition), it was decided to use it during the upcoming full-scale wind-tunnel tests. These model tests were completed during November 1961, and are reported in KAC Report G-113-31(36).

At about this time a simulator flying qualities pilot evaluation was conducted at North American Aviation, Columbus Division, on their visual analog VTOL simulator.
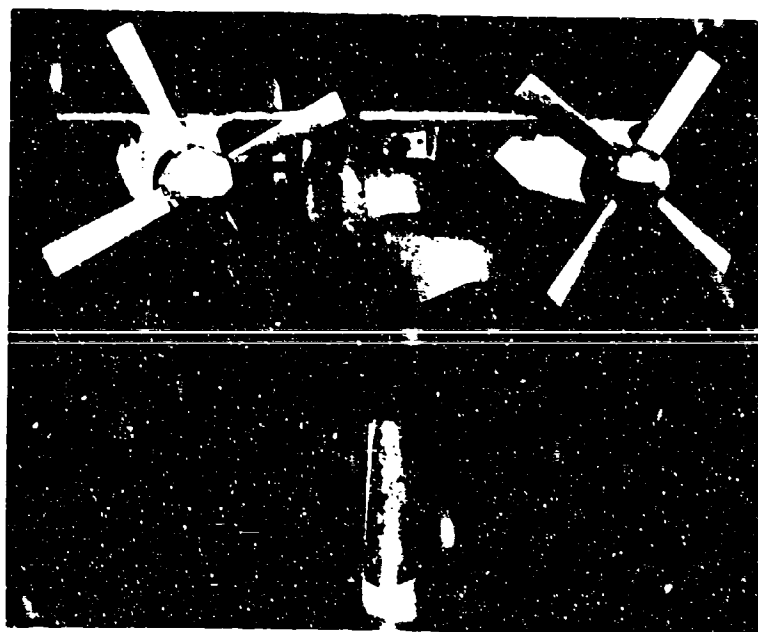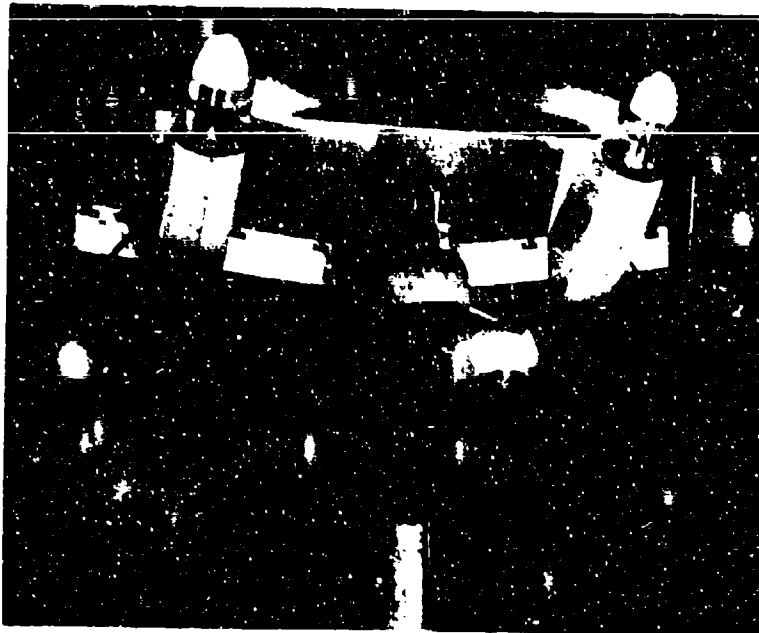
17

Figure 5

1/8-Scale Wind Tunnel Model

The estimated flying qualities were evaluated by pilots from BuWeps, Kaman, NASA, and NAA. The dynamic stability and control characteristics in hovering flight were found to be flyable but with sufficient unpleasant characteristics to hamper satisfactory sustained hovering operation. The results of the mid-transition and conventional flight evaluation showed the expected improvement of flying qualities with speed. The flight characteristics at 100 knots were generally rated satisfactory for normal operation, but with slightly unpleasant characteristics. This simulation program is reported in NAA Report NA60H-672(50), NATC Patuxent Report No. 1-Final Report (51), and KAC Report G-113-7 Appendix C(12). As a result of the hovering evaluation, it was recommended that a stability augmentation system be installed.

Upon completion of the aircraft it underwent functional tie-down testing, as shown in Figure 6. All the pilots who participated remarked on the smoothness of operation. Several times the landing gear shock struts were fully extended, the tires doughnut-shaped, and the spring-lines taut. But, tethered flight was prohibited prior to full-scale tunnel testing.

Following these tests, the K-16B was shipped to NASA, Ames Research Center (ARC), for full-scale tunnel testing.

Before installation in the tunnel all systems were checked out on a static thrust stand where hover data in the areas of rotor thrust and control effectiveness were also taken. The wind tunnel operation was concerned with rotor thrust, control effectiveness, wing stall in transition, and blade flapping and damping in forward flight. The installations of the aircraft both on the thrust stand and in the tunnel are shown in Figures 7 and 8.

The analysis of the data indicates that the methods developed for the analytical treatment of propulsive rotor performance are valid - that the deficiency in performance disclosed by the data can be directly attributed to non-optimum test hardware. Wing stall buffet in transition may limit the effectiveness of the K-16B flight research program. No problems arose with blade flapping and damping in forward flight - test results agreed very well with analytical predictions that showed the rotor to be well damped with very little flapping.

At low flight speeds the rotor operates the same as a helicopter rotor with offset hinge. At cruising speed

Figure 6
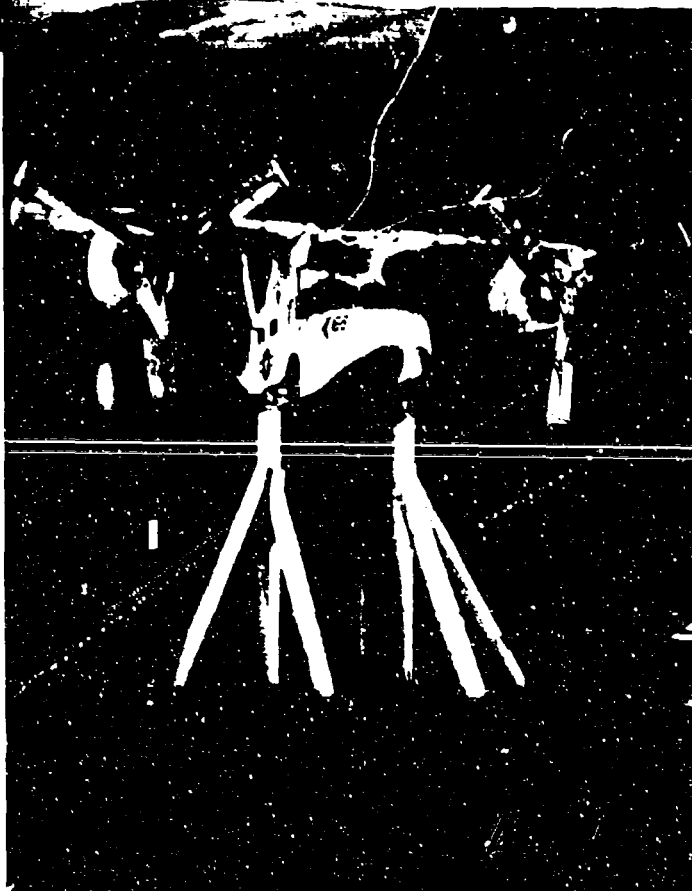Tie-down Operation

20

Figure 7

Thrust Stand
Installation

Figure 8

Full-Scale
Wind Tunnel
Installation

the cyclic flap control is phased out and blade motion is defined solely by the airplane attitude and motion. A theory was derived describing the force and motion characteristics of a flapping rotor operating in high-speed conditions, and model tests carried out to verify its qualitative accuracy.

The rotor derivatives with respect to the perturbation velocities are obtained from methods similar to those used in helicopter analyses. But, a further complication is introduced because the forces and moments generated by the rotor-wing combination are with respect to the wing axes system; thus, a resolution is necessary to relate the forces and moments into the stability axes system.

The rotor derivatives are complex due to the implicit relationships that exist between the rotor variables. This system is necessarily further complicated by the incorporation of a factor to account for a variable inflow, and by the increase in rotor natural frequency caused by the offset hinge. All this requires that existing theory be modified to include a cyclic variation of inflow and lift coefficient which occurs for a rotor operating at other than its natural frequency. A description of these rotor derivatives will be found in KAC Report G-113-7(12).

A negative damping contribution is indicated by this method, whereas a positive damping is calculated using the simplified helicopter methods. The principle difference is the negative damping contributed by the rotor H-force at a speed condition. However, a flapping hinge offset will always result in a relatively smaller negative contribution for the offset always contributes a positive damping term (NACA TN3492)(52). This damping term is a result of the hub moment due to pitching velocity. At cruising speeds, the positive damping due to the hub moment is balanced by the negative damping due to the rotor H-force.

At high flight-speeds the forces and moments produced by a rotor are essentially a function of blade geometry, mass distribution, motion, and the position and motion of the rotor shaft. Once these parameters are known, the forces and moments produced by the rotor become a straightforward integration operation. All the terms except the blade motion are readily available; hence, the basic theoretical problem is the prediction of the blade motion.

Because of these considerations the K-16B 1/8-scale model rotor and instrumentation was borrowed from DTMB to conduct company-funded tunnel tests. In the end, however,

22

we used only the instrumentation, and built a model rotor that was inertially and aerodynamically similar to a full-scale rotor.

Test conditions were set in excess of K-16B conditions, and were the equivalent of a full-scale 2.2g symmetrical pullout at 390 knots. The full-scale pitch rate would be 4.3 degrees/second.

The theory predicted that for these conditions the longitudinal and lateral flapping should be zero. The longitudinal flapping due to a steady angle-of-attack of 7.4 degrees should be 3.43 degrees, and the lateral flapping 5.54 degrees. However, the gyroscopic moments acting on the blade due to the pitching rate produce strong negative flapping and numerically cancel the flapping due to angle-of-attack.

Review of this preliminary test data indicates agreement with theoretical predictions - longitudinal and lateral flapping were zero.

DYNAMICS

Dynamic structural design was approached by conventional mechanical stability and flutter analyses, substantiated by vibration testing to confirm calculated frequencies and mode shapes. While precise correlation between calculated and test frequencies was not obtained, analysis proved in every case to be conservative.

A vibration survey was performed on the rotor/wing combination available from the aerodynamic research test stand. In addition, an analysis was made of the mechanical instability characteristics of the airplane configuration both in flight and on the ground (KAC Report G-113-10)(15). It was determined that the ranges of mechanical instability associated with the wing modes were the most critical. To insure freedom from instability in these modes for both ground and flight operation, it was necessary to install a centering spring in the lag freedom of the blades so that the static in-plane natural frequency of the blades was 50 r/s. With this blade frequency the remaining modes were not critical.

The flutter analysis followed conventional practice, and indicated that no flutter problem exists in the airplane (KAC Report G-113-6(11).

23

Upon completion of the airframe a mechanical instability and flutter survey was run. This test setup is shown in Figure 9. Structures of equivalent mass and inertia replaced the engines, transmission, and rotors. Excitation was effected by rotating eccentric weights in the plane of the rotor; excitation force levels were adjusted by changing the eccentric masses. A sweep of the frequency range from approximately 80 rpm to 1000 rpm was made, both wing down and wing up, at discrete percentages of airborne weight. It was found that rotor and structural damping were more than adequate to preclude divergent oscillations in those regions of resonance that appear in the operating range. These tests are reported in KAC Reports G-113-27 and -30 32, 35).

In KAC Report G-113-28(33) is presented an analysis to determine the torsional natural frequency of the drive system. The purpose of the analysis was to insure there were no natural frequencies near rotor (3 per rotor rev) or drive system (2 per engine rev) excitations to cause high torsional stresses in the drive system. The 3-per-rotor-rev excitation is due to the three-bladed rotor; the 2-per-engine-rev to the drive shaft universal joints. It was found that the natural frequencies obtained are out of the range of the 3-per-rev excitation, but not of the 2-per-rev when the original aluminum drive shafting is used. Replacing the aluminum shaft with a dimensionally similar steel shaft brings the natural frequency out of the critical range.

The propeller-nacelle-wing combination was also investigated for whirl flutter for various ratios of forward velocity over tip-speed (KAC Report G-113-41)(40). The analysis was divided into three stages of increasing complexity: (1) inertial system with rigid hub (without blade flapping or aerodynamic loads); (2) inertial system with articulated hub in flapping; (3) complete system which adds the aerodynamic forces to the inertial system of (2). This approach has the advantage of allowing a closer check of the equations of motion, and permitting the observation of the effects of the addition of more complex terms in the system. Further, the effect of the blade flapping degree of freedom on the gyroscopic coupling in the inertial system may also be noted. Results of the analysis indicated the absence of this phenomenon over the range of ratios that had to be considered.

Figure 9

Vibration and Flutter Test

25

STRESS ANALYSIS

Static Structure

Structural problems encountered during design were few in number in view of the conventional design approach; pivotally mounting the wing to the fuselage was the main exception. Again, conventional structural elements were used, so few problems from a stress analysis point of view were encountered.

The analytical treatment of structure followed the normal pattern of development of flight, ground, and water loads (KAC Reports G-113-14, -15, -16)(19/21), and fuselage/wing attachment loads (KAC Report G-113-22(27). Various stress analyses of such as the wing, nacelle, fuselage, tail, alighting gear, transmission mount (KAC Reports G-113-19(24); -23(28); -25(30); -26(31); -18(23); and -17(22), respectively) were also published. The wing was proof-load tested in two conditions adjudged critical; these tests are reported in KAC Reports G-113-11 and -12(16/17). In the event of a deficiency in the JRF-5, the extent of the modification or the limits of operating restrictions were to be reported to the Bureau for decision whether the modification would be made or the operating restriction accepted.

The aircraft was designed structurally to Specifications MIL-A-8629 Class VU, and MIL-S-8698, with additional requirements written into an addendum to attempt to fill the gaps in these helicopter and fixed-wing specifications.

The wing was proof-load tested in two conditions determined to be most critical – wing bending in 3-point landing, and wing torsion in symmetrical landing approach. Loads were applied through whiffle-trees by load-trays and hydraulic cylinders. The test setup can be seen in Figure 10. In both tests proof-load was reached with no apparent structural inadequacies. As load was being removed after the last test, a malfunction of a test actuator resulted in an inadvertent over-load and local yielding of the wing. For the forthcoming full-scale tunnel operation, structural integrity was restored by a temporary repair; a suitable permanent repair, adequate for safe flight, has been designed (KAC Report G-113-12)(17).

The fuselage stress analysis showed the structure to be adequate for the design loads except for two landing conditions – a drift landing and a one-wheel landing. Both conditions result in negative margins on the main landing
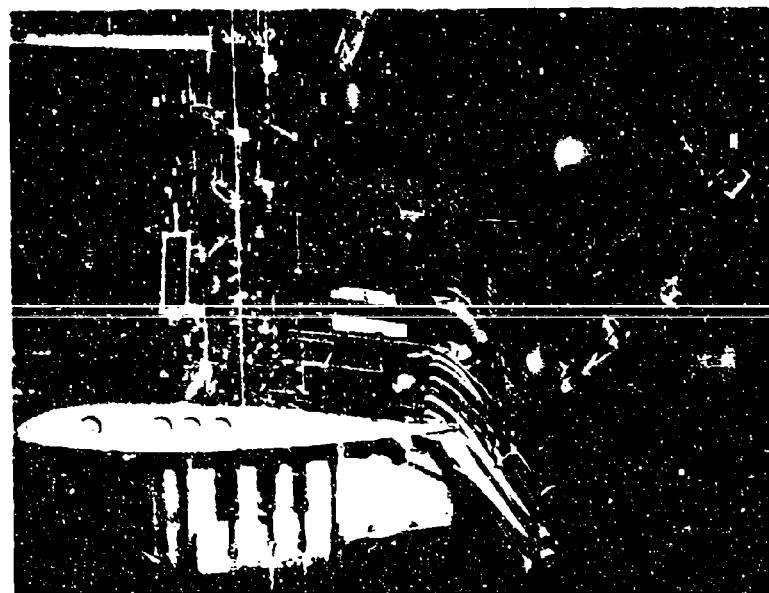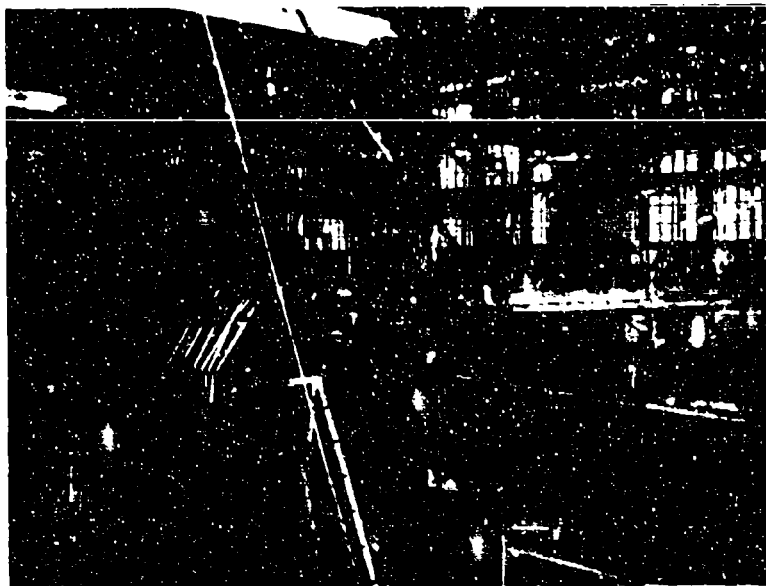
Figure 10

Wing Proof-load Tests

gear backup structure. A modification that will eliminate the negative margins is presented in KAC Report G-113-25 Appendix 1 (30).

The alighting gear stress analysis disclosed that the JRF-5 is compatible with the K-16B criteria except for a negative margin in the upper drag link as a result of a drift landing condition. A method of eliminating this negative margin is presented in KAC Report G-113-18 Appendix A (23).

The empennage analysis (KAC Report G-113-26)(31) indicated that the elevator, rudder, and rudder tab were more than adequate for the design loads. Because of the need to increase the vertical fin area by adding a tip cap to improve directional stability, stiffeners had to be added to the existing spar to increase bending strength. It was also necessary to add doublers to the horizontal stabilizer spar-cap to accommodate the higher required flutter speed of the K-16B.

The stress analyses of both the nacelle and the transmission mount show these structures to be adequate for the critical air, ground, and water load conditions (KAC Reports G-113-23, and -17 (28,22) respectively.

Dynamic Systems

The dynamic systems are defined as the airframe control system to the rotor azimuth and to the surface controls; the rotor including blade flap controls from and including the azimuth; and the drive system. Stress analyses of these systems were supported by controls proof-load test, blade-flap control system fatigue test, blade-flap retention fatigue test, and power-and-drive system endurance test.

The aircraft flight control system consists of conventional components such as pushrods, cranks, quadrants, and cables. Because some of the portions were superimposed on existing JRF-5 systems, the JRF-5 design limit loads were used. The stress analysis indicates that all components are structurally acceptable (KAC Report G-113-9)(14).

Upon completion of the controls installation, a system proof-load test was performed. All control systems - airplane mode, helicopter mode, and engine controls - to the azimuth and to the control surfaces were tested. Appropriate loading beams were installed at the cockpit controls, and surface locks installed as required. Loads were applied by load trays or calibrated hydraulic cylinders. All tests were

made with no apparent yielding of the systems or system support structure. Controls excursions were performed with no interference in the systems (KAC Report G-113-13)(18).

Although the stress analysis of the propulsive-rotor (KAC Report G-113-24)(29) disclosed no negative margins, two failures in the flap retention during endurance stand operation caused authorization of fatigue testing of the retention system. This was expanded to include fatigue testing of the blade-flap control system.

The retention fatigue test (KAC Report G-113-35) (39) led to significant improvement in the life of both the flap and its retention. The configuration cycled in the last test was duplicated for use in the tunnel program at ARC, where it was used with complete confidence. This fatigue test operation is shown in Figure 11.

The level of operation for the controls fatigue test (KAC Report G-113-33)(37) was established at the estimated maximum continuous load level. Although the system demonstrated adequate life at this level, during actual operation at continuous higher cyclic input levels, operating lives of bearings were unacceptably short. The fatigue setup is shown in Figure 12.

The two rotors are driven through reduction gearboxes by YT58-GE6 engines in wing-mounted nacelles. Power take-offs from the main reduction gearboxes are interconnected through the wing to permit either engine to drive both rotors in the event of a single engine failure.

The structural integrity of all details of the drive system was substantiated using approved methods of stress analysis (KAC Report G-113-21)(26). Though some areas showed higher levels of pitting and bending stresses than could be accepted for unlimited life, they are within the working limits of the experimental nature of the program.

A power-and-drive endurance bench stand, shown in Figure 13, was used to qualify the rotor and drive system (KAC Report G-113-34)(38). Because of the similarity of the left-hand and right-hand drive systems, the endurance stand duplicated only the left-hand installation of engine, drive system, and rotor. In addition, the cross-shaft installation to and including the accessory-drive gearbox at the aircraft centerline was included. This program was delayed by: (1) a drive shaft failure, and (2) two failures in the blade-flap retention.
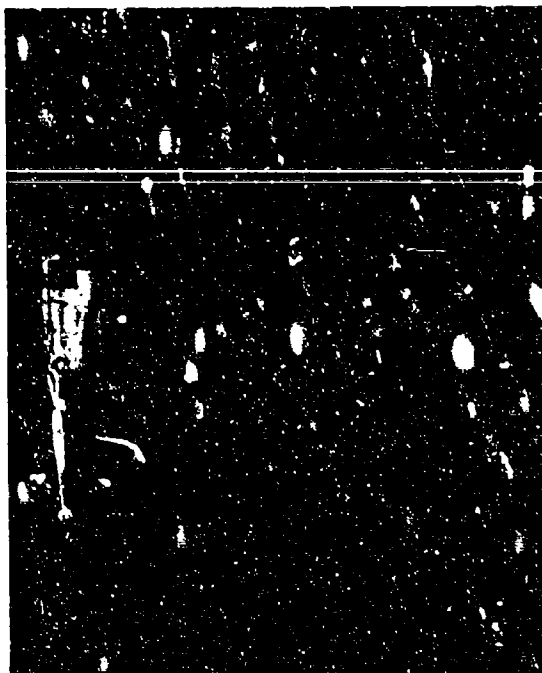
Figure 11

Blade-flap
Fatigue Test

Figure 12

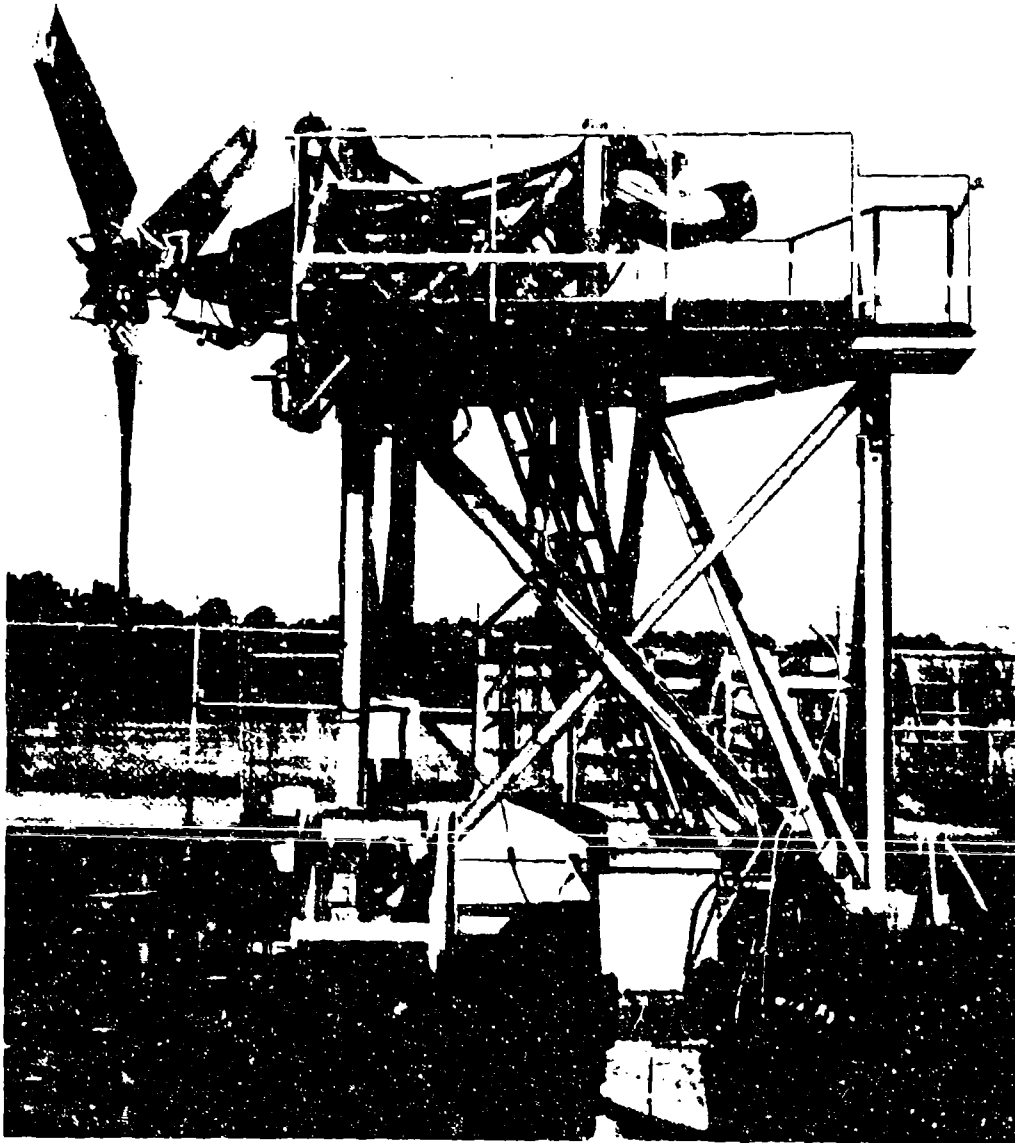Blade Flap Control
Fatigue Test

30

Figure 13

Power and Drive
Endurance Bench Stand

31

During this discussion of analyses and tests a number of problems were mentioned. These problems and their actual or probable solutions are touched on in the "Test Article Development" section.

TEST ARTICLE
DEVELOPMENT

Preceding sections presented a review of the various analyses and tests that evaluated the V/STOL capabilities of the K-16B. A number of difficulties were mentioned. This section will touch problems actually solved, and remaining problems with their probable solutions. It is divided into major subsystems of propulsive-rotor, airframe, and power-and-drive.

PROPULSIVE ROTOR

It is possible to accurately predict propulsive-rotor performance - final analysis and data show good correlation. The rotor that was tested developed thrust somewhat short of the original prediction. This was not entirely unexpected. The program did not permit incorporating product improvements upon the availability of additional criteria resulting from previous testing and refinements in analytical techniques. The program was designed as a research effort, and in such a role the rotor configuration that was tested has proved to be a useful tool.

Hover Characteristics

In the design of helicopter rotors the assumption of uniform inflow is commonly used to determine cyclic effectiveness. This approach had been applied to the propulsive-rotor. Data from the Phase II research test stand indicated that a more rigorous variable inflow theory must be applied. Comparison of test results with calculations based on the latter theory disclosed excellent agreement.

Control in hover (and transition) is obtained by blade-flap cyclic deflection, in the proper phase, to rotate the tip-path plane and consequently the direction of thrust. This tip-path rotation plus the blade centrifugal forces acting on offset flapping hinges, produces moments to attain precision helicopter-type control.

Cyclic sensitivity, which is the amount of flapping for a particular cyclic flap deflection, is a function of the flapping hinge offset, pitch-flapping coupling, the first mass moment, and the thrust coefficient. A particular control moment can be generated by proper choice of these characteristics.

When the cyclic sensitivity analysis is compared with the static thrust stand test points, agreement is good. When the sensitivity is used to determine total control moment, agreement again is good. Because directional control is a function of cyclic sensitivity, it too will be as predicted. Our analysis carried the measured components of the control moment to a point that separates the aerodynamic results from the mechanical system. Such a common base for comparison is the wing axis system before control compensation is introduced. When this is done, the directional control in the wing axis system is found to be just as predicted by the final methods of analysis. The results of the tests at NASA, Ames Research Center (ARC), were affected by an off-optimum control compensation in the mechanical system (NASA TN D-2538)(53), designed to earlier estimates of control characteristics.

Pitching moment test data (Ibid), when shown as a function of longitudinal flapping, is in good agreement with analysis. If plotted as a function of longitudinal stick position, agreement again is good. However, it was less than the predicted moment (KAC Report G-113-4)(12). The available control was limited to 0.6 of the design value because of an interference in a swashplate. In addition, full hovering thrust was not produced during the tests, and cyclic sensitivity is a function of thrust coefficient.

Transition Performance

In transition, aircraft operation is determined in part by the thrust of the rotor, and of control moments and forces by the rotor about and along the three axes.

One purpose of the blade-flap is to improve the static thrust capability without penalizing the high-speed forward flight efficiency which a highly cambered or wider blade would do - its purpose is not to improve the rotor-blade efficiency throughout the speed range by continued flap deflection. The concept allows the designer to select a blade profile and activity factor compatible with the high-speed propeller requirements, but by collective flap deflection attain the higher lift coefficients required for hover performance. For the high-speed configuration the flaps are fully retracted, returning the blade to the thin profile needed for efficient propeller performance. The collective flap is reduced as the thrust decreases, and when halfway through the transition the flaps are fully retracted. The transition tests in the wind tunnel (NASA TN D-2538) (53) were run with a constant 13 degrees of blade-flap collective deflection, so poorer propeller efficiencies would

34

be expected at the higher speeds tested. The appropriate configuration for the ARC test point at 150 knots is collective flap fully retracted and blade pitch at 34 degrees. The run at this velocity was made in the transition configuration and merely established an anchor point for the curve of propulsive-rotor performance in transition.

The comments concerning control in the hovering mode also apply in transition. The cyclic sensitivity does drop off however, principally because of the reduction in thrust coefficient with speed. At the same time the phasing gradually shifts as a function of the advance ratio in the transition - decreasing as the advance ratio increases, then increasing as the advance ratio decreases again. During this time the tail is becoming effective.

Although the cyclic sensitivity was greater than anticipated, because of wing stall the untrimmed pitching moment was so large it severely curtailed the control available for maneuvers.

Performance Improvement

To improve the performance of the rotor, a number of configuration changes (blade flap extent, solidity, tip speed, twist, airfoil section) have been considered. Two possible configurations were reviewed. The first is essentially the same as the present rotor in over-all dimensions. The second has an increased diameter, chord, and flap span. Both take advantage of an increase in rotational speed, and a clean-up of blade tip design. (The present blade-flap control linkage results in higher aerodynamic drag at the tip. It is not possible to precisely calculate the power loss due to this added drag, but it is estimated at 3 to 4 percent.) Table I describes the basic (existing) configuration and the two revised configurations.

Table I

Rotor Particulars

	Basic	Blade A	Blade B
Diameter	15'2"	15'2"	15'10"
Blade Chord	18"	18"	20"
Flap Extent, r/R	.54 to .98	.54 to .98	.35 to .98
Tip Speed, max	575 fps	635 fps	664 fps
Airfoil of Outboard 50% of Blade	$163^5 09$	16509 (modified)	16509 (modified)
Airfoil Design Camber	.35	.5	.5
Tip Region	Dirty	Clean	Clean

35

The hover performance map for the basic blade is shown in Figure 14; for Blade A in Figure 15; and for Blade B in Figure 16. These maps were used to determine the hover capabilities of the new configurations, shown in Figure 17. The effect on high-speed performance is shown in Figure 18.

It will be noted that by virtue of the blade flap, static thrust has been optimized without penalty in cruising propulsive efficiency. It can be concluded that the degree of rotor modification represented by Blade A, when powered by a T58-GE8, will provide sufficient margin of static thrust to assure adequate vertical flight performance of the K-16B at any feasible gross weight.

The concept of integrated design lift coefficient for estimating propeller performance is based on the assumption that the propeller operates at the design angle of attack, $\propto C_i$, at each station along the blade. For the normal propeller, designed for maximum efficiency in cruise, the concept is valid because the radial variation in ideal angle of attack can be made coincident with the twist distribution for cruise operation. In this case static thrust is of secondary importance. For VTOL aircraft, static thrust is of primary importance.

Efficient high static thrust requires that the camber be high and the twist in the order of -12 degrees and linear. A blade designed with these characteristics will have poor efficiency at the low thrust coefficients required for cruise. The propulsive-rotor, because its blades are of variable camber, reconciles the two requirements.

Figure 19 compares the static figures-of-merit for two conditions of the improved Blade A. In the one condition, $\delta_o = 0$ degrees, or the equivalent of an invariant propeller. In the other condition, $\delta_o = 5$ degrees. In the first condition, note that with basic camber alone the blade cannot generate the required thrust at the design of 10,000 pounds. However, increasing the camber by 5 degrees of flap deflection, the 10,000 pounds of thrust produced at a reasonable figure-of-merit. By retracting the flap a propeller cruise efficiency of 0.85 is attained.

A conventional propeller designed for this same cruise efficiency (0.85) would be equivalent to propulsive
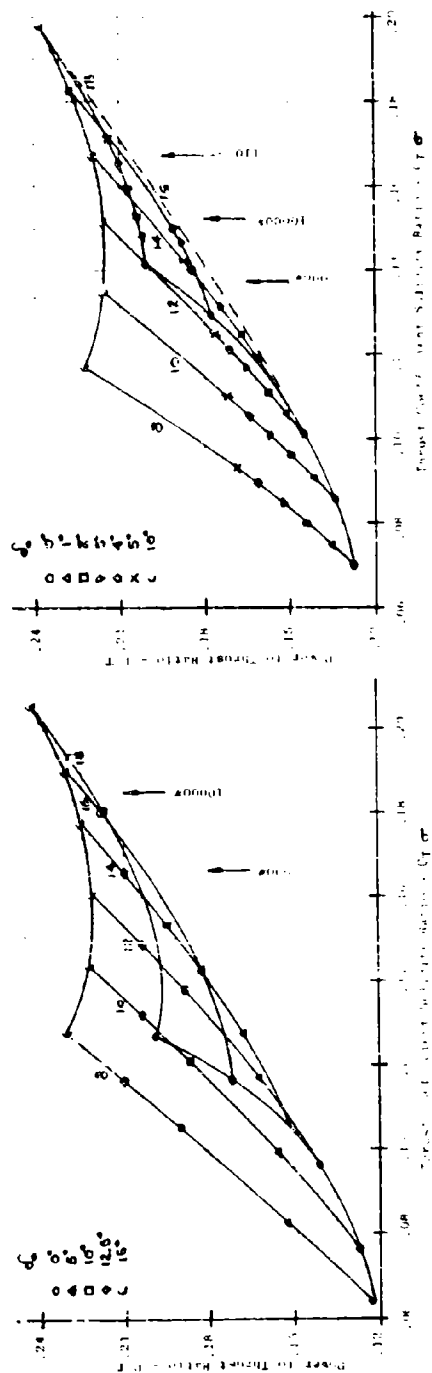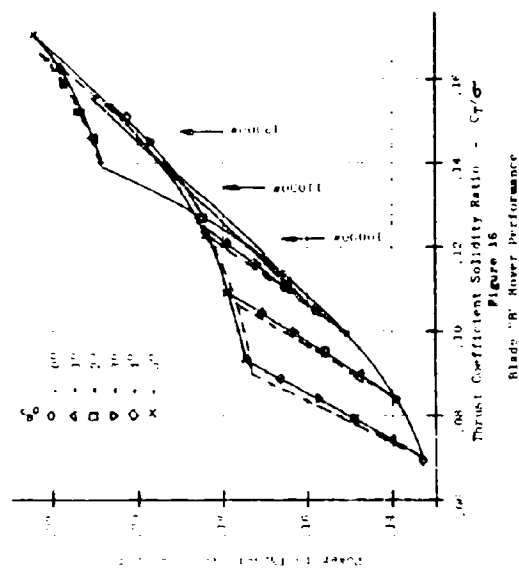
Figure 14

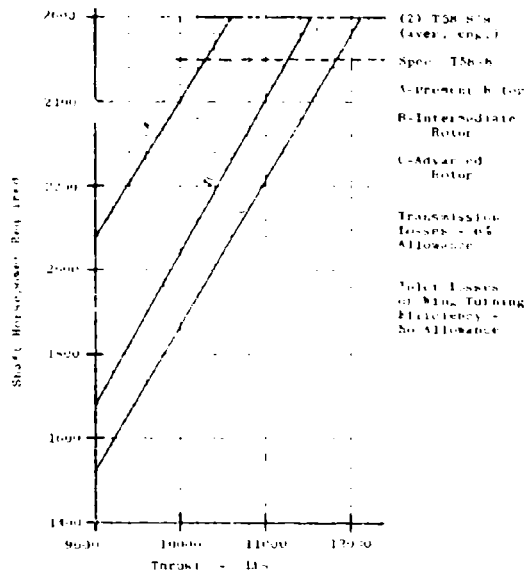Basic Blade Hover Performance

Figure 15

Blade "A" Hover Performance

Figure 16

Blade "B" Hover Performance

37

Figure 17
Hover Capability

Figure 18
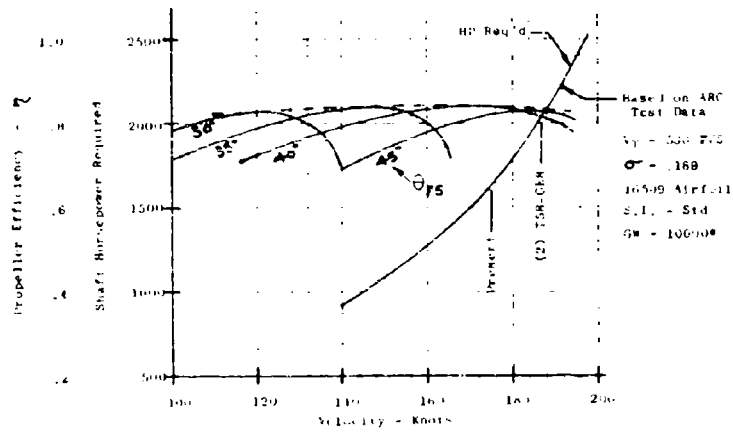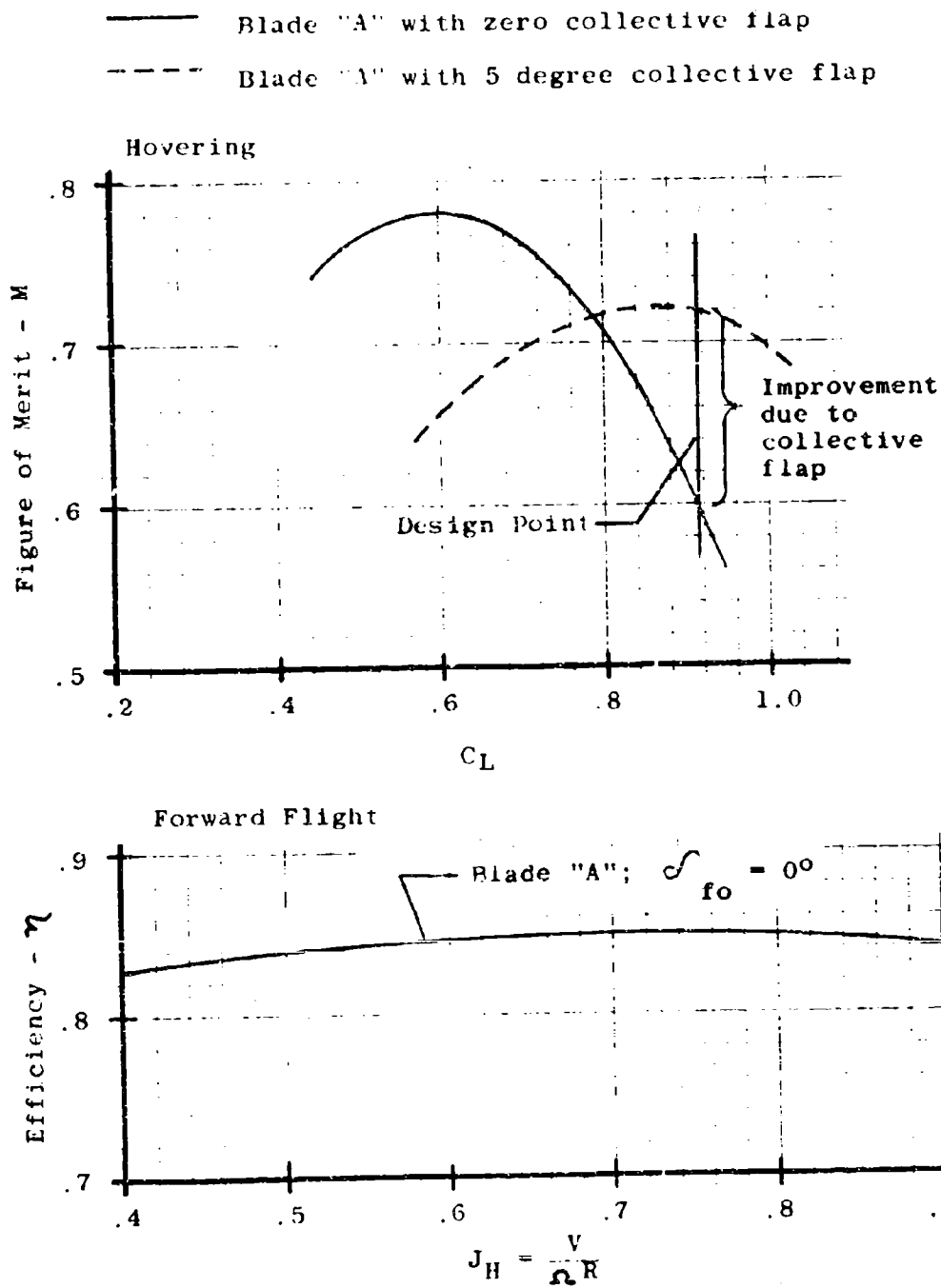K-16B High Speed Performance

38

Figure 19
Propulsive Rotor Performance

rotor "A" with flap retracted, in terms of geometry, twist, and camber. Hence it would have the same low figure-of-merit in hover, and therefore would be unacceptable. Were the propeller designed for a higher cruise efficiency, there would be a further degradation in hover performance. To meet the required hovering performance, the blade chord, number of blades, or amount of camber would have to be increased, resulting in poorer propulsive efficiency in cruise. To develop 10,000 pounds of thrust with the present test rotor requires a collective flap deflection of 13 degrees for a C_T/σ of 0.185, resulting in a figure-of-merit of 0.62. By increasing the tip speed of Blade A from 595 to 635 fps the C_T/σ required for 10,000 pounds of thrust is reduced to 0.152, which requires only 5 degrees of collective flap for a figure-of-merit of 0.72. Indeed, 11,000 pounds of thrust can be developed at a C_T/σ of 0.166 with 6 degrees of flap and a figure-of-merit of 0.71.

This configuration change demonstrates the performance that is possible with the K-16B rotor. Although the analysis concentrated on improvement of hover performance, the concept is not that narrowly defined. It lends itself to performance flexibility in systems trade-off studies. Consider the following plot. This is a hover per-

Cruising Efficiency, η
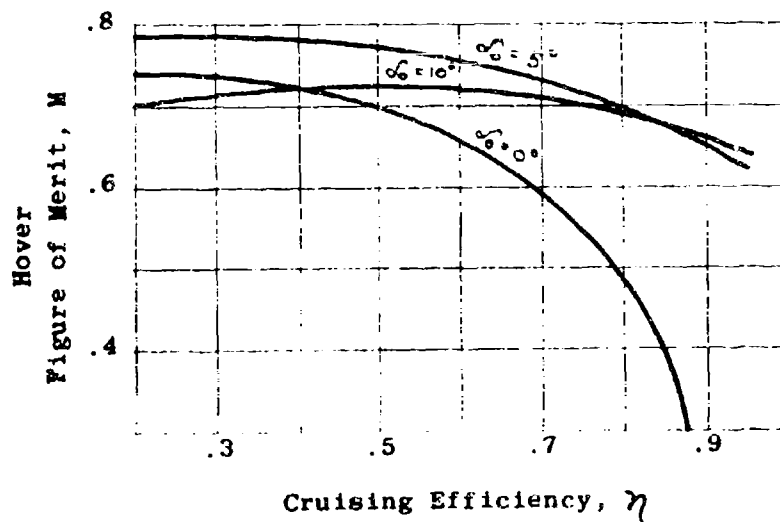
formance map crossplotted to cruise efficiency. It is based
on estimates of performance of one airplane, and varies
propeller blade camber. The propulsive-rotor blade-flaps
are appropriately stowed in cruise, of course

Note the curve for an invariant-camber propeller,
α_o = 0°. When designed for hover, its figure-of-merit is

in excess of 0.7 but its cruise efficiency is low. Now con-
sider the other extreme of the curve. Cruise efficiency is
high but hover efficiency is very low. The curve for collec-

tive flap of 10 degrees (α_o =10°) is indicative of the per-

formance improvement with variable camber blades. Note
that at the same maximum cruise efficiency of the fixed-
camber blade there is just a modest decrease in hover figure-
of-merit. It can also be seen that a range of trade-offs
can be made between hover efficiency and cruise efficiency.
And, when a reduced efficiency, either hover or cruise, is
acceptable, it is not improbable that there may be a cross-
over point. Then there may be no performance advantage of
the propulsive-rotor, but the hover control advantage will
continue to exist.

The flexibility of the concept makes it possible
to configure a propulsion unit to be the best compromise
for a system mission profile, whether it be long range and
short hover time, short range with long hover time, or any
mission in between. Unlike the relative trade-off inflex-
ibility of an invariant-camber propeller, the propulsive-
rotor allows a systems analysis to balance cruise efficiency
against hover efficiency.

Component Hardware

The rotor hub had been designed as a fully artic-
ulated system. Analyses performed in an Air Force study
(Egerton and Giansante - 54) indicated a substantial poten-
tial weight savings of a semi-rigid rotor as compared to a
fully articulated rotor. Several test runs with le d-lag
freedom locked out were made on the Phase II test stand. A
marked improvement in the smoothness of operation was noted.

Though the stress levels recorded during this run-
ning were within the limits of test stand operation, the
stress levels that would be encountered in maneuvering
flight would call for a complete redesign of the hub. In-
stead, a unique lead-lag restraint was designed. It provides
the in-plane freedom of blade motion to relieve blade and

41

hub stresses of the original design, yet the natural frequency of the complete system is so tuned that mechanical instability is avoided. Obviously, the weight saving of a complete redesign could not be obtained; however, with the primary objective that of obtaining research data, the weight penalty could be tolerated.

Blade-flap retention is provided by a tension-torsion cable mechanically secured at the root of the blade and attached to the flap spar. In the original design the cable was attached to the spar by a threaded connection to a fitting bonded to the spar. A connection of this type was more amenable to fabrication, assembly, and handling.

During power-and-drive bench stand operations, a failure occurred in a thread relief of the fitting bonded to the flap. Metallurgical inspection revealed a fatigue failure resulting from flap bending loads. The cable end fitting was changed to a ball-and-socket arrangement that becomes permanently bonded into the flap through a phenolic block.

A second retention failure occurred, this time in the bond between the phenolic block and the spar structure. Inspection disclosed an incomplete bond between the phenolic block and the plywood leading edge. The designed area of the bond was more than sufficient to support the loads - this was substantiated by pull-tests of the two remaining flaps. However, to reduce the sensitivity to quality variations - a factor in this failure - the joint layup was redesigned. Subsequent flaps have given no evidence of difficulty.

Further significant improvement in flap reliability developed as a result of parallel fatigue testing (KAC Report G-113-35)(40). In all, seven fatigue tests of the flap and retention were performed, permitting establishment of reasonable S-T curves for wind tunnel and flight operation.

Although the flap configuration used during the ARC tests had adequate fatigue life, it is suspected that structural deformation of the flaps, which were rather flexible, may have affected rotor performance.

By applying the construction techniques used in the aluminum-spar, honeycomb-stiffened UH-2 helicopter servo-flap to the K-16B flap a decided improvement in flap stiffness can be attained. The only essential difference from the UH-2 flap structure would be a fiberglass skin, necessary to allow for the relatively sharp twist of the K-16B flap. Dynamic analysis of this flap also indicates that fatigue strength

will be far greater than that of the present flap.

The economics of the program dictated austerity in all areas. System trade-off studies resulted in the present blade-flap control linkage, which is a push-pull system consisting of links, a long spanwise rod, and an offset crank driving a flap horn by an external chordwise rod. The trade-off studies reviewed the impact of dual hydraulic actuators versus single hydraulic actuators to operate the rotor swashplate. If a suitable mechanical system is available in the event of a hydraulic failure, then the expense of a dual system can be avoided. In this case, a hydraulic failure will place the rotor control loads on the pilot's stick; these must be within the pilot's capabilities. The control system geometry that was selected permitted including a mass balance that introduces a cyclic centrifugal force in opposition to the aerodynamic force produced by cyclic flap deflection, resulting in emergency loads within the pilot's capability. This allowed the use of a single actuator.

Operation disclosed high pressure-velocity (P-V) loads on many of the bearings, and serious lubrication problems at the blade tip because of the high centrifugal forces on the components. These problems are particularly manifest at sustained higher levels of cyclic input, such as would be expected during wind tunnel operation.

Belleville springs were used in the tuned lead-lag system of the rotor. As a result of several fatigue failures, a spring development program was pursued. The end requirements compelled a change of material, control of the grain orientation of the metal, and improved fabrication of the springs. Modified springs were in the airplane during testing at ARC. No evidence of malfunctioning appeared.

Component Improvement

The K16 rotor concept has been damned by faint praise because of these problems. Theoretically, the concept is considered a unique and promising solution to the control and static thrust problems of propeller-driven V/STOL aircraft. Practically, it has been denigrated because of the difficulties we experienced with research hardware. This judgement does not consider the state-of-the-art advances in bearing and structure technologies in the ten years since the propulsive-rotor was first designed.

As a result of the emphasis the Military has placed on the contribution of relubrication of rotor and control system oscillating bearings to the maintenance bur-

den, and of the demands of the space sciences, major advances
have been made in the development of self-lubricating bear-
ings and of elastic hinges; specifically, the KACarb bearing
and the elastomeric bearing.

KACarb bearings have a dry, solid, permanently-
lubricated bearing surface that is designed for high-load,
high-velocity oscillating or rotating conditions. They have
a consistent and low coefficient of friction, and P-V capac-
ities that are a minimum of four times greater than the best
quality aircraft bearings heretofore available. They are
also unique in that they can operate for short periods at
excessive P-V loadings with no damage to the bearing. In one
application, they operated for a limited time at a P-V load-
ing in excess of 900,000 - more than ten times the design
limit - with no damage to the bearing.

The elastomeric bearing is constructed of alter-
nate layers of metal and elastomer. The applied load is es-
sentially normal to the lamination orientation; the function-
al displacement is parallel to the laminations. Lamina
thickness is small for the elastomer to operate in the visco-
elastic range, and at the same time, support appreciable com-
pressive stress without extrusion at the edge boundary.

Both types of bearings were selected by Kaman for
the blade articulation of a rotor re-entry vehicle wind tun-
nel model for ARC (Contract NAS 2 - 2107). The model, shown
in the figure, is a four-foot diameter, semi-articulated
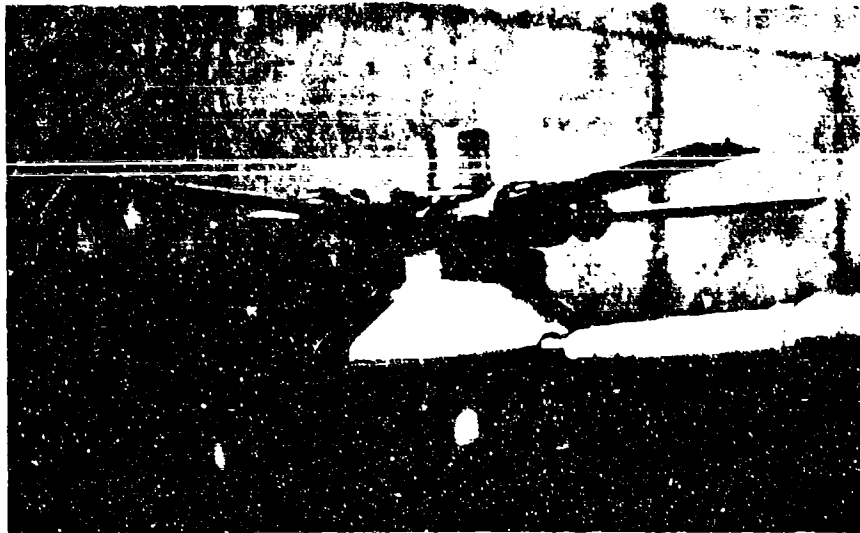
rotor complete with both cyclic and collective pitch. The elastomeric pitch bearings are but 1-3/8 inch in diameter. The flapping bearings are KACarb bearings.

The application involves operating frequencies in excess of 100 cps - well beyond the state of the art for normal oscillating bearings - operating rpm of 6300, and a design load in excess of 10,000 pounds. Recent operation was at M = 3.5 in gliding flight with cyclic and collective input. After 70 hours, the bearings were inspected - and reinstalled in the model.

In the original propulsive-rotor, the flap control system had the most critically loaded bearings operating at a frequency of about 12 cps, operating rpm of 725, and a design load of 1200 pounds. A damaging factor was the loss of lubricant because of the CF environment. (KACarb and elastomeric bearings require no lubrication.)

Configuration studies have evolved a new system geometry of considerable promise. This is made possible by separating into three systems the functions of supporting the end shear load on the flap, the centrifugal retention load of the flap, and the hinge moment required to drive the flap. The entire control system is removed from the high CF environment at the blade tip and is operated inboard where the loads are considerably lower. Component fatigue lives are greatly improved, and the new system will be stiffer than the original system by an order of magnitude. (Control system flexibility was a problem during testing.) Insufficient control bearing failure rate data are available to run a quantitative reliability analysis, but a qualitative analysis of the new system with KACarb bearings shows a reliability improvement approaching two orders of magnitude. Removal of the control cranks, external actuating rod, and flap horn at the tip results in an aerodynamically efficient airfoil in the high-velocity tip area.

Hub configuration studies have led to an integrated rotor-and-hub assembly. The physical characteristics of a propulsive-rotor blade are such that in-plane bending loads can be easily accommodated by the blade, permitting elimination of lead-lag bearings. A swashplate for flap control, and an actuator for blade pitch control, are integral with the hub assembly. Full advantage is taken of the characteristics of KACarb and elastomeric bearings. The case would bolt to solid structure, and because bending loads are not taken in a propeller shaft, a light quill shaft can drive the rotor. By integrating the blades, hub, and flap controls into a total system, the propulsive-rotor is removed from the

specialty design field characteristic of helicopter rotor
systems. It can be applied as a sub-system to any propel-
ler-driven V/STOL airplane.

AIRFRAME

During the later stages of the research test stand
the Model K-16B aircraft was authorized for the purpose of
assisting the Bureau in the establishment of both flying
qualities and structural specifications for the coming gener-
ations of V/STOL aircraft.

Performance

One phase of the program required a wind tunnel
stability investigation using a powered 1/8-scale model.
Aerodynamic predictions of suitable stability were generally
substantiated except for directional instability with the
wing down, wing flaps retracted, and rotors on. It was de-
termined that:

- the basic very high wing configuration
  contributed large side-wash character-
  istics that kept the vertical tail
  angle of attack low in the low yaw
  range.
- the rotors contributed a large desta-
  bilizing yawing moment variation:
- the dynamic pressure at the tail was
  not appreciably reduced.

Strain-gage balance data of the propeller side
force indicated that the model propeller contributed about
twice the destabilizing yawing moment coefficient that the
full-scale rotor was estimated to do. The model configura-
tion was made stable using either a combination of end-
plates and 20-degrees of dihedral of the horizontal tail, or
by additional area to the upper portion of the vertical tail.
Of the two, the latter was chosen.

When the aircraft configuration was initially es-
tablished, a trade-off was indicated between simplicity of
wing structure and wing stall in transition. It was reasoned
that though there would be transition stall, because of the
low "q's" the stall would be of relatively little signifi-
cance. So, design effort was concentrated on deriving the
simplest and lightest wing structure for a rather awkward
structural situation typical of tilt-wing types.

46

There was no surprise at the indication of transition stall in the model tests, but results from NASA research and the V-76 program seemed to indicate that the stall was a more serious problem than we had previously believed. As a consequence, additional 1/8-scale model testing was programmed. A number of the changes investigated included a drooped leading edge, leading edge slats, and an increase in flap chord. All the changes resulted in improvements in the model's characteristics; the best improvement was with the leading edge slats. However, the improvement with the drooped leading edge was also significant. Because the latter was the simplest change and could be made as a removable glove, it was chosen as the modification to be tried during the full-scale wind tunnel tests.

Full-scale tunnel testing showed that at conditions in which the K-16B was balanced, the wing was stalled. With the plain leading edge, stall was indicated between 25 and 70 knots. Contrary to expectations, the improvements anticipated with the modified leading edge did not materialize. However, even with the wing stalled, in the slipstream the wing tilt-angle required to balance the aircraft in a level flight transition is satisfactorily predicted.

A brief wind tunnel investigation was made at ARC with the drooped leading edge over the wing outboard of the center section, and a leading edge slat over the center section. This slat, just long enough to cover the center section, was one that ARC had used in another program. The slat helped the center section, but then stall would occur between the slat and the propeller slipstream and spread span-wise. As a result, the drooped leading edge had little beneficial effect. No investigation was made using stall fences to halt the propagation.

The horizontal tail was also stalled throughout most of the transition, probably as a result of being in the turbulent wake of the wing. The limited tests with the center section slat produced a considerable improvement in the flow over the tail. But there is a rather large variation in downwash angle over the speed range, causing the tail to produce undesirable nose-up pitching moments during the latter part of the transition. It appears that a variable incidence tail is called for to correct the moments.

An analysis in the following section (Full-Scale Wind Tunnel Test) shows slipstream stall to be eliminated and center section stall to be minimized by using leading edge slats. The elimination of stall will improve the flow over the tail, making it more effective in assisting control of the airplane.

47

The demands made of the propulsive-rotor for K-16B hover capability are supplemented by deflection of the slipstream with a minimum loss through an angle sufficient to make the resultant force vertical.

Initial tests of wing lift effectiveness were made on the Phase II bench stand. They indicated a turning angle of 21.8 degrees. Later, 1/8-scale tests indicated a static thrust turning effectiveness of 20 degrees. The drag data from the ARC tests were so scattered that any angle from 4 degrees to 22 degrees could be obtained. It was possible, though, by working backward from the thrust data and keeping reasonable drag values, to estimate values of 16 degrees and 95 per cent for the turning angle and efficiency, respectively. The analytical procedures, therefore, are believed useful for preliminary prediction of turning angles and efficiencies. This subject is treated in detail in the correlation of the full-scale test data.

The effectiveness of the K-16B wing-flap combination can be further improved by increasing the flap chord. Future designs will probably include larger flap span, narrower nacelles, and possibly double-slotted flaps to further improve slipstream turning angle.

Performance Improvement

The effect of stall on handling qualities is most critical for the approach conditions because the approach will be a low-speed transition condition; the airplane will be in the low-speed condition for appreciable lengths of time; wing stalling makes the flying qualities the worst in this condition. In addition, the effect of stall on the power required is of importance in relation to minimum engine-out speed or minimum approach speed.

The tendency of flaps to reduce stall in transition is primarily a result of the flaps turning the propeller slipstream through a substantial angle, thereby reducing the angle of attack of the wing-propeller combination and consequently the wing angle of attack. The increase by the flap of the basic maximum lift coefficient of the wing is a contributing factor.

The effect of the flap in deflecting the slipstream determines the wing attitude angle required to sustain the aircraft in equilibrium flight at a particular speed condition. By increasing the size of the flap there will be an increase in flap lift effectiveness, thus requiring a

lower wing tilt angle with the resultant lower wing angle of
attack. Further improvement will result from changing to a
down-at-center propeller rotation. Down-at-center rotation
delays inboard stall because of the reduced angle-of-attack,
and the strong tip vortex tends to keep the tip area from
stalling.

As a corrollary, the elimination of wing stall will
improve the flow over the tail, making it more effective in
the transition.

With flapped wings, it is now apparent to make con-
siderable use of leading-edge high-lift devices to avoid
early leading-edge separation, so that maximum potential of
the trailing-edge flaps can be realized.

Structure

The K-16B flight envelope approaches that of
operational aircraft. Extensive static and dynamic struc-
tures stress analyses supported by several tests were per-
formed. On the whole, little difficulty was encountered
because of the conservative approach to design, but a few
problems did arise.

The fuselage and landing gear stress analyses
showed the JRF-5 to be structurally adequate for the K-16B
criteria except for two minor areas. The modifications are
simple and are outlined in KAC Reports G-113-25 App. I (30)
and G-113-18 Rev. A (23).

The wing stress analysis was substantiated by
proof-load testing of two conditions adjudged most critical.
While relieving load following completion of the final test,
a malfunction of test equipment caused a momentary very high
localized load, resulting in some damage to the wing. A
temporary repair consisting of a doubler over the existing
lower skin and covering one rib bay was determined to be
adequate for all projected ground and wind tunnel testing.
A permanent repair, adequate for flight, has been planned.

Structural dynamic analyses were substantiated by
a vibration survey of the complete airframe. Some of the
data showed high lateral peaks at the hub on the upper side
of the operating range with anti-symmetric excitation. The
motion was noticeable on the left-hand nacelle. Local stif-
fening reduced the amplitude and raised the frequency of
this peak out of the operating range. The end result of the
testing found that rotor and structural damping were more
than adequate to prevent divergent oscillations in those

49

regions of resonance that might appear in the operation range (KAC Report G-113-27)(32).

As a result of the evaluation of hovering flying qualities on the NAA analog simulator, the Bureau requested that a stability augmentation system be investigated for the K-16B. It was found that several systems of relatively little complexity had already been developed, including some under contract to the Navy, and that two of the systems were compatible with K-16B requirements. The system selected was a three-axis rate damping system in which gain and authority were 30 per cent, and both gain and authority under the control of the pilot in stepped inputs. The system was composed of stabilization networks and gyros developed for the HTL-7 helicopter and of hydraulic dampers used in the F100C damper system.

POWER-AND-DRIVE SYSTEM

The power-and-drive system has had two particular problems - failure of the sprag-type over-running clutch in the main transmission, and turbine rub in the YT58-GE6 power turbine. Considerable effort has been expended on these problems and, to date, a significant improvement has been made in reducing the rate of failure. Solution of the one problem will undoubtedly lead to solution of the other.

After failures of two of the original sprag clutches, a change was made to a higher capacity unit. Following a failure of this unit, a detailed analysis of the drive system was completed. This analysis, substantiated by test, indicated that a resonance occurred close to two-per-rev of the engine drive shaft.

The effective misalignment of the engine drive shaft is 1.86 degrees. Bench tests of the clutch revealed that sprag engagement caused elliptical deflections of the outer race that were proportional to the applied shaft torque. This caused the clutch to act as a torsional spring of much lower rate than a structural analysis based on radial loading would indicate.

An eleven-degree-of-freedom torsional analysis indicated a natural frequency of 11,755 cpm in the fifth mode. This is almost exactly two-per-rev. An earlier but simpler analysis had not detected this frequency.

To corroborate analysis, and to determine the effect of the torsional damping inherent in the system, a rig

runup test was performed with strain-gages on the driveshaft. Results showed a torsional natural frequency at 11,400 cpm, and vibratory torque (two-per-rev) of +1200 lb-in, or 20 per cent of normal steady torque in the driveshaft. Calculation of the shape of the fifth mode indicated that the vibratory torsion in the transmission input shaft, from the Hookes-coupling excitation in the engine driveshaft, would be 37 per cent of normal torque. During an attempt to obtain further data, the excessively high two-per-rev torque resulted in failure of the sprag unit.

To reduce the resonant amplification, the torsional natural frequencies were shifted by changing the driveshaft from aluminum to a dimensionally identical steel shaft, resulting in a 3:1 reduction in torsional vibratory loads.

The fact that the high vibratory loadings experienced in this case were caused by an effective misalignment of only 1.86 degrees illustrates the potential seriousness of Hookes-joint dynamic excitation.

Concurrent with the sprag clutch problems was a turbine-rub problem. Measurements of the vibration on the YT58 main reduction gearbox indicated a strong two-per-rev of this part. By adding a redundant mount to the gearbox, the vibration level was reduced and life of the power turbine increased slightly.

Further investigation into the source of this vibration indicated that additional reduction in the level could be obtained through redesign of a special universal joint adjacent to the gearbox. When incorporated into the airplane while at ARC, another increment of improvement resulted. A natural question would be - why not use a constant velocity joint? Simply, system geometry and envelope prevented the use of any available standard unit.

These drive system problems are probably due to two factors - the necessary structural and drive system geometry to accommodate the engine installation, and to unknown and unanticipated dynamic problems in the engine itself, introduced by the unorthodox installation.

The limited data taken on the power-and-drive system vibratories indicate that the largest magnitude exists in the engine-engine driveshaft-angle box area. A vibration survey of the airframe-installed system will disclose the source. If in the driveshaft system, a redesign to incorporate constant-velocity Zurn or Bossler joints will eliminate the two-per-rev forcing function of the present joints. If

in the engine, then it must be qualified for all-angle operation, assuming the present nacelle-mounted installation is to be kept. Eliminating these vibratories will eliminate the sprag clutch and turbine rub problems.

Early in the endurance stand operation a failure occurred in the main transmission input shaft. It was a fatigue failure attributed to high vibratory bending moments arising from the cantilever design of the shaft on which the sprag clutch was installed. The shaft was redesigned and the clutch relocated to provide better support for the shaft.

MISCELLANEOUS

Upon completion of the airplane it underwent functional tie-down testing. No particular schedule of operating hours was programmed; tie-down was to be merely a functional checkout. During the testing, which accumulated slightly in excess of 6 hours, all systems were operated both with and without the power-and-drive system running. Operation included traversing the wing through its tilt range with the rotors operating at rated power and rpm; operating the wing-flap system; controls -- both airplane and helicopter; and the various ancillary systems. The remote instrumentation set-up for the full-scale wind tunnel operation was also checked out.

None of the blade-flap control problems that were to arise at ARC and on the endurance stand were evident during this operation. This could well-be because the pilots were not holding high cyclic inputs for any appreciable length of time. The major problem encountered was excessive control break-out forces resulting from a multiplicity of small-diameter pulleys required to accommodate the existing fuselage structure. To correct, a boost system using existing in-house components has been designed.

52

FULL-SCALE THRUST STAND
_____ and WIND TUNNEL PROGRAM

Following functional tiedown testing, the K-16B was
shipped to NASA, Ames Research Center (ARC), for a brief
evaluation in the 40x80 foot wind tunnel. Operation of all
aircraft systems while in the tunnel was by remote control;
similarly, data was taken remotely. It was a mandatory re-
quirement of ARC that prior to wind tunnel tests all systems
- airframe, remote control, instrumentation - be demonstrated
on a static thrust stand. This operation was expanded to
take hover data in the areas of rotor thrust and control ef-
fectiveness - data that could not be taken in the tunnel be-
cause of recirculation. The wind tunnel operation was con-
cerned with rotor thrust, control effectiveness, and wing
stall in transition, and blade flapping and damping in for-
ward flight.

The results of the thrust investigation at both the
static stand and the wind tunnel denote that the thrust de-
veloped by the presently configured rotor is approximately
10 percent less than that projected in the original design.
Control effectiveness is dependent to some extent on devel-
oped thrust, so there is a decrease in control moment com-
pared with that originally predicted. Wing stall charac-
teristics appeared more severe than those encountered during
1/8-scale model wind tunnel tests. No problems arose as a
result of the blade flapping and damping investigation - the
rotor was well damped and responded as predicted.

Working from the ARC data we have shown the valid-
ity of the analytical treatment of rotor performance; that
the performance degradation was due to off-optimum test
hardware. The off-optimum characteristics result from a
rotor designed before the availability of adequate criteria,
and not updating the hardware as additional criteria did
become available, because the program was a research effort,
not a product improvement program. By varying several para-
meters of the rotor system, sufficient thrust can be provid-
ed to assure vertical flight performance of the K-16B at any
feasible gross weight. This thrust improvement will also
provide an increment of improvement in control effectiveness.

The stalling tendencies can be improved on all sec-
tions of the wing by two modifications. One is to increase
the size and effectiveness of the wing flap. An increase in
flap lift effectiveness will require a lower wing tilt angle
to sustain the aircraft, and so a lower wing angle of attack.

The second modification is the installation of leading edge
slats. Because slats sustain load they reduce wing loading,
hence angle of attack required. At the same time, a well-
designed slat will increase the stalling angle of attack.
An analysis has indicated that the stall in the area of the
wing swept by the slipstream can be eliminated, and that
center section stall can be greatly alleviated, both in
level flight and at reasonable rates of descent during
transition.

A generalized treatment of the problems has been
given in the preceding section. This section will present
an analysis and correlation of the test data. In Appendix
C are descriptions of the test equipment and operation, and
in Table VI of the appendix are parameters of the various
test runs. In Appendix D is the derivation of analytical
methods for determining propulsive-rotor performance in
hover, transition, and forward flight.

HOVER

The usual propeller is designed to operate in the
cruising condition at the ideal angle of attack for each sec-
tion along the blade. This can be done because the radial
variation in ideal angle of attack can be made coincident
with the twist distribution for the design condition. But
this leads to a rather highly twisted blade (about 40 de-
grees) with a hyperbolic distribution. In this case, static
thrust is of secondary importance. However, for the VTOL
aircraft static thrust is of primary importance.

Either camber or blade area must be increased to
generate enough static thrust for vertical take-off. Fur-
thermore, the twist should be lower with a linear distribu-
tion. But a blade with these characteristics will have un-
acceptably poor efficiency at the low thrust coefficients
required for partial power cruise. Hence, there is a cruis-
ing efficiency penalty inherent in a high-activity-factor,
static-thrusting propeller.

For example, to satisfy hovering requirements a
highly-cambered airfoil is necessary to obtain a high blade
loading. But the rapid drop in required thrust from hover to
forward flight forces the propeller to operate at low thrust
coefficients in cruise. To operate efficiently at these low
coefficients, a low solidity and a lower camber is needed to
keep blade loading near the maximum lift/drag ratio on the
blade section. It would appear profitable to vary camber to
provide a high camber in hover and a lower camber in cruise.

We accomplish this camber variation by flaps in the blades. This allows the selection of a blade profile that is compatible with the high-speed propeller requirements, but by collective flap deflection attain the higher lift coefficients (because of the greater virtual camber) required for hover performance, and with ample margin for necessary cyclic control without stall.

Performance (Propulsive-Rotor)

Tests were made on a static thrust stand to determine the performance and controllability of the aircraft in simulated hovering flight. Because the K-16B propulsive-rotor blade loading is varied by introducing camber with a flap on each of the blades, static performance tests were run with various values of collective blade-flap deflection, δ_o.

A schematic force diagram of the static stand is shown in Figure 20.
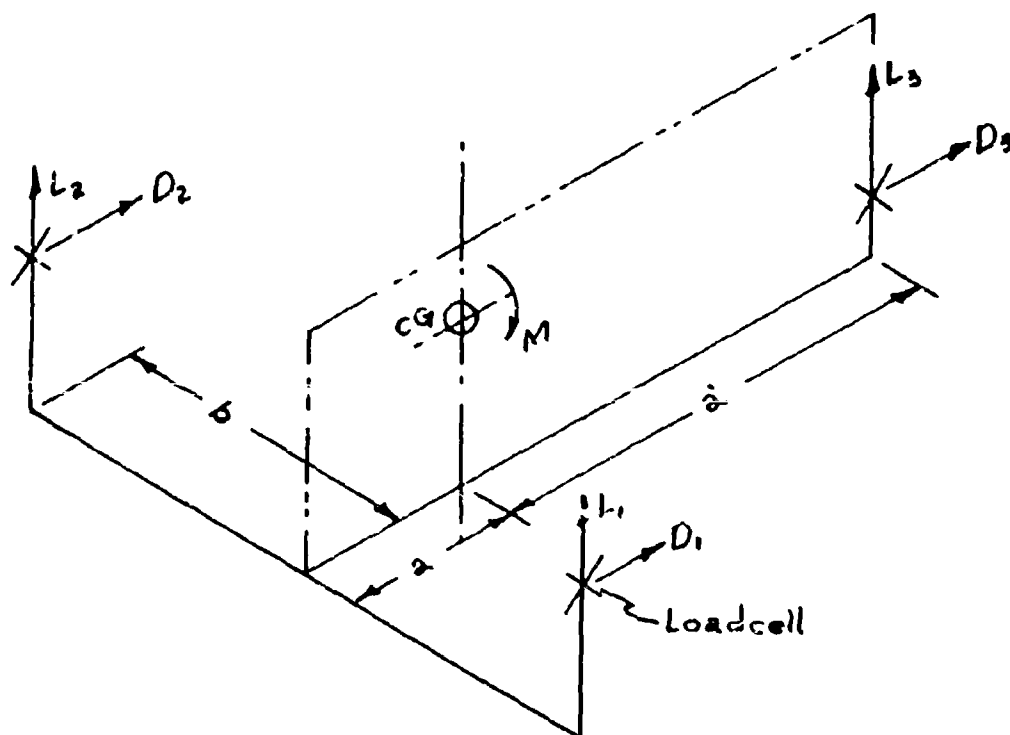
Figure 20
Force Diagram

55

Thrust was not measured directly. The aircraft was
mounted on three load cells corresponding to the three wheels,
lift and drag forces were measured, and pitching moment de-
termined. The resultant of the lift and drag is essentially
the thrust except for the drag of the nacelle and that part
of the wing affected by the slipstream. With the wing flaps
up, this has been estimated to be a drag of 6.07q, which
yields an approximate nacelle and wing slipstream drag of 1.3
percent of the thrust. Therefore, the resultant force is
less than the rotor thrust by about 60 pounds in 4500 pounds.
The resultant force is presented as a function of shaft horse-
power in Figure 21a, and is compared with the results of a
static-thrust strip-analysis (Appendix D, Figure 83).

Both the calculated and the test results were re-
duced to shaft horsepower at the engine output shaft. The
turbine output power was corrected for both engine reduction
gear losses and for lose for operating at non-optimum rpm.
Engine inlet temperature was measured near the compressor
face. Inlet pressure was not measured, so no correction was
made for inlet duct losses, although the loss is estimated to
be 2 percent.

Insufficient data were obtained for the construc-
tion of a complete performance map of thrust versus power for
various flap deflections. Nevertheless, the experimental
data that were obtained agree fairly well with the envelope
of the calculated performance map (Figure 21b). The drag due
to the flapped wing in the slipstream seems to be reflected
in the test data of the figure where, with 46 degrees of wing
flap, the resultant force is reduced by 300 pounds for the
same power.

Because of the agreement between the analytical and
the experimental results, the analysis can ascertain the ele-
ments that determine performance. For example, subtracting
transmission losses from the test point corresponding to
7700 pounds of resultant force $(C_T/\sigma = 0.163)$ at 15 degrees

of collective flap (Point A, Figure 21a) moves it to the left
for a rotor horsepower of 1523. The rotor figure-of-merit is
then 0.615. This point closely corresponds to the peak of
the theoretical curve for a collective flap deflection of
12.5 degrees, shown in Figure 83. Figure 22 shows the radial
variation of M, C_T/σ, and L/D for this condition.

Figure 22a discloses that the mean figure-of-merit
is reasonable despite local discontinuities. The dip at Sta.
.50 is caused by vortices generated at the flap inboard junc-
ture; that at Sta. .95 by the flap/tip juncture and the drag
of the external chordwise flap-control rod. The lift-drag
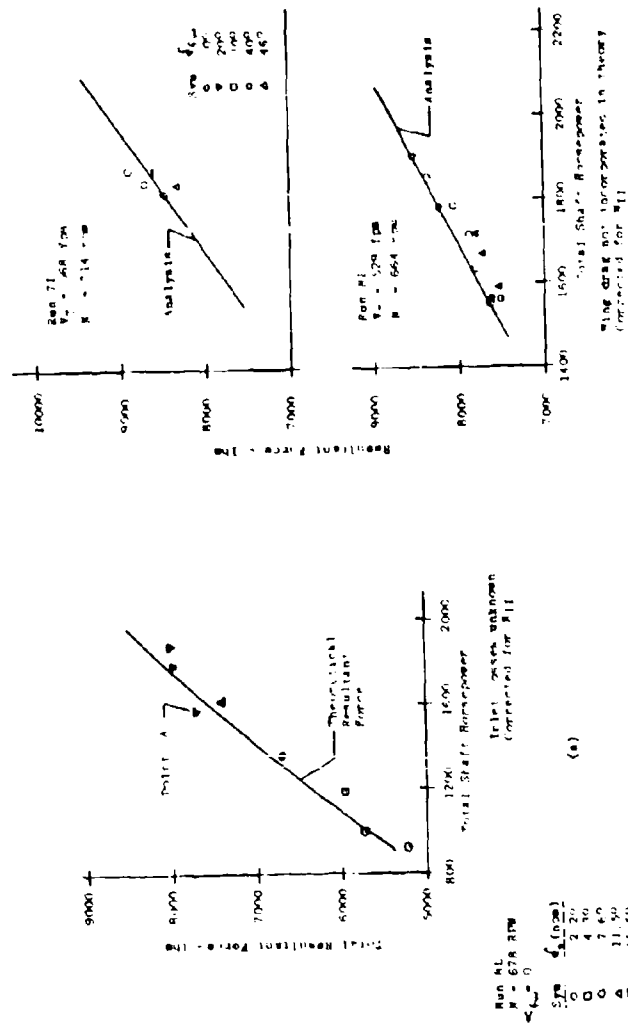
Figure 21.

Shaft Horsepower

Comparison of Analysis and Test Data

(a)   Radial Station - x

$C_T \sigma = .163$
$M = .62$

(Point "A" of Figure 32)

(b)   Radial Station, x

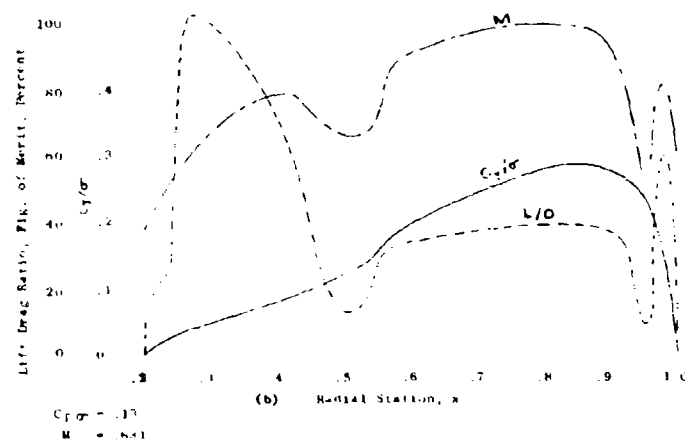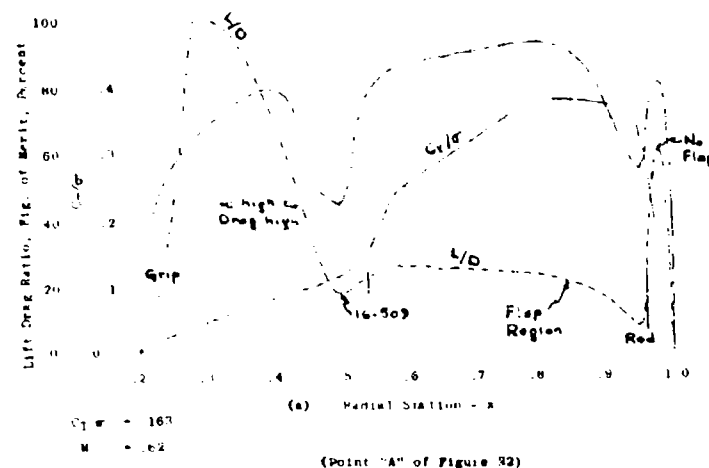$C_T \sigma = .13$
$M = .831$

Figure 22

Calculated Rotor Radial Distributions

58

ratio in the flap region is fairly low, because of the drag
due to the 15 degrees of flap deflection.

A number of possible changes to the rotor, discuss-
ed in the preceding section, led to a reduction of deflection
from 13 degrees to 5 degrees. Figure 22b illustrates the ad-
vantages to static figure-of-merit by so reducing the col-
lective deflection. The reason is, the variation of drag co-
efficient increment with flap deflection is approximately
parabolic, whereas the lift coefficient varies linearly.
Hence, there is a better L/D at low flap deflections than at
high flap deflections.

With lower flap deflections, though, a lower thrust
coefficient is obtained at the original design tip speed. An
increase in tip speed permits the required thrust to be gen-
erated at the lower coefficient, as is shown in Figure 22b.
However, tip speed is limited by the onset of drag and lift
divergence because of compressibility. When this occurs, the
required thrust can be attained only by an increase in basic
camber. But, the inability to decrease basic camber when
thrust requirements drop off at cruise leads to negative
thrust on large portions of the blade, and decreases the
blade lift-drag ratios. There is, then, an optimum combina-
tion of blade design parameters and variable camber for any
particular thrust-speed variation.

Performance (Wing-Flap)

The performance of the wing-flap combination in the
static thrust condition is manifested by the slipstream turn-

ing angle $\left(\theta\right)$, and the turning efficiency F/T; that is, the

percentage of thrust that is left after the slipstream is
turned. Turning angle test results are given in Figures 23,
24, and 25.

The aircraft was tested with the fuselage mounted
in a nose-up attitude (approximately 14 degrees which is 3
degrees greater than normal ground attitude), and the wing in
several tilt positions. Lift and drag forces were measured
in the vertical and horizontal directions, respectively. Re-
ferring to the diagram:
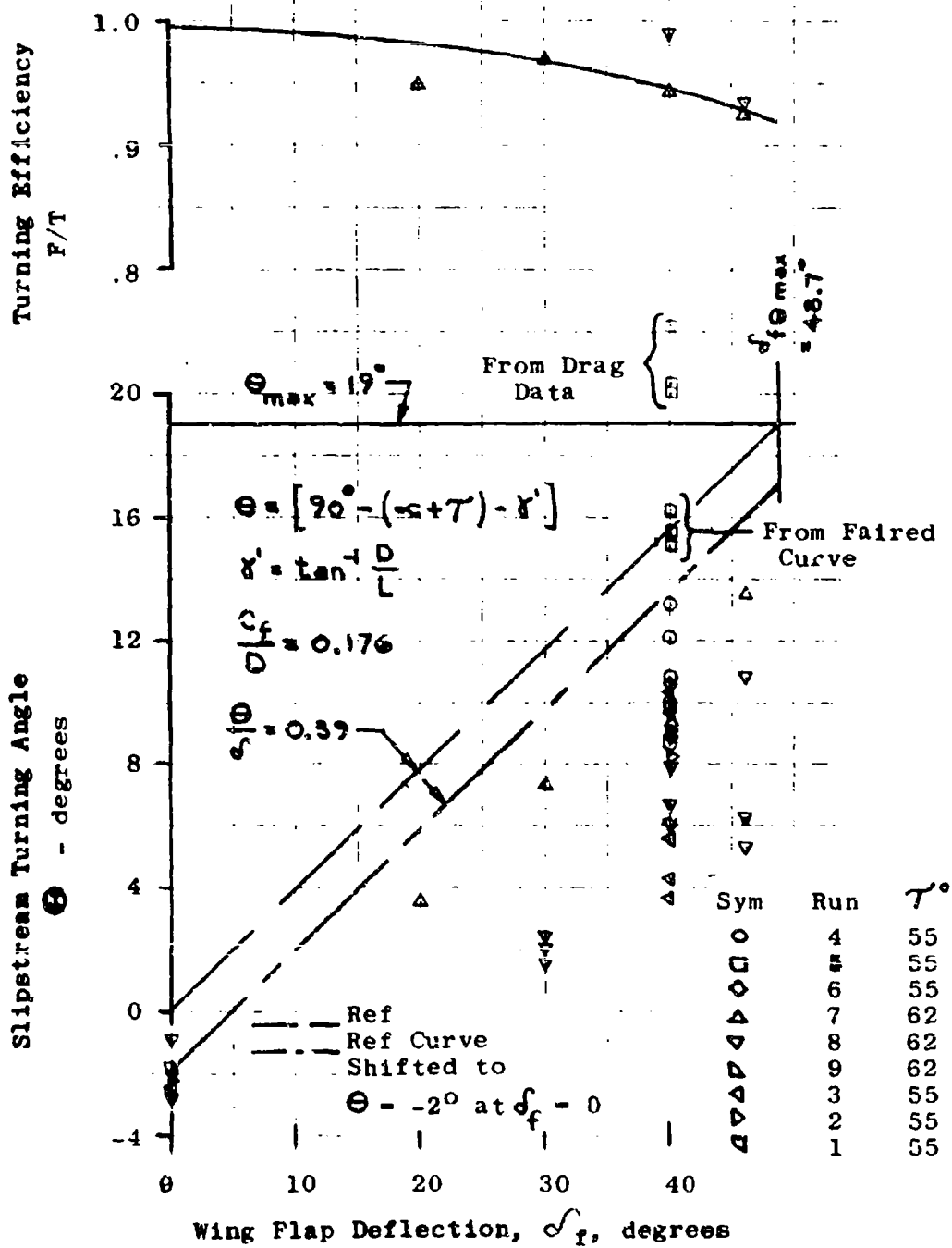
(Diagram on next page of text)

Figure 23
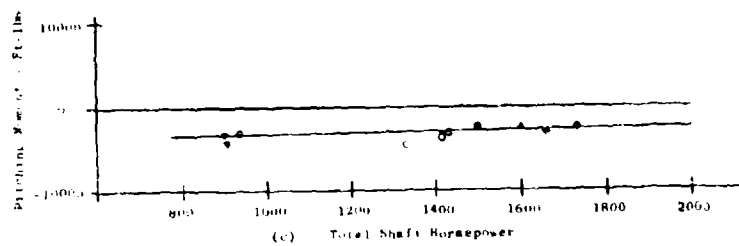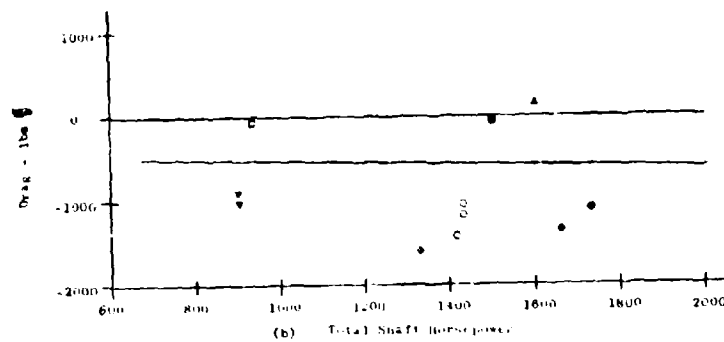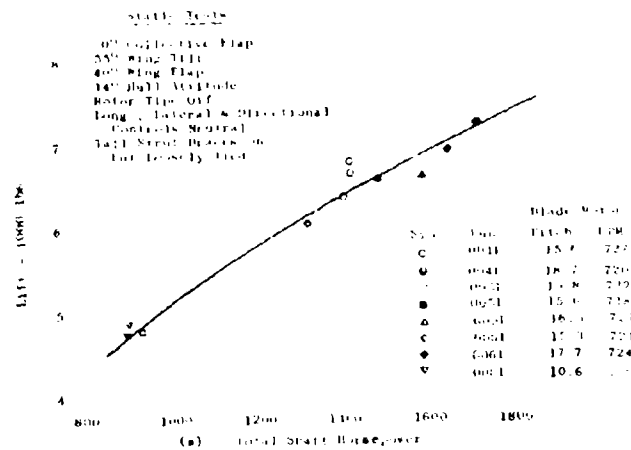Turning Angle and Efficiency
(Static Test Results)

Sym	Run	Blade Pitch	RPM
○	601	15.7	723
◑	604	18.7	720
·	605	1.8	732
●	657	15.0	724
△	603	18.0	724
◇	606	17.0	721
◆	661	17.7	724
▽	661	10.6	

(a)   Total Shaft Horsepower

(b)   Total Shaft Horsepower

(c)   Total Shaft Horsepower

Figure 24

Variation of Aerodynamic Characteristics
with Total Engine Power

Sym	Run	Blade Pitch	Rotor RPM
Open	0071	10 9	714
Shaded	0781	19 1	684
Flagged	008L	11 5	614
Flagged & Shaded	008L	12 5	601
	008L	11 2	604
	008L	10 4	604
	008L	11 2	864
	008L	12 8	664
	009L	7 6	724

Sym	
	0°
	20°
	30°
	40°
	46°

62.6° Wing Tilt
14° Hull Attitude

(a) Total Shaft Horsepower

(b) Total Shaft Horsepower
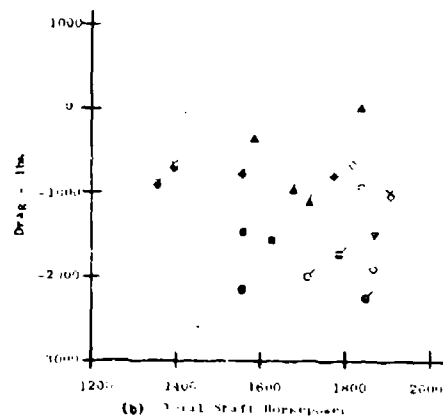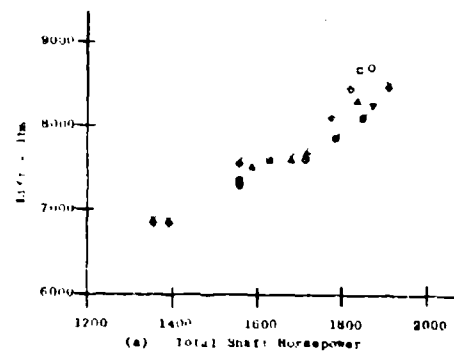
Figure 25

Variation of Lift and Drag
With Total Engine Power
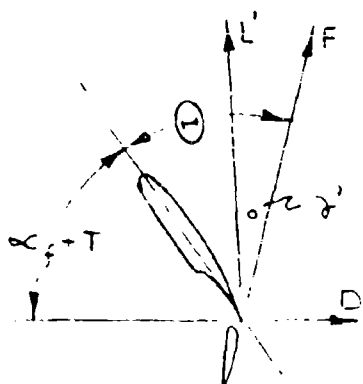
Slipstream turning

angle $= 90 + \gamma' - (\alpha + \tau)$ (1)

where $\gamma' = \tan^{-1} \dfrac{D}{L}$

The slipstream turning angles obtained from the data of Figure 24 and 25 are shown in Figure 23. The large scatter in the drag curves of Figures 24 and 25 have a more profound effect on turning angle than on resultant force. For example, using the Run 5 data from Figure 24, turning angles of from 20 to 22 degrees are obtained. But taking the drag data from the faired curve, angles from 14 degrees to 16 degrees are obtained. Including the drag data from other runs, turning angles as low as 4 degrees were obtained with 40 degrees of wing flap deflection. The scatter in the drag data is such that turning angles determined using these data are inconclusive. One possible reason may be the extrinsic tail wind that prevailed during most of the tests which would change the wing angle of attack in the slipstream, with its consequent effect on the measured lift and drag components.

An indication of the turning efficiency can be had by observing the ratio of the resultant force with the wing flaps deflected to that with the wing flaps neutral, at the same pitch angle. The assumption made under these conditions is that the drag of the nacelles and plain wing is negligible compared to the drag of the wing with the flaps extended. These results are shown at the top of Figure 23 and are labelled F/T.

Figure 2 of NACA Memo 1-16-59L(55) was used as an aid to interpret the results of these tests. With .40$\overline{C}$ flap, the flap chord diameter ratio is 0.174. Using the faired curve (Ibid), a turning angle of about 19 degrees is indicated. If the data points of this figure are used instead of the faired curve, a turning angle of 16 degrees is probable, which is in approximate agreement with most of these test results. The turning efficiency for the slotted flaps, intimated in the reference, is not quite attained in these tests.

An analytical approach toward interpreting these results can be made by reducing the slipstream turning angle, Θ, and efficiency, F/T, in terms of ordinary wing lift and drag coefficients. Referring to the next sketch:

$$\frac{F}{T} = \frac{1}{T}\sqrt{L^2 + (T-D)^2} \qquad (2)$$

In hover, $T_C'' = 1.0$

and

$$k_i^2 q'' = q_{res} \qquad \text{(KAC Report G-113-4)(9)}$$

$$T = \frac{T_C'' q_{res}}{k_i^2} \frac{N\pi R^2}{S_S} S_S \qquad (3)$$

Substituting equation (3) into (2), and dividing through by $(q_{res}S)$:

$$\frac{F}{T} = \frac{1}{\frac{N\pi R^2}{S}}\sqrt{C_L^2 k_i^4 + \left[\frac{N\pi R^2}{S} - k_i^2 C_D\right]^2} \qquad (4)$$

Similarly,

$$\Theta = \tan^{-1}\frac{L}{T-D}$$

Substituting equation (3) into the above:

$$\Theta = \tan^{-1}\frac{k_i^2 C_L}{\frac{N\pi R^2}{S} - k_i^2 C_D} \qquad (5)$$

Thus, the turning angle Θ and efficiency F/T can be expressed in terms of ordinary lift and drag coefficients C_L and C_D.

64

To determine the value of C_L and C_D for equations
(4) and (5), the test data can be used. For example, rearranging Equation (5):

$$C_L = \frac{\tan \Theta}{k_1^2} \left[\frac{N \pi R^2}{S} - k_1^2 C_D \right] \qquad (6)$$

and using Equations (4) and (6)

$$C_D = \frac{N \pi R^2}{S k_1^2} - \frac{C_L}{\tan \Theta}$$

The constant, k_1, is the proportion of the theoretical velocity in the ultimate wake that actually exists at the aerodynamic center. As it is not precisely known, the values of C_L and C_D are presented as a function of k_1 in

Figure 26. They are given for the basic configuration with .40$\overline{C}$ wing flap for one of the points shown in Figure 23, for

a turning angle of (Θ = 16 deg) and an efficiency of (F/T =

0.95). The maximum value of k_1 (0.79) is the theoretical

value found by the momentum theory of KAC G-113-4, Appendix B (9).

The C_L and C_D curves of Figure 26 reveal some rea-

sonable values of C_L, C_D, and k_1, which are likely to yield a

measured Θ and F/T. The lift and drag coefficients must

first be corrected for the effect of partial span flaps, for only a portion of the wing is immersed in the slipstream. The flap lift and drag increments can be obtained from NACA WR L-441 (56), or from the power-off wind tunnel data, exhibited in Figure 27, corrected for partial span by the method of NACA TN 3911 (57). Applying these corrections leads to a lift coefficient of 0.75, and a drag coefficient of 0.23. Referring to Figure 26, these values of lift and drag coeffi-

cient in turn lead to a turning angle, Θ, of 16 degrees at

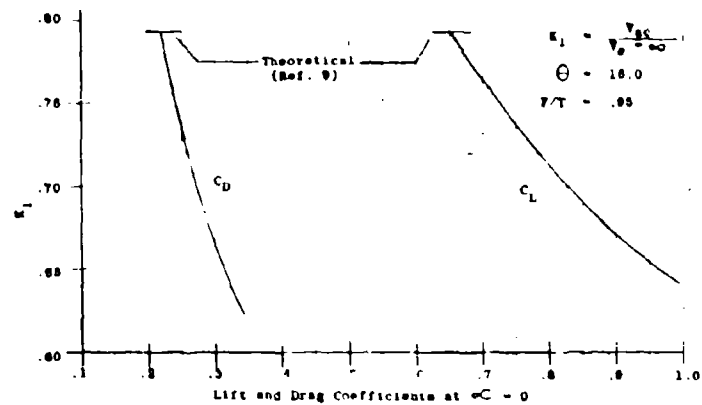a k_1 of approximately 0.74. This seems to indicate that the

Figure 20

Lift and Drag Coefficients
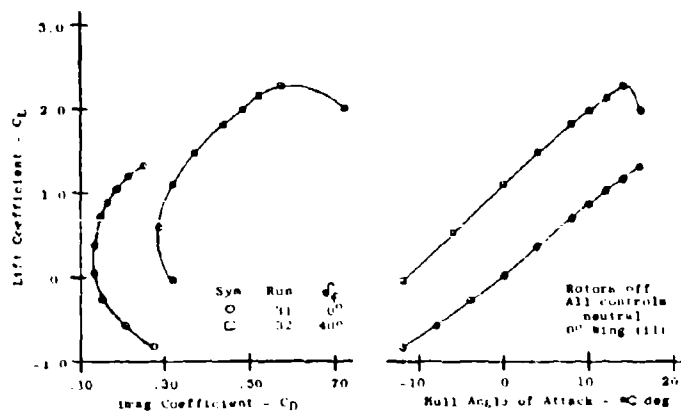Corresponding to
Faired Turning Angle and Efficiency

Figure 21
Variation of Drag Coefficient
and Hull Angle of Attack
with Lift Coefficient

66

slipstream velocity at the aerodynamic center is less than that theoretically inferred from momentum considerations.

The effect of lift and drag coefficients on the slipstream turning efficiency and angle is more graphically illustrated in Figure 28. It was constructed using Equations (4) and (5). This figure implies that it is more beneficial to increase the flap lift increment rather than to reduce the drag coefficient. Using this figure, with $k_1 = 0.75$ and

$\ominus = 16$ degrees, the lift coefficient is 0.725 at a drag

coefficient of 0.25. Increasing the lift coefficient to 1.025 increases the turning angle to 22.2 degrees, and the turning efficiency from 0.945 to 0.975. The figure also shows that with given lift and drag coefficients, only one turning angle can result unless the velocity, k_1, at the aerodynamic center changes.
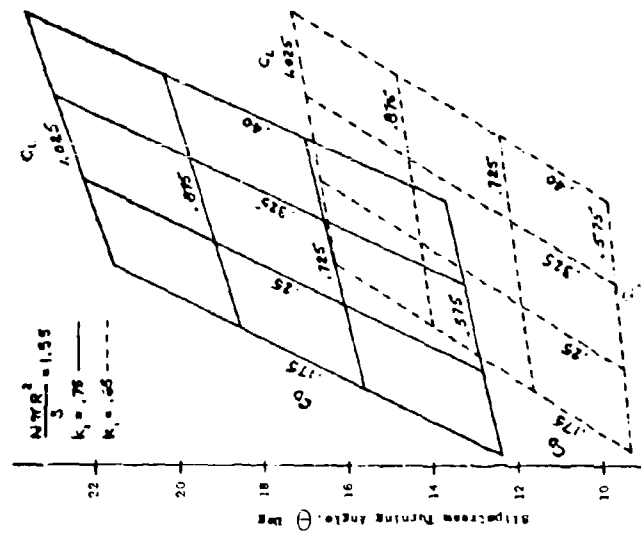
With the previously derived values of lift and drag coefficients, and a value of 0.74 for k_1, the resulting angle

is 16 degrees and the efficiency 94.3 percent. These points agree fairly well with the test points of DTMB Report 998 (47), and somewhat with those given in NACA Memo I-16-59L (55) by the test points for the same configuration, namely,
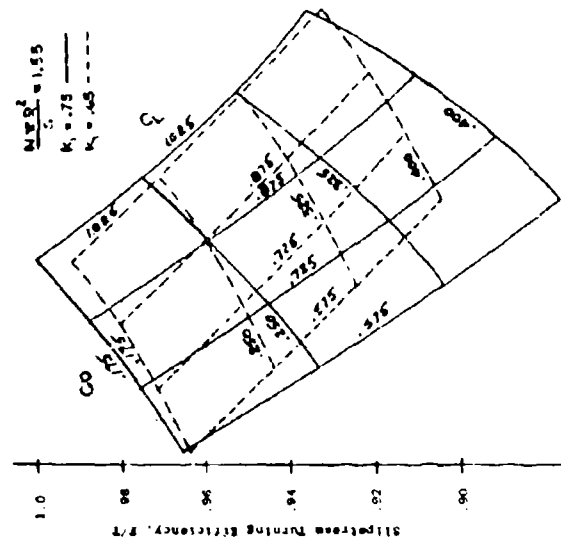
$\ominus = 16$ degrees, $F/T = 0.98$. These charts, therefore, can

serve as a guide to the effect of configuration changes on turning efficiency and angle. Table II summarizes the angles and efficiencies indicated by various methods for this condition.

(Table II on next page of text)

67

(b)   Effect of Lift and Drag Coefficients
on Turning Efficiency

(a)   Effect of Lift and Drag Coefficients
on Turning Angle

Figure 26

Effect of Lift and Drag Coefficients on Slipstream
Turning Angle and Efficiency

Table II Turning Angles and Efficiencies								
Configuration			Source	C_L	C_D	k_1	$\ominus$ Deg.	F/T
Flap	σ_f	Gap						
.40C Fowler	40°	.015 C_f	Present Tests	.54	.22	.79	13.5	.94
* ↑	↑	↓	Present Tests	.75	.27	.75	16	.943
			Present Tests	1.09	.325	.6	15.5	.945
↓	↓	↑	Ref 55 Test Points				15.5	.985
.40C Fowler	40°	.015 C_f	Ref 55 Test Points				19	.98

* Used in subsequent analyses

Controllability

Control of the K-16B in hovering and low-speed
flight is primarily attained by cyclic flapping and collect-
ive pitch displacement of the rotor blades. Longitudinal
control moments are the result of the cyclic deflection of
the blade flap, which induces flapping about the axis paral-
lel to the wing span. Lateral and directional control mo-
ments are functions of differential blade pitch between the
left and the right rotors, and of lateral cyclic flapping.
The lateral and directional controls must be properly phased
to result in control moments about the respective body axis.
For example, lateral flapping results in a yawing moment
about the vertical axis through the wing. Because of the
partial wing-tilt, this moment has two components in the body
axes - yaw and roll. To counteract the rolling moment re-
sulting from lateral flapping, differential collective pitch
is introduced in the opposite sense. The system is fully de-
scribed in KAC Report G-113-4 (9). (Also see Appendix A).
It was one of the purposes of the full-scale tests to deter-

mine the degree to which compensating moments were necessary
to obtain pure body axis moment control. Another purpose
was to determine the amount and phase relationship of blade
flapping, and the cyclic blade-flap deflection. This rela-
tionship is called "cyclic sensitivity".

Cyclic Sensitivity

Part of the control moment is due to a centrifugal
moment about the rotor hub resulting from the offset flapping
hinge and the blade flapping (Ibid). The flapping hinge off-
set changes the cyclic sensitivity and the natural frequency
of flapping to bring the system off resonance. The degree to
which the system is off-resonance is a function of the offset,
the first mass moment about the flapping hinge, pitch-flap-
ping coupling, and the thrust coefficient for the particular
flap-chord ratio. The flapping equations of motion are given
in Appendix D. These equations yield the longitudinal cyclic
sensitivity and phase angle shown on Figure 86. The para-

meter $\mathcal{Y}/\gamma$ in this figure is defined as:

$$\frac{\mathcal{Y}}{\gamma} = \frac{e m_b \bar{r}}{\rho a c R^4}$$

where: e = flapping hinge offset, ft
        m_b = blade mass, slugs

        $\bar{r}$ = distance from the flapping hinge to
            blade c.g.
        c = blade chord, ft
        R = blade radius, ft
        a = lift curve slope

It is apparent from Figure 86 that for constant
offset, such as exists on the K-16B rotor, as the blade gets
heavier or the c.g. moves outboard, the longitudinal cyclic
sensitivity is reduced and the phase angle moves from 90 de-

grees. The introduction of negative δ_3 brings the flapping

motion back toward resonance and returns the cyclic sensi-
tivity. Point A of Figure 86 indicates the position of the
original design of the K-16B rotor. Subsequent modifications
led to a blade that is represented approximately by Point C.

The δ_3 angle built into the blade is -28 degrees, and the

azimuth is indexed at 21 degrees. As a result, the phasing
was expected to be about 13 degrees off at the maximum thrust

coefficient, and the cyclic sensitivity down to 0.47. Of course, at lower thrust coefficients, the cyclic sensitivity would be further reduced as shown by the figure.

Besides cyclic sensitivity and phase angle, the total controllability depends upon the amount of moment obtained from a given amount of blade flapping. Using the analysis of Appendix D, the hub-moment and total moment are shown in

Figure 87 as a function of $\mathcal{Y}/\gamma$ and α_3 angle for the normal

thrust coefficient. This figure shows that the longitudinal component of the hub-moment and the total moment both in-

crease with either an increase in $\mathcal{Y}/\gamma$, or an increase in

negative α_3 angle. It increases with the latter because the

system is brought closer to resonance and the cosine approaches unity.

Test Results: The measured cyclic sensitivity is shown ir Figure 29 compared with the results of the analysis
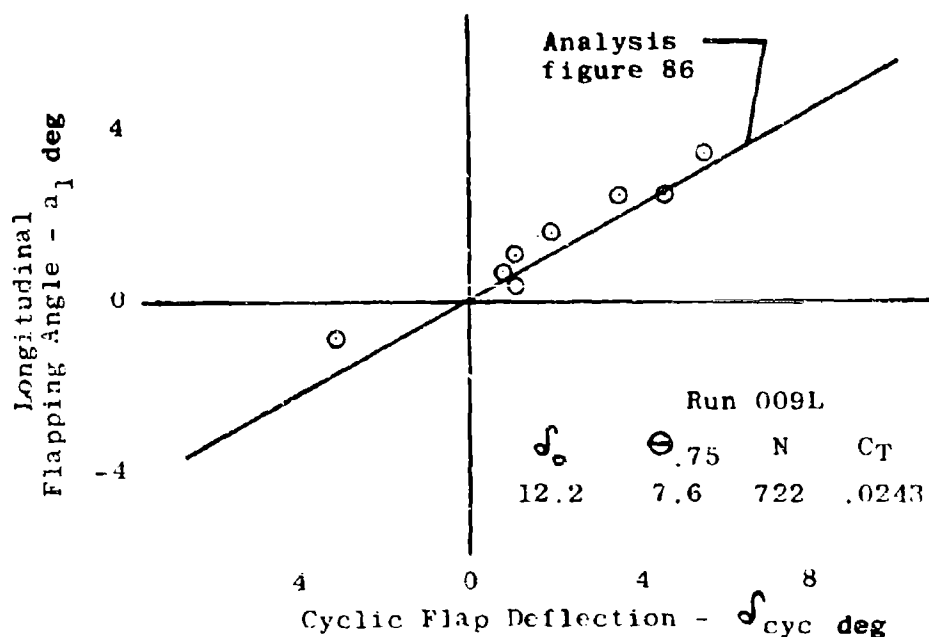
Figure 29
Comparison of Cyclic Sensitivity

71

given in Appendix D; Figure 86, for the particular thrust co-
efficient (in this case the resultant force coefficient).
Also, in Figure 30 is shown the total pitching-moment com-
pared with the analytical results given in Figure 87. The
cyclic sensitivity for Run 4 could not be measured for the
flap-deflection potentiometer was not fully installed. The
total pitching-moment however, as a function of longitudi-
nal flapping is in good agreement, so the cyclic sensitivity
must also be in good agreement.

It is not the pitching moment given in KAC Report
G-113-4 (9) for full cyclic input at full thrust. There are
two reasons for this. First, in these tests total cyclic
input amounted to only 15 degrees of cyclic flap deflection
instead of the design 25 degrees used in the original analy-
sis (Ibid). Second, as shown in Appendix D, Figure 86, cy-
clic sensitivity is a function of the thrust coefficient.
Full hovering thrust was not attained in these tests, and the
cyclic sensitivity is diminished. In addition, part of the
pitching-moment is due to the thrust force; for example:

$$\frac{dM}{da_1} = \frac{dM_H}{da_1} + T\left[x_h + \frac{dC''_{Lw}}{da_1}\left(\frac{S}{\pi R^2}\right)\right] \tag{7}$$

and $$M_1 = \frac{dM}{da_1}\left[\frac{da_1}{d\delta_1}\right]\frac{d\delta_1}{d\delta_s}\delta_s \tag{8}$$

where: $da_1/d\delta_1$ - cyclic sensitivity

Because the cyclic sensitivity is a function of the thrust,
the hub moment is also a function of the thrust. These two
reasons - the restriction in cyclic flap deflection to 15
degrees, and the lower thrust of the tests - fully explain
the difference between these results and the analytical de-
sign projections of G-113-4.

Wing Straightening: An interesting point of these
tests is evident in Figure 30c. When the stick is displaced
forward, the rotor flaps forward (the disc tilts forward).
The rotor thrust vector points more forward; the vertical
component of the thrust is reduced and the horizontal compo-
nent increased. At the same time, the forward tilt of the
disc redirects the slipstream, causing an increase in the
wing angle of attack, and the wing lift and drag are in-
creased. The vertical component of the wing lift, then, in-
creases when the corresponding component of the thrust is

72

Figure 30

Comparison of Experiments
and Analytical Pitching Moment

73
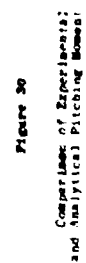
Total Power (nom.)

Run 0041
O 1415
□ 1731

Static Test Conditions

55° Wing Tilt
40° Wing Flap
14° Hull Attitude
100% Longitudinal Sensitivity

Blade Tips Off
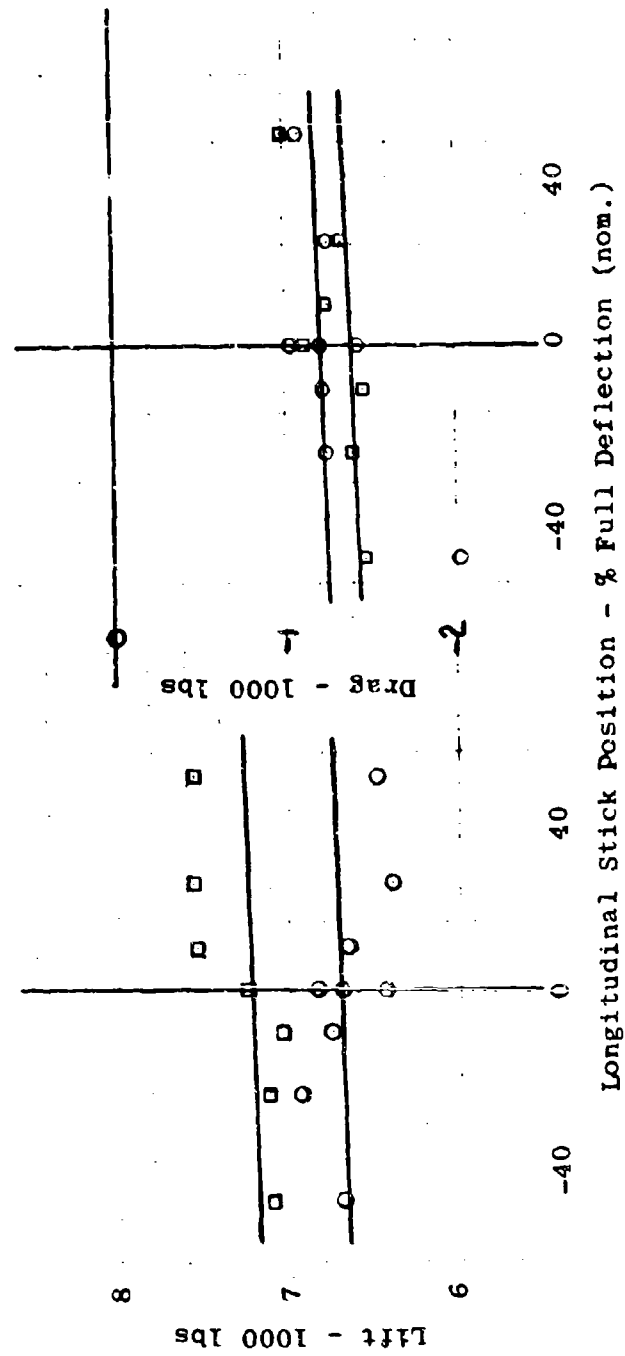Tail Strut Braces on
but Loosely Tied
Zero Wind

Drag - 1000 lbs

Lift - 1000 lbs

Longitudinal Stick Position - % Full Deflection (nom.)

Figure 30c
Variation of Lift and Drag with
Longitudinal Stick Position

reduced, and the horizontal component of the wing lift and drag increases to counterbalance the increase in forward horizontal component of the thrust. The two effects of the rotor and wing tend to cancel each other, or, the wing tends to straighten the slipstream and there is little change in aircraft lift and drag with cyclic control. Figure 30c shows the cancellation is almost total within the experimental accuracy. This reduces the thrust moment by changing the moment arm to approximately the distance from the hub to the wing aerodynamic center, rather than from the hub to the CG.

Cyclic Power: Another effect of cyclic control is the power required. According to the analysis of Appendix D, both profile and induced power are effected. Figure 31 compares the calculations with the results of Run 009L. This
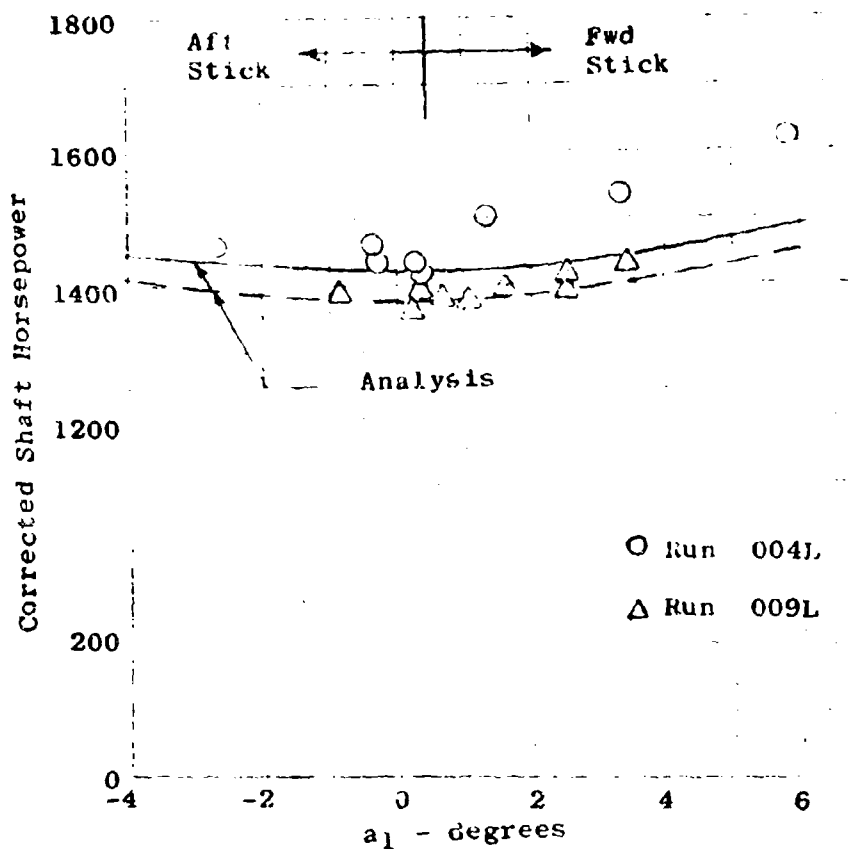
Figure 31

Power for Cyclic Control

75

power-required can be compensated by a suitable kinematics linkage in the engine control geometry, or by an isochronous governor.

Lateral Directional Rotor Control

The lateral-directional control moments are obtained on the K-16B by a proper proportioning of differential collective pitch between the two rotors, and of lateral cyclic rotor flapping. The details of the functions are given in KAC Report G-113-4 (9) and in Appendix A, but will be summarized here for completeness.

Lateral control is obtained by differential blade pitch, that is, increasing the thrust on one rotor and decreasing it on the other. Because of the partial wing tilt, both a rolling moment and a residual yawing moment result. The induced yawing moment is compensated by the introduction of lateral cyclic flapping. Directional control is obtained by lateral cyclic blade flapping. This causes a sideways tilt of the rotor thrust vectors, producing a yawing moment about the wing yaw axis, as well as a centrifugal hub moment in the same direction. Again because of the partial wing tilt, a rolling moment is induced about the body axis. This rolling moment is compensated by the introduction of differential blade pitch in the opposite sense. The introduction of both compensating controls is effected as a function of wing tilt through appropriate linkages. It is one of the purposes of these tests to determine the degree to which the primary controls and the compensating control linkages accomplish their purpose.

The tests should indicate the cyclic sensitivity, or the amount of flapping produced by the cyclic flap deflection. In this case, the lateral cyclic sensitivity should be the same as the longitudinal for the same thrust level. The comparison is shown in Figure 32.

An adequate analysis of the results of controllability tests entails carrying the measured components of the control moments to an aerodynamically common base; ie, a point that separates the aerodynamic results from the mechanical system. Only in this way can the results be interpreted in physical terms independent of the functioning of a mechanical system. Such a common base for comparison is the wing axis system before control compensation is introduced.

Blade flapping is a result of aerodynamic moments on the blade, and depends on the blade-flap input. The test should express the wing axis yawing moment for the amount of flapping obtained. This was determined from the body axis
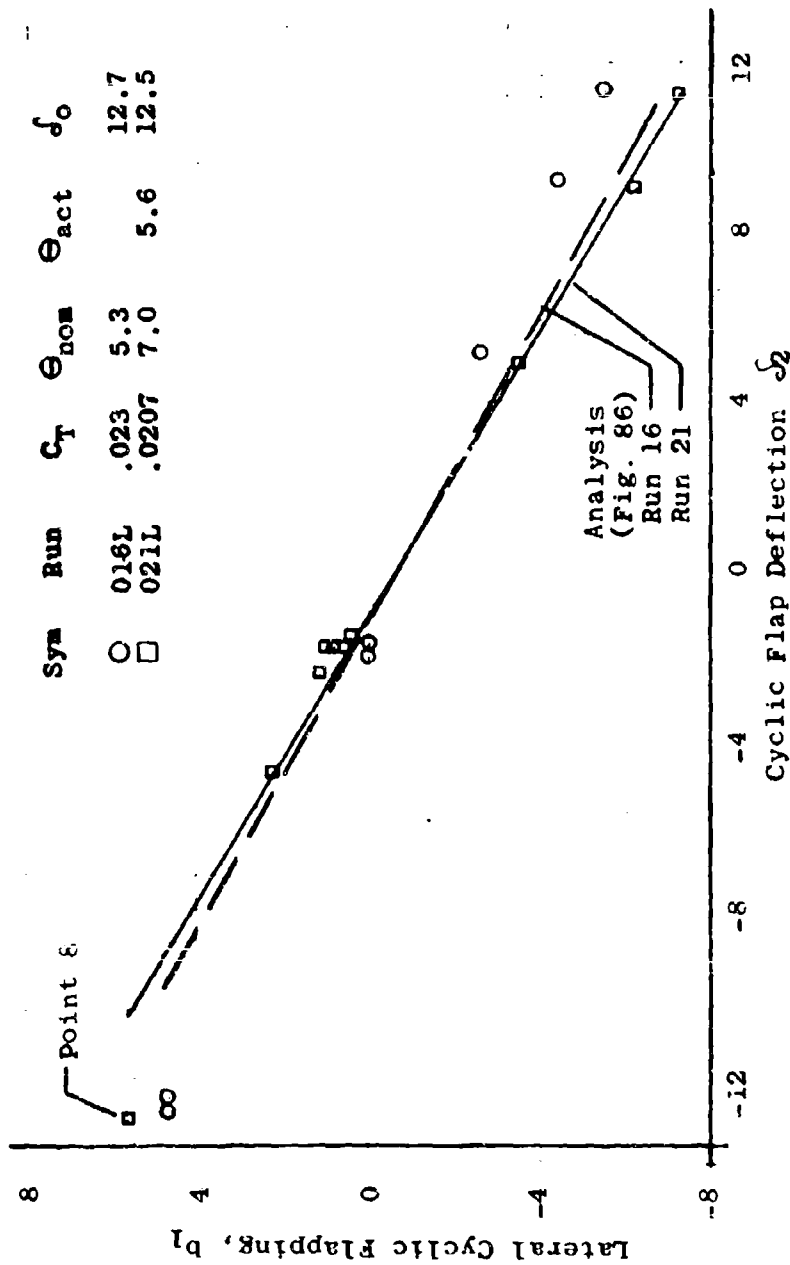
76

Figure 32
Comparison of Cyclic Sensitivity with
Lateral Flapping

measurements (Figure 33) by a transfer of axes, and are shown in Figure 38. If the primed moment symbols denote the wing axis system and the unprimed symbols the body axis system, these axis transfer equations are:

$$\left. \begin{array}{l} N' = L \sin \mathcal{T} + N \cos \mathcal{T} \\ L' = L \cos \mathcal{T} - N \sin \mathcal{T} \end{array} \right\} \tag{9}$$

The wing axis yawing moment is a function of a hub moment, a thrust moment, and a yawing moment contributed by the spoilers when the stick is deflected laterally according to the following equation taken from KAC Report G-113-4 (9):

$$N' = \left[\frac{\partial M_H}{\partial b_1} + T x_h \right] b_1 + \frac{F}{T} \bar{y} \cos \Theta \frac{dT}{d\Theta} \triangle \Theta + N_s \tag{10}$$

The corresponding wing-axis-system rolling moment is:

$$L' = \frac{F}{T} \bar{y} \sin \Theta \frac{dT}{d\Theta} \triangle \Theta + \frac{dQ}{d\Theta} \triangle \Theta + L_s \tag{11}$$

(When the rudder pedal is depressed there is no spoiler projection, so N_s and L_s are eliminated.)

Substituting the previously determined component parts (F/T, Θ, etc) into equations (10) and (11) will reveal the contribution of each part to the over-all moment.

The experimental results will be consistent if the wing-axis rolling and yawing moments, determined by inserting the experimentally established components into equations (10) and (11), agree reasonably well with those found directly when using the axis transfer equation (9). The same moments obtained by inserting the analytical components into equations (10) and (11), when compared with the other two methods, will furnish an insight into the precision with which such moments can be estimated.

First, consider the case when the stick is deflected laterally (Run 021L). The measured body axis rolling and yawing moments are shown in Figure 33b. In this case, the principal control is differential collective pitch with lateral cyclic as compensation for the yawing moment that is
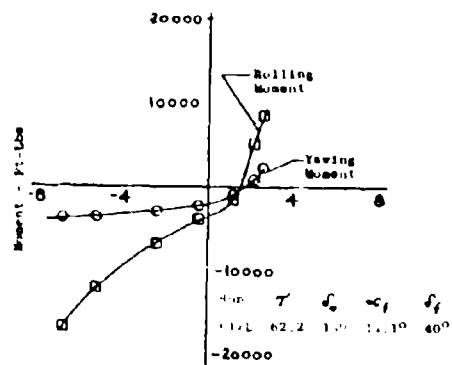
(a)
Differential Blade Pitch, Δθ, Degs.
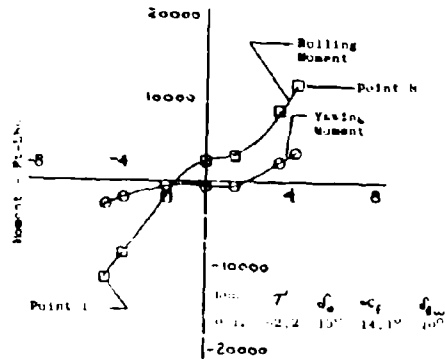
(b)
Differential Blade Pitch, Δθ, In. N.

Figure 33
Lateral Control Characteristics

79

produced. The cyclic flap deflection, flapping angle, and right rotor pitch are given in Figure 34 as functions of lateral stick deflections. The F/T and $\hat{(-)}$ of equations (10) and (11) were taken from Figure 23. Two other items for insertion into the equations are the variations of thrust and torque with pitch. The analytical values are found in Figure 35 with any experimental values obtained also entered. The thrust results of Runs 004L, 005L, and 008L ($\hat{\sigma}_o = 14.8$) show reasonable trends.

The thrust-pitch slopes obtained from the strip analysis are in good agreement with these results. At the low values of flap deflection, however, the absolute values of blade pitch are about one degree high. This is a result of centrifugal twisting moments as shown in KAC Report G-111-4 (5). The thrust value of Run 021L was determined by taking the torsional flexibility into account. The shape of the torque-pitch curves is similar to those found analytically (Figure 35). The absolute value is not directly involved in the equations, but only the slopes.

The differential collective pitch must now be accounted for. Blade pitch was measured on the right rotor only. The reasonableness of an equal pitch increment on the left rotor can be determined by working backwards from the experimental results (Figure 33) with the aid of the vector diagram of Figure 36. Point 8 corresponds to the last point of Figure 33 for right stick deflection. The body-axis rolling moment (L) is 13,000 ft-lb, and the yawing moment (N) is 3500 ft-lb. Starting from the plot of this test point on the vector diagram (Figure 36a), the first component to be analyzed is that due to lateral cyclic flap.

From oscillograph record 1696, b_1 was found to be +1.3 degrees. The right rotor pitch is 8.1 degrees for neutral stick. Correcting for centrifugal twist, from KAC Report G-111-4 this becomes 5.9 degrees, which according to Figure 35 yields a thrust of 2940 lb, or 5880 lb for two rotors. The wing-axis yawing moment (N') due to lateral cyclic is:

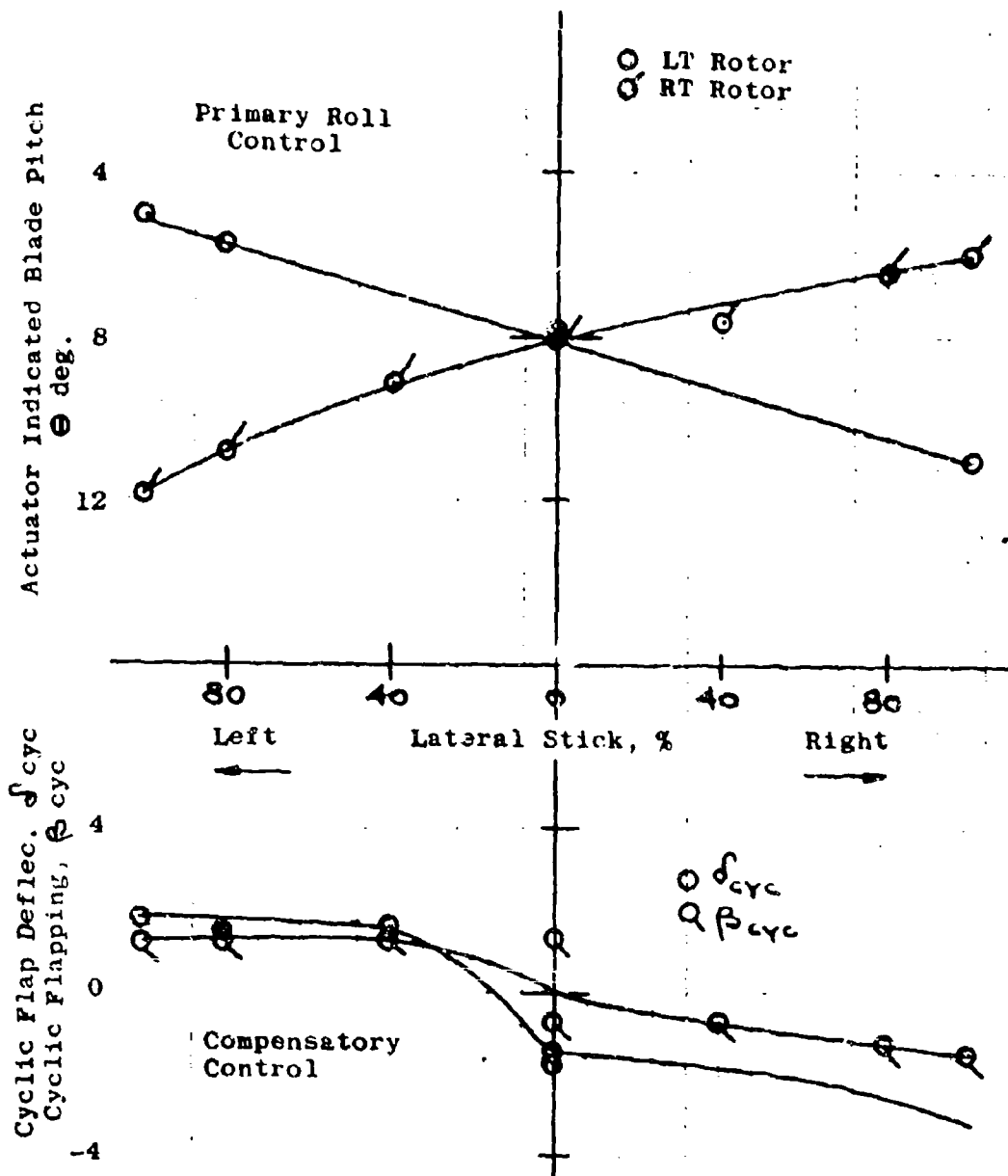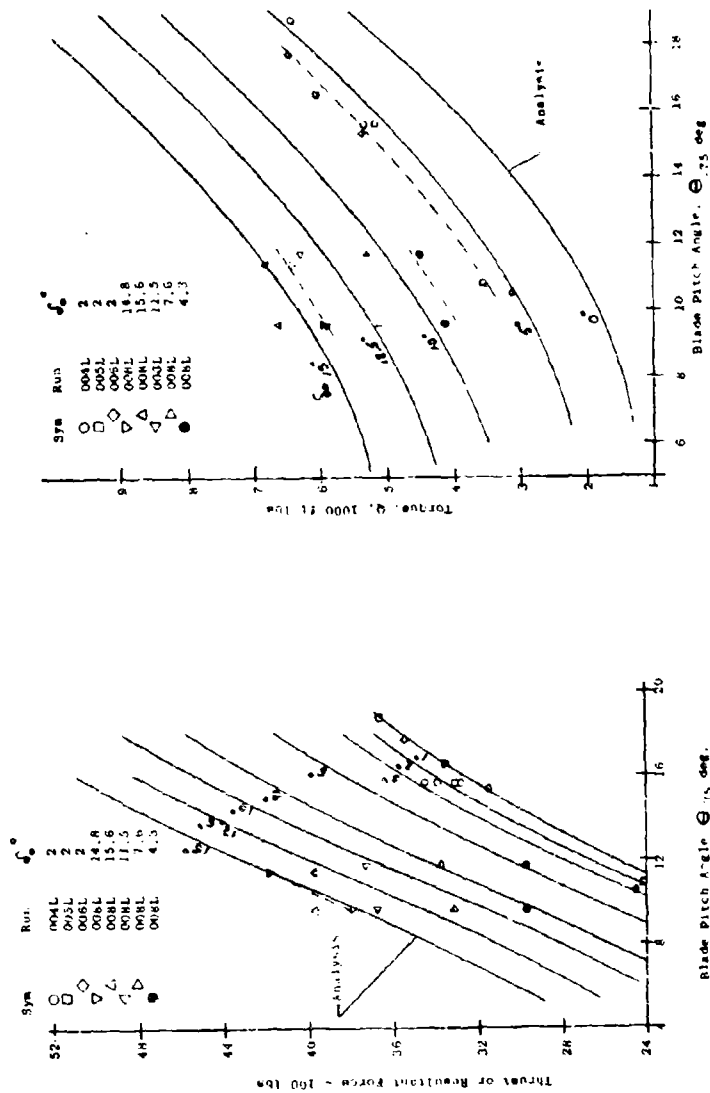$$N' = \left[\frac{\partial M_H}{\partial b_1} + T x_h \right] b_1$$
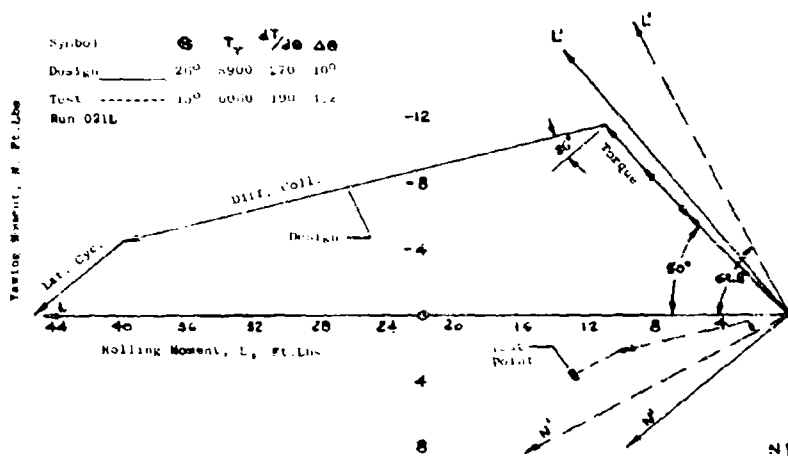
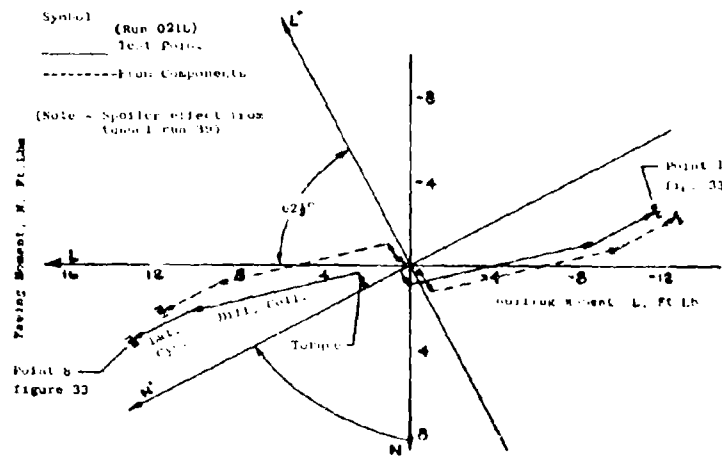**Figure 34**
Control Motion With Lateral Stick Excursion

81

Figure 35

Variation of Thrust and Torque
With Blade Pitch Analysis

Figure 36

Vector Diagram Analysis of Lateral Control Moments

which for this case is:

$$N' = \left[1735 + \frac{5880\,(8)}{67.3}\right]\left[+1.3\right] \approx +3320 \; ft\text{-}lb$$

The 1735 ft-lb/deg (99800 ft-lb/rad) for the hub moment deri-
vative is given in Figure 87, and is corrected by 4 percent
for the reduced thrust.

      This is laid out on the vector diagram (Figure
36a), starting from the test point and parallel to the N'
axis. This is straightforward.

      Next must be determined the effect of differential
collective pitch. The effect of this pitch increment is to
produce a thrust moment component parallel to the wing yawing
axis, and a lift moment component parallel to the wing roll-
ing axis. Because the blade pitch was measured only on the
right rotor, the pitch on the left rotor was determined by
applying the same pitch increment between static calibration
and dynamic deflection on the left rotor as had occurred on
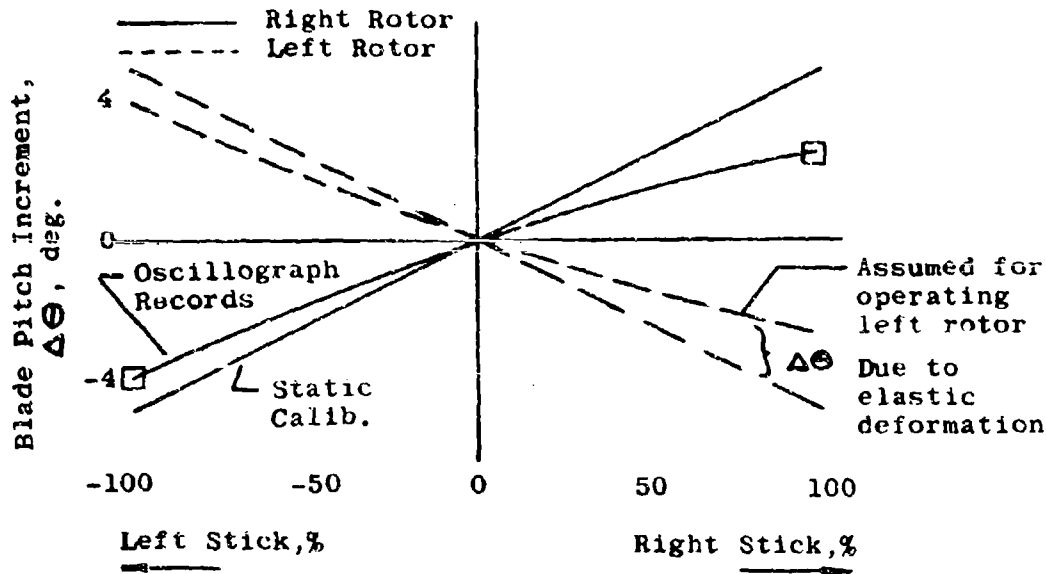the right (Figure 37). The total actuator-indicated differ-

Figure 37
Increment in Differential Collective at Actuator
Due to Elastic Deformation

ential collective pitch was so found. The values of 5.6 and
10.8 for full right stick were corrected for blade centrifu-
gal twist (G-111-4)(5) to yield a final $\triangle\ominus$ of 4 degrees.

The values of differential collective pitch shown on Figure
34 were corrected for centrifugal twist, whereas the raw data
presented in NASA TN 2538 (53) and by Weiberg (58) were not
so corrected.

The thrust moment component is given by:

$$N'_T = \frac{F}{T} \, \overline{y} \, \cos\ominus \, \frac{dT}{d\ominus} \, \triangle\ominus$$

Referring to Figure 23, the slipstream turning angle $\ominus$ and

efficiency F/T are approximately 16 degrees and 0.94 respec-
tively. From Figure 35 the average thrust-pitch curve slope
is 190 lb/deg. Substituting these factors into the foregoing
equation, the thrust moment component becomes 8,000 ft-lb,
drawn parallel to the N' axis on the vector diagram of Figure
36a. The lift component of the differential collective input
is just the sine component:

$$\frac{F}{T} \, \overline{y} \, \sin\ominus \, \frac{dT}{d\ominus} \, \triangle\ominus = \frac{8000(.259)}{.965} = 2150 \, ft\text{-}lb \, \cdot$$

This is laid out parallel to the L' axis, and the vector
marked "Differential Collective" can be drawn.

The torque component is straightforward and can be
obtained from Figure 36 as

$$\frac{dQ}{d\ominus} \, \triangle\ominus$$

where $\quad \dfrac{dQ}{d\ominus} = \dfrac{220 + 150}{2} = 185 \, ft\text{-}lb/deg$

$$Q = 185(4) = 740 \, ft\text{-}lb$$

parallel to the wing rolling axis, L' (Figure 36a).

The vector diagram now shows a negligible amount of
wing axis rolling moment to be furnished by the spoilers, and

a rolling and yawing asymmetry. The rolling asymmetry is a
little less than that shown in Figure 33a for zero stick.
The dotted vector diagram shows the point that would be cal-
culated using the foregoing components plus the effect of
spoilers. The spoiler effect was found from tunnel tests
(Run 39), suitably corrected for the dynamic pressure and
wing area affected by the slipstream (G-113-4)(5). The
spoiler rolling moment is $L_S' = 0.145T$ and the corresponding

yawing moment is $N_S' = 0.0695T$ for the 43 degrees of spoiler

projection. The final end point, Figure 36a,

$$L = 11,600 \text{ ft-lb}$$
$$N = 2,200 \text{ ft-lb}$$

is within the experimental accuracy of the test as shown by
the scatter in the data. Points corresponding to left stick
(Point 1) are also shown in the vector diagram.

Having the component parts for equations (10) and
(11), the wing-axis rolling and yawing moments were obtained
by the three methods, namely:

1. Directly from measurements using the axis
    transfer equations;
2. Using equations (10) and (11) with experi-
    mentally determined components such as

    T, b_1, F/T, $\ominus$, $\dfrac{dT}{d\ominus}$, $\dfrac{dQ}{d\ominus}$;

3. Using equations (10) and (11) with analyt-
    ically determined components.

They are compared in Figure 38 for Run 021L as functions of
total differential pitch when lateral stick is applied. In
general, the comparison is in good agreement. One reason for
the scatter in the yawing moment is the scatter in the b_1

compensating blade flapping. For example, at neutral $\triangle \ominus$,

the b_1 is the same as at full right stick, 1.3 degrees,

whereas it should have reduced to zero.

Design Analysis: The various components can now be
analyzed with respect to the original design (Figure 36b de-
rived from G-113-4)(9). The reduction in slipstream turning
angle from 26 degrees to less than 16 degrees had little ef-
fect on the rolling moment inasmuch as the required addition-
al wing tilt did not change the direction of the differential

collective vector. The reduction in the magnitude of the differential collective pitch, however, had an appreciable effect. The design differential pitch was 10 degrees, whereas the actual differential pitch (as tested) was 5 degrees at the actuator, and 4 degrees due to centrifugal twist and elastic deformation (Figure 38). The low spoiler effectiveness in hover would reduce the lateral cyclic compensation required, provided adequate differential collective pitch and its corresponding torque were provided (Figure 36b). The reduced thrust levels also led to a reduction in the effect of the differential collective pitch because the thrust-pitch derivative was lowered.

It is therefore important in the design of any control system that uses differential collective pitch to account for all elastic deformations and the effect of reduced thrust effectiveness, particularly if operation at reduced thrust levels is expected.

Directional Control

The rolling and yawing moments measured upon pedal deflection appear as a function of blade lateral flapping angle, b_1, in Figure 39. Depressing the pedal deflects the blade flaps cyclically so that the rotors flap in the direction of the depressed pedal. Therefore, in the wing axis, lateral flapping is the logical aerodynamic characteristic leading to a yawing moment.

The prime factors leading to a wing-axis yawing moment are the hub and the thrust moments due to cyclic flapping. The relationship between blade-flap cyclic deflection and lateral flapping for Run 021L is given in Figure 32. The analysis was made with equations (10) and (11), using the measured values of lateral flapping, b_1, and the compensating differential collective pitch, $\triangle\theta$. The wing-axis rolling and yawing moments calculated with the latter equations were converted to the body axes, for comparison with the measured values, by the following axis transfer equations:

$$L = L'\cos\tau + N'\sin\tau$$
$$N = N'\cos\tau - L'\sin\tau$$

(12)

where the primed symbols denote the wing axis system.

Considering the scatter in the data, the analysis based on the equations is fairly accurate as is evident in
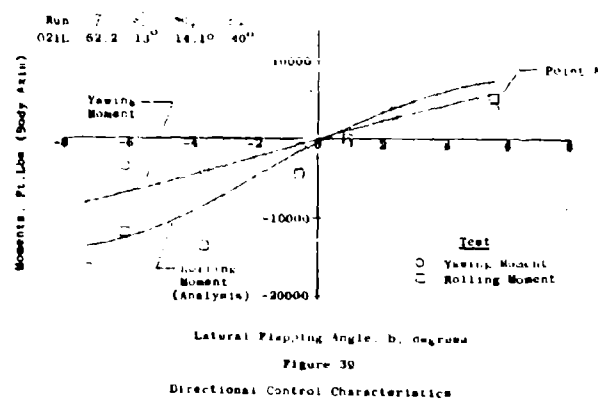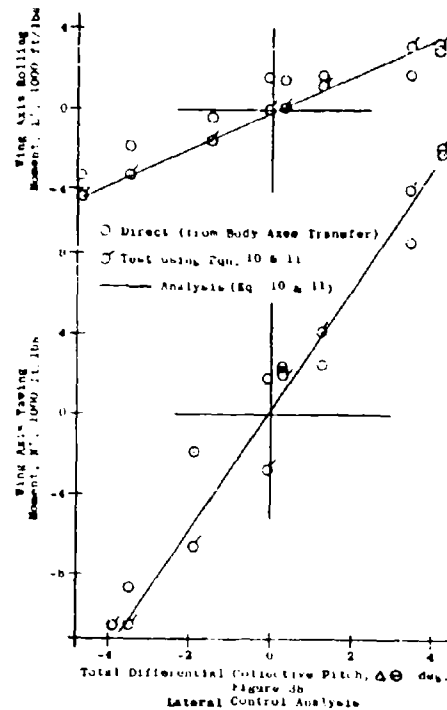
Figure 38
Lateral Control Analysis

Figure 39
Directional Control Characteristics

Figure 39. The accuracy with which yawing moment can be ana-
lytically predicted is better illustrated by referring the
measured values to the wing axis system (Figure 40). In this
system, lateral cyclic flapping directly furnishes yawing mo-
ment. This comparison verifies that the wing-axis yawing mo-
ment can be determined analytically.

The manner in which wing-axis yawing and rolling
moments combine to form body-axis yawing and rolling moments
can best be illustrated by a vector diagram similar to the
one used in the lateral control analysis. The point marked
"Point 8" on Figure 39 (b_1 = 5.5 deg) is analyzed vectorially
in Figure 41 by way of illustration.

Starting from "Point 8" on the vector diagram, the
compensating differential collective pitch, when corrected
for elastic deformation, was -2.55 degrees. When combined
with the F/T and $\bigcirc\!\!\!\!H$ from Figure 23, the $dT/d\bigcirc$ from Figure 35,
and using equation (10), it results in the differential col-
lective triangle shown. Applying the torque derivative from
Figure 35 brings the vectors to just the other side of the
wing yawing axis, N'. Combining the hub moment and the
thrust moment derivatives due to lateral cyclic, and using
equation (10) as follows:

$$N' = \left[\frac{\partial M_H}{\partial b_1} + \frac{Tx_h}{57.3}\right] b_1$$

parallel to the wing yaw axis, yields a slightly asymmetric
body-axis rolling and yawing moment that is fairly close to
that obtained experimentally (Figure 40).

Design Analysis: Several facts can be gleaned from
the comparison of the direct and the componential methods for
determining wing-axis rolling and yawing moments (Figures 40
and 41). The most important is that wing-axis yawing moments
can be predicted analytically. Secondly, in the tests there
was insufficient compensating differential collective pitch,
quite probably because elastic deformation was not accounted
for. (See bottom of Figure 40)

The original design is compared with the test re-
sults and several alternatives in the vector diagram of Fig-
ure 42. The reduced slipstream turning angle called for an
increase in wing-tilt. This in turn had an adverse effect on
the body-axis yawing moment, the change being proportional to
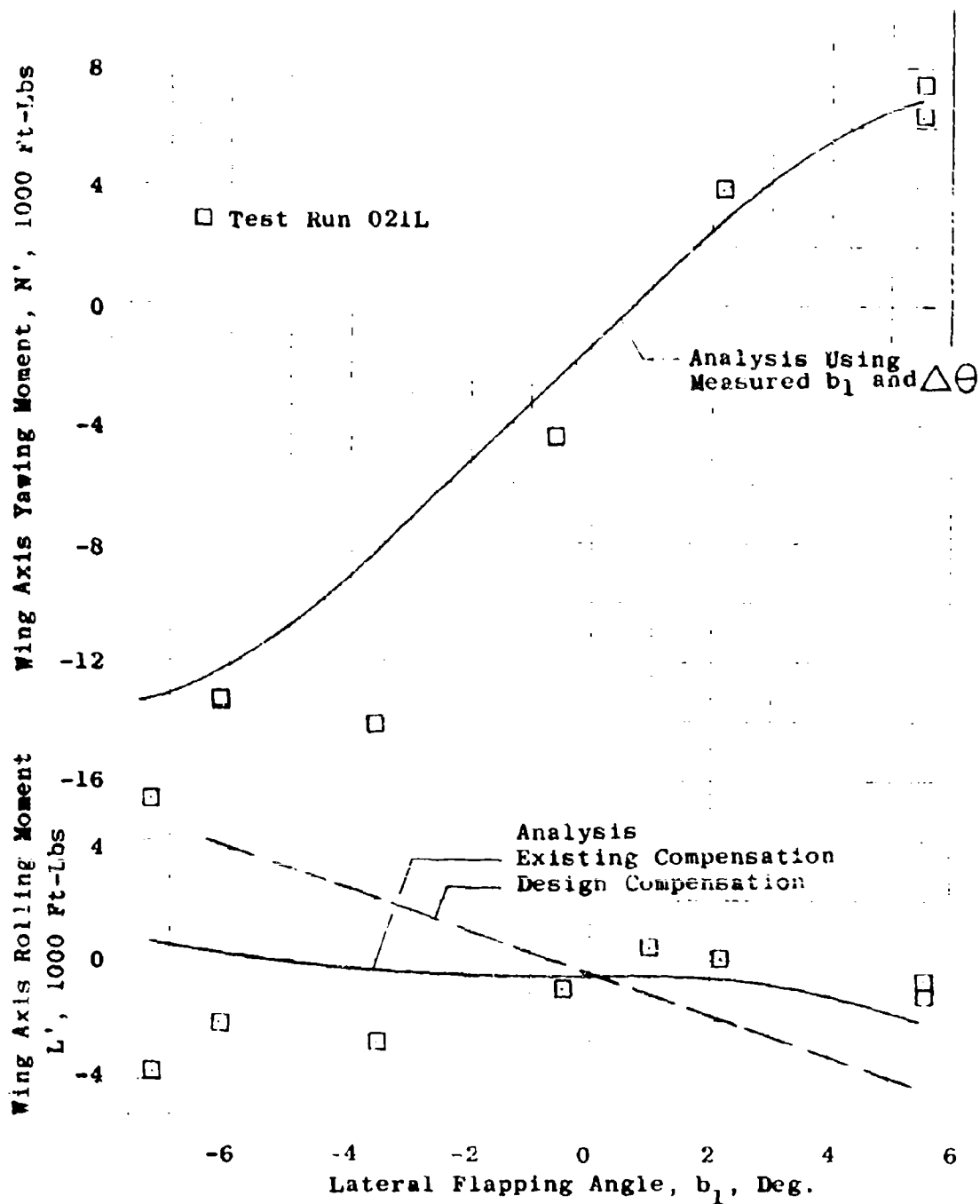
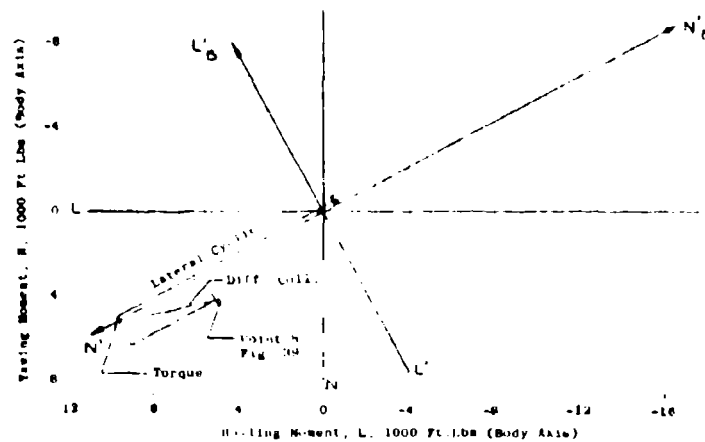Figure 40

Wing Axis Moments Due to Pedal Deflection

Figure 41
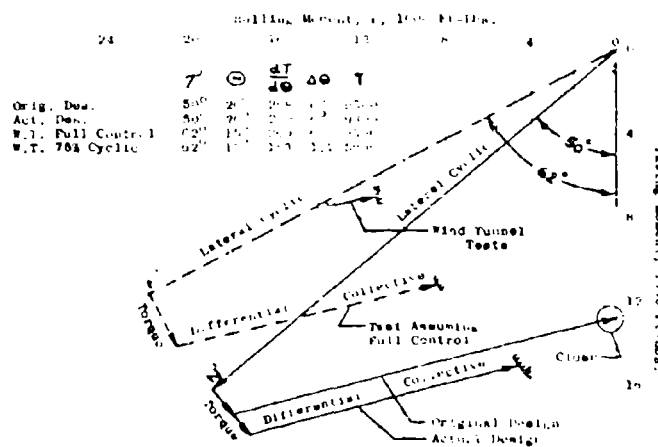Vector Diagram Showing Directional Control Analysis

Figure 42
Vector Diagram Showing Control Moment Distribution

the cosine of the tilt angle. The increased tilt required more differential collective for compensation, which was not available because of control system geometry.

To summarize, the analytical methods applied to the rotor static performance lead to the explanation for a test-rotor figure-of-merit little better than most helicopter rotors. The principal reasons are: the large flap deflections and flap junctures cause high drag and, therefore, low section L/D; drag of the outboard chordwise control rod.

The results of the wing performance tests are inconclusive in establishing a slipstream turning angle because of the large scatter in the drag data. However, reasonable values of wing-flap lift and drag increments are analytically shown to lead to a good average value of the test points for turning angle and efficiency. The turning angle of the flaps was reduced principally because of the reduced span of the flaps.

Rotor control is a function of the moments and forces generated by blade cyclic flapping and differential collective blade pitch. The flapping is induced by cyclic flap deflection, the relation between them known as cyclic sensitivity. The cyclic sensitivity, and subsequent moments obtained in the tests, is almost exactly those analytically determined. They are not those of G-113-4 (9) for the original design however, because of mechanical restrictions in cyclic flap deflections, and the reduced thrust levels of the tests.

The portion of the controllability dependent upon the slipstream turning angle and efficiency reflects the reduction in turning angle from the design value as well as the reduced thrust levels, and tends to substantiate the values deduced from the analysis of the wing-flap performance data.

TRANSITION

In the transition phase of a tilt-wing airplane, the vertical force is gradually transferred from the propellers to the wing (or conversely). This is most efficiently performed when the wing can sustain the greatest portion of the vertical load at the lowest possible speed. A large flap-lift effectiveness requires a lower wing tilt angle to sustain the aircraft, thus, a lower wing free-stream angle of attack. A lower wing angle of attack at any speed will reduce the tendency to stall in the transition.

Airplane Performance

Wind tunnel tests of the K-16B show that at condi-
tions in which the aircraft would be balanced (lift equals
weight, thrust equals drag) the wing was stalled. Figure 43
shows the analytically determined wing slipstream angle of
attack throughout a level-flight transition. With the unpro-
tected leading edge, stall is exhibited between 25 and 70
knots, even in the slipstream.

With no slipstream across it, the center section is
stalled until the total wing angle of attack is reduced to
subcritical values at the end of the transition. The stall
is a result of the pylon wedges which become exposed when the
wing is tilted, the large chordwise extent of the tiltable
portion of the center section, and the lack of leading edge
protection.

The analytical trim procedure of Appendix D, which
accounts for center section stall, was used together with
data for certain representative slats to eliminate stall in
the slipstream and minimize it at the center section of the
K-16B. The center section stall boundary moved from 75 to 50
knots. The elimination of stall on the wing improves the
flow over the tail, making it more effective so that it will
assist the rotor in trimming the aircraft in this flight re-
gime. At the same time, the out-of-trim moments will be
greatly reduced.

Trim Angle of Attack

The free-stream angles of attack shown in Figure 43
were calculated using the longitudinal trim analysis given in
Appendix D. These angles are for a K-16B gross weight of
9300 pounds. Because of wing stall, a lift of 9300 pounds
was only once attained in the transition tests. The effect
of the slipstream is duplicated (ie, the wing angle of attack
is the same) if the disc-loading/q is the same. Also, the
free stream q is determined by the lift equilibrium. Hence,
the measured tunnel dynamic pressure need only be multiplied
by the ratio of the wing loadings to determine the attitude
angles corresponding to lift equilibrium of the aircraft in
flight. This was done in NASA TN D2538 (53) and the test
points are shown in Figure 43a.

Prior to the full-scale tests, the 1/8-scale
powered-model was tested with various Fowler flap configura-
tions and leading edge devices. The attitude angles for lift
and drag equilibrium from these tests are shown in Figure
43B, as well as those from both calculations and full-scale
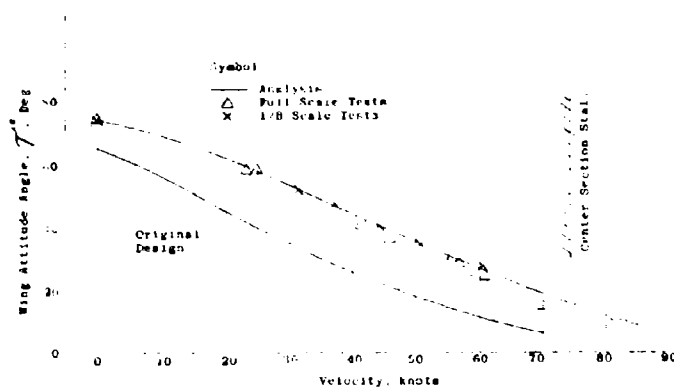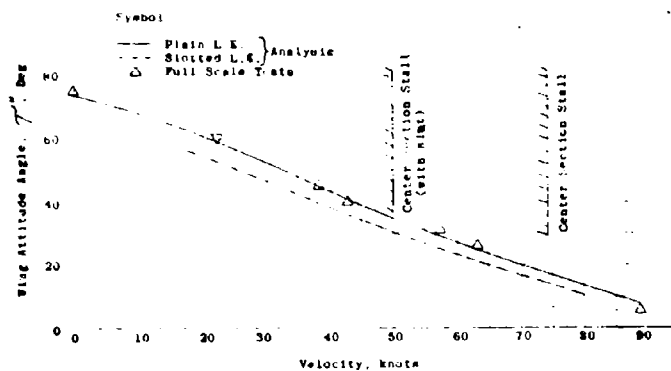tests corrected to 9300 pounds. The figure shows good agree-

Figure 43

Wing Attitude Angle for Level Flight Transition

94

ment in all three methods. Data from the 1/8-scale model tests are shown in Figure 44.

Figure 43b reveals a convexity in the curve of attitude angle for equilibrium flight, whereas the original design was concave. The shape of the curve is indicative of the amount of rotor thrust (and power) required for balance, and points up the extent of the wing stall problem. The tuft sketches (Figure 45) imply a rapid outboard spread of the center section stall that is triggered at fairly low angle of attack by the wing pylon wedges that become exposed as the wing is tilted. The cross-shaft cover protrudes ahead of the leading edge and generates vortices at its edges, which also assisted the outboard spread of the center section stall.

The combination of the high aircraft drag (Figure 27), and the rapid spread of the center section stall resulted in aircraft lift and drag balance at a well-stalled portion of the lift curve for all four transition points that were tested (Figure 46).

Rotor Thrust Estimate

No provision was made for measuring rotor thrust in the wind tunnel tests. For a particular test an approximation of the $T_C{}''$ was made, using the results of the 1/8-scale model tests given in Figure 44, and computing the slipstream based lift and longitudinal force coefficients as:

$$C_L{}'' = C_L(1 - T_C{}'') \tag{13}$$

$$C_X{}'' = -C_D(1 - T_C{}'') \tag{14}$$

These were compared with the results of the 1/8-scale model tests, endeavoring to match the results in the low angle of attack range below the stall. Additional approximations were made, the process continuing until the best possible match was obtained. This was then considered the thrust coefficient $T_C{}''$ to be used in the analysis to establish rotor parameters of power, cyclic sensitivity, and control. The results of this approach are shown in Figure 44 with symbols, and the 1/8-scale model results as bold lines. Only three thrust coefficients were tested in the 1/8-scale model runs and three different thrust coefficients estimated for full-scale for the same configurations, but the "carpet plot" method of presentation allows fairly accurate interpolation to be made.
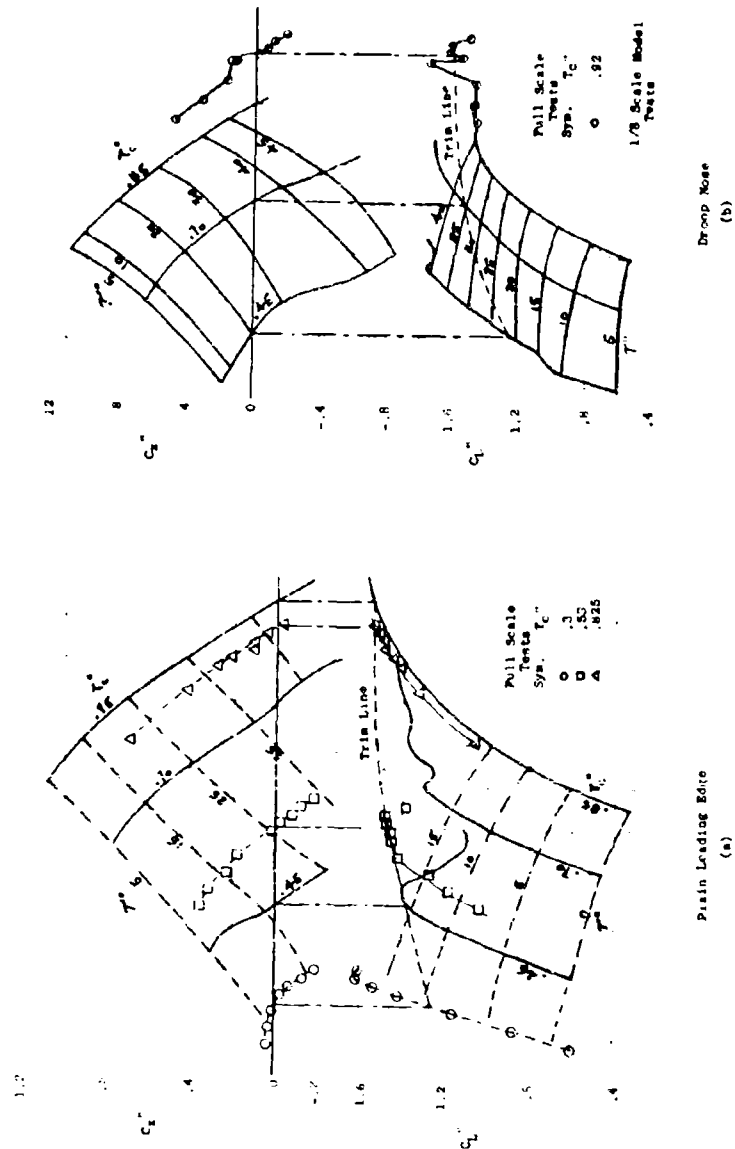
95

Figure 44

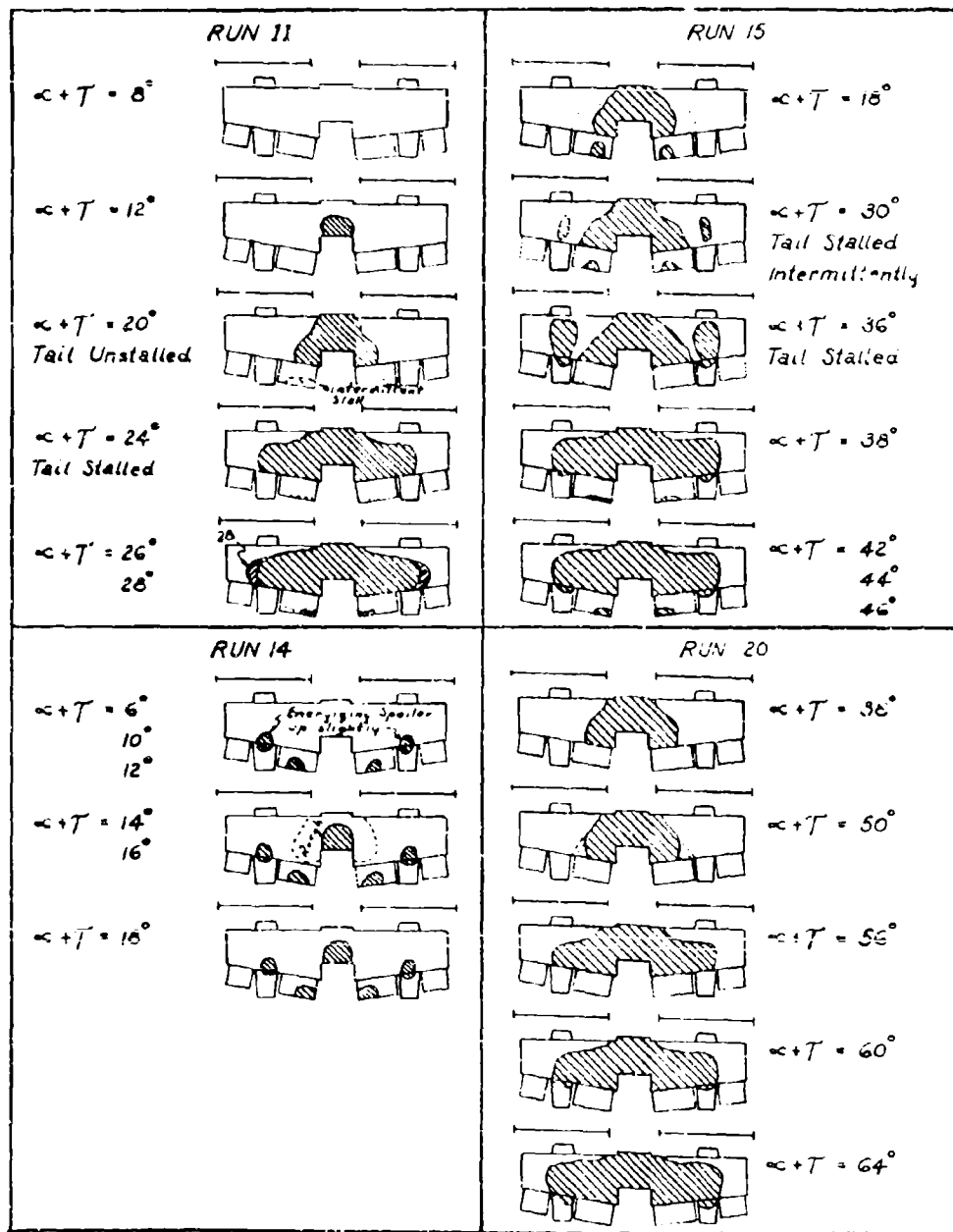Comparison Of 1/8 Scale Model And Full Scale
Aircraft Test Results.

Figure 45
Wing Stall Patterns

(a) Plain Leading Edge

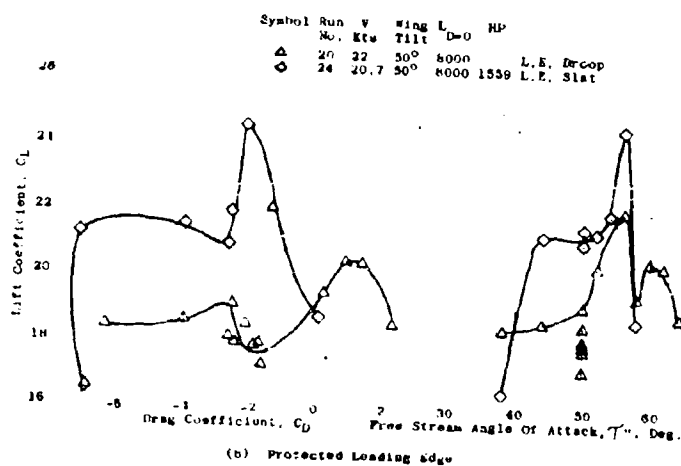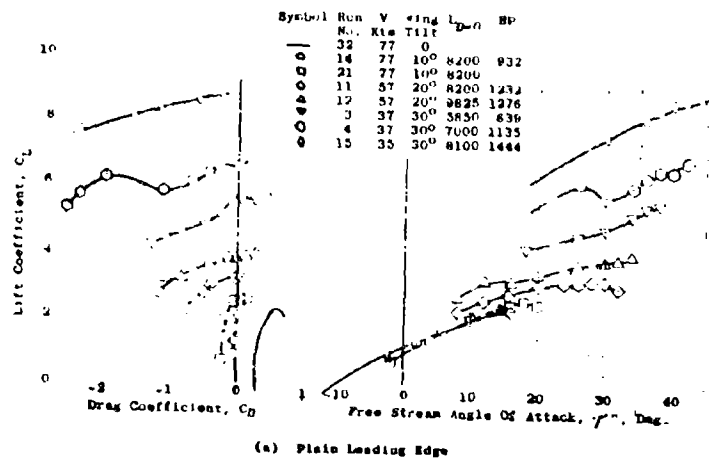(b) Protected Leading Edge

Figure 46

Lift and Drag Characteristics

<u>Power</u>: The power required for balanced level
flight from the tunnel runs is presented in Figure 47, as is
an analysis of Appendix D, Figure 84, for the appropriate
values of μ , λ , and C_T. It will be noted that these re-

sults are different from those given in Figure 22 of NASA
TN D2538 (53). There are two essential reasons for this dis-
crepancy. First, the values in Figure 22 (Ibid) are for a
9300 lb aircraft, whereas those in Figure 47 herein are for
the actual lift attained in the tests. It was considered
advisable in an analytical correlation to avoid the addition-
al uncertainties of a method for extending both profile power
and induced power to apply to a higher gross-weight vehicle.
The second reason is indicated by Figure 48, which shows dif-
ferent amounts of power reduced from the same data. The NASA
points are the first three points of Figure 25 of TN D2538.
Because no reason is known for the discrepancy and the total
difference would militate against the analysis, it is advis-
able to give, in detail, the steps taken to reduce the engine
data to SHP. Run 4, Figure 48, ill be used to illustrate
the procedure.

In Run 4 a lift of 7000 lb was attained when suffi-
cient power was introduced for drag balance. The power re-
quired was 1135 HP, and was obtained as follows:

1. The inlet temperature, as measured from
    the inlet duct thermocouples, was found

    to be 77°F leading to a $\sqrt{\theta_2}$ of 1.0165.

2. From a "blip" count on the oscillograph
    records (Traces 2 and 3) the gas producer
    speeds were found to be 23760 rpm and
    23900 rpm for the left and right engines,
    respectively.

3. From the calibration charts for the spe-
    cific engines these led to values of

    $$\frac{HP_{PT}}{\sigma_2\sqrt{\theta_2}}$$ of 595 and 636, respectively.

4. The inlet temperature and test section

    pressure led to a σ_2 of 0.964.
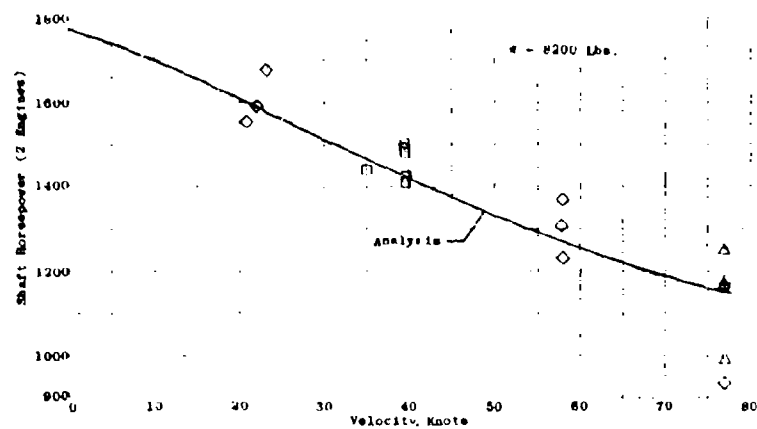
5. Multiplying the values from the calibra-

99

W = 8200 Lbs.

Shaft Horsepower (2 Engines)

1600

1600

1400

Analysis

1200

1000

900

0   10   20   30   40   50   60   70   80
Velocity, Knots

Figure 47
Horsepower At Drag Balance

$\tau = 30°$
V = 37 Knots

10

Drag Balanced Lift, 1000 Lbs.

KAC Reduction

Run 15

Run 4

Run 3

NASA
Reduction
Fig. 26
Ref. 53

10   12   14   16   18   20
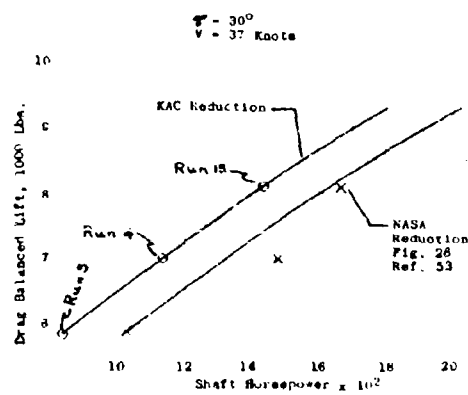Shaft Horsepower x 10^2

Figure 48
Extrapolation To Normal Gross Weight

100

tion chart by $\sqrt{2}\sqrt{\theta_2}$ led to HP$_{PT}$ of

584 and 623 for the left and right engines, respectively.

6. The correction for operating off the optimum RPM depends on the power turbine speed, N$_2$. This is obtained

   .rom the rotor "blip" count, Trace 1, multiplied by the gear ratio. For this case it is 675(26.32) = 17750 rpm.

7. This is corrected to standard conditions for entry into the G.E. chart (CA 123). This chart is entered both for the actual and optimum rpm (19,500), and the difference noted. In this case it is a loss of 20 HP for each engine, resulting in a total loss of 39.2 HP when corrected for temperature.

8. This is subtracted from HP$_{PT}$'s obtained

   from Step 5, leaving 564 and 603, respectively.

9. The main gearbox loss is furnished by the engine manufacturer as a function of power turbine speed. For this case, it was 16 HP for each engine, leaving net turbine shaft horsepower of 548 and 587 for the left and right engines, respectively.

This procedure was used in the reduction of all the power data in this report, inasmuch as there is often a fair discrepancy between the N$_1$ as indicated by the tachometer and that obtained from the oscillograph record. There are many small corrections which, if neglected, lead to erroneous values of power.

The analysis of Figure 84 agrees fairly well with the experimental values. It must be pointed out however, that the wing was in deep stall when drag balance occurred. The power required consequently was higher than it would be had there been no stall.

101

Rotor Performance

The rotor is designed to provide high thrust for hovering flight, so the mean lift coefficient is high with collective flap deflection. As the thrust requirements drop off with forward speed, the propulsive-rotor becomes less efficient because the blade sections are operating at lower lift-drag ratios. The collective flap is retracted as the thrust drops off, and when nalfway through the transition is fully retracted.

Propulsive Efficiency

Most of the transition tests of the K-16B were run with a constant 13 degrees of blade-flap collective deflection. In an actual aircraft transition, of course, flap deflection would be reduced from the optimum hover value to zero in forward flight.

A thrust calibration was made at two airspeeds, 39 and 77 knots, assuming thrust equals drag. (These are the first two series of points in Figure 8c of TN D2538 (53)). This calibration was to be run with zero collective flap deflection, but there was an inadvertent deflection of 2.3 degrees. At the point at which the aircraft is balanced, Figure 49 indicates a power of 1080 HP. At this point the rotor propulsive efficiency was 53 percent. The calculated efficiency was 57.8 percent. Agreement is good, especially since in the tests the flap was deflected 2.3 degrees when supposedly retracted, and the strip analysis in forward flight does not provide for a collective flap deflection.

The transition flapping analysis of Appendix D was used to determine the effect of flap deflection on rotor efficiency at these speeds. The comparison is shown in Figure 50. A reduction in efficiency of about 2 percent is indicated for the 2.3 degrees of collective flap deflection. This brings closer the agreement between analysis and experimental results.

With the alleviation of wing stall in the transition, the power will drop off with speed as the induced power is reduced. At higher speeds, when the required thrust and advance ratio both increase, the efficiency will also increase. At 140 knots (the last series of points of Figure 8c of TN D2538) rotor efficiency was not investigated. A mechanical restriction limited the pitch angle to 26 degrees (which results in a negative thrust at this advance ratio), and the flaps were not fully retracted. These last points, then. are not the result of a thrust calibration, but are the incidental results of a test to investigate rotor blade flapping at high speed.
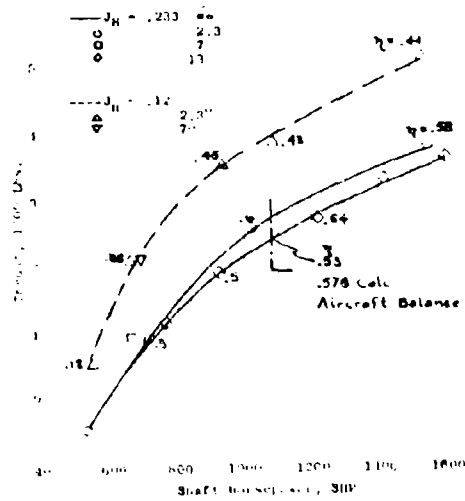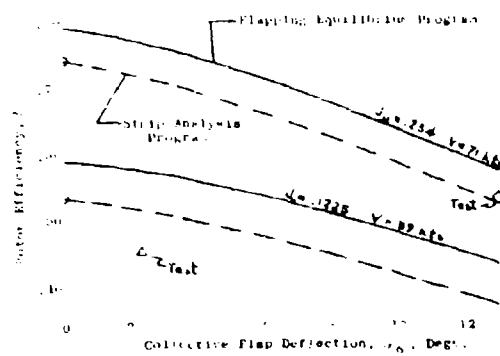
102

Figure 49
Thrust Calibration

Figure 50
Effect of Collective Flap Deflection On Rotor Efficiency

Control

At the low end of the transition speed spectrum, the aircraft is controlled by propulsive-rotor cyclic lift. The magnitude is dependent upon cyclic sensitivity, which has been discussed in the "hover" section. A particular required control moment for low-speed control can be obtained from an optimum combination of blade design parameters. As speed increases, the cyclic control is phased out and the aerodynamic surfaces take over.

The complete equations of blade flapping motion are given in Appendix D, and the cyclic sensitivities for the present K-16B are shown in Figure 88.

Longitudinal

The cyclic sensitivities of the wind tunnel tests are compared in Figure 51 with the results of an analysis from Appendix D, Figure 88. At the two lowest tunnel dynamic pressures the agreement is good, but at the two higher dynamic pressures the analytical results are conservative. The most likely reason for the conservatism is a variation of the cyclic inflow factor with forward speed. The factor used was derived from hovering control considerations. But in transition the induced velocity, which is modified by the cyclic inflow factor, is a smaller proportion of the total inflow.

In Figure 52 control moments are shown as functions of the longitudinal flapping angle. They are presented as functions of the resulting flapping angle, a_1, rather than cyclic flap deflection, $\widehat{\sigma}_{1_L}$, to remove the effect of scatter in the cyclic sensitivity. The control power from the analysis of Appendix D, Figure 88, is also shown. Fair correlation is evident, but with test results signifying a higher control moment per degree of flapping than does the analysis in the linear range.

Test results (Figure 52) include the effect of the elevator. The analysis also does, but estimated values of $dC_m/d\sigma_e$ from XAC Report G-113-4 (9) were used. It is prudent to compare the estimated and the test values of this parameter. Figure 53 shows that the calculated elevator effectiveness (slope of curve) from Reference 9 is not too different from the results of Runs 33, 34, and 36 (Figure 31 of NASA TN D2538) (53), although the experimental value is slightly higher than the calculated value.
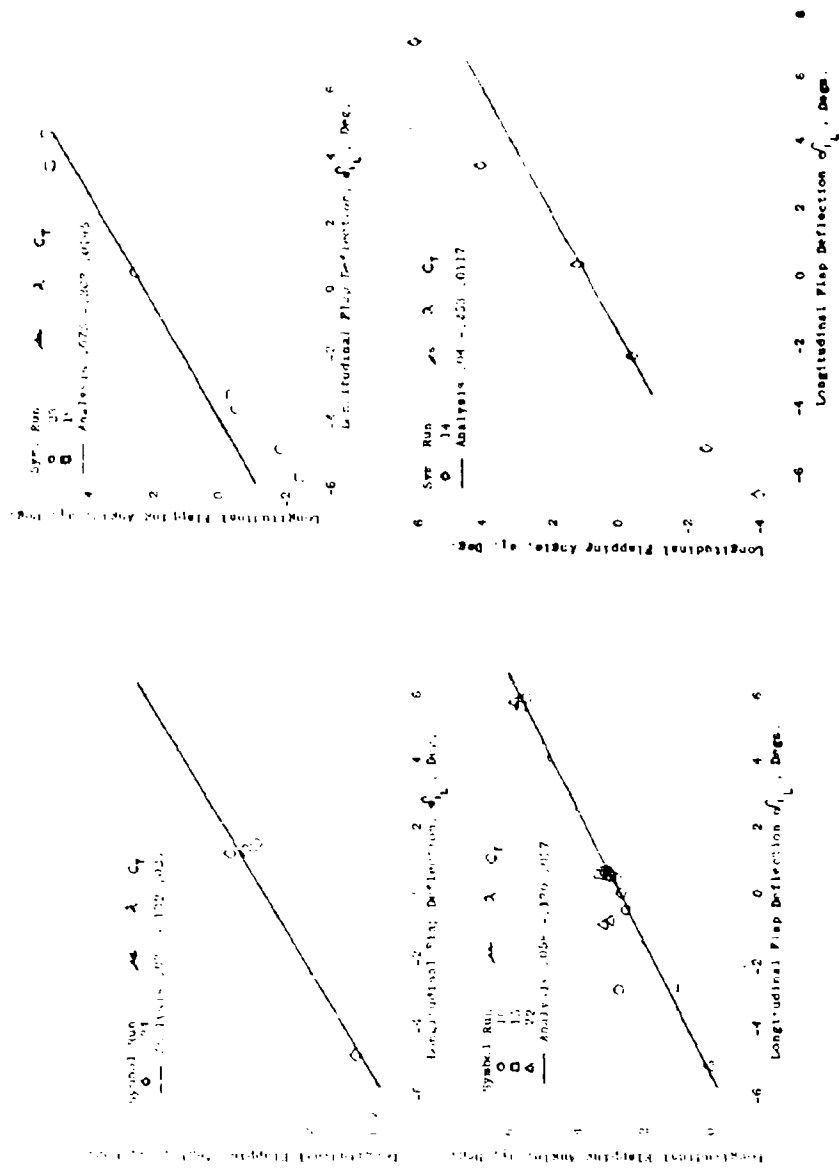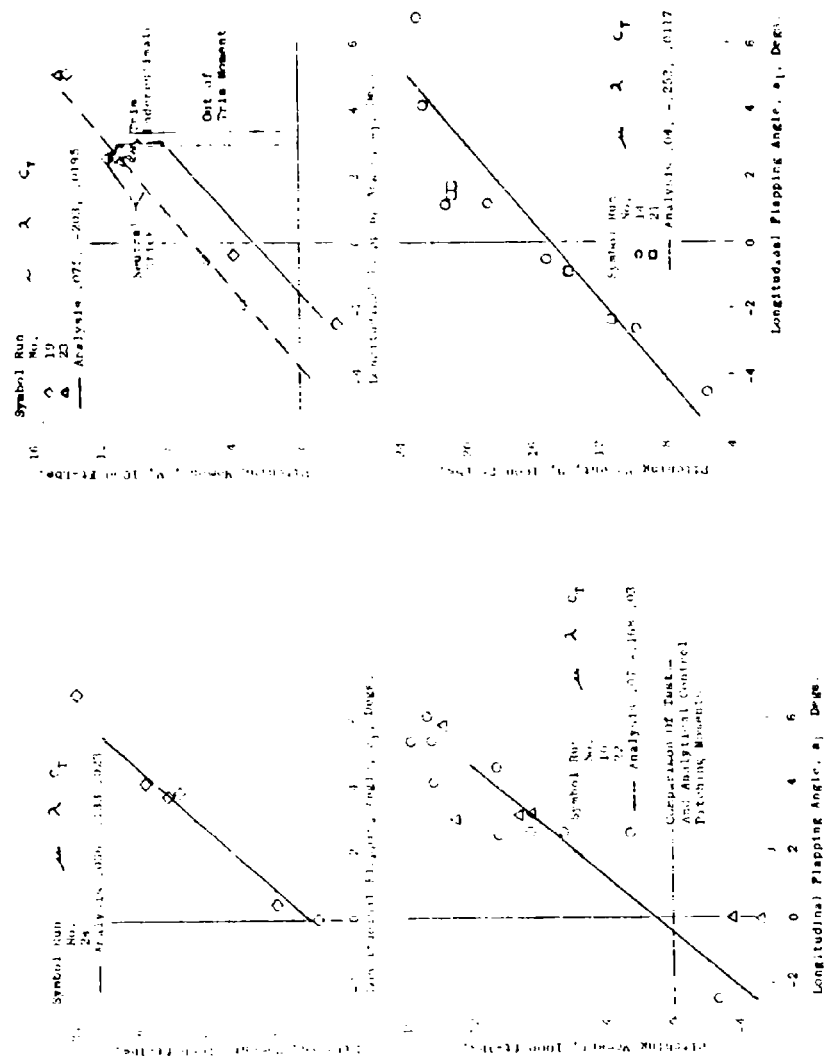
Figure 51

Longitudinal Cyclic Sensitivity

Figure 52

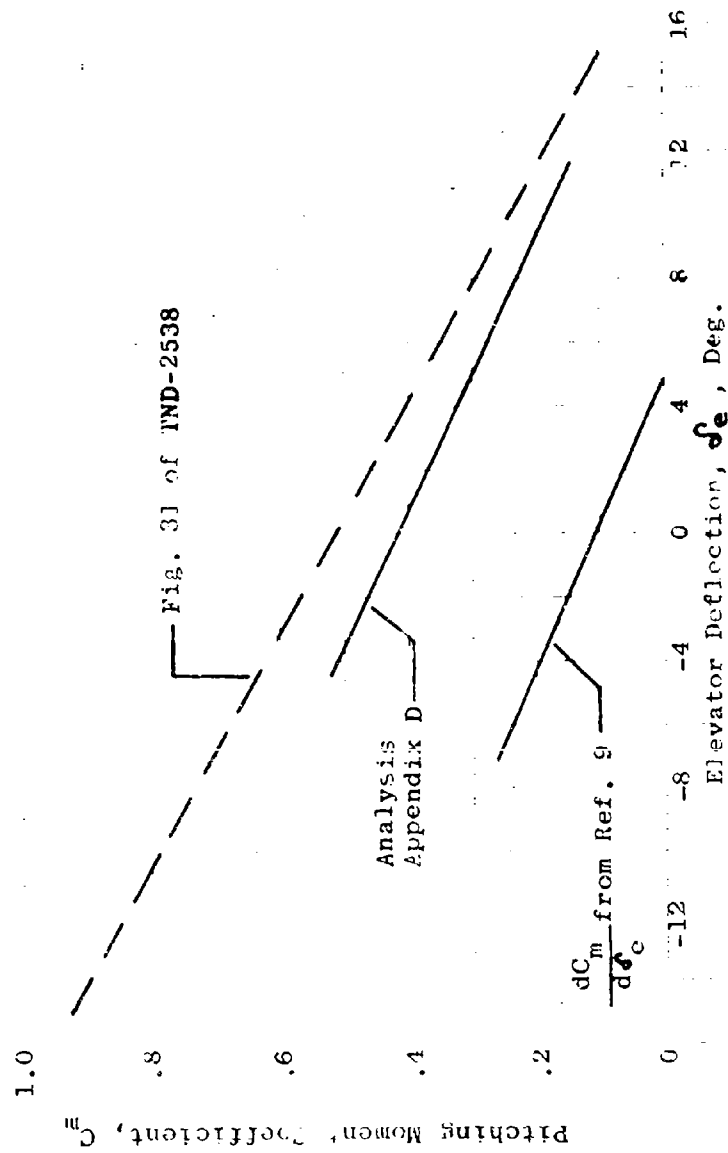Comparison of Test And Analytical Control Pitching Moments

Figure 53

Comparison Of Analytical And Test Values Of Elevator Effectiveness

The increment in pitching-moment coefficient due to the elevator can be expressed as:

$$\Delta C_{m_t}'' = \frac{dC_m}{d\delta_e} \frac{d\delta_e}{d\delta_{i_L}} \delta_{i_L} \left(1 - T_c'' \right) \tag{15}$$

and:

$$\Delta M_{te} = \Delta C_{m_t}'' q'' S \bar{c}$$

$$= \frac{dC_m}{d\delta_e} \frac{d\delta_e}{d\delta_{i_L}} \delta_{i_L} q S \bar{c} \tag{16}$$

or:

$$\frac{dM_t}{da_1} = \frac{dC_m}{d\delta_e} \frac{d\delta_e}{d\delta_{i_L}} \frac{1}{da_1/d\delta_{i_L}} q'' S \bar{c} \tag{17}$$

Substituting:

$$\frac{d\delta_e}{d\delta_{i_L}} = .96 - .0192 \text{ from Ref. 9} \tag{18}$$

$$\frac{da_1}{d\delta_{i_L}} = .56 \text{ from Figure 88 for Run 19}$$

$$\frac{dC_m}{d\delta_e} = .027/\text{deg from Figure 53}$$

$$q = 11.2 \text{ for Run 19}$$

into the above equation yields 474 ft-lb/deg, which is but about 20 percent of the total control moment of 2200 ft-lb/deg that is developed. Of course, the elevator effectiveness increases with airspeed. The foregoing figures apply to an airspeed of 58 knots.

During the elevator effectiveness tests, the controls could not hold the deflection against the airstream. The difference in moment slope, dM/da_1, (Figure 52) is approximately equal to the loss in elevator effectiveness, $dC_m/d\delta_e$ related through equations (17). This is an indication of control system deflections.

108

Figure 52 also indicates an "out of trim" moment from tests with stick neutral. The "stick neutral" point of Run 19 on the figure shows a moment of approximately 11,000 ft-lb. (This is the same as shown in Figure 25 of TN D2538 for a lift of 8800 lb.) The calculated moment of 7000 ft-lb reflects the difficulty in estimating the drag of the various components of a stalled flapped wing, part of which is in the slipstream and part of which is not. Because of the influence of vortices shed by either end of the cross-shaft cover at the center section, both induced and profile drag of that portion of the wing are difficult to estimate without drag build-up tests.

Lateral-Directional

In the K-16B, hover lateral control is obtained by differential blade pitch with lateral cyclic flapping to compensate for the residual yawing moment. As the wing is brought down in transition, the yawing moment component increases, so more lateral cyclic is required to compensate. Finally, the speed is great enough so that spoilers provide sufficient roll control and differential collective is phased out. Similarly, directional rotor control in hover is lateral cyclic with differential collective pitch providing the compensation for the residual rolling moment. As the wing tilt is reduced, the compensating differential collective pitch is phased out, for the rudder is becoming effective.

Lateral and directional control excursions were made at a wing tilt of 40 degrees under conditions similar to Run 15 (Figure 51a). The lateral cyclic sensitivity would be expected to be identical to the longitudinal, but 90 degrees out of phase. The results are displayed in Figure 54. A comparison of this figure with the lower half of Figure 51 shows a similar slope, although greater than the analytical slope. Calculations underestimated the moments, most likely as a result of a reduction in effective cyclic inflow factor, which reduction was neglected in the analysis.

Pedal Deflection

Pedal depression brings about lateral cyclic flap deflection and a compensating differential collective pitch to provide pure body-axis yawing moment. The body-axis yawing and rolling moments due to pedal depression are considered a function of lateral flapping in Figure 55.

An analysis of the wing axis yawing and rolling moment shows substantial agreement with the maximum right rudder depression that was tested (Point 1). Pitch was
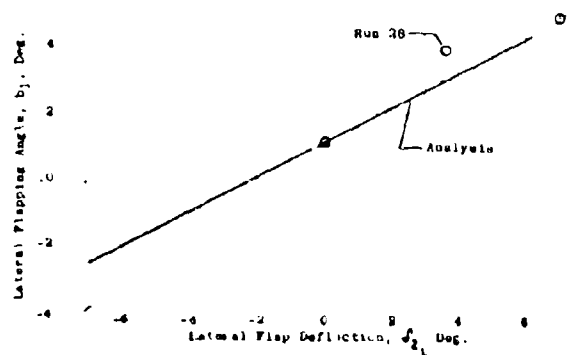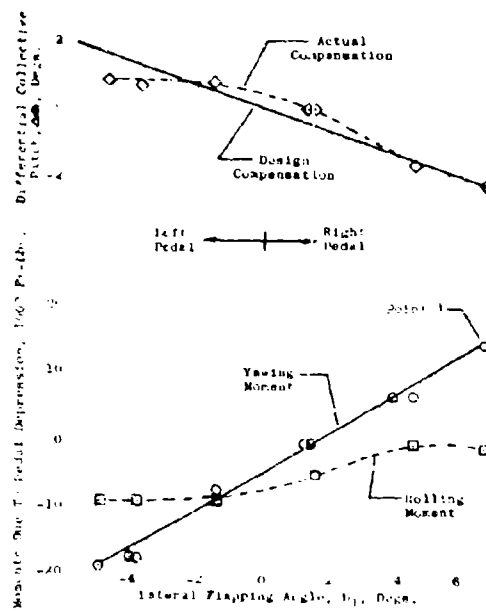
Figure 54
Lateral Cyclic Sensitivity

Figure 55
Moments Due To Pedal Depression

measured on the right rotor only. For the left rotor, the differential collective pitch was determined using Figure 37.

The experimental compensating differential collective pitch variation, shown in Figure 55, reveals substantial agreement with the design compensation (KAC Report G-113-4) (9) for right pedal depression. The residual rolling moment is small. For left pedal depression however, there was insufficient compensation and the residual rolling moment was high. A similar result was noticed in the static stand tests (Figure 39). This anomoly has not been investigated in detail, but may be due to asymmetry in compensating linkage adjustment.

Lateral Stick

The control input of lateral stick deflection is differential collective pitch with lateral cyclic introduced to compensate for the induced yawing moment. Figure 56 shows the rolling and yawing moments for lateral stick. The lack of accurate yaw compensation is immediately apparent (the negligible variation of b_1 flapping with differential pitch). The same thing was apparent in the hovering tests (Figure 40). The probable explanation is that so little compensating lateral cyclic is required, deflection or lost motion in the control system linkages prevented the correct cyclic flap input.

In summary, rotor cyclic sensitivity and control power can be accurately predicted for hovering flight and low-speed transition flight (Figures 51, 86, 88). At higher speeds in transition, the analysis underestimates the experimental values. The reasons for the conservatism are not precisely known, but they are probably associated with a reduction in cyclic inflow factor. The analysis indicates the physical properties that determine rotor control power. By proper proportioning of these parameters, any reasonable amount of control power can be attained. Because the analytical predictions are conservative rather than optimistic, plenty of control is available and proper proportioning can readily be attained. The mechanical design of the K-16B airframe control system, however, would require stiffening, re-adjustment, and reduction of lost motions before it could be considered satisfactory for flight.

Forward Flight Flapping

An articulated rotor minimizes the one-per-revolution root-bending stresses in the transition phase of tilt-wing operation. But because the blades are hinged, in
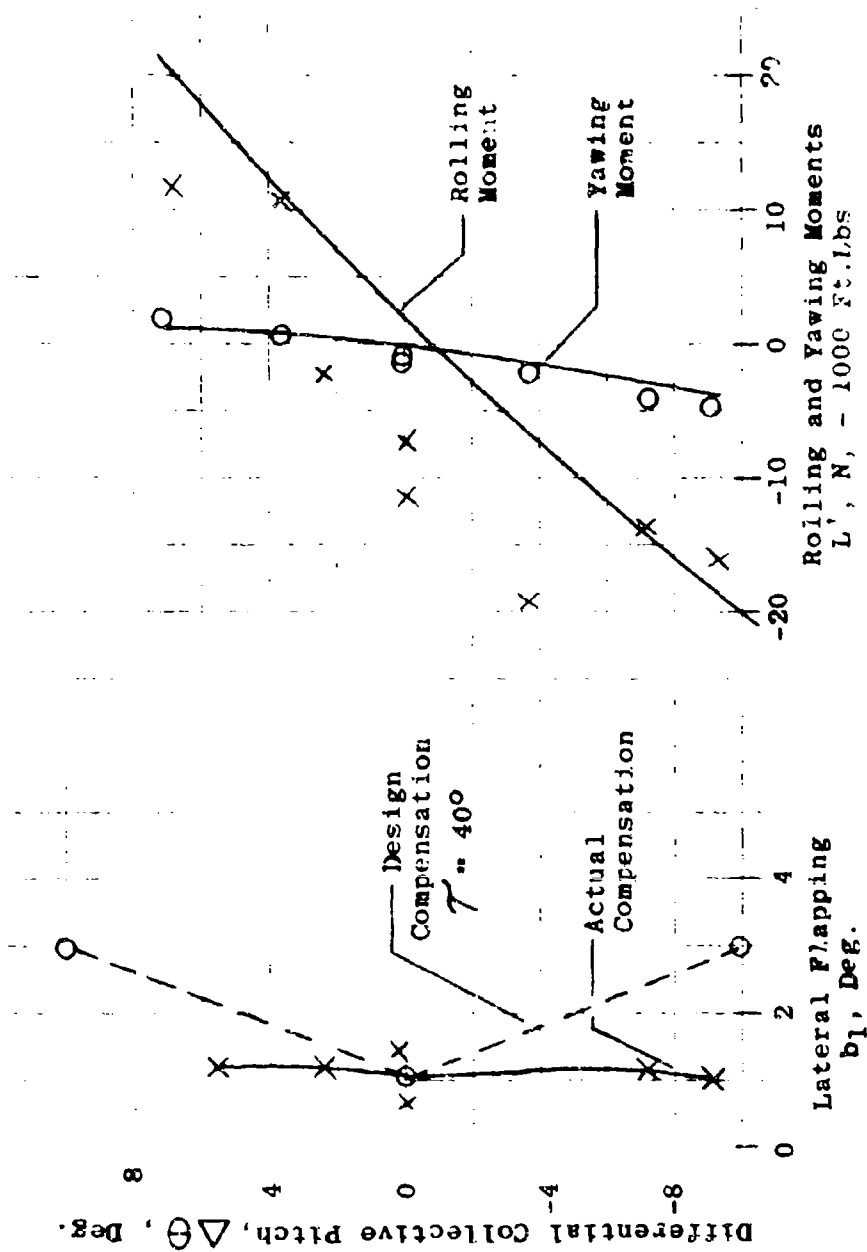
111

Figure 56

Moments Due to Lateral Stick Deflection

forward flight they will flap back in response to angle of attack changes. It is important that this flapping remain within reasonable bounds.

Figure 57 shows the results of the wind tunnel tests of blade flapping for the K-16B rotor. Because rotor blade longitudinal flapping effectively tilts the rotor thrust vector, the resulting vertical component is akin to the well-known normal force of a hingeless propeller. The

results indicate that the slope $\partial a_1 / \partial \alpha_c$ increases with

advance ratio J_H (see lines marked J_H = .25 and .40). But

even at a J_H of 0.43 (137 knots) the longitudinal flapping

is only about 1/3 degree per degree change in angle of attack. The principal reason for the low value of forward flight flapping sensitivity of the K-16B rotor is the relatively large flapping hinge offset. The centrifugal force moment about the offset flapping hinge acts as an effective spring that is proportional to the offset and the first mass moment. Therefore, the longitudinal flapping sensitivity is inversely proportional to the offset. The analysis in Figure 57 is that from Appendix D under "Transition Performance". It is general and valid for any value of

inflow ratio, λ, and can be used for forward flight in-

vestigations. A simpler analysis based on single harmonic flapping was used to construct Figure 85 to point out the effect of several blade parameters on the forward flight longitudinal flapping derivative. The figure shows that high first-mass-moment, flapping hinge offset, and pitch-flapping coupling all reduce flapping.
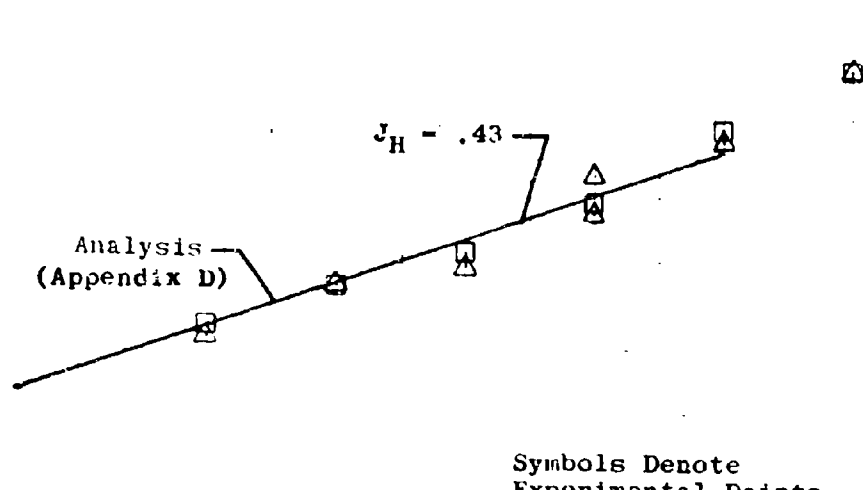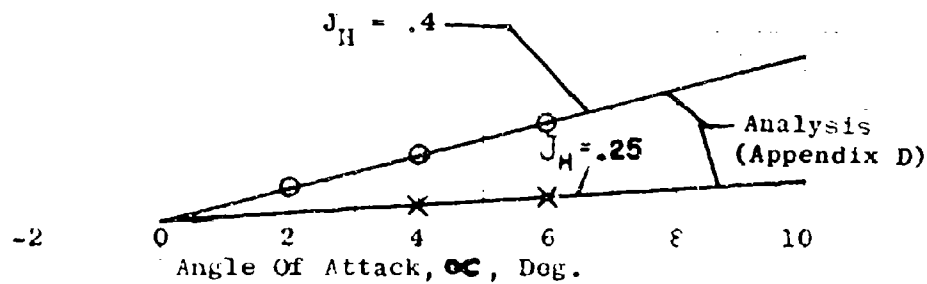
Figure 57
Rotor Forward Flight Longitudinal Flapping

114

CONCLUSIONS

The propulsive-rotor has demonstrated its potential to provide stable, powerful, positive control throughout the entire low-speed regime at a minimum power loss, fuel consumption, and weight. It does this in a unified propulsion/control package not requiring additional auxiliary control devices.

This control system is analogous to the helicopter rotor cyclic control concept, operates in much the same manner, and produces comparable control forces and moments by cyclically deflecting a trailing edge flap in each blade. Collective deflection of these flaps provides variable camber blades that permit best compromise between static thrust and propeller cruise efficiency. Flapping freedom of the blades reduces out-of-plane vibratory bending stresses at the high angles of attack characteristic of VTOL and STOL transition operation.

The concept was tested on ground bench stands, and in full-scale wind tunnel testing or a partially deflected-slipstream, tilt wing airplane. The particular model, designed in advance of adequate aerodynamic and aeroelastic criteria, did not demonstrate the maximum potential of the propulsive-rotor. However, when correction is made for the non-optimum design of test hardware, the correlation of analysis with thrust and control data obtained at NASA, Ames Research Center, shows the validity of the analytical treatment of performance.

Airframe problems were the result of either a non-optimum configuration stemming from the limited basic data available during the design phase, but now correctible with straight forward design approaches based on currently-available data; detailed hardware deficiencies which would yield to further conventional development effort; or problems, basic to the VTOL configuration, which have been experienced in later programs, and on which research data are now available. The VTOL airframe is now quite well understood.

The propulsive-rotor, however, is unique and still a valuable concept. Data from the K-16B program has been correlated with analysis and the analytical methods improved since the early design analysis. Present methods accurately check wind-tunnel performance and control results, and can be used for reliable parametric analysis of propulsive-rotors for operational use.

Studies have resulted in a new rotor system design which resolves the problems that appeared in test hardware. Aerodynamic analyses show that the new rotor design will provide a sufficient margin of static thrust to assure adequate vertical flight performance of the K-16B, and that control performance will meet the requirements of Specification MIL-H-8501A. Recent developments in high-capacity, nonlubricated control bearings now make the propulsive-rotor concept practical as well as theoretically feasible. Dynamic analysis of a new flap retention and control system geometry show acceptable bearing P-V loads, and a very marked improvement in both fatigue life and in system stiffness.

The airplane was designed to furnish an airframe whose size, design load factors, and performance characteristics were compatible to those required for an anticipated military mission. Structural analysis substantiated by test has demonstrated the ability of the K-16B to safely operate in the prescribed envelope.

Wind tunnel tests at NASA, Ames Research Center, disclosed a rather severe wing stall buffet in transition with an unprotected leading edge. A leading edge modification that proved very beneficial on the 1/8-scale model did not improve full-scale results as significantly as expected.

The problem appears to be endemic with the tilt-wing concept. One solution has been at least partially successful on the XC-142. Analyses have indicated how the stall of the K-16B wing can be alleviated or eliminated during transition both in level flight and at reasonable rates of descent.

That the use of wing flaps tends to reduce transition stall has been well documented, but no entirely satisfactory method for analysis of the wing-stall problem has been developed. At the present, only wind tunnel tests of a particular configuration can resolve the problem. However, as a result of the correlation between analysis and K-16B test data, it is believed that the analytical procedures are useful for initial prediction of turning angles and efficiencies.

REFERENCES

Ref.
No.

1. Brackson, ... and Gardiner, ...

2. ...

3. ...

4. ...

5. ...

6. ...

7. Zen, J., "Methods of Analysis in Five Flight Loading Conditions", Kaman Aircraft Corp., No. G-113-2, 15 December 1959

8. Egerton, H.S., "Pilot Comport and Mockup Review", Kaman Aircraft Corp., No. G-113-3, 12 February 1959

9. Fitzsimiek, J.F., Zen, J., and Castle, G., "Estimated Flying Qualities of the Kaman 16B VTOL-STOL Aircraft", Kaman Aircraft Corp., No. G-113-4, 20 February 1959

10. Ciannante, N., and Below, H.C., "K-16B Estimated Airloads Report", Kaman Aircraft Corp., No. G-113-5, 15 July 1959 (revised 6 January 1960 and 16 June 1960)

11. Guenther, H.M., "Flutter Analysis of the Kaman K-16B VTOL/STOL Research Aircraft", Kaman Aircraft Corp., No. G-113-6, 15 October 1959 (revised 22 August 1960)

12. Zen, J., Ciannante, N., and Fitzpatrick, J., "Estimated Flying Qualities of the Kaman K-16 VTOL/STOL Aircraft, Part II, Dynamic Stability in Transitional Flight", Kaman Aircraft Corp., No. G-113-7, 20 November 1959

13. Wheeler, R., "Model K-16B Estimation Weight and Balance Report", Kaman Aircraft Corp., No. G-113-8, 18 December 1959

14. Bassier, R.B., "Structural Analysis of Flight Controls", Kaman Aircraft Corp., No. G-113-9, 21 January 1960

15. Jones, R., "Mechanical Instability Analysis of the Kaman K-16B VTOL/STOL Research Aircraft", Kaman Aircraft Corp., No. G-113-10, 15 January 1960

16. Gardiner, M.B., and Rozdilski, T.J., "Proof Load Test of the K16B VTOL STOL Research Amphibian wing for a Symmetrical Landing Approach", Kaman Aircraft Corp., No. G-113-11, 10 March 1960

17. Gardiner, M.B., and Bovenzi, J.F., "Proof Load Test of the K16B VTOL STOL Research Amphibian wing for a Symmetrical 3-point Landing", Kaman Aircraft Corp., No. G-113-12, 18 March 1960

18. Gardiner, M.B., and Bovenzi, R., "Proof Load Tests of the K16B VTOL STOL Research Amphibian Control Systems", Kaman Aircraft Corp., No. G-113-13, 15 July 1960

19. Bovenzi, J.F., "K-16B Flight Loads", Kaman Aircraft Corp., No. G-113-14, 11 April 1960

20. Bovenzi, J.F., "K-16B Ground Loads", Kaman Aircraft Corp., No. G-113-15, 8 April 1960

21. Jacquier, M., "K-16B Rotor Loads", Kaman Aircraft Corp., No. G-113-16, 8 April 1960

22. Bovenzi, J.F., "Load and Stress Analysis K-16B Transmission Mount", Kaman Aircraft Corp., No. G-113-17, 11 April 1960

23. Bovenzi, J.F., "Stress Analysis - K-16B Alighting Gear", Kaman Aircraft Corp., No. G-113-18, 11 April 1960

24. Bovenzi, J.F., and Rozdilski, T.J., "K-16B Wing Stress Analysis", Kaman Aircraft Corp., No. G-113-19, 11 July 1960

25. Bovenzi, J.F., "K-16B Fuselage Wing Attach Loads", Kaman Aircraft Corp., No. G-113-20, 9 June 1960

26. Kaloskines, I.M., "Stress Analysis of the K-16B Drive System", Kaman Aircraft Corp., No. G-113-21, 9 May 1960

27. Jacquier, M., "Unit Shears and Bending Moments - K-16B Wing", Kaman Aircraft Corp., No. G-113-22, 9 June 1960

28. Rozdilski, T.J., and Bovenzi, J.F., "Stress Analysis - K-16B Nacelle", Kaman Aircraft Corp., No. G-113-23, 21 June 1961

29. Poullishen, P., "K-16B Rotor Stress Analysis", Kaman Aircraft Corp., No. G-113-24, 18 November 1960

30. Rozdilski, T.J., and Bovenzi, J.F., "Stress Analysis - K-16B Fuselage", Kaman Aircraft Corp., No. G-113-25, 6 January 1961

31. Rozdilski, T.J., "Stress Analysis - K-16B Empennage", Kaman Aircraft Corp., No. G-113-26, 1 August 1960

32. Flannelly, William and Schuett, Erich, "Mechanical Instability Report", Kaman Aircraft Corp., No. G-113-27, 1 October 1960

33. Greene, Kenneth H., "K-16B Torsional Analysis", Kaman Aircraft Corp., No. G-113-28, 16 March 1962

34. Egerton, H.S., "Model K-16B V STOL Research Airplane - Final Report - Part II", Kaman Aircraft Corp., No. G-113-29, November 1962

35. Greene, H., "Flutter Test Report", Kaman Aircraft Corp., No. G-113-30, 24 October 1960

36. Fitzpatrick, J., "Longitudinal Characteristics of the K-16B Aircraft Based on 1/6-scale Model Wind Tunnel Test Results", Kaman Aircraft Corp., No. G-113-31, 20 November 1961

37. Egerton, H.S., "Model K-16B Rotoprop Flap Controls Fatigue Test", Kaman Aircraft Corp., No. G-113-33, December 1962

38. Egerton, H.S., "K-16B Lower and Drive System Bench Static Programme Test", Kaman Aircraft Corp., No. G-113-34, December 1962

39. Egerton, H.S., "Model K-16B Rotoprop Flap and Flap Reflection Fatigue Test", Kaman Aircraft Corp., No. G-113-35, November 1962

40. Gallardo, Vincente Jr., "Propeller-Nacelle Whirl Flutter Analysis of the K-16B Amphibious VTOL/STOL Aircraft", Kaman Aircraft Corp., No. G-113-41, August 1962

41. Fay, C.B., "A Cursory Analysis of the VTOL Tilt-wing Performance and Control Problems", Annals of the New York Academy of Sciences, Vol. 107, Art. 1, March 1963, pp 102-146

117

42   Anderson, R.C., and Blackburn, W.K., "Ground and Flight Test Evaluation of the Kaman Modified Servo-flap Rotor System", Kaman Aircraft Corp., No. T-85, 15 June 1955

43   McCoubrey, G.A., and Michel, D., "Analytical Study of a Modified Kaman Servo-Controlled Rotor System with Results from Small Scale Model Tests", Kaman Aircraft Corp., G-43, 19 December 1952

44   Gamble, R.F., and Rollrock, R.H., "Report of Preliminary Tests of the Kaman Aircraft Corp., G-51, 24 June 1953

45   Himmelskamp, H., "Profiluntersuchungen an einem Umlaufenden Propeller" (Profile Experiments on a Rotating Propeller), Thesis Gottingen (1945), Reports of the Max Planck Institute, Gottingen, November 1950

46   Kuchemann, D., "Types of Flow on Swept Wings", Journal of the Royal Aeronautical Society, Vol. 57, No. 515, November 1953

47   Burgan, Elmer T. and Matthews, John T., "Wind Tunnel Tests of a 1/8-Scale Powered Model of the Kaman K-16B VTOL/STOL Airplane', Navy Department, David Taylor Model Basin, Aero Report 998-Problem Assignment 1-32-08, February 1961

48   Kelly, John A., "Effects of Modifications to the Leading Edge Region on the Stalling Characteristics of the NACA 63,012 Airfoil Sections", NACA TN 2228, 1950

49   Harris, T.A., and Lowry, J.G., "Pressure Distribution Over an NACA 23012 Airfoil with a Fixed Slot and a Slotted Flap", NACA TR 732, 1942

50   A'Harrah, R.C., "Results of a Pilot Evaluation Study of the Flying Qualities of the Kaman K16B Airplane", North American Aviation, Columbus Division, NA60R-672, 31 October 1960

51   Anon, "Estimated Flying Qualities of Kaman Model K16B VTOL/STOL Aircraft as Provided by the NAA Simulator", NATC Patuxent River, Report No. 1, Final Report, 31 September 1960

52   Falabella, G. W., and Meyer, J.R. Jr., "Determination of Inflow Distributions from Experimental Aerodynamic Loading and Blade-Motion Data on a Model Helicopter Rotor in Hovering and Forward Flight", NACA TN 3492, November 1955

53   Weiberg, James A., and Guilianetti, Demo J., "Wind-Tunnel Investigation of a Tilt-Wing VTOL Airplane with Articulated Rotors", NASA TN D-2538, March 1965

54   Egerton, H.S., and Giansante, N., "A Study of the Feasibility of using a Semi-rigid or Articulated Rotor on a Tilt-wing VTOL Aircraft", Wright Air Development Center, Wright-Patterson Air Force Base, WADC TR58-34, October 1958

55   Kuhn, Richard E., "Semi-empirical Procedure for Estimating Lift and Drag Characteristics of Propeller-Wing and Flap Configurations for Vertical and Short Take-off and Landing Airplanes", NASA Memo 1-16-59L, 1959.

56   Harris, T.A., and Purser, P.E., "Wind Tunnel Investigation of an NACA 23012 Airfoil Section with Two Sizes of Balanced Split Flaps", NACA Wartime Report L-441 (ACR November 1940)

57   Lowry, J.G., and Polhamus, E.C., "A Method for Predicting Lift Increments due to Flap Deflection at Low Angles of Attack in Incompressible Flow", NACA TN 3911, 1957

58   Weiberg, James A., "Static Stand Tests of the Kaman K-16B Airplane", Memorandum for Director, NASA-Ames, August 17, 1962

59   Anon, "Guide for Planning Investigations in the Ames 40x80 Foot Wind Tunnel", NASA Ames Research Center, January 1957

60   Gessow, A., and Crim, A.D., "A Method of Studying the Transient Blade Flapping Behavior of Lifting Rotors at Extreme Operating Conditions", NACA TN 3366, 1955

61   Sikorsky, I.A., "Correlation of Helicopter Performance Equations". Paper presented at 25th Annual Meeting of the Institute of the Aeronautical Sciences, January 28-31, 1957, IAS Preprint No. 694

62   Meyer, J.K., and Falabella, G., "The Effect of Blade Mass Constant and Flapping Hinge Offset on Maximum Blade Angles of Attack at High Advance Ratios", Proceedings of the 8th Annual Forum of The American Helicopter Society, May 15-17, 1952

63   Gessow, A., and Myers, G.C., Aerodynamics of the Helicopter, MacMillan Co., New York, 1951

64   Reeder, John P., and Whitten, James B., "Some Effects of Varying Damping in Pitch and Roll on the Flying Qualities of a Single Rotor Helicopter", NACA TN 2889, 1952

65   Crim, A.D., "Hovering and Low-Speed Flying Qualities of VTOL Aircraft", Navy Department, Bureau of Aeronautics, Research Div., Report DR-1888, April 1958, Pg 2

66   Salmire, Seymour and Tapscott, R.J., "The Effects of Various Combinations of Damping and Control Power on Helicopter Handling Qualities During Both Visual and Instrument Flight", NASA TN D-58, October, 1959

67   Tapscott, R.J., "Criteria for Control and Response Characteristics of Helicopters and VTOL Aircraft in Hovering and Low-speed Flight", Institute of Aeronautical Sciences, Paper No. 60-51, 1960

68   A'Harrah, R.C., and Kwiatowski, S.F., "A New Look at V/STOL Flying Qualities", Institute of Aeronautical Sciences, Paper No. 61-62, 1961

69.   Kuhn, Richard W., and Draper, J. W., "An Investigation of a Wing-Propeller Configuration Employing Large-Chord Plain Flaps for Low Speed Flight and Vertical Takeoff", NACA TN 3307, 1954.

118

FIGURES

119

SYMBOLS

a   perpendicular distance between wing chord line and rotoprop shaft centerline, ft

a   lift-curve slope

a^s angle between rotor thrust vector and rotor resultant force

a_1 longitudinal flapping angle, rad

a_o rotoprop coning angle, rad

b   wing span, ft or number of blades per rotor

B   number of blades

b_e portion of wing span immersed in slipstream, ft

b_t horizontal tail span

b_1 lateral flapping angle, rad

c   wing chord or rotor blade chord, ft

$\bar{c}_e$ elevator root mean square chord, ft

$\bar{c}$ wing mean aerodynamic chord, ft

c_w wing chord directly behind rotoprop

c_e average wing chord immersed in slipstream

c_l section lift coefficient

c_{d_o} section profile drag coefficient

C_D drag coefficient, $\dfrac{D}{qS}$

C_{D_e} drag coefficient on wing in slipstream

C_D'' drag coefficient, $\dfrac{D}{q''S}$

C_L lift coefficient, $\dfrac{L}{qS}$

C_{L_e} lift coefficient on that portion of the wing in slipstream

$C_{L_{\alpha}}$ lift curve slope, $\dfrac{\partial C_L}{\partial \alpha}$

C_{L_t} lift coefficient of the horizontal tail

C_L'' lift coefficient,

C_{L_w}'' wing lift coefficient, $\dfrac{L_w}{q''S}$

C_l rolling-moment coefficient, $\dfrac{L'}{qSb}$

C_H rotor longitudinal force coefficient

C_m pitching-moment coefficient, $\dfrac{M}{qS\bar{c}}$

C_{m_h} pitching-moment coefficient increment of the hull

C_{m_t} pitching-moment coefficient increment due to the horizontal tail

C_M'' pitching moment coefficient, $\dfrac{M}{q''S\bar{c}}$

C_n yawing-moment coefficient

C_{n_R} increment in yawing-moment coefficient due to rotoprop operation

ΔC_{n_v} increment in yawing-moment coefficient due to vertical tail

C_q torque coefficient, $\dfrac{Q}{\rho \pi R^2 (\Omega R)^2 R}$

C_T thrust coefficient, $\dfrac{T}{\rho \pi R^2 (\Omega R)^2}$

C_X'' longitudinal force coefficient, $\dfrac{X}{q''S}$

C_Z rotoprop normal force coefficient normal to relative wind at infinity

D   rotoprop diameter, ft

d_t perpendicular distance from the thrust line to the elevator hinge line

e   flapping hinge offset, ft, or span efficiency factor

f   flat plate drag area

H   rotor longitudinal force ($\perp$ thrust)

H_e elevator, rudder and spoiler hinge moments
H_r
H_s

I_1 rotoprop blade flapping moment of inertia $\displaystyle\int_o^R r^2 dm$ slugs ft^2

I_{YR} rotoprop blade product of inertia $\displaystyle\int_o^R y r \, dm$ slugs ft^2

i_t horizontal tail incidence, deg

J   jet thrust

J_H rotor forward flight advance ratio, $\dfrac{V}{\Omega R}$

K_1 V_e/V_{∞} ratio of velocity at a point in the slipstream to theoretical velocity in developed slipstream

K   factor accounting for cyclic inflow through the rotoprop disc, $\dfrac{1}{1 + \dfrac{6}{\sigma a}\left(-\lambda + \dfrac{C_L/\sigma}{\sqrt{\lambda^2 + \mu^2}}\right)}$

l_t horizontal tail length, ft

L   lift, lb

l_v vertical tail length, ft

L' rolling-moment, ft. lb

l_p distance from wing mean aerodynamic center to rotor hub, ft

M   pitching-moment, ft. lb

M_{o_w} wing pitching-moment at zero angle-of-attack, ft. lb

M_f hull pitching-moment, ft. lb

M_H rotor hub moment, ft. lb

N   number of propellers

N_1 engine gas generator RPM

N_2 engine power turbine RPM

n   yawing-moment, ft. lb

n_z normal acceleration

q   free stream dynamic pressure, lb/sq. ft. or pitching velocity, rad/sec

q'' $q + \dfrac{T}{\pi R^2}$

120

$q_{Res,R}$	resultant dynamic pressure at the propeller disc, vector sum of q and $\dfrac{T}{4\pi R^2}$, lbs sq ft
q_{Res}	resultant dynamic pressure at the wing aerodynamic center. Vector sum of q and $\dfrac{k_1^2 T}{\pi R^2}$ lb sq ft
q_t	average dynamic pressure at tail, lb sq ft
r	rotor blade radial station, ft
R	rotor blade radius ft
S	wing area, sq ft
S_f	reference area for fuselage coefficients
S_m	wing area in the slipstream, sq ft
S_R	wing area outside the slipstream, sq ft
S_t	horizontal tail area
S_v	vertical tail area
T	thrust, lbs
T_w	linear twist, degs or rad
T_c	thrust coefficient, $\dfrac{T}{\rho V^2 D^2}$
T_c''	thrust coefficient, $\dfrac{T}{q''\pi R^2}$
V_e	velocity in slipstream at wing a c
W	aircraft weight
W_f	fuel flow, lbs hr
X	longitudinal force, lb
x	nondimensional blade radial station
x_1	inboard end of propeller flap as percent blade radius
x_{CG}	perpendicular distance from wing aerodynamic center to center of gravity
x_h	distance along shaft line from propeller hub to center of gravity, ft.
Y	side force, lbs.
z_{CG}	perpendicular distance from wing chord plane to center of gravity, ft.
z_h	perpendicular distance from propeller shaft line to center of gravity, ft.
x,y,z	body axis system
x',y',z'	wing axis system
α	angle of attack, deg.
α_w	angle of attack of wing in slipstream, deg

|	
α_t	horizontal tail angle of attack, deg.
α_h	hull angle of attack, deg
β	blade flapping angle
γ	Lock's no. $\dfrac{c a_c R^4}{I_1}$
δ_n	propeller collective flap deflection, rad
δ_1	propeller longitudinal flap deflection, rad
δ_2	propeller lateral flap deflection, rad. or engine inlet pressure to standard ambient pressure ratio
δ_3	pitch-flapping coupling angle
δ_{1L}	longitudinal swash plate deflection, rad.
δ_e	elevator deflection, deg
δ_{f_w}	wing Fowler flap deflection, deg
δ_r	rudder deflection, deg
δ_m	spoiler deflection, deg
α_d	flap lift effectiveness derivative,
ϵ'	downwash at tailplane, power off, deg
ζ	blade mass factor, $\dfrac{(\Omega/R)R^2}{I_1}\int_{r/R}^{1}(x-\tfrac{r}{R})dm_b$ (ref. 6) rotor efficiency
η_t	horizontal tail efficiency factor
η_v	vertical tail efficiency factor
Θ	blade pitch angle, deg.
Θ	wing flap slipstream turning angle
λ	wing straightening factor
λ	rotor inflow ratio
μ	rotor advance ratio
ξ	propeller flapping hinge offset,
ρ	air density
σ	propeller solidity ratio
τ	wing-hull tilt angle, deg.
τ'	angle between rotor resultant force and free stream velocity
τ''	angle between wing chord line and free stream velocity for steady level flight, deg.
ϕ	propeller blade inflow angle
ψ	rotor azimuth angle from downstream in direction of rotation
Ω	rotor rotational speed, rad sec.

APPENDIX A
# PRINCIPLES OF PROPULSIVE
ROTOR CONTROL

Numerous V/STOL aircraft have been and are continuing to be evaluated by the Military. A recurring problem has been that of securing adequate control in hover and transition. Repeatedly, control power alone has been obtained by auxiliary devices, frequently with limited success. The propulsive rotor eliminates the need for any such auxiliary devices. All three modes of control are inherent in the rotor. The following pages contain an explanation of the forces and moments that are generated by it.
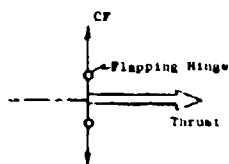
Equilibrium Condition

1. Thrust vector is perpendicular to tip path plane and along center line of shaft

2. Centrifugal forces on the mass of the blades cancel.
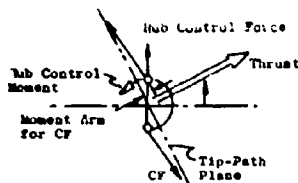
Cyclic Control Causes the Rotor to Tilt

1. Thrust vector tilts in direction that the tip path plane tilts, causing an increment of thrust on the hub perpendicular to the shaft axis, which is used as a control force.

2. Because one side of the rotor flaps down and the other flaps up, the centrifugal forces acting on the offset flapping hinge of the blades have different moment arms. This causes a hub moment in the direction that the rotor tilts, about an axis perpendicular to the shaft axis.

Cyclic Control
Principle
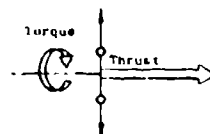
Equilibrium Condition

1. Thrust is fixed at a certain amount.

2. Torque is also fixed and the direction of the moment is opposite to the direction of rotation of the rotor.
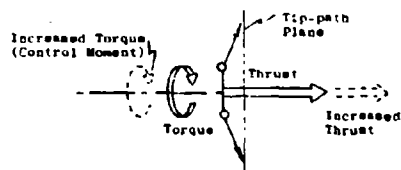
When Collective Pitch is Increased

1. Thrust increases giving a positive increment of thrust (dotted line) perpendicular to and away from the tip path plane, and which is used as a control force.

2. Torque increases giving an increment of moment (broken line) about the shaft axis opposite to the direction of rotor rotation, and is used as a control moment.

3. The slipstream velocity of the air from the rotor increases, causing an increase of the lift (up force) at the wing (shown later).

When Collective Pitch is Decreased

1. Thrust decreases causing a negative control force increment into the tip path plane.

2. Torque decreases causing control moment in direction of rotation

3. Velocity of slipstream air over wing decreases causing reduction of lift or a down control force on wing
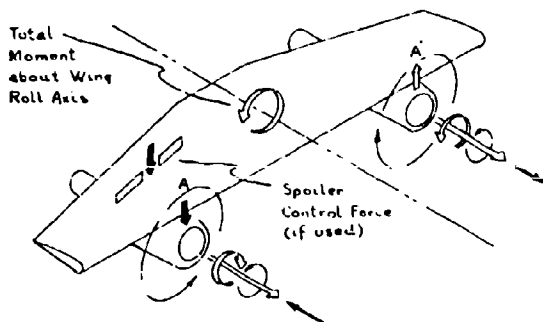
Collective Control
Principle

122

These are the basic sources of control. To complete the picture, the controls must be related to the airplane as a whole. But the problem is complicated by the fact that the direction and magnitude of the control forces will change in the transition from hovering to forward flight. During transition, the control moment axes rotate with respect to the body axes which must be controlled. The control system must be programmed to combine the forces along, and moments about the control moment axes into pure forces and moments on the body axes. This means that both the body axes and the control moment axes must be considered. It is necessary to separate the wing from the airplane to understand the control moments that can be applied to it.

The three control axes of the wing are:
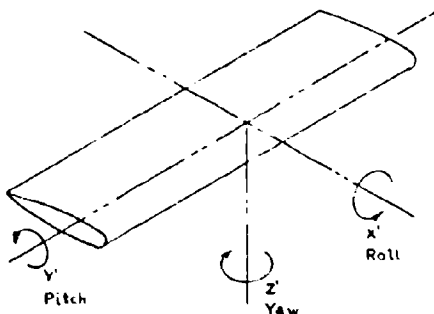
Control moments about an axis can be applied either by a moment on another axis (such as a shaft axis) parallel to the axis, or by a force at a given moment arm distance.

For moments about the roll axis, X':

Under equilibrium conditions, the thrust is equal on both rotors, and the torques are equal but in opposite directions. Roll control is obtained by differential collective pitch. When rolling left-wing up, right-wing down, the thrust on the left rotor is increased and that on the right rotor decreased an equal amount. The differential torques are additive in the same direction. There is also an increase in lift on the left wing and a corresponding decrease in lift on the right wing (due to slipstream) yielding a moment in the same direction (A-A'). If spoilers are used, the right wing spoilers are extended, causing a further down force on the right wing, and therefore a moment in the same direction. The total rolling moment is the vector sum of these moments.

For moments about the pitching axis, Y':
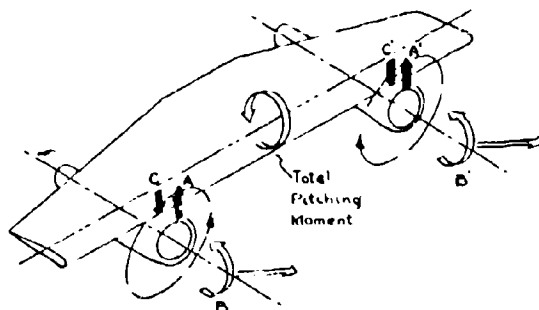
Pitch control is obtained by longitudinal cyclic control which tilts both rotor tip path planes in the same direction. If the tip-path planes tilt so that the thrust vectors point up, the wing pitches leading edge up. The two upward increments of thrust (A-A') cause a moment about the pitch axis because they act at a moment arm distance ahead of the Y' axis. The hub moments (B-B') act in the same direction and add to the thrust moment to give total pitch control moment. A residual up-force (A-A') is cancelled by the loss in lift on the wing (C-C') because of the change in angle of attack from the tilting of the rotor.

For moments about the wing yaw axis, Z':
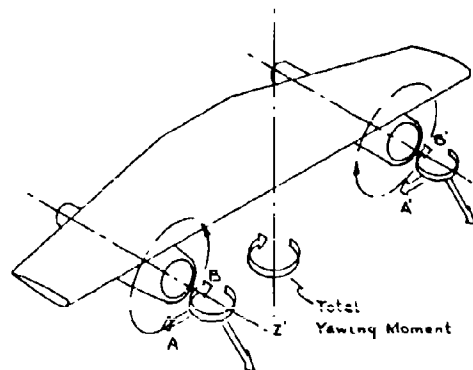
Yaw control is attained by lateral cyclic control. Here, both rotors tilt in the direction of yaw. In the same manner as pitch control, the sideward increments of thrust (A-A') and the hub moments combine to yield a total control moment about the yaw axis.

These, then, are the basic sources of control about the three wing axes. To complete the loop, the controls must be related to the aircraft as a whole. When the wing is down, its three axes are parallel to the aircraft stability axes and, therefore, the wing control moments can apply to the aircraft controls equally as well. But when the wing is tilted, the wing and aircraft axes are no longer parallel.

As can be seen in the following sketch, the stability axes of the airplane (solid lines) are located through the center of gravity; also, the Y and Y' axes are still parallel. Hence, moments about the aircraft pitch axis will produce pure moments about the aircraft pitch axis. But the X and X' axes, and the Z and Z' axes are displaced from each other by the angle of wing tilt, γ.

123
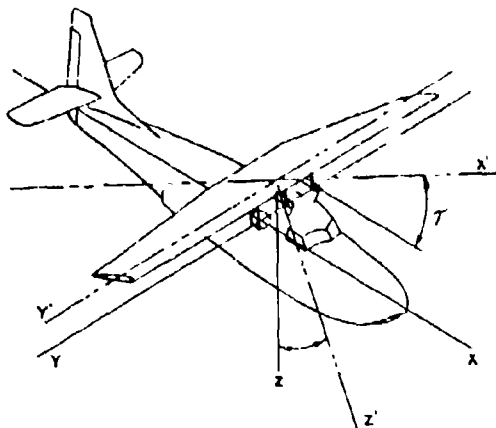
Differential thrust produces a moment about the longitudinal axis that is perpendicular to the resultant thrust vector. If $\tau = 90°$, this will be pure roll about the body axis. If the fuselage has an incidence angle, roll will be with respect to earth axes, causing some positive yaw coupling (right yaw with right roll). Thus, differential collective pitch will give nearly pure rolling moment, so long as we keep the body level. There will be an induced yaw due to differential torque (which will depend upon the direction of propeller rotation) and to differential wing lift (because of slipstream). At partial wing tilt, there is also an induced yaw. In any case, the yaw is compensated by the automatic introduction of directional control. With appropriate programming, differential collective pitch will result in pure rolling moment for any combination of tilt and slipstream turning.

Lateral cyclic produces a moment in the plane of the propeller shaft axis. At 90° tilt, it is pure roll; at 45° tilt it is positively-coupled roll and yaw of equal magnitude. At 90° tilt, lateral cyclic can be used in conjunction with differential collective pitch to augment roll control. This will require less extra propeller thrust for equal control. The advantages will be less power transfer across the interconnecting shaft, and the possibility of higher design C_T/σ for the propeller. The side force accompanying the rolling moment is also advantageous, for it will produce translation with a reduction in angular rotation.

At 90° tilt, yaw control can be produced by differential longitudinal cyclic and/or differential wing flap. A combination might be optimum. Out of ground effect, wing slipstream straightening reduces the effectiveness of differential longitudinal cyclic. In ground effect, slipstream spreading makes differential wing flap ineffective. A combination can be made that would be fairly constant with altitude.

If partial tilt is used, about 45° is maximum for good yaw effectiveness from lateral cyclic. But there will also be positive roll coupling. This will call for the introduction of differential collective to balance the coupling. Differential wing flaps will also produce yaw, probably with small negative roll coupling. There might be a combination of lateral cyclic and differential wing flap that will give pure yaw, depending on the airframe design geometry.

The K-16B used a partial tilt concept. As noted earlier, only about 18° of slipstream deflection was finally obtained, requiring the wing plane to assume an attitude of approximately 74° in hover. At this high attitude, lateral cyclic produced mainly rolling moment; thus, directional control of the aircraft was inadequate. Design changes would be required either to increase slipstream deflection to permit tilt angles of the order of 45°, or to change directional control from lateral cyclic to differential longitudinal cyclic plus wing flaps.

An interconnect between the wing and the control system determines the routing of pilot control inputs. Thus, in the wing-down position, the rotor cyclic control is divorced from the control inputs, and the pilot operates the aerodynamic surfaces. As the wing is tilted, the interconnect actuates a Kaman-patented linkage that proportionally changes the sense of direction of the pilot's control inputs, permitting control to the rotor. In the K-16B, this also decreased control to the rudder and elevators.

124

The K-16B configuration consists of a partially tilting wing mounted on a modified JRF-5 fuselage. The general arrangement is shown in Figure 5, at right. In each of the wing mounted nacelles is installed a YT58 GE8 engine. To keep the engines within their qualified flight envelope as the wing is tilted, they are installed at a 35 degree nose-down attitude. Through a reduction gearbox each engine drives a propulsive rotor. The power and drive system in each nacelle are interconnected by a cross shaft in the wing leading edge, thus avoiding a serious asymmetrical thrust problem in the event of one engine failure.

The various major structural and dynamic areas are briefly described in the following paragraphs. A summary of pertinent dimensional characteristics will be found at the end of this appendix.

ROTOR SYSTEM

The propulsive rotor is a 15 ft 2 in diameter, three bladed system. Disc loading is in the order of 25 lbs/ft². Variable camber is provided in the form of deflectable trailing edge flaps on the blades, permitting the best compromise between static thrust in hover and propeller cruise efficiency. Flapping freedom within ±20 degrees, and a tuned restraint by Belleville springs in lead lag are provided. Outboard of the flapping hinge is a blade feathering hinge. The only significant departure from current helicopter rotor practice lies in the relatively small diameter and higher operating speeds employed, present maximum rotor rpm being 725. The rotors, shown in Figures 58 and 59, rotate in opposite directions to cancel torque.

The airfoil section is an NACA 16-509 modified in the flap area, and is constant from Blade Sta. 42 to the tip. Blade chord is constant at 18 in., with a spanwise washout of .3387 degrees per inch. The submerged flap has an envelope of 80 percent of blade chord and 55 percent of actual blade span.

The hub (Figure 60) is composed of two flanged plates mechanically joined together by bolt attachment to a spindle disposed on the centerline of the assembly. At 10 percent of rotor radius and equally disposed at 120 degrees are three universal crosses, each retained in the hub assembly by a double-row tapered roller bearing in the lower plate and a needle bearing in the upper plate. Blade flapping occurs around one axis of this cross, lead-lag about the other.

The rotor control system incorporates a swash plate (Figure 61) mounted on the propeller shaft. The swash-plate consists of a stationary member in which is mounted a rotating member, the assembly in turn mounted on a spherical ball seat assembled on the propeller shaft. Both cyclic and collective control of the rotor is accomplished by displacement of the swashplate, the swashplate motion is translated through appropriate linkages into motion of the blade flaps. Angular displacement of the swashplate results in a sinusoidal blade flap motion as the rotor revolves. Fore and aft displacement of the swashplate causes a simultaneous collective flap deflection of all three flaps that is not affected by rotor rotation.

POWER AND DRIVE SYSTEM

A schematic diagram of the drive system is displayed in Figure 62. The engine is installed at a 35 degree nose-down attitude to keep it within its qualified flight envelope as the wing is tilted. This requires an intermediate gearbox to permit drive into the main transmission because structural considerations prevented installing the engine so that it could drive directly into the main box. The intermediate gearbox steps up the engine rpm of 6000 in hover to the main gearbox input rpm of 8500. Two stages of reduction - the first a 2.31:1 spur-gear mesh, the second a 4.31:1 planetary train - reduce the input rpm to the 725 rotor rpm in hover. On the main box input shaft is installed a conventional sprag-type free wheeling unit which automatically disengages the engine in the event of an engine failure. Opposed hand rotation of the rotors is secured in the first stage reduction by adding an idler gear in the spur gear train in one box. Other than that, both left-hand and right-hand drives are identical.

The two main boxes are interconnected by a cross-shaft in the leading edge of the wing. Two spiral bevel gear meshes, a lower and an upper, together with a vertical shaft in the main box complete the interconnection. At 725 rpm the cross-shaft rpm is 3200. Driven by this cross-shaft and substantially at the aircraft centerline is an accessory-drive gearbox.

The qualified flight envelope of the YT58 GE8 engine has resulted in an unusual installation. With a possible wing steady state in the order of 70 degrees in hover, installing the engine at a 35 degree nose down attitude kept it within 5 degrees of the qualified 30 degree nose up, which was considered acceptable. The qualified nose down attitude is 45 degrees. We had considered installing the engines in the fuselage but discarded this because the continual carriage of high horsepower through long drive shafts resulted in several design difficulties in the areas of weight, shafting, couplings, and bearings. Unfortunately, the final power and drive system had imposed on it a number of unforeseeable extraneous problems because of the unorthodox installation (KAC Reports G-11-29, and 341-14, -38).

STRUCTURE

The wing design is conventional, consisting of a six spar distributed flange type sheet metal structure. In general, the criteria for VU class aircraft (MIL A 8629) were used for structural design. The wing is shown in Figures 63 and 64. For structural simplicity reasons it was desired to have the wing tilt axis at approximately 60 percent MAC to provide the wing with sufficient torsional and bending strength. This position also results in a negligible shift of the rotor and wing forces with respect to the CG.

Forty per cent mean chord Fowler flaps, one segment inboard and one segment outboard of the nacelle, are installed. Each flap is a built-up sheet metal structure using formed spars and ribs with sheet metal skin. Flap motion is programmed by the classical two-track system.

The reasons for using a wing-flap combination have been enumerated. For the K-16B the system was designed to provide a maximum wing-fuselage angle of 64 degrees when in hovering flight. Our approach considered two alternatives: one, 90 degree wing tilt; two, a reasonable degree of slipstream turning and partial wing tilt. We chose the latter. Though there is a turning loss associated with slipstream deflection, and the rotor vertical force a component of thrust (rather than full thrust at 90 degrees), the initial lower tilt was expected to aid in reducing transition stall. We were also confronted with an engine installation problem.

Spoilers, used for roll control, are simple builtup sheet metal structure and extend from Wing Sta. 57 to the tip (Figure 65). They are installed as three interconnected segments inboard of the nacelle, two interconnected segments outboard of the nacelle, and an "assist" spoiler above the nacelle. The "assist" spoiler is pin-hinged at its trailing edge, the others at their leading edge.

The nacelle (Figure 66) is of semi-monocoque construction of the concentrated flange type, consisting of four corner longerons, two upper longerons, and transverse frames. "Zee" sections are used as panel breakers. Machined fittings provide for wing and transmission mounting and for engine installation.

A surplus JRF-5 fuselage was modified to accommodate the tilt-wing. The wing center section was removed, and the fuselage frames in the area strengthened and extended to form support pylons for the tilt-wing (Figure 67). A fixed center-section trailing edge bridges the pylons, forming a bent. To the front spar of the bent are attached two wing trunnion fittings about which the wing tilts (Figure 68).

As in the original JRF-5, the K-16B employs tip-floats to furnish a heeling righting moment. However, the attainment in a tilt-wing aircraft is not that simple. With a solid attachment of float-to-wing, as the wing is tilted the float will depart from its heel-stability waterline position. Thus, as in the K-16B, one float strut must be extensible and programmed to wing tilt to maintain the original heel-stability position of the float.

FLIGHT CONTROL SYSTEM

One of the fundamental criteria established by Kaman for any proposed V/STOL aircraft required that the pilot's controls be simple, conventional, and devoid of any unusual characteristics calling for special pilot skills. Although the K-16B concept centers on the combined control features of an airplane and a helicopter, the controls presentation to the pilot and the technique for their operation are nearly identical with those of conventional airplanes. The pilot's basic controls consist of a
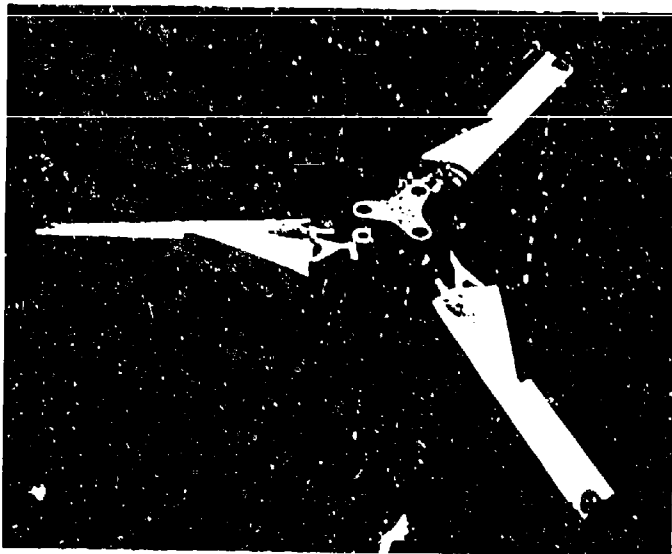
Figure 1

General Arrangement
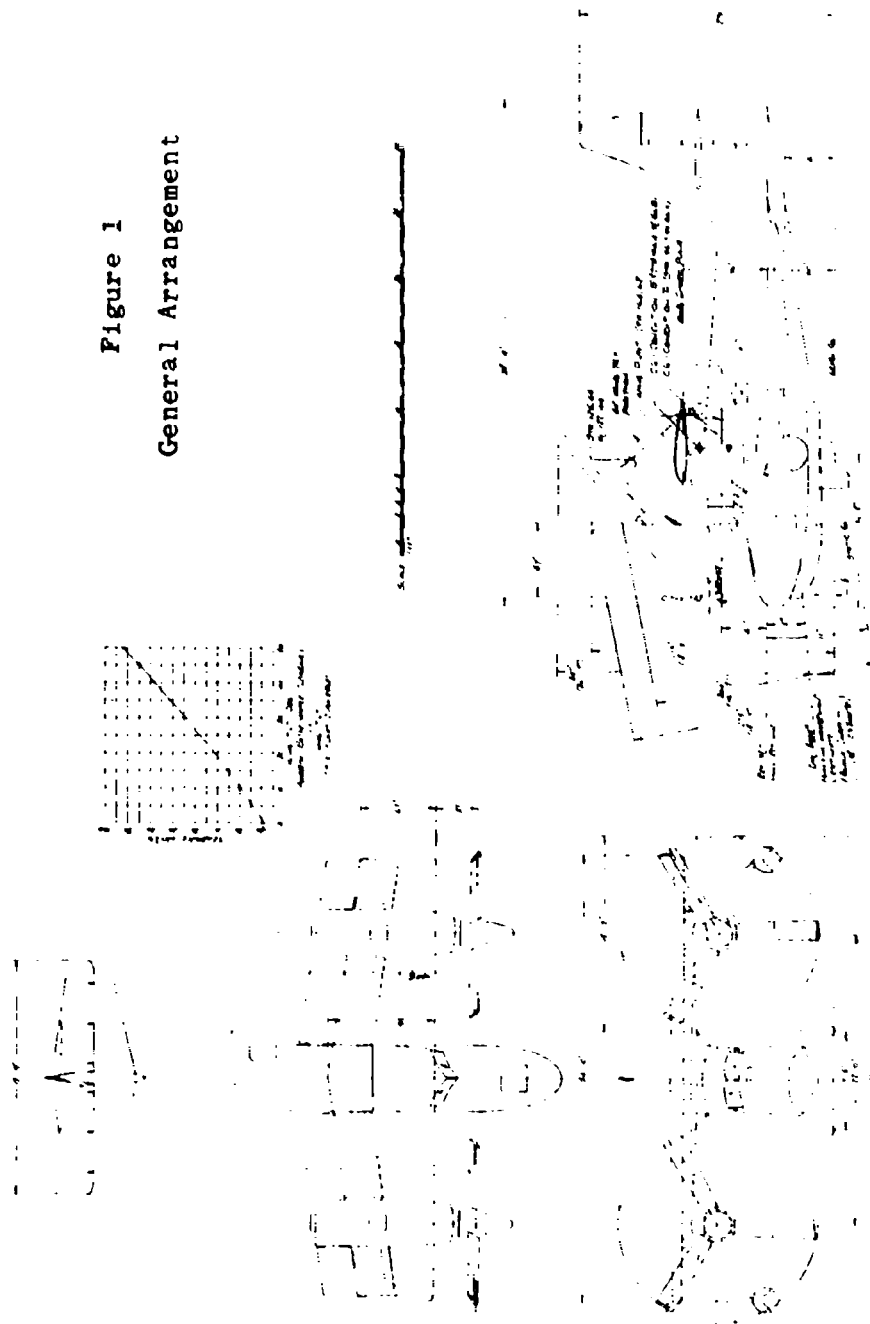
Figure 58
Exploded View
of
Propulsive Rotor

Figure 59
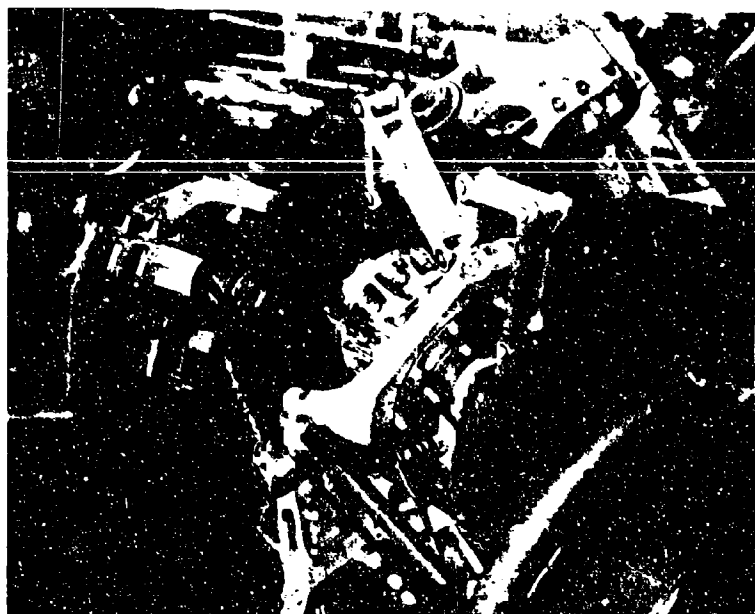Propulsive Rotor
Assembly
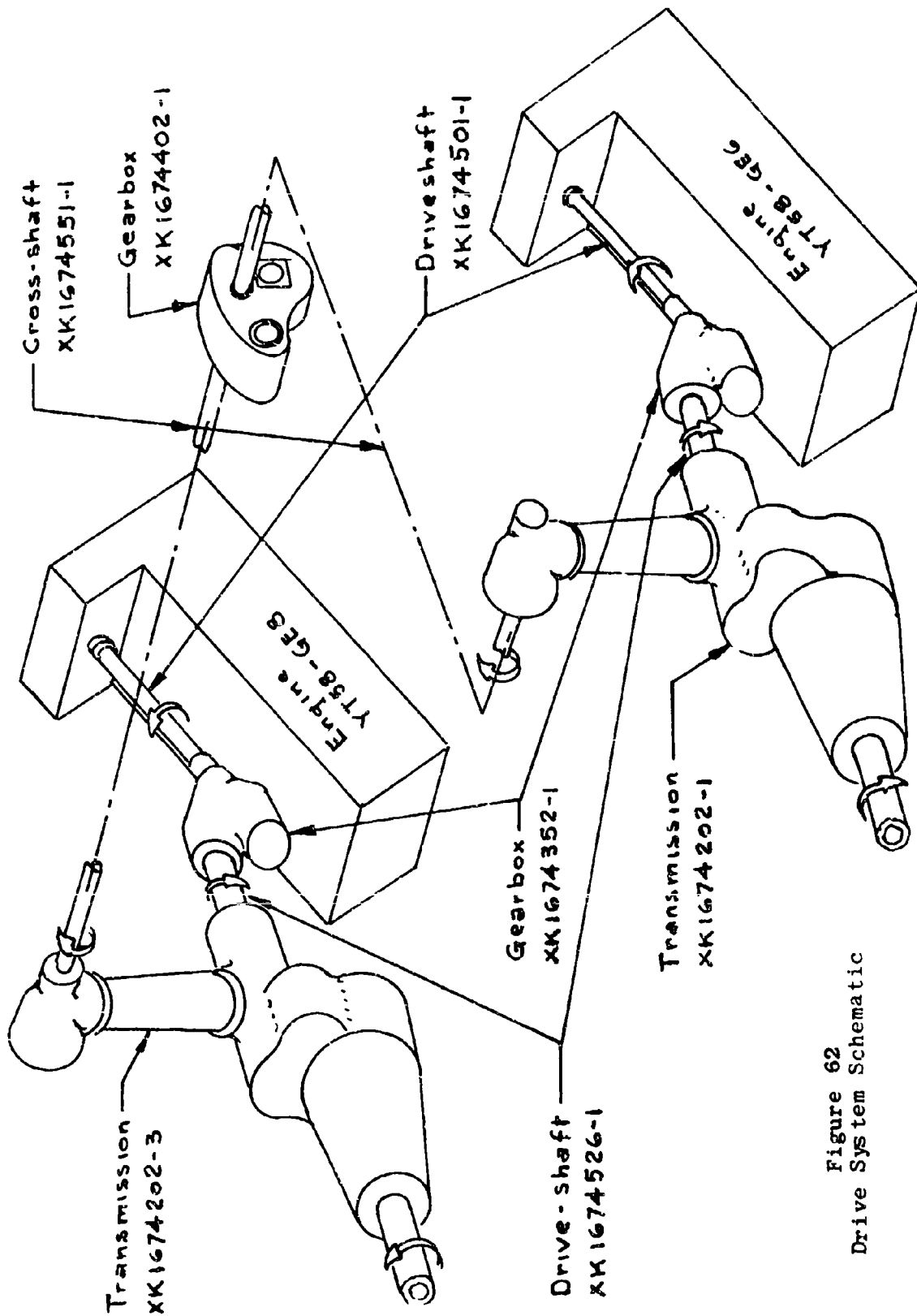
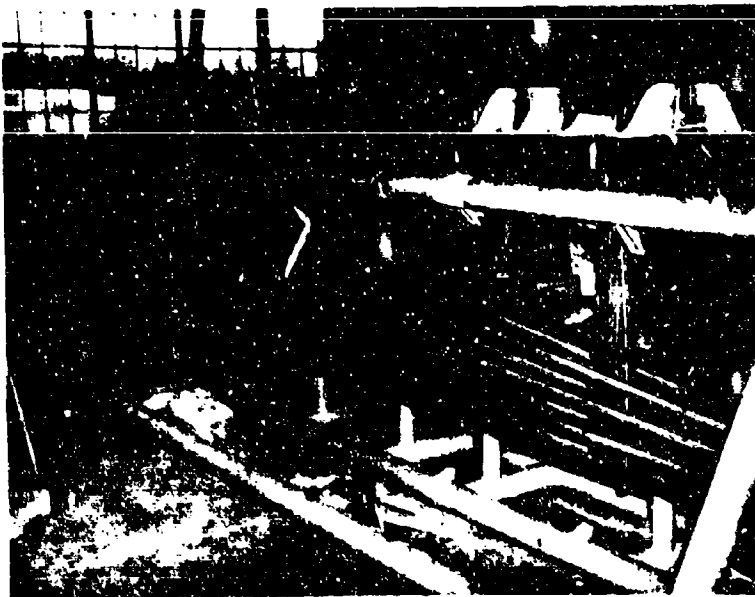127

Figure 60
Rotor Hub

Figure 61
Swashplate

Cross-shaft XK167455I-1

Gearbox XK167440Z-I

Driveshaft XK16745OI-I

Engine YT58-GE6

Engine YT58-GE8

Gearbox XK167435Z-I

Transmission XK16742OZ-I

Transmission XK16742OZ-3

Drive-shaft XK167452G-I

Figure 62
Drive System Schematic

Figure 63
Wing Structure
Internal

Figure 64
Wing Structure
External

130

Figure 65
Spoilers
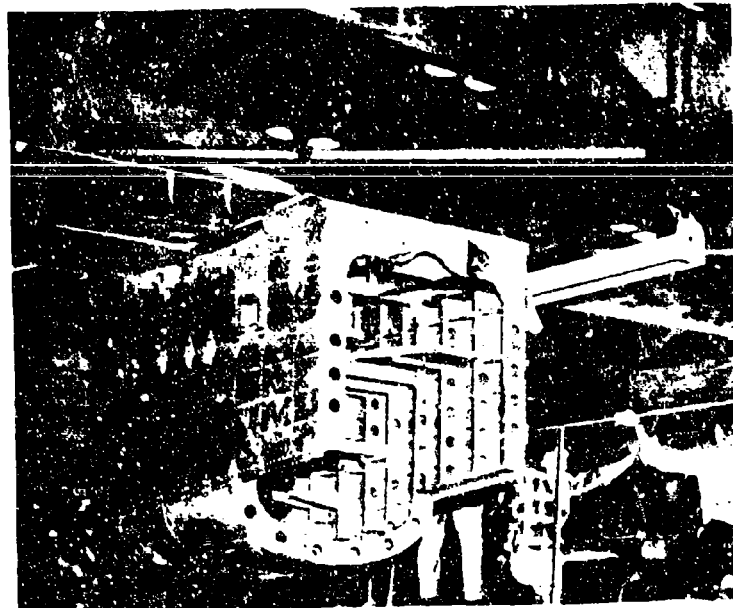
Figure 66
Nacelle

Figure 67
Fuselage
Pylon Framing

Figure 68
Wing Tilt
Trunnions

132

single stick, rudder pedals, and thrust control. The controls presentation is substantially the same as that found in any multi engine fixed wing aircraft except for the substitution of a stick in place of the JRF wheel at the right-hand station. This change was made at the request of the company's test pilots who felt that stick control, being similar to that of a helicopter, would eliminate a first flight variable. A report of an informal cockpit mockup review is presented in KAC Report G-113-3 (8).

Both roll and pitch control, whether helicopter or fixed wing, are secured with either the stick or the wheel. Yaw control in both regimes is obtained with conventional pedals. On both the stick and the wheel is a beeper switch that controls wing tilt.

On a centrally located console are two conventional engine-condition control levers and a rotor-thrust control lever. In the airplane regime this latter control performs essentially the same function as does a throttle. In the helicopter regime it is used to control rotor thrust to maintain altitude and is in fact collective pitch. At the aft end of the console is a conventional wing flap control.

On the thrust control lever is a "beeper" switch by which the pilot can phase in or out the degree of rotor control-sensitivity. Although in operational aircraft rotor control-sensitivity could be programmed by wing tilt, or wing flap, or some other and suitable parameter, it is advisable that in research aircraft, rotor control-sensitivity be directly responsive to the pilot so that varied sensitivities and harmonization programs can be investigated in flight. To further increase the flexibility of flight research, four additional switches are mounted on the instrument panel for individual control of sensitivities of blade-flap collective, pitch, roll, and yaw.

Cyclic and collective blade-flap control runs are cable and push-rod to the rotor swashplate where they terminate at three servo-actuators that control swashplate motion. Blade-pitch control runs are also cable and push-rod to another servo-actuator which in turn controls blade pitch setting. Rudder, elevator, spoiler, and engine controls are cable or push-rod, as applicable.

Surface control effectiveness is obviously small at low airspeeds. The converse is not necessarily true in the case of rotor controls because the system is designed to low-speed requirements, and hence, a constant or direct

control input throughout the operating range may be found to yield excessive control at the higher airspeeds. Provision has been made, therefore, for a means by which the rotor controls input may be varied automatically and gradually from maximum to zero (or conversely) as a function of wing tilt. This device is simply a linkage in which the input to-output ratio is varied by means of an adjustable fulcrum on the input lever. This linkage, patented by Kaman, is in current use in the control system of production HOK, HUK, and HH43 helicopters.

It is of special significance to note that proportioning of rotor control to surface control is a continuous action that is accomplished both gradually and automatically. There is no transition point at which the pilot must change his flying technique. The maneuver is continuous, and can more accurately be described as an extension of airplane flying techniques down to zero airspeed conditions.

SYSTEMS

Electrical, electronic, and hydraulic systems are conventional and simple in concept, in keeping with the philosophy of simplicity and austerity demanded by the program. Insofar as possible, "off-the-shelf" components were used as is or with minor modifications, rather than designing components for a particular function. This has resulted in some penalties in weight, and in space problems, but worthwhile from the economy viewpoint.

It was necessary to specifically design the wing tilt actuator system. Trade-off studies indicated that an electromechanical system would possess several advantages over a hydraulic system, not the least being a simpler and more positive irreversible mechanism. As the system now exists, two interconnected electromechanical actuators are used, each driving an irreversible Acme-threaded strut. The actuator bodies are fuselage mounted, one on each side, and the struts pin-jointed to the bottom surface of the wing front spar.

A question at this time of establishing design parameters was - what should be the rate of wing tilt? Pitching analyses indicated that the Navy's experience with wing-flap extension and retraction would make a reasonable parameter; so wing tilt rate was set at the Navy's spec rate of 5 degrees per second for flap operation. On top of this, an emergency wing-down rate of 3-seconds was imposed.

133

Table III

Summary of Principal Design Dimensions

Wing and Control Surfaces

Span (wing)	34 ft-0 in
Root Chord	96 in
Tip Chord	67 in

Areas

Wing	231 sq. ft.
Wing Flap	71 sq. ft.
Horizontal Tail	76 sq. ft.
Vertical Tail	58 sq. ft.
Spoilers (projected half-span)	5 sq. ft.

Mean Aerodynamic Chord

Flap Stowed	82.3 in
Flap Extended	112.2 in
Lateral Distance from A/C	95.2 in

Wing Incidence	0 deg

Angular Movement of Control Surfaces

Elevator	± 25 deg
Rudder	± 14 deg
Spoiler	61 deg max
Wing Flap	50 deg max

Center of Gravity Location

Normal Gross Weight	9300 lbs

Condition "A"

Wing Down - Clean Condition

Distance Aft LE - MAC	31.7 in
Distance Below LE - MAC	41.1 in
Percent MAC	.385

Moment of Inertia

Lateral, I_x	20,400 slugs ft^2
Longitudinal, I_y	11,500
Directional, I_z	37,000

Condition "B"

Wing Up 50° - LG down - flaps extended

Distance Aft LE - MAC	5.5 in
Distance below LE - MAC	62.6 in
Percent MAC	.107

Moment of Inertia

Lateral, I_x, up 50°	22,450 slugs ft^2	
up 65°	25,250	
Longitudinal, I_y, up 50°	13,620	
up 65°	14,350	
Directional, I_z, up 50°	26,400	
up 65°	26,100	

Rotor

Configuration	3-bladed
Blade Section (modified in flap area)	NACA 16-509
Diameter	15.17 ft
Blade Chord (constant)	18 in
Flapping Hinge (percent radius)	5.2
Disc Area	181.0 sq. ft.
Solidity	0.189
Blade Flap	
Chord	9.85 in
Span	38.19 in
Angular Movement	
Blade Pitch (.75R)	15° to 45°
Blade Flap	
Collective	10° max
Cyclic	±25°

Pilot Control Movement and Corresponding Blade/Flap Deflection

Fore and Aft Stick	±7 in - ±20° flap angle
Left and Right Stick	±7 in - ± 5° blade angle
	± 4° flap angle
Pedal	±3.25 in - 3° blade angle
	15° flap angle

Power and Drive

Engines (2)	YT58-GE6
Normal Rated Power	875 HP
Military Rated Power	1024 HP

Operating Conditions in Hover

Engine Output Shaft to Intermediate Gearbox	6000 rpm
Input Shaft (Intermediate Gearbox to Main Gearbox	6500 rpm
First Stage Reduction (Spur)	4.07:1
Second Stage Reduction (Planetary)	2.2:1
Output (Rotor)	735 rpm
Cross-shaft	3900 rpm

134

APPENDIX C
DETAILS OF FULL-SCALE
TUNNEL TESTS

TEST EQUIPMENT

The K-16B is described in Appendix B, a general arrangement is displayed in Figure 5.

Test operations at NASA, Ames Research Center (ARC) were conducted in two phases:

- Operation upon an outdoor static thrust stand for systems checkout and taking of hover data,
- Wind tunnel operation in transition and fixed-wing flight.

A description follows of the thrust stand expressly designed for the K-16B program, a description of the 40x80 foot wind tunnel will be found in 'Guide for Planning Investigations in the Ames 40x80 Foot Wind Tunnel' (CR).

The thrust stand was constructed on the apron outside the hangar of the ARC Aircraft Service Branch. The orientation axis was fixed in a South-South line with the airplane headed South. Height above the ground and the fuselage angle of attack were also fixed. The stand structure was assembled into 'see' form from steel shapes. At the extremes of the cross bar and the foot of the leg were masts in the way of the aircraft landing gear. Extending forward from the cross-bar, substantially at the main gear pick-up masts, were two additional members to aid in pitch stabilization. The entire structure was lagged to the concrete apron, and some 10,000 lbs. of steel blocks placed onto the stand structure. The aircraft landing gear was replaced by adapters which, through load cells, mounted the airplane to the stand.

The main landing gear masts were laterally braced to outboard; the tail mast was not braced. Initial running disclosed that the stand had a severe resonance in yaw, permitting the aircraft to approach the threshold of instability. Additional bracing was installed - laterally between the main masts and laterally at the tail mast.

The final configuration of the stand can be seen in Figure 69. The load cells installation can be seen in Figures 70 and 71.

Though the static stand was adequate for the original purpose of systems checkout, it left much to be desired when the program was expanded to include the taking of hover data. Because it was completely exposed to the weather, test operations could not be conducted under controlled conditions. Heavy rains and winds of 10 knots or higher frequently required curtailing or waiving test operations. The effect of lesser winds, and perhaps more importantly, the fixed orientation of tail to essentially constant prevailing wind, is a moot question, but it does give rise to doubt of the quantitative validity of some data - particularly slipstream turning and drag data. It is unfortunate that the universal thrust stand that ARC was projecting at the time of negotiating the program was not available. However, despite the limitations of the stand as built, data of some value was obtained.

In the background of Figure 68 will be seen a trailer in which were installed a remote control console, and all recording and indicating instrumentation.

All aircraft systems were remotely controlled from the console (Figure 72). Control inputs were accomplished by electromechanical linear actuators installed in the ship cockpit (Figure 73). The actuators were attached, respectively, to the thrust control (blade pitch), fore-and-aft control to the port yoke, lateral control to the starboard stick, and yaw control to the rudder pedals. Engine fuel-control-unit operation was by pneumatic master rod slave actuators. All instruments required to monitor ship systems were conveyed from the aircraft panel and installed in the remote control console panels. Through series cable connections the console became an extension of the aircraft's indicating system - not a parallel system.

The right-hand propulsive rotor was instrumented to furnish both rotor control motions and rotor stresses, the transmission and engine installations to furnish vibration and temperature levels, the control system to measure control inputs. Several areas of the structure were strain-gaged to monitor stresses. The extent of the remote control and instrumentation systems installed in the airframe can be appreciated from the fact that these systems weighed 910 lbs.

This instrumentation was recorded at both the thrust stand and the wind tunnel. A tabulation of the instrumentation and method of recording will be found in Table IV, Appendix C.

Additional instrumentation was set up by ARC to secure force data at the thrust stand. The force-indicating loadcells measurements were transmitted to indicating Microvolt Potentiometers (IMP's) whose readings were recorded both visually and photographically.

At the wind tunnel all recorded force and moment through a dual system. Scales in the balance house beneath the test section are rigged to print their readings on tapes. Strain gage readings from within the scales are fed to IMP's located in the control room adjacent to the tunnel test section. The data recorded on the IMP's are passed through a small computer that averages the readings and simultaneously typing out and cardpunches each data point. This computer is manually fed such data as tare number and wing tilt angle. The punched cards are later introduced into a computer program that corrects for such items as static weights and tunnel wall effects to give final data for each run.

A camera was mounted at a hatch in the tunnel ceiling abaft the airplane to record tuft patterns on the wing. The camera was oriented by observers at this station who were kept in communication with the control room via an intercom system.

Kaman recorded data on three 12-inch oscillographs, and visually recorded indicator readings at the control console.

TEST OPERATIONS

Following assembly of the K-16B a functional tie-down checkout of all ship systems was run. The airplane was then disassembled and on 26 September 1960 air-freighted via MATS C-143 to NASA, Ames Research Center, Moffett Field, California. An equipment malfunction in the C-133 compelled it to terminate at Travis AFB where the K-16B and its ancillary equipment were transferred to C-124's for transshipment to Moffett Field.

Re-assembly of the airplane and installation of remote control and instrumentation equipment proceeded rapidly, and by mid-November the thrust stand installation was ready for operation; however, a transmission failure at the power-and-drive endurance bench stand at the Kaman facility cancelled thrust stand operation (KAC Report G 113-34) (38). During the next several months a number of major assemblies were removed from the aircraft for use at the endurance bench stand.

By mid-November 1961 endurance operations had sufficiently progressed to warrant a return to ARC to start re-assembly of the airplane. During January 1962 the K-16B was installed on the thrust stand (Figures 74 and 75), but completion of the remote control and instrumentation installations was delayed by the need to erect a new test control facility. The unit furnished was not the one used the previous year and proved to be too small for efficient operation.

While the airplane and thrust stand were being readied for operation, ARC and Kaman personnel had arrived at a standard operating procedure. This was predicated on the division of responsibility as contained in the contract governing calling for this test program. Kaman's responsibility lay with re-assembly of the aircraft, operational checkout of equipment, and maintenance of the airplane during the test program. ARC's responsibility was the establishment of the test format (with Kaman aerodynamic consultation support if requested) and test operation.

Prior to operating a thrust stand - or wind tunnel - test configuration the K-16B would undergo a pre-flight inspection and an instrumentation calibration if such were necessary. Meanwhile, the test run schedule was established. No formal test schedule was set for the entire program, rather, a run schedule was determined on the results of the preceding runs. However, a tentative schedule outline was prepared and will be found in Table V, Appendix C.

In all respects the airplane was operated by remote control. The engines would be started and rotors

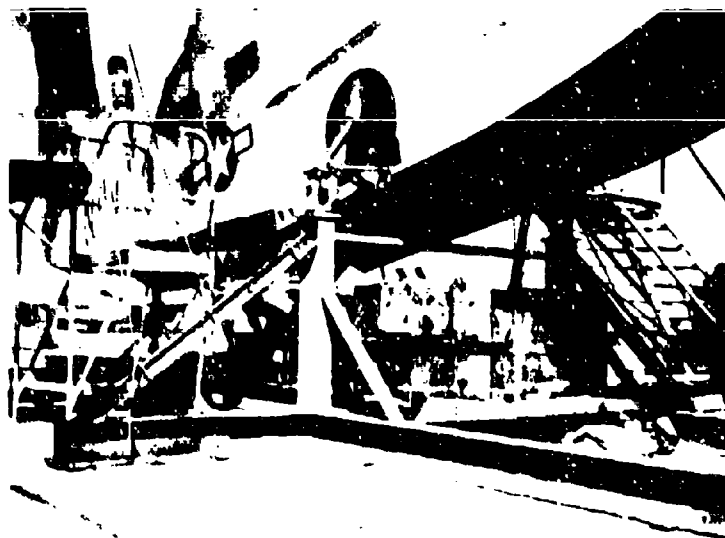Figure 69

Thrust Stand Assembly
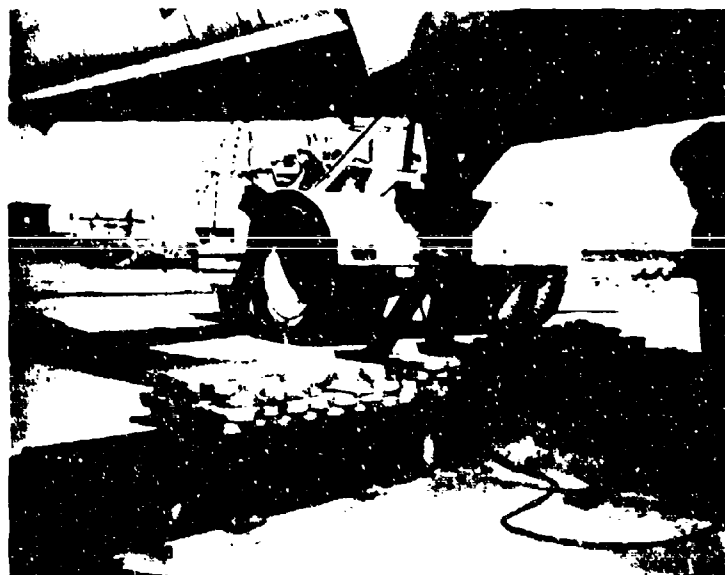
Figure 70

Main Gear Load Cells
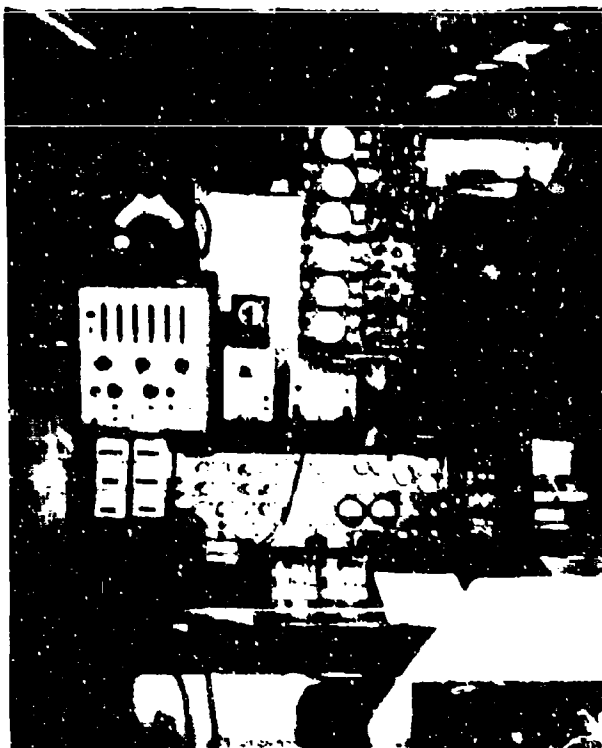

Figure 71

Tail Gear Load Cell
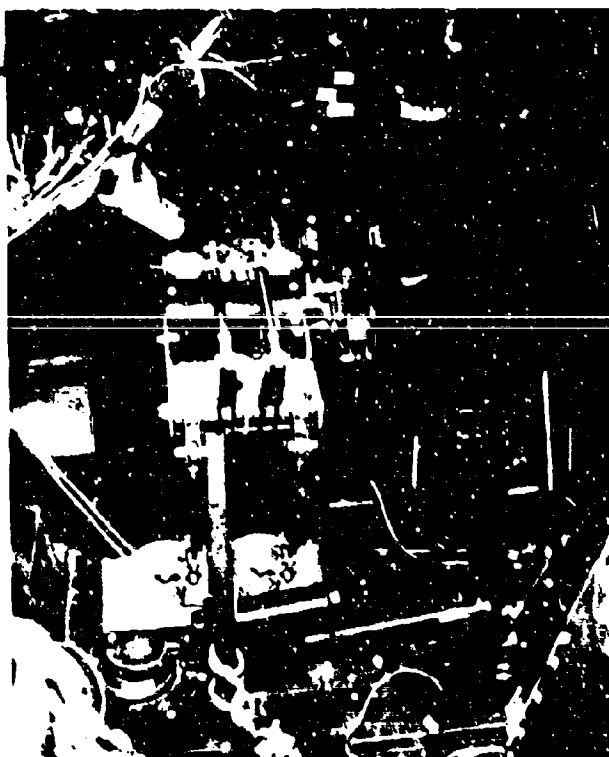
137

Figure 72

Remote Control Console

Figure 73
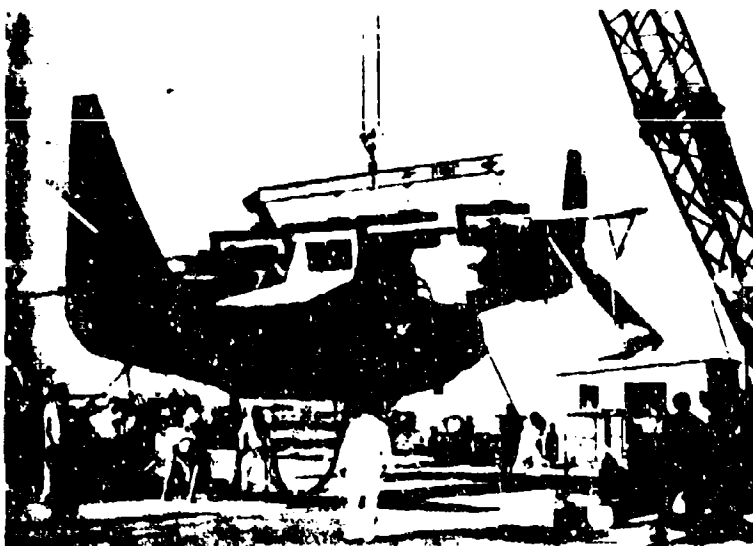
Control Input
Actuators
in Cockpit

Figure 74
Installing on Thrust Stand

Figure 75
Thrust Stand Installation
Complete

brought up to the rpm desired for the run, then the particular test configuration would be set.

The ARC Project Engineer was the coordinator for all test personnel stationed in the control-and-test trailer. (This was also true at the wind tunnel control room). It was his responsibility that all data recordings were taken before the next point in the test run was called and set. Operational safety was the responsibility of the Kaman Project Engineer who, during running, would station himself at an advantageous position to observe the aircraft. Both Project Engineers and the operator at the control console were always in communication with each other by intercom.

Initial thrust stand runs, the first of which was made on 6 February 1962, were concerned with system check-outs and rotor dynamic balance. A chronological log for the thrust stand and wind tunnel operations will be found in Table VI, Appendix C.

Early run-ups manifested a violent resonance in yaw of the thrust stand. Additional bracing reduced the vibration to a still substantial but probably acceptable level. This rework — and for that matter all activity on the aircraft — was delayed by two straight days of heavy rains and high winds. In fact, the prevalence of rain and winds of 10 knots or higher frequently caused waiving test operations.

By 12 March several thrust and cyclic test runs had been made. (Views of the operation are shown in Figures 76 and 77). On this date the normal post-run inspection disclosed that a wing trunnion fitting had failed in fatigue. (Reported in weekly telecon progress report to RAAD-322) The failure (Figure 78) was believed attributable to the substantial, remaining low-frequency vibration of the airplane on the thrust stand structure, on top of prior fatigue damage during the thrust stand resonances. This fitting, of which there are two, was designed in aluminum. Because a similar vibration problem could well exist in the wind tunnel balance system, both fittings were duplicated in steel. Procuring new fittings and installing them took the better part of 8 weeks.

Early in May, several days after restarting the thrust stand program, a sprag clutch in one transmission failed. In view of the experience with sprag clutch failures at the power-and-drive endurance stand, the sprag clutch in each transmission was replaced with a lockout for thrust stand and wind tunnel operation only. This also required a change of drive shafts to retune the system because of the change in system frequency due to the lockout.

Late in June, following shutdown of the final test run on the thrust stand, it was found that the igniter bracket on the left-hand engine had failed. Upon pulling the engine it was discovered that a front engine-mount-fitting mounting hole in a structural support fitting had elongated, and that there were several cracks in adjacent sheet metal structure (Figure 79). The opposite hand engine was pulled. No distress was noted in the fitting but cracks in the sheet metal were found, similar to those in the left-hand nacelle. (Reported in weekly telecon progress report to RAAD-322)

Dynamic balancing of the rotors had to be done on the airplane. During initial operations a slight dynamic unbalance in the left-hand rotor, aggravated by the too-soft thrust stand in reaction on approach to instability, resulted in initial damage to the mounting hole causing decay in the design fit, with this inadvertent clearance, subsequent running permitted "chucking" of the mounting system and further damage to the fitting. The cracks in the sheet metal components were caused by an extraneous lateral load resulting from a two-per-rev forcing function of the engine drive shaft Hooke joints. A new form of joint had become available, was installed, and significantly reduced the forcing function. The area in question is not susceptible to inspection after engine installation.

During the down-time for this repair the planned maintenance to prepare the airplane for the wind tunnel was completed. Because this included replacement of the blade flaps, the K-16B was left on the thrust stand so the new blade/flap assemblies could be dynamically balanced. This period of maintenance and repair fortunately caused no delay to the tunnel operation for we were on standby status.

On 9 and 10 August, rotor balance runs were made. On 20 August the ship was removed from the thrust stand and towed to the 40x80 foot tunnel. On the last day of the month the airplane was lifted into the tunnel and secured to the three tunnel pylons that are mounted on the floating balance frame. Figures 80 and 81 show the hoisting of the

ship into the tunnel and the completed installation. Electric power lines, fuel lines, remote control leads, and instrumentation cables were run through the pylon fairings to the test control room adjacent to the tunnel test section, and tunnel operation started on 5 September. Figure 82 shows one point in this operation.

Operating procedure in the tunnel followed a more or less standard pattern. Following maintenance, and cleaning of the airplane by inspection, approximately 30 minutes were required to ready the tunnel for operation. This preparation consisted of synchronizing the electric motor-generator set for the tunnel fans, closing the overhead doors, and coordinating zero readings in the balance scales and the IMP's. When this was done the normal preflight checkout could be made.

Following this preparation, both engines would be started and idled with fire-guard on hand. When the fireguard was removed and the tunnel access door closed, the rotors would be brought up to test rpm. At this time the tunnel operator normally would be instructed to extend the tail strut to bring the airplane to an angle of attack of -12 degrees, and to raise tunnel 'q' to that required for the particular test. Simultaneously, the aircraft operator would establish the first test point configuration — setting blade collective flap, wing flap, and power with blade collective pitch. If wing tilt was required, it would be put in after the ship was at -12 degrees to avoid stall hysteresis as much as possible.

Arriving at the first data point was often a time-consuming process as thrust and power had an influence on tunnel 'q' and vice versa. This was further complicated by the fact that the engines had to be in close balance — a feat not easily accomplished with the pneumatic throttle actuator system and the YT58-6 engine droop characteristics.

As soon as a data point was reached, data recording would start. ARC would record its IMP data on the computer, photos of the wing tufts would be taken, and we would record our data. Following this, the tunnel operator would be instructed to take his data on the scale tapes.

Learning to coordinate this data-taking took a while, but the average time per point was gradually reduced to about one to one-and-one-half minutes. Often between data points ARC would compute total drag and lift to note where drag crossed from negative to positive, and to assure that wing and flap loadings did not exceed stress limits. In the latter part of the program experience had so developed it was possible to make two runs back-to-back, eliminating the extra time required to start up and reset conditions for the tunnel and the ship.

Following the end of a data run the ship was brought to the wing down-flaps up condition, idled, then shut down. The tunnel would then require airing for from one-half hour to an hour, depending upon how long the engines had been run, before personnel could enter the tunnel to service the ship.

Once tunnel operations started, in a period of slightly over two weeks — 5 September to 21 September — some 23 hours of powered-on operation was logged. During this time two major items of maintenance were one-engine change because of foreign object damage, and two instances of power turbine cuts. These caused little delay to the program. On 21 September the rotors were removed and on 24 September powered-on runs had been completed and the airplane removed from the tunnel.

DETERMINATION OF ENGINE POWER

Engine shaft horsepower is determined by the following steps:

1. Read N_1 rpm for each engine from the oscillograph traces.

2. Correct N_1 to ambient conditions by dividing N_1 by $\sqrt{\Theta_2}$ where

$$\Theta_2 = \frac{\text{Compressor Inlet Temperature } (^\circ R)}{519}$$

or

$$\frac{\text{Compressor Inlet Temperature } (^\circ F) + 460}{519}$$

3. Enter the appropriate engine calibration curve for the particular engine in use with $N_1/\sqrt{\Theta_2}$. Proceed to the curve labeled $HP/\delta_2\sqrt{\Theta_2}$ and horizontally to the $HP/\delta_2\sqrt{\Theta_2}$ scale.
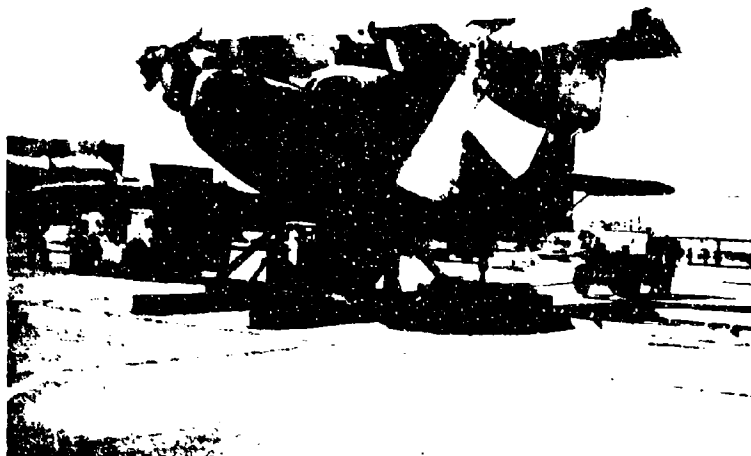
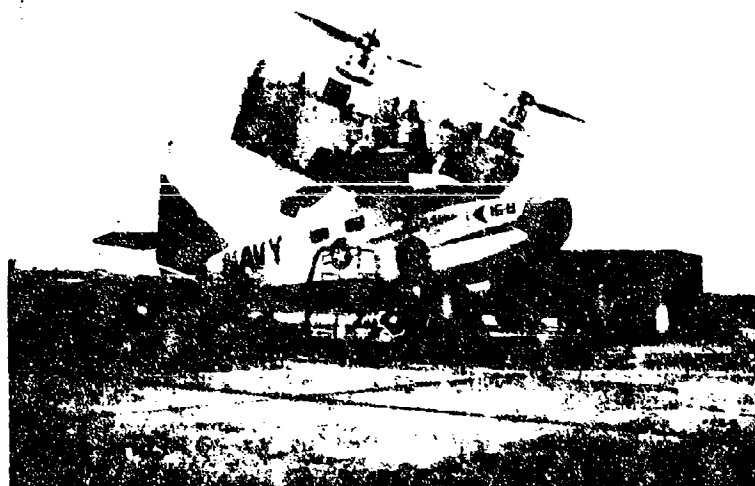Figure 76
Thrust Stand Operation - Wing Down

Figure 77
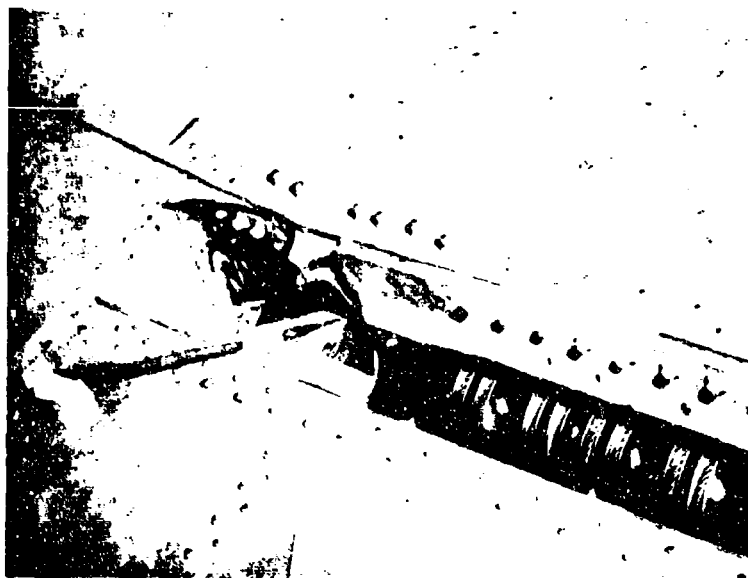Thrust Stand Operation - Wing Up

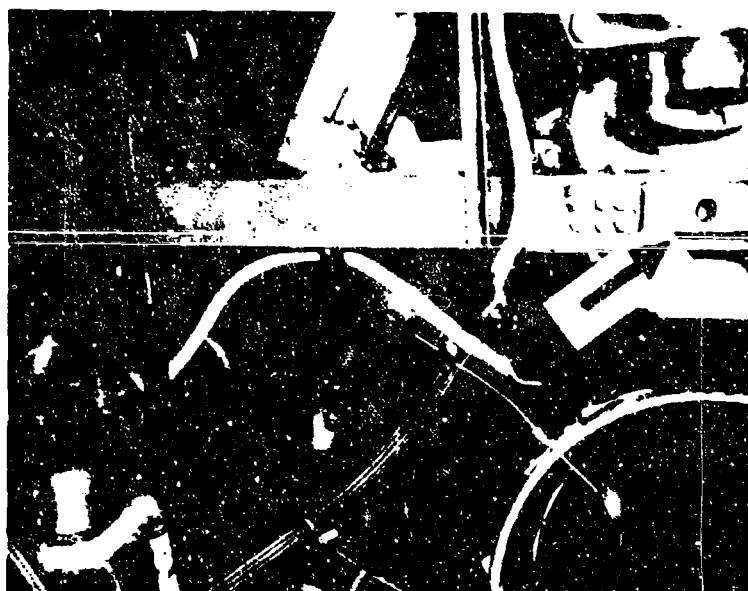141

Figure 78
Wing Trunnion Fitting

Figure 79
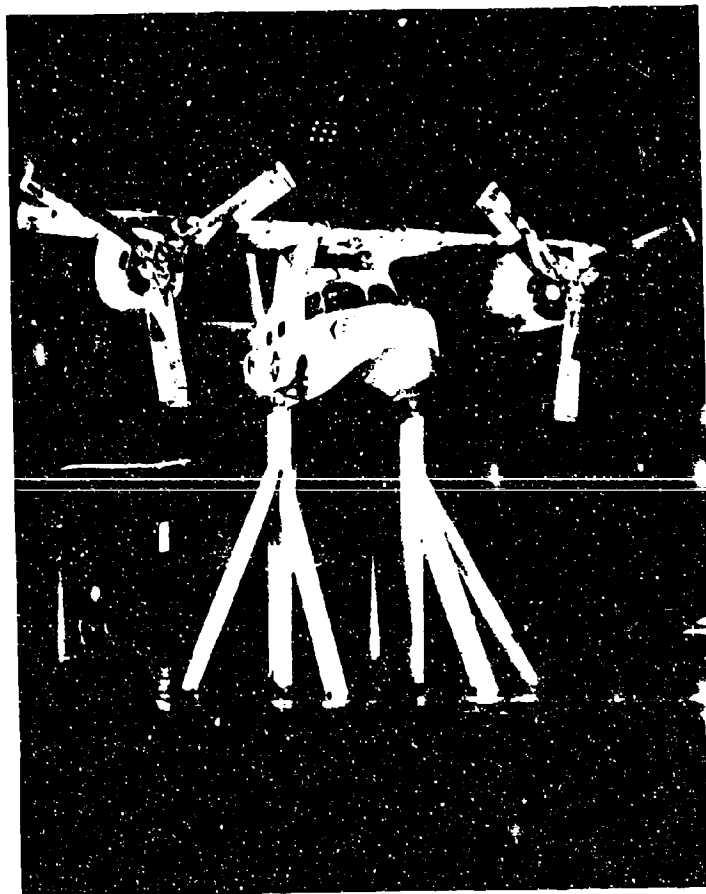Engine Mount Support Fitting

142

Figure 80
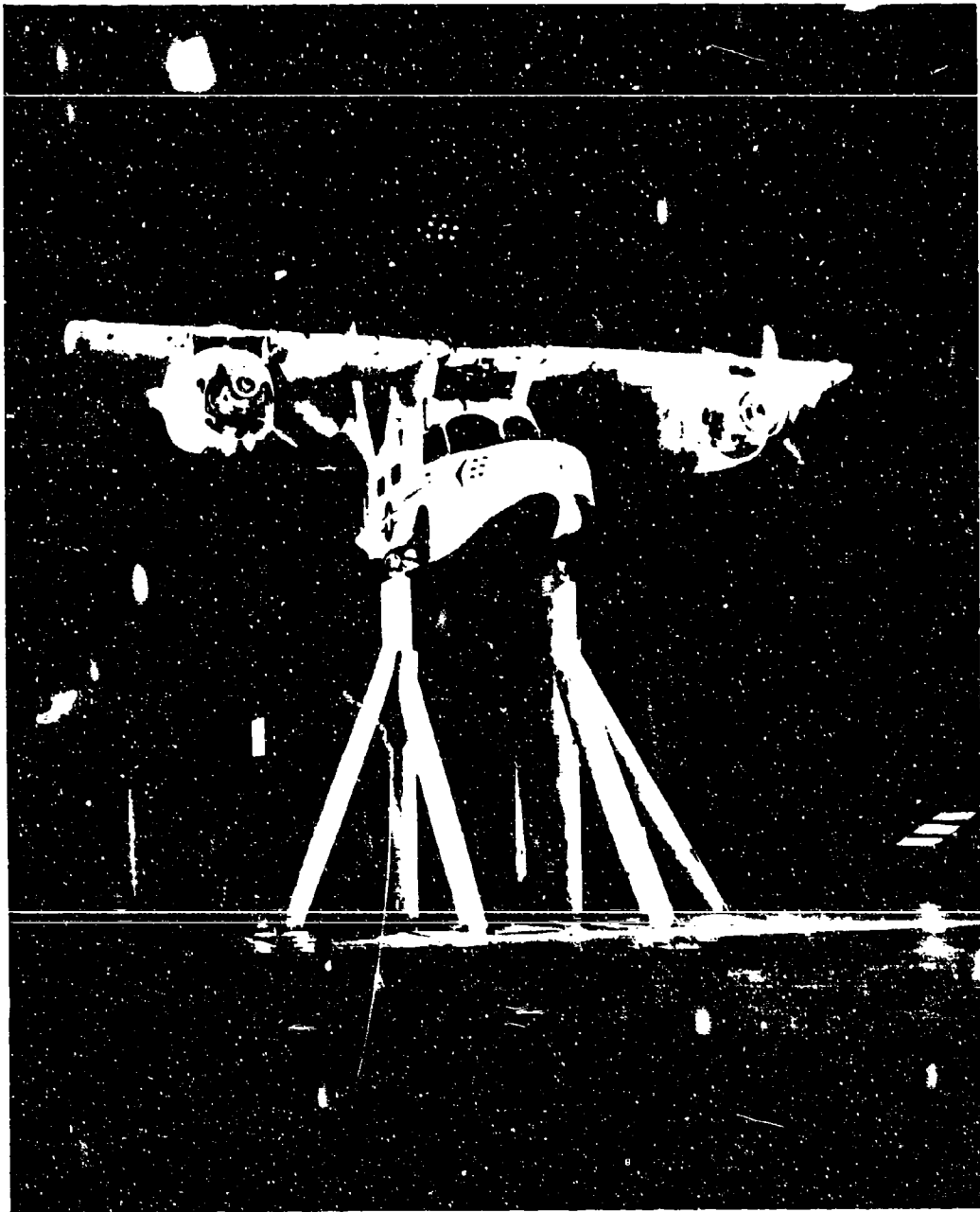Installing
in
Tunnel

Figure 81

Installation
Complete

143

Figure 82
Tunnel Operation

4. Find the horsepower by multiplying $HP/\delta_2\sqrt{\Theta_2}$ by $\delta_2\sqrt{\Theta_2}$ where

$$\delta_2 = \frac{Compressor\ Inlet\ Pressure}{29.92}$$

5. Read the rotor rpm from the oscillograph trace and multiply by the gear ratio to obtain N_2 rpm of the engine.

6. Correct N_2 to ambient (standard) condition by dividing N_2 by $\sqrt{\Theta_2}$.

7. If N_2 is above or below calibration operating rpm of 19,500, look up the power loss or gain from "Output Power vs Output Speed" graphs furnished by the engine manufacturer. Enter the $N_2/\sqrt{\Theta_2}$ at the operating rpm and proceed vertically to the closest operating N_1 rpm curve, then proceed horizontally to the corrected "Output" scale, $HP/\delta_2\sqrt{\Theta_2}$. Do the same for the calibration N_2 rpm of 19,500. The differ-ence between the two readings is either a loss or gain in horsepower. If the engine is operating below calibration rpm it is a loss; if operating above it is a gain.

8. Subtract or add this value to the horse-power previously computed. This is the horsepower avail-able from the engine power turbine before entry into the main reduction gear (MRG) box.

9. To obtain the shaft horsepower, subtract the power loss through the MRG box. The values of power loss are furnished by the engine manufacturer for the average gearbox horsepower losses versus N_2 corrected rpm.

10. Subtract this horsepower loss from the engine horsepower available from the power turbine (step 8) to arrive at the final or shaft horsepower.

Comparison of the calculated horsepower using this method compares favorably with the horsepower deter-mined using torque strain gages mounted on the MRG output shaft.

Table IV			
Instrumentation and Method of Recording			

A. Recorded on Oscillograph

1. Blade flatwise bending moment	Strain gages at Sta 49 at point of maximum thickness - RH blade	8. Engine oil-in temperature	Thermocouple at tank exit - both engines
2. Blade edgewise bending moment	Strain gages on arm to Belleville springs - RH blade	9. Engine reduction gear oil-in temperature	Thermocouple at tank exit - both engines
3. Blade flap control rod	Strain gages on chordwise rod - RH blade	10. Throttle position - percent	Potentiometer measures percent of full travel - both engines
4. Blade flap bending moment	Strain gages on spar at flap mid-span - RH blade	11. Inlet duct temperature	Two thermo-electric probes
5. Rotoprop azimuth position	Magnetic pickup on rotor shaft	12. Angle box oil-in pressure	Common with main transmission
6. Blade flap travel	Potentiometer on hub "L" crank - RH blade	13. Angle box oil-in temperature	Common with main transmission
7. Blade flapping	Potentiometer on flapping pin - RH blade	14. Main transmission oil-in pressure	Pickup on common line with angle gearbox
8. Rotor shaft vibratory torque	Strain gage torque bridge on RH main shaft	15. Main transmission oil-in temperature	Pickup on common line with angle gearbox
9. Main transmission vibratories	Vibration pickups - fore and aft - at top of cross-shaft take-off housing - both transmissions	16. Engine vibration	NASA installation requirement - both engines (a) Fore and aft on MRG box (b) Fore and aft on engine nose (c) Lateral at gas generator aft ring

10. Stresses and strains

a. Rt. rear engine mount link	Strain gage	17. Rotor blade collective pitch input	Potentiometer measuring stroke of actuator - RH blade
b. Wing tilt screw-jack clevis	Strain gage on each clevis	18. Blade flap collective input sensitivity	Potentiometer at actuator
c. Wing flap follower rod	Strain gage	19. Rotoprop roll input sensitivity	Potentiometer at actuator
d. Transmission mount	Strain gage on each (8) diagonals	20. Rotoprop yaw input sensitivity	Potentiometer at actuator
e. Wing trunnion fittings	Strain gage	21. Rotoprop pitch input sensitivity	Potentiometer at actuator
f. Wing front spar-cap splices	Strain gages (a) WS 69.6 (b) WS 131.4	22. Rudder pedal input	Potentiometer at rudder pedal
g. Wing rear spar-cap splices	Strain gages (a) WS 0 (b) WS 25.5 (c) WS 86.2	23. Rudder travel	Potentiometer at rudder hinge
		24. Fore-and-aft stick input	Potentiometer at stick
h. Gas generator - N_1 rpm - percent	Tachometer and electric counter - both engines	25. Elevator travel	Potentiometer at elevator hinge
i. Power turbine - N_2 rpm - percent	Tachometer and electric counter - both engines	26. Lateral stick input	Potentiometer at stick
		27. Spoiler travel	Potentiometer on spoiler linkage

B. Visually recorded

		28. Wing tilt - percent	Servo at pivot point in pylon
1. Power turbine temperature - T_5	Thermocouple - both engines - (G.E. installation)	29. Wing flap travel	Servo in cockpit - null balance with servo actuator on flap
2. Gas generator - N_1 rpm - percent	Tachometer and electric counter - both engines	30. Nacelle temperature	Thermocouple above engine shaft
3. Power turbine - N_2 rpm - percent	Tachometer and electric counter - both engines	31. Thrust stand force indicating load cells	NASA installation - Indicating Microvolt Potentiometers
4. Fuel boost pressure - psi	Low pressure warning light - both engines		
5. Engine fuel pressure - psi	G.E. installation - pickup on fuel control unit		
6. Engine oil-in pressure - psi	G.E. installation	In addition, at the wind tunnel Indicating Microvolt Potentiometers read the tunnel balance scales and fed the information into a small computer.	
7. Engine reduction gear oil-in pressure - psi	G.E. installation		

146

Table V
General Outline – Thrust Stand and Tunnel Tests

A. __Longitudinal Tests__

  1. __Static Thrust Tests (Hovering)__

   a. Run at 725 rpm with $\delta_o = 13°$; $\delta_{fw} = 35°$, $40°$, $45°$, $50°$

   b. Hull angle of attack, $\alpha_h = 11°$ (fixed α_h at thrust stand)

     1. Set wing tilt angle, τ, at $40°$, $50°$, $60°$, $65°$

     2. For each τ set longitudinal stick positions of 40% and 10% forward, neutral, and 10%, 20%, and 50% aft

     3. For each condition of α_h, τ, for horizontal and vertical equilibrium go through an excursion of lateral stick position, then an excursion of right pedal deflection

     4. Record: lift "L", Drag "D", side force "Y", rolling moment "l", pitching moment "m", and yawing moment "n". Also, τ, α_h, stick positions δ_r, H_t, δ_s, engine parameters T_2, P_2, T_5, N_2, N_1, blade flap deflection and blade flapping

     5. Compute moments about C.G. position which varies with wing tilt.

  2. __Transition Tests__

   a. Test dynamic pressure should correspond as closely as possible to level flight dynamic pressure at the particular τ (where $\tau' = \tau$, α_h). Run at $\delta_o = 13°$, $\delta_{fw} = 40°$.

   b. At a particular value of "q" and τ vary the collective pitch Θ until the "a" = force = 0

   c. Run through excursions in α_h (keeping x = 0 by varying Θ) through L = 9000 lbs for each of several values of longitudinal stick position

   d. Run at 4 or 5 values of "q" and τ. At each "q" go through small excursions in speed.

   e. Record: "L", "D", "m", α_h, τ, δ, β, Θ, longitudinal stick position δ_a and engine parameters T_2, P_4, T_5, N_2, N_1

  3. __Forward Flight Tests__

   a. Run at 630 rps, constant power, wing down, $\delta_o = 0$

   b. For flaps up: Run NRP, .6NRP, $T_c = 0$

   c. For flaps down 40°: Run .6NRP, .3 NRP; $T_c = 0$

   d. Set elevator angles for control system design loads at the chosen "q"

     1. Run through angle of attack range at several constant δ_e and constant power for the various power conditions, both flaps up and flaps down

   e. Record: "L", "D", "m", "H", α, δ_e, β, N_5, T_5

  4. __Lateral Control Effectiveness Tests__

   a. Flaps Up

     1. Run at .6NRP at 2 or 3 angles of attack

     2. Run through a spoiler deflection range, or alternately:

     3. Run through a small angle of attack range at several spoiler deflections

   b. Flaps down 40"

     1. Wind down - .3NRP as in (a)

     2. Wing of ≈ 50"

       (a) Run at the "q" appropriate for the τ'.

     3. Deflect lateral stick using spoiler deflection as a guide. At several spoiler deflections and constant values of τ' record the following:

     4. Record: L, D, Y, m, n, l, H_s, δ_s, α, δ_r, δ, β, Θ, lateral stick deflection δ_l, T_5, N_2

B. __Yaw Tests__

  1. __Transition Tests__

   a. Flaps down 40", $\delta_o = 13°$, 725 rpm. Run at same "q's" and τ' as in longitudinal tests

   b. At each "q" and τ' combination of longitudinal tests select at least 3 τ' for trimmed level flight equilibrium

     ($\tau' = \tau$, α_h = constant for any T_c")

     1. Depress pedal keeping lateral stick neutral (for example - 20)

     2. Run through a range of yaw angles

     3. Repeat at other pedal positions for each τ'. (for example - 40%, 60%, 80%)

   c. Repeat at other "q's"

   d. Record: L, D, Y, m, n, l, δ_r, δ_s, α_h, τ, Θ, β, T_5, N_2, δ_o

  2. __Forward Flight__

   a. Set zero rotor sensitivity. Run at constant power.

   b. Flaps up - NRP; .6NRP; $T_c = 0$

   c. Flaps down - .6NRP; .3NRP, $T_c = 0$

   d. Run at two α's, both flaps up and flaps down

   e. Set δ_r at several values. Run through yaw range.

   f. Record: L, D, Y, m, n, l, H_r, δ_r, Θ, δ_o, β.

Table VI

Chronology of Thrust Stand and Wind Tunnel Operation

Date	Run Time	Data Taken	Remarks	Date	Run Time	Data Taken	Remarks
		- Thrust Stand Operation -		3/9/62	0:08		Run aborted - covers of remote cable dog-bones between stand and control rods pulled free when wing flaps lowered - strap covers in place
1/25/62	0:12	None	N_2 rotors - LH engine check				
1/25/62	0:13	None	N_2 rotors - RH engine check	3/12/62	0041 0:31	Cyclic: N_1 = 95%, N_2 = 90%; T = 55°; δ_f = -46°, δ_o = 0°, Θ = -18.7° max	Full F & A stick - 5% pitch sensitivity
2/6/62	0:12	N_1 = 54%, N_2 = 20%; RH pickups - vibratories at transmission	vibration survey with both engines and both rotors	3/12/62	0005L 0:10		Run aborted - underground main fuel tanks empty
2/6/62	0:07	N_1 = 55%	LH engine only - yaw resonance in stand on threshold of ground resonance - main anchor beam worked loose from leg bolts - rework started to stiffen and return test stand structure	3/12/62	0006L 0:20	Polar: N_1 = 94%, N_2 = 50%, T = 55°, δ_f = -46°, δ_o = 0°, Θ = 10.8° max	Post-run inspection disclosed failed wing trunnion fitting
2/19/62	0:08	N_1 = 12%, N_2 = 42%, RH pickups	vibration survey of stiffened test stand	4/27/62	0007L 0:24	Polar: with variable δ_f & N_2 - N_1 = 96%, N_2 = 90% max; T = 62°, δ_B = 13°, Θ = 10.9° & 13.6°	N_2 reduced to 88% with Θ = 13.0°
2/20/62	0:25	N_1 = 84%, N_2 = 86%, RH pickups	RH rotor balance runs - RH engine and rotor only				
2/21/62	0:28	N_1 = 89%, N_2 = 97%; RH pickups	RH rotor balance runs - RH engine and rotor only	4/27/62	0008L 0:50	Polar: with variable δ_o - N_1 = 94%, N_2 = 86%, T = 62°; δ_f = 0°, Θ = 9.6°	Hold constant N_2 & Θ, varying δ_o
2/21/62	0:16	N_1 = 70%; N_2 = 65%, RH pickups	LH rotor balance runs - LH engine and rotor only				
2/22/62	0:04	N_1 = 59%, N_2 = 20%, RH pickups	LH rotor balance runs - LH engine and rotor only - compressor stall	5/3/62	0009L 0:18	Cyclic: N_1 = 92%, N_2 = 90%; T = 62°, δ_f = 40°, Θ = 7.7°, δ_o = 13°	Run aborted - seized RH transmission oil pump by failed clutch from clutch
2/26/62	0:10	N_1 = 84%, N_2 = 82%, RH pickups	LH rotor balance runs - LH engine and rotor only - compressor stall - change LH engine				
2/28/62	0:03	N_1 = 94%, N_2 = 87%, RH pickups	Balance run both rotors - RH engine only	5/16/62	0:16	Cyclic: N_1 = 92%, N_2 = 91%; T = 62°, δ_f = 0°, δ_o = 13°, Θ = 6.1°	
2/28/62	0:06	N_1 = 86%, N_2 = 84%, RH pickups	LH rotor balance runs - LH engine only				
3/1/62	0:22	N_1 = 86%, N_2 = 84%, RH pickups	LH rotor balance runs - LH engine only	5/17/62	0:20	Cyclic: with variable T - N_1 = 92%, N_2 = 90%, T = 7° & 62°, δ_f = 0, δ_o = 13°, Θ = 6.1°, 30 units F & A stick at T = 7°, 44 units fed and 40 units aft at T = 62° and 100% pitch sensitivity, 30 units R & L rudder pedal, and 30 units R & L stick at 100% control sensitivities	
3/2/62	0:04	N_1 = 88%, N_2 = 90%, RH pickups	LH rotor balance runs - LH engine only				
3/2/62	0:03	N_1 = 82%, N_2 = 84%; RH pickups	Balance check run - both rotors and both engines				
3/2/62	0:05	N_1 = 87%, N_2 = 91%; RH pickups	Balance check run - both rotors and both engines - wing tilt 65°				
3/7/62	001L 0:13	N_1 = 92%, N_2 = 90%	Functional check of aircraft and instrumentation				
3/8/62	002L 0:14	Polar: N_1 = 94%, N_2 = 92%, T = 55°; δ_f = 46°, δ_o = 13°, Θ = 15.6°					
3/8/62	003L 0:16	Polar: N_1 = 95%, N_2 = 92%, T = 55°, δ_f = 46°, δ_o = 13°, Θ = 14.1°	insufficient throttle - rerig				

148

Table VI (cont'd)

Date	Run Time	Data Taken	Remarks	Date	Run Time	Data Taken	Remarks
5/18/62	0:29	Cyclic with variable T, δ_o, δ_f - & N_2; $N_1 - 90\%$; $\Theta - 6.1^\circ$; $\delta_f -$ 0°; 30 units - F & A stick at $T -$ 0° & 62°, $\circ - 0^\circ$ & 13°, $N_2 - 85\%$ & 90%. Full L & R rudder & full L & R stick at $T - 62^\circ$, $\delta_o - 13^\circ$. $N_2 - 90\%$	Run at 100% respective control sensitivities	6/27/62	01RL 0:23	Variable thrust & cyclic; $N_1 - 95\%$, $N_2 - 91\%$, $T - 62^\circ$, $\delta_f - 40^\circ$, $\delta_c - 6.5^\circ$ - 30 units RLA stick & full RAL stick at $\delta_o - 10.4^\circ$	Post inspection disclosed failed engine mount fitting
5/22/62	010L 0:24	Cyclic with variable $N_2 - T$; 62°, $\delta_f - 100^\circ$, $\delta_c - 40^\circ$, $\delta_o -$	Run at 100% respective control sensitivities	8/9/62	019L 0:19	$N_1 - 86\%$, $N_2 - 91\%$, RR pickup	Rotor balance run
5/24/62	011L 0:37	Cyclic ρ: $N_1 - 92\%$ & 96%; $N_2 - 91\%$, $T - 62^\circ$, $\delta_f - 40^\circ$, $\delta_o - 11.0^\circ$ - 35 units fwd stick & 10 units aft stick at 100%, pitch sensitivity	Failure in bearing retention of anti-torque scissor in azimuth	8/10/62	020L 0:28	$N_1 - 85\%$ to 95%, $N_2 - 95\%$ RR pickup	Rotor balance run
				8/10/62	021L 0:22	$N_1 - 91\%$, $N_2 - 91\%$ RR pickup	Rotor balance run
6/15/62	012L 0:34	Cyclic $N_1 - 95\%$, $N_2 - 91\%$, $T - 62^\circ$, $\delta_f - 40^\circ$, $\delta_o - 10.4^\circ$. $\Theta - 6.1^\circ$ - Pull LAR stick at 100% pitch, roll & yaw sensitivities		8/20/62	022L 0:17	11 hr - 14 min - Thrust stand time	Final system check-out
6/18/62	013L 0:35	Cyclic $N_1 - 91\%$, $N_2 - 91\%$, $T - 62^\circ$, $\delta_f - 40^\circ$, $\delta_o - 10.4^\circ$. $\Theta - 6.1^\circ$ - Pull right & full left stick & full right & full left rudder independently at 100% pitch, roll & yaw sensitivities				Wind Tunnel	
				9/5/62	1 0:11	Check-out run	Run aborted - generator seating. Generator oil - ship wiring changed to be compatible with tunnel AFP
6/18/62	014L 0:16	Cyclic $N_1 - 91\%$, $N_2 - 91\%$, $T - 62^\circ$, $\delta_f - 40^\circ$, $\delta_o - 10.4^\circ$		9/5/62	2 0:22	Check-out run	Failed check-valve in RH ENG oil line - replaced valve
6/20/62	015L 0:17	- Full LAR rudder at 100% pitch, roll, & yaw sensitivities		9/6/62	3 0:37	Polar: $q - 5.0$, $\alpha - -12^\circ$ to -12°, $T - 30^\circ$, $\delta_f - 40^\circ$, $\delta_o - 80$ units, $N_1 - 84\%$, $N_2 - 88\%$	RH engine compressor stall on shut-down Inlet guide vane actuator bracket cracked. Replaced bracket
6/21/62	016L 0:44	Variable thrust & cyclic run; $N_1 - 92\%$ & 96%, $N_2 - 91\%$, $T - 62^\circ$, $\delta_f - 40^\circ$, $\delta_o - 10.4^\circ$, $\Theta - 13.3^\circ$. Full RAL stick at MRP		9/7/62	4 0:58	Polar: $q - 5.0$, $\alpha - -12^\circ$, $T - 30^\circ$, $\delta_f - 40^\circ$, $\delta_o - 80$ units, $N_1 - 91\%$, $N_2 - 84\%$	FOD in PH engine compressor - slowed blades
6/21/62	017L 0:38	Cyclic at MRP; $N_1 - 96\%$, $N_2 - 91\%$, $T - 62^\circ$, $\delta_f - 40^\circ$, $\delta_o - 10.4^\circ$, $\Theta - 13.3^\circ$ - 40 units right & full left rudder pedal - 20 units LAR stick		9/7/62	5 0:13		Run aborted. Measured high engine vibration. Pickup wiring questioned. Corrected wiring
				9/7/62	5 0:30	Vibration survey $N_2 - 84\%$ to 91%	RH engine wandering 700° 's at idle. Inlet guide vane actuator bracket cracked. Replaced CEC vibration meter recalibrated
				9/11/62	6 0:47	Polar: $q - 5.0$, $\alpha - -12^\circ$ to 14°, $T - 30^\circ$, $\delta_f - 40^\circ$, $\delta_o - 30$ units, $N_1 - 89\%$ to 84%, $N_2 - 89\%$	FOD RH engine. Compressor blade root damaged. Change in engine surge 310. Replace first stage bushings

149

Table VI (cont'd)

Date	Run Time	Data Taken	Remarks	Date	Run Time	Data Taken	Remarks
9/12/62	7 0:24		Run aborted. Cold temp-op. Adjust throttle	9/16/62	15 1:00	Pitch control excursion: q = 5.6, $\alpha = 8^\circ$, $\tau = 30^\circ$, $\delta_f = 40^\circ$, $\delta_o = 80$ units, pitch sensitivity 100%, stick to -21 & -13 units	
9/13/62	8 0:58		Run aborted. Fuel leak in RH engine – fuel control unit malfunction				
9/13/62		Polar: q = 5.6, $\alpha = -16^\circ$, $\tau = 30^\circ$, $\delta_f = 40^\circ$, $\delta_o = 80$ units, $N_1 = 94\%$ to 95%, $N_2 = 88.5\%$	Lost trace of collective-pitch potentiometer. Cleaned pot. Recalibrated blade-pitch.			Polar: q = 4.0, $\alpha = -12^\circ$ to -16°, $\tau = 30^\circ$, $\delta_f = 40^\circ$, $\delta_o = 80$ units, $N_1 = 94\%$ to 96%, $N_2 = 89\%$	Run aborted. High tunnel ambient temp. High turbine oil overtemp.
9/13/62	0:27		Run aborted – hydraulic pressure light flickered	9/16/62	16 0:20		
9/13/62	9 0:20		Run aborted. Both azimuth rate and pitch sensitivity changed to 100%. Azimuth control okay	9/16/62	17 1:08	Polar: q = 21 (80 kt), $\alpha = 0^\circ$ to 6°, $\tau = 0^\circ$, $\delta_o = 0$ units. D = 0, $N_1 = 91\%$ to 95%, $N_2 = 87.5\%$. Check flapping response with wing tilt.	
9/13/62	10 0:41	Pitch control excursion: q = 5.6, $\alpha = -6^\circ$, $\tau = 30^\circ$, $\delta_f = 40^\circ$, $\delta_o = 80$ units. Stick to 40 & -40 units	Elevator locked. Pitch sensitivity changed to 50% to lessen influence of elevator buffet.			Polar: q = 37.2 (100 kt), $\alpha = 0^\circ$ to 6°, $\tau = 0^\circ$, $\delta_f = 0^\circ$, $\delta_o = 0^\circ$, D = 0, $N_1 = 85\%$ to AR 5%, $N_2 = 88\%$	
9/14/62	11 1:26	Polar: q = 12.0, $\alpha = -12^\circ$ to -14°, $\tau = 20^\circ$, $\delta_f = 40^\circ$, $\delta_o = 80$ units, $N_1 = 94\%$ to 88%, $N_2 = 88\%$				Polar: q = 48 (120 kt), $\alpha = 0^\circ$ to -4°, $\tau = 0^\circ$, $\delta_f = 0^\circ$, $\delta_o = 0^\circ$, D = 0, $N_1 = 88.5\%$ to 90.5%, $N_2 = 88\%$. Flapping response check.	
9/14/62	12	Polar: q = 12.0, $\alpha = -12^\circ$ to -14°, $\tau = 20^\circ$, $\delta_f = 40^\circ$, $\delta_o = 80$ units, $N_1 = 94.5\%$ to 99%, $N_2 = 88.5\%$				Polar: q = 56 (150 kt), $\alpha = 0^\circ$ to 4°, $\tau = 0^\circ$, $\delta_f = 0^\circ$, D = 0, $N_1 = 91\%$ to 92.5%, $N_2 = 87\%$. Flapping response check.	Power turbine rub – LH engine replaced shroud. Leading edge gloves added to wing.
9/14/62	13 1:20	Pitch control excursion: q = 12.0, $\alpha = 8^\circ$, $\tau = 20^\circ$, $\delta_f = 40^\circ$, $\delta_c = 80$ units, pitch sensitivity to 100%, stick to -35 to -30 units	Replace spacers in azimuth scissors trunnion	9/18/62	18 1:33	Polar with LE gloves: q = 5.6 (40 kts), $\alpha = -12^\circ$ to -15°, $\tau = 30^\circ$, $\delta_f = 40^\circ$, $\delta_o = 80$ units, $N_1 = 93\%$ to 94%, $N_2 = 89\%$	
	14	Polar: q = 21.0, $\alpha = -12^\circ$ to 4°, $\tau = 10^\circ$, $\delta_f = 40^\circ$, $\delta_o = 80$ units, $N_1 = 89\%$ to 92.5%, $N_2 = 88.5\%$					

150

Table VI (cont'd)

Table VI (cont'd)

Date	Run Time	Data Taken	Remarks	Date	Run Time	Data Taken	Remarks
9/20/62	26 1:07	Polar, flapping response check - $q = 67.3$ (110 kt), $T = 0^o$, $\delta_f = 0^o$, $\delta_o = 0^o$, $N_1 = 94\%$ to 98.8%, $N_2 = 87.5\%$. Polar, flapping response check - $q = 75.5$ (130 kt), $\alpha = -4^o$ to -10°, $T = 0^o$, $\delta_f = 0^o$, $\delta_o = 0^o$, $N_1 = 90\%$ to 94 kt, $N_2 = 87.5\%$. Visual check, wing stall - $q = 5.6$ (40 kt), tunnel tail strut stuck at 8°, T varied from 0 to 50°, $\delta_f = 40^o$, $\delta_o = 40$ units, MRP	Power turbine rub - RH engine: replaced shroud		28	Lateral directional check $q = 5.6$ (40 kt), $\alpha = 0^o$, $T = 40^o$, $\delta_f = 40^o$, $\delta_o = 80$ units, $N_1 = 93\%$ to 97%, $N_2 = 88\%$. roll & yaw sensitivity 100%, right stick to 50 units, left stick to 50 units, right rudder to 40 units, left rudder to 47 units	Elevator lock removed
9/21/62	27 1:37	Thrust calibration $q = 21$ (RH kt), $\alpha = 0^o$, $T = 0^o$, $\delta_f = 0^o$, $\delta_o = 0$ Vary thrust to MRP at $N_2 = 88\%$ Reduce N_1 from 96.5% to 77% holding N_2 constant Repeat for $\delta_o = 40$ units & 80 units Thrust calibration $q = 5.6$ (40 kt) same as above except in reverse order, i.e. $\delta_o = 80$ units, 40 units, 0 units		9/21/62	29 0:53	Elevator effectiveness check $q = 21$ (90 kt), $\alpha = 0^o$, $T = 10^o$, $\delta_f = 40^o$, $\delta_o = 80$ units, $N_1 = 94.5\%$ to 93.2%, $N_2 = 88.5\%$, pitch sensitivity 0%, stick to 47 & 50 units; $\alpha = 12$ (60 kt), $\alpha = 0^o$, $T = 20^o$, $\delta_f = 40^o$, $\delta_o = 80$ units, $N_1 = 92.2\%$ to 96%, pitch sensitivity 0%, stick to 42 & 50 units	Following continuous record of wing tilt, run aborted because of oil leak in RH nacelle. Rotors & hubs removed from A/C for props off data
					22 hr	24 min - Wind tunnel time	
					35 hr	38 min - Total time	

152

APPENDIX D
METHOD FOR DETERMINING
ROTOR PERFORMANCE

The requirements of propeller geometry for high propulsive efficiency in both static and high-speed conditions are somewhat contradictory. VTOL aircraft propeller design becomes a compromise between conflicting requirements of hovering and cruising flight. To minimize the cruising efficiency penalty, which a high activity-factor static thrusting propeller entails, it is advantageous to operate the hovering propeller at as high a blade loading as possible. For example, to satisfy hovering requirements a highly cambered airfoil is necessary to attain a high blade loading. The rapid drop in required thrust from hovering to forward flight, however, forces the propeller to operate at very low thrust coefficients in cruise. To operate efficiently at low thrust coefficients, a low solidity is required to keep the blade near the maximum lift-drag ratio on the blade section. The advantages are apparent for varying the camber to provide a high camber when hovering and a lower camber in cruise.

The propulsive rotor achieves variable camber by incorporating plain flaps on the outboard portion of the blades. Mean lift coefficients of 1.0 have been attained in rotor tests when the blade was cambered for a design lift coefficient of 0.5 (KAC Report G-111-4)(5). There is, of course, a drag penalty due to flap deflection which also enters into the determination of the compromise rotor.

To minimize aircraft weight a minimum propeller diameter, and consequently a relatively high disc loading, is chosen. It then becomes necessary to determine the best compromise between cruising efficiency and hovering figure of merit at the required thrust.

Because a VTOL propeller must often operate in the high angle of attack condition (the so-called "Aq" condition), a rigid propeller is subjected to severe 1-per-rev root bending stresses which will increase blade weight. The propulsive rotor minimizes this problem by allowing blade flapping freedom in the manner of a helicopter rotor.

The method of analysis for hover, transition, and forward flight is given in the following paragraphs.

HOVER

In the strip-analysis method of analysis the propeller blade is considered to be formed of several sections, each functioning in a two-dimensional flow field. The resultant elemental lift and drag forces acting on the profile are resolved into thrust and torque components which can be integrated to determine total thrust and torque of the blade.

From vortex theory considerations, the velocity at any section is the resultant of the rotational velocity of a blade element and an interference velocity due to the trailing vortex system. The forces and velocities acting at a typical blade element are shown in the following velocity diagram.
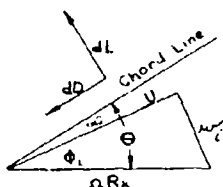
Hover Velocity Diagram

From the vortex theory the equation for induced flow at an element is:

$$w_i = \frac{\Gamma B}{4 \pi r \sin \phi_i} \tag{1}$$

From fluid flow theory the lift on an element can be expressed by two equations:

$$dL = \frac{\rho}{2} C_l U^2 c \, dr \tag{2}$$

$$dL = \Gamma U \rho \, dr \tag{3}$$

Equating these two expressions results in an expression for circulation (Γ) as a function of the non-dimensional lift coefficient:

$$\Gamma = \frac{1}{2} C_l c U \tag{4}$$

and substituting (4) into equation (1) gives:

$$w_i = \frac{B C_l c U}{8 \pi r \sin \phi_i} \tag{5}$$

From the velocity diagram

$$\tan \phi_i = \frac{w_i}{U} \tag{6}$$

Substituting equation (6) into equation (5), letting $x = r/R$ and replacing the expression for rotor solidity by the notation (σ), results in

$$\sigma C_l = 8 x \sin \phi_i \tan \phi_i K_G \tag{7}$$

where K_G is the Goldstein correction for blade tip energy loss.

With a collective flap deflection, C_l is given as

$$C_{l_b} = a \, c_f \, \delta_o \quad \text{in the flap region.}$$

Using equation (2), the lift per unit span is

$$\frac{dL}{dr} = \frac{\rho}{2} C_l U^2 c$$

Referring to the hover velocity diagram, the differential thrust and torque on any one blade section may be written

$$\frac{dT}{dr} = \frac{dL}{dr} \cos \phi_i - \frac{dD}{dr} \sin \phi_i \tag{8}$$

$$\frac{dQ}{dr} = r \left[\frac{dL}{dr} \sin \phi_i + \frac{dD}{dr} \cos \phi_i \right] \tag{9}$$

By inserting $dr = R \, dx$ and introducing the non-dimensional coefficients C_l and C_d, the relations for total elemental thrust and torque may be written

$$\frac{dT}{dx} = \frac{B}{2} \rho U^2 c R \left(C_l \cos \phi_i - C_d \sin \phi_i \right) \tag{10}$$

$$\frac{dQ}{dx} = B \frac{\rho}{2} U^2 c R^2 x \left(C_l \sin \phi_i + C_d \cos \phi_i \right) \tag{11}$$

where, in the flapped region, for C_l in the above equation is substituted $C_l = a c_f \delta$, and for C_d is substituted

153

$$C_{d_b} + A_1 + B_1 \delta + C_1 \delta^2$$

Again considering the velocity diagram, the resultant velocity at the section can be expressed as

$$U = \Omega R x \cos \phi_i \qquad (12)$$

Substituting the preceding equation into (10) and (11), and introducing the dimensionless parameters C_T/σ and C_Q/σ results in

$$d\frac{C_T}{\sigma} = \frac{x^2}{2}\left[C_l \cos \phi_i - C_d \sin \phi_i\right]\cos^2 \phi_i \, dx \qquad (13)$$

$$d\frac{C_Q}{\sigma} = \frac{x^3}{2}\left[C_l \sin \phi_i + C_d \cos \phi_i\right]\cos^2 \phi_i \, dx \qquad (14)$$

and since C_p as defined is equal to C_Q

$$d\frac{C_p}{\sigma} = \frac{x^3}{2}\left[C_l \sin \phi_i + C_d \cos \phi_i\right]\cos^2 \phi_i \, dx \qquad (15)$$

The total forces produced by the rotor are then determined by a summation of the elemental thrust and torque along the blade span.

$$\frac{C_T}{\sigma} = \frac{1}{2}\int_{x_o}^{x_b} x^2 \left[C_l \cos \phi_i - C_d \sin \phi_i\right]\cos^2 \phi_i \, dx \qquad (16)$$

$$\frac{C_p}{\sigma} = \frac{1}{2}\int_{x_o}^{x_b} x^3 \left[C_l \sin \phi_i + C_d \cos \phi_i\right]\cos^2 \phi_i \, dx \qquad (17)$$

In the original derivation of the vortex theory equations, the rotor was assumed as a disc, that is, composed of an infinite number of blades. When calculating the performance of a rotor, a tip loss factor must be included to account for the reduction in thrust at the blade tip region incurred by air spillage about the blade tips. In the present analysis an allowance for the blade tip energy loss is included by including the Goldstein correction in the determination of the induced angle at the blade section.

Because the blade does not extend to the center of rotation the summation limits at the blade inboard end must be altered to include the presence of the hub and retention. For the analysis, the integration for the thrust and power coefficients is extended to the 20 percent radius station. Applying the corrected limits of integration to equations (16) and (17)

$$\frac{C_T}{\sigma} = \frac{1}{2}\int_{.2}^{x_1} x^2 \left[C_l \cos \phi_i - C_d \sin \phi_i\right]\cos^2 \phi_i \, dx$$
$$+ \frac{1}{2}\int_{x_1}^{1} x^2 \left[C_l \cos \phi_i - C_d \sin \phi_i\right]\cos^2 \phi_i \, dx \qquad (18)$$

$$\frac{C_p}{\sigma} = \frac{1}{2}\int_{.2}^{x_1} x^3 \left[C_l \sin \phi_i + C_d \cos \phi_i\right]\cos^2 \phi_i \, dx$$
$$+ \frac{1}{2}\int_{x_1}^{1} x^3 \left[C_l \sin \phi_i + C_d \cos \phi_i\right]\cos^2 \phi_i \, dx \qquad (19)$$

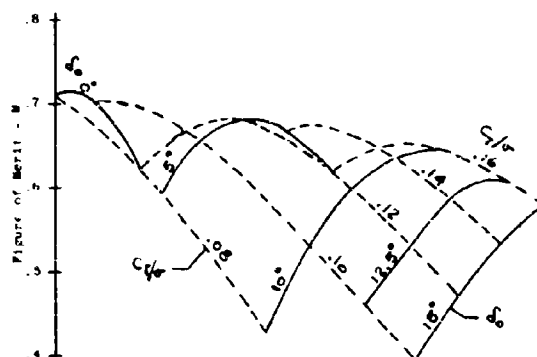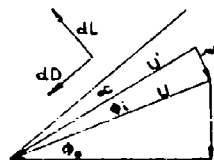The results of calculations for the K-16B rotor are given in Figure 83.

Figure 83
Static Thrust Performance Analysis

FORWARD FLIGHT

The forward flight performance equations were derived using the vortex theory in a manner similar to the hover analysis. The forces and velocities acting at a typical blade element are shown in the following figure.

Forward Flight Velocity Diagram

The induced velocity at an element may be written

$$w_i = \frac{B C_l c U}{8 \pi r \sin \phi_o} \qquad (20)$$

Considering the velocity diagram with the assumption ϕ_i is a small angle and thus $\cos \phi_i \approx 1.0$, the resultant sectional velocity is

$$U' = U \cos \phi_i \approx U \qquad (21)$$

154

ard

$$\phi_i \approx \tan \phi_i \approx \frac{w'}{U} \tag{22}$$

Substitution of equation (22), the notation for rotor solidity (σ), and $x = r/R$ into equation (20) results in

$$\sigma C_i = \theta x \phi_i \sin \phi_0 k_u \tag{2?}$$

Following the same analysis as in hover, the differential thrust and torque on any one section may be written

$$\frac{dT}{dx} = B \frac{\rho}{2} U^2 cR\left(c_i \cos\phi_0 - c_d \sin\phi_0\right) \tag{24}$$

$$\frac{dQ}{dx} = B \frac{\rho}{2} U^2 cR\left(c_i \sin\phi_0 + c_d \cos\phi_0\right) \tag{25}$$

Referring again to the sketch, the resultant elemental velocity is

$$U = \frac{\Omega k_x}{\cos\phi} \tag{?}$$

Introducing this expression and the non-dimensional coefficients C_T/σ and C_P/σ into equations (24) and (25) results in

$$d\frac{C_T}{\sigma} = \frac{x^2}{2}\left[\frac{c_i \cos\phi_0 - c_d \sin\phi_0}{\cos^2\phi}\right] dx \tag{27}$$

$$d\frac{C_Q}{\sigma} = d\frac{C_P}{\sigma} = \frac{x^3}{2}\left[\frac{c_i \sin\phi_0 + c_d \cos\phi_0}{\cos^2\phi}\right] dx \tag{29}$$

The rotor total thrust and torque are determined by an integration of the preceding expressions, using the proper integration limits as described in the hover analysis. The final equations become

$$\frac{C_T}{\sigma} = \frac{1}{2}\int_{.2}^{1} x^2\left[\frac{c_i \cos\phi_0 - c_d \sin\phi_0}{\cos^2\phi}\right] dx$$

$$\frac{C_P}{\sigma} = \frac{1}{2}\int_{.2}^{1} x^3\left[\frac{c_i \sin\phi_0 + c_d \cos\phi_0}{\cos^2\phi}\right] dx$$

The problem is to determine the thrust and power coefficients for the complete range of forward flight velocities. This is effected by choosing a range of blade angles compatible with the above. The procedure followed is similar to that for the hover analysis. Because these analyses involve iterative procedures, they have been programmed for machine solution.

TRANSITION

In hovering and high-speed forward flight, standard propeller vortex theory methods can be used for performance analysis. In the transition regime, however, the inflow angles are so large these methods no longer apply. Accordingly, for an articulated propulsive rotor, helicopter methods must be used. Although this method is not as accurate as the strip analysis for static thrust, it can be used for general parametric studies for static thrust and power by merely setting the advance ratio μ to zero.

During transition, the approach velocity is resolved into components that are parallel and perpendicular to the shaft axis. The parallel component and the induced

portion is non-dimensionalized with respect to tip speed and is designated λ. The perpendicular component is also non-dimensionalized with respect to tip speed and is designated μ. The transition power is a function of these two parameters as well as the components of the blade flapping motion and the flap deflection.

Rotor performance in transition is solved by an iterative numerical procedure of the blade flapping equation of motion for a series of points in the azimuth cycle. It is essentially that described in TN 3366 (83) but with several improvements. Because the actual equation of motion is solved, there is no restriction on advance ratio, inflow ratio, or forward speed, and there are no small angle assumptions. It incorporates the same NACA two-dimensional airfoil data as the hover program, which includes both stall and Mach number effect, as well as the same flap lift and drag characteristics. The equation also provides for the insertion of an arbitrary pitching velocity. It is also useful for analyzing blade flapping in high-speed forward flight.

The motion of a rotor blade is found by solving the differential equation of motion about the flapping hinge. The blade is represented by a rigid line as shown in the figure.
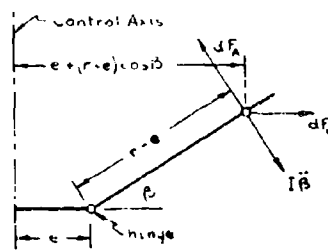
Its mass per unit length may vary along its length. It is constrained to stay in a plane which is rotating with constant speed, Ω, about an axis called the control axis, so that no lag hinge is considered. In this plane, the blade is free to rotate about a point that is a distance "e" from the control axis, representing an offset flapping hinge. Each element of the blade is considered to have two forces acting on it – a centrifugal force and an aerodynamic force. The aerodynamic force is found under the assumption that each element of the blade behaves as a two-dimensional airfoil in a uniform flow field identical to that of each element of the rotor radius.

The inflow velocity parameter, λ, is assumed to be uniform over the rotor disc. No feathering action of the blade is considered because the motion is found with respect to the control or no-feathering axis.

The differential equation of motion about the flapping hinge, which expresses the equilibrium of the centrifugal and aerodynamic moments with the inertia moment, is set up and solved numerically. The assumptions are:

- Two-dimensional flow at each section;
- Use of steady-state airfoil data;
- Constant inflow velocity over the rotor disc;
- Constant rotational speed about the control axis;
- Rigid blade.

Referring to the sketch, the differential equation of motion obtained by equating the moments about the flapping hinge is:

$$I\ddot{\beta} - M_c - M_w = M_A \tag{31}$$

The centrifugal force, dF_c, on a portion of blade dr' with mass $m \, dr'$ is:

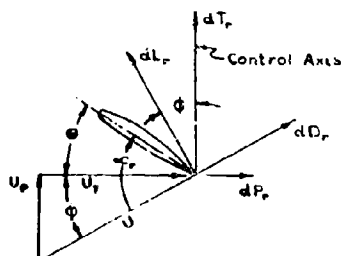$$dF_c = m \, dr' \, \Omega^2 (e + r'\cos\beta)$$

where

$$r' = (r - e)$$

and where Ω is the rotational velocity about the control axis, and $(e + r'\cos\beta)$ is the radius of the element dm' from that axis. The moment arm about the flapping hinge is $(r'e)\sin\beta$, so the total centrifugal moment is:

$$M_c = -\Omega^2 \sin\beta \int_1 mr'(e + r'\cos\beta)dr'$$

$$= -\Omega^2 \sin\beta\cos\beta \int_1 mr'^2 dr' - \Omega^2 e \sin\beta \int_1 mr' dr' \qquad (32)$$

The aerodynamic force on a blade section is shown in the next sketch.

(Figure: sketch showing dT_r, Control Axis, dL_r, ϕ, dD_r, U_p, U_T, U, dP_r, ϕ, θ)

The velocity (U) is the relative velocity composed of the components U_T perpendicular to the control axis, and U_p parallel to it. The elementary forces acting on the blade are dL_r perpendicular to U, and dD_r parallel to it. These give rise to an elementary thrust force, dT_r, parallel to the control axis, and dP_r perpendicular to it, which are given by:

$$dT_r = dL_r \cos\phi + dD_r \sin\phi \qquad (33)$$

$$dP_r = dD_r \cos\phi - dL_r \sin\phi \qquad (34)$$

The force dP_r is parallel to the flapping hinge and produces no moment. The force dT_r is the same as dF_A shown in the previous sketch, and has an arm r'. So the aerodynamic moment is:

$$M_a = \int_A (dL_r \cos\phi + dD_r \sin\phi)r'dr' \qquad (35)$$

Here, the integral is taken over that portion of the blade, A, that is aerodynamically effective. Allowance can then be made for excluding the shank of the blade near the hinge in the lifting aerodynamic effects.

By using lift and drag coefficients based on the section chord, C, equation 35 can be written:

$$M_A = \frac{1}{2}\rho \int_A U^2 c(c_l \cos\phi - c_d \sin\phi)r'dr' \qquad (36)$$

where in the flap region C_l is given as $C_l = C_{l_{table}} - a\alpha_f\delta$

and C_d as $C_d = C_{d_{table}} + A_f + B_f\delta + C_f\delta^2$, as in the hover analysis.

The speed, U, can be expressed in terms of the flight speed, V, rotor angle of attack, α, rotational speed, Ω, inflow velocity parallel to the control axis, v, and azimuth angle, ψ. Rotor angle of attack, α, is taken

positive when the rotor is tilted back in the usual autogiro convention. The velocity due to flapping, $r'\dot\beta$, is included in U_p. The velocities are:

$$U_T = \Omega(e + r'\cos\beta) + V\cos\alpha \sin\psi$$

$$U_p = V\sin\alpha\cos\beta - v\cos\beta - V\cos\alpha\cos\psi\sin\beta - r'\dot\beta$$

which can be non-dimensionalized as:

$$U_p = \cos\beta(V\sin\alpha - v) - V\cos\alpha\cos\psi\sin\beta - r'\dot\beta \qquad (37)$$

$$\frac{U_p}{\Omega R} = \lambda\cos\beta - \mu\cos\psi\sin\beta - x'\beta^* \qquad (38)$$

$$\frac{U_T}{\Omega R} = \zeta + x\cos\beta + \mu\sin\psi \qquad (39)$$

The inflow angle, ϕ, is obtained from the preceding figure as:

$$\phi = \tan^{-1} U_p/U_T$$

or:

$$\phi = \tan^{-1}\frac{\lambda\cos\beta - \mu\cos\psi\sin\beta - x'\beta^*}{\left(\frac{e}{R} + x'\cos\beta\right) + \mu\sin\psi} \qquad (40)$$

and the angle of attack, α_r, as:

$$\alpha_r = \phi + \theta - \beta\tan\delta_3 \qquad (41)$$

where δ_3 represents the coupling between pitch and flapping. Along with the Mach number, U/a, α_r, determines c_l and c_d from airfoil section data.

If the quantities V, α, v, Ω, θ, δ_3, a, and $\dot\beta$ are known, M_A can be found at any azimuth, ψ.

It can be shown that when a rotor is rotated at a constant angular velocity in inertial space about an axis perpendicular to the spin axis (precession about the "y" axis of the rotor, for instance), the rotor blades experience a vibratory flapping moment that would, if the blade were rigid, produce a net rotor rolling moment about the aircraft "x" axis. Thus, the behavior of an infinitely rigid rotor with respect to precessional velocities would be exactly equivalent to a gyroscope operating with the same angular momentum (some propellers approximate this).

The articulated rotor, by virtue of its flapping hinges, cannot transmit blade flapping moments to the hub, and hence must react this vibratory gyroscopic flapping moment (due to precession about the "y" axis) by other means. It does this by assuming a longitudinal flapping angle (with respect to a plane perpendicular to the spin axis) that produces a vibratory change in blade angle of attack. This in turn produces an aerodynamic flapping moment just sufficient to balance the gyroscopic flapping moment. This resultant tendency for the tip path plane to lag the shaft plane in an articulated rotor that is precessing in inertial space is well-documented. The incre-

mental flapping angle ($\Delta a_{l_s} = \frac{-16q}{\gamma\Omega}$) produces a rotor

moment about the aircraft cg due to resultant force vector rotation and, where offset flapping hinges are employed, hub moment effects. Thus, the moment due to tip path plane lag is essentially a rotor damping in pitch contribution to the airframe.

The aforementioned vibratory airload which results from the tip path plane lag is in a direction so that it subtracts from the airload on the retreating blade and increases the airload on the advancing blade for nose up pitching motion of the tip path plane. This tends to load that side of the rotor disc most capable of carrying the load and, by unloading the side of the disc least capable of carrying load, provides retreating-blade stall relief.

The expression for the additional flapping moment due to precession of the rotor in space can be independ-

ently derived and super-imposed upon the flapping equation of motion.

Consider a particle rotating at constant angular velocity ($\Omega = \dfrac{d\psi}{dt}$) in the x, y plane of a rectangular coordinate system. If this coordinate system is in turn rotating about its "y" axis at an angular velocity (q = $\dot{T}$) with respect to an inertial space axis system (x, y, z), the absolute accelerations of the mass particle are developed as follows:
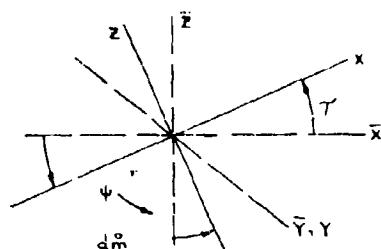
The absolute positions of the particles are:

$$x = -r \cos\psi \cos T$$
$$y = -r \sin\psi$$
$$z = -r \cos\psi \sin T$$

The absolute accelerations are:

$$\ddot{X} = -2r\Omega\sin\psi\sin T \, \dot{T} + r\cos\psi\cos T \, \dot{T}^2$$
$$\qquad + r\Omega^2\cos\psi\cos T + r\cos\psi\sin T \, \dot{T}$$

$$\ddot{Y} = -\Omega^2 r\sin\psi \qquad\qquad (1-)$$

$$\ddot{Z} = 2r\Omega\sin\psi\cos T \, \dot{T} + r\cos\psi\sin T \, \dot{T}^2$$
$$\qquad + r\Omega^2\sin T\cos\psi - r\cos T \, \dot{T}\cos\psi$$

These acceleration can be resolved into the rotor axis system by:

$$\ddot{X} = \ddot{X}\cos T + \ddot{Z}\sin T$$
$$\ddot{Y} = \ddot{Y} \qquad\qquad (1-)$$
$$\ddot{Z} = \ddot{Z}\cos T - \ddot{X}\sin T = 2r\Omega\dot{T}\sin\psi - r\ddot{T}\cos\psi$$

Only the "z" acceleration is of interest because flapping moments are being considered here. The additional blade flapping moment is given by:

$$\psi \Sigma \Delta M = -\int_0^R r\ddot{z}\,dm$$

$$= (-2\,\Omega\dot{T}\sin\psi + \ddot{T}\cos\psi)\int_0^R r^2\,dm \qquad (14)$$

Thus, the equation of motion for a flapping rotor blade precessing at constant angular velocity ($\dot{T} = q$) may be written:

$$I_1\ddot{\beta} + M_c + 2\,I_1\,\Omega q \sin\psi = M_A \qquad (45)$$

It is convenient to write the equation in terms of non-dimensional quantities. To do this, β is considered a function of the azimuth angle, ψ , rather than the time, t. Noting that for constant rotational speed Ω, ψ, and t are related by ($\psi = \Omega t$), the time derivatives of β can be changed to derivatives with respect to ψ as follows:

$$\dot{\beta} = \frac{d\beta}{dt} = \Omega\frac{d\beta}{d\psi} = \Omega\beta^*$$

$$\ddot{\beta} = \frac{d^2\beta}{dt^2} = \Omega^2\frac{d^2\beta}{d\psi^2} = \Omega^2\beta^{**}$$

Here the asterisk denotes differentiation with respect to ψ. All lengths are made non-dimensional by division by R, the blade radius, and all velocities by division by ΩR, the tip speed. In this way the following dimensionless quantities are defined.

$$x' = r/R, \quad u_T = U_T/\Omega R, \quad u_P = U_P/\Omega R$$

$$\mu = \frac{V\cos\alpha}{\Omega R}, \quad \lambda = \frac{V\sin\alpha - v}{\Omega R}, \quad u^2 = u_T^2 + u_P^2$$

Then, written non-dimensionally:

$$\beta^{**} = \frac{M_A + M_c + M_q}{\Omega^2 I} \qquad (46)$$

The calculation proceeds from an arbitrary starting point for any given combination of advance ratio, μ, inflow ratio, λ, and collective pitch, Θ.

Initially, the blade is assumed to have a particular value of flapping angle β, and its first derivative β' at zero azimuth position. This starting assumption defines the instantaneous section angle of attack distribution along the blade and consequently permits the evaluation of the aerodynamic and inertia moments. The subsequent azimuthal history of the blade may then be calculated for small increments in azimuth position. The blade is brought through a number of complete revolutions until flapping convergence is achieved. Radial flow effects are accounted for by multiplying the profile torque and H-force by appropriate factors derived from IAS Preprint 694 (61). The converged motion and the integrated rotor forces and moments are independent of the initial assumption of blade motion. The output from the program consists of the integrated torque and forces along and perpendicular to the flight path as well as the conventional thrust and H-force. In addition, the flapping motion is given, and the angle of attack distribution is given at every radial station and at every azimuth. Rotor control axis angle of attack is also oriented and rotor power coefficients calculated using this program are given in figure 84.

Although defined in this "transition" section, the flapping equilibrium equation is valid at all speeds. It was used to calculate the forward flight flapping presented in figure 52. To illuminate the effect of blade properties on the forward flight flapping derivative a simplified analysis was made; the results are shown in figure 53.

157

$$\lambda = -\frac{V}{\Omega R}\cos\mathcal{T}^\circ\left[\frac{1}{2} + \frac{1}{2}\sqrt{1 + \frac{1}{\cos^2\mathcal{T}^\circ}\left(\frac{T_c'}{1-T_c'}\right)}\right]$$

$$\mu = \frac{V}{\Omega R}\cos(90-\mathcal{T}^\circ) \qquad C_T = \frac{1}{2}\left(\frac{V}{\Omega R}\right)^2\frac{T_c'}{1-T_c'}$$
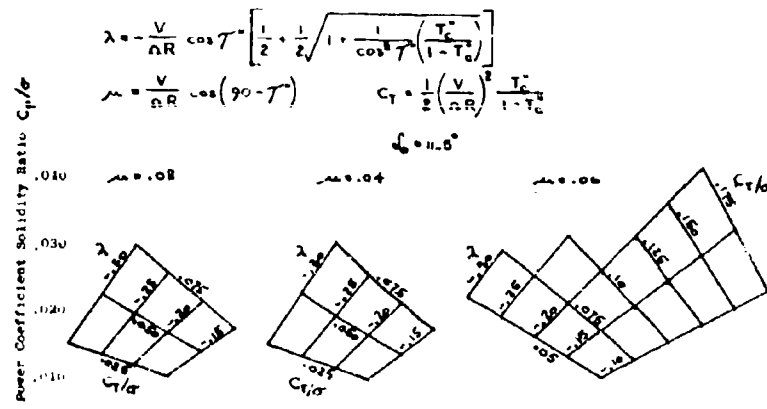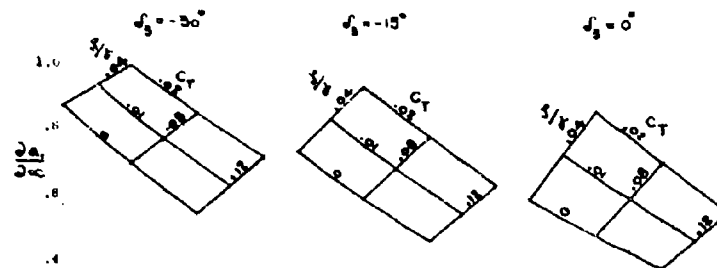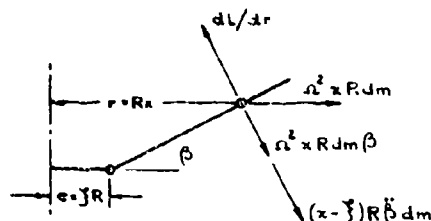

Figure 84 E-16b Rotor Transition Performance

Figure 85
Effect Of Blade Characteristics On Longitudinal Flapping
in Cruising Flight

ROTOR CONTROLLABILITY IN HOVERING FLIGHT

The forces acting on a mass particle of a hinged rotor are as follows:

The equilibrium of moments about the flapping hinge results in the equation:

$$\int_{\bar{\jmath}}^{1}(\jmath - \bar{\jmath}/R)\,dL = \int_{\bar{\jmath}}^{1}\left[xR^2\Omega^2(x-\bar{\jmath})\beta + (x-\bar{\jmath})^2R^2\ddot{\beta}\right]dm \quad (47)$$

Assuming single harmonic flapping only:

$$\beta = -a_1\cos\psi - b_1\sin\psi$$
$$\ddot{\beta} = a_1\Omega^2\cos\psi + b_1\Omega^2\sin\psi$$
$$x(x-\bar{\jmath}) = (x-\bar{\jmath})^2 + \bar{\jmath}(x-\bar{\jmath})$$

Substituting the expressions for β and $\ddot{\beta}$ into equation 47 yields:

158

$$\int_{\mathfrak{F}}^{1}(x-\mathfrak{F})dT = (\Omega R)^2 \int_{\mathfrak{F}}^{1}\left[(x-\mathfrak{F})^2(a_o - a_1\cos\psi - b_1\sin\psi)\right.$$
$$+ \mathfrak{F}(x-\mathfrak{F})(a_o - a_1\cos\psi - b_1\sin\psi)$$
$$\left. + (x-\mathfrak{F})^2(a_1\cos\psi + b_1\sin\psi)\right]dm \qquad (48)$$

By definition:

$$I_1 = R^2 \int_{\mathfrak{F}}^{1}(x-\mathfrak{F})^2 dm$$

$$\mathfrak{F} = \frac{\mathfrak{F}R^2}{I}\int_{\mathfrak{F}}^{1}(x-\mathfrak{F})dm$$

Substituting these expressions into equation 48 yields for the inertia terms on the right hand side:

$$\frac{M_i}{I\Omega^2} = a_o(1+\mathfrak{F}) - a_1\mathfrak{F}\cos\psi - b_1\mathfrak{F}\sin\psi \qquad (49)$$

For the aerodynamic portion, assume a linear lift curve slope:

$$dL = \frac{\rho}{2}(\Omega R)^2 x^2 c a \propto \qquad (50)$$

where:

$$\propto = \Theta + \Phi + T_w(x-.75) - \alpha_f \delta - \beta\tan\delta_3 - \frac{(x-\mathfrak{F})\dot\beta}{\Omega x}$$

Assuming a single harmonic response for β:

$$\beta = a_o - a_1\cos\psi - b_1\sin\psi$$
$$\dot\beta = \Omega(a_1\sin\psi - b_1\cos\psi)$$
$$\delta = \delta_o + \delta_1\sin\psi + \delta_2\cos\psi$$

and $-\frac{\lambda}{x}$ for Φ for hovering flight.

Substituting the above harmonic components of β and δ into equation 50, the expression for dL/dx becomes:

$$\frac{dL}{dx} = \frac{\rho}{2}(\Omega R)^2 c a R x^2\left[\Theta + T_w(x-.75) - \frac{\lambda}{x} - a_o\tan\delta_3\right.$$
$$+ a_1\tan\delta_3\cos\psi + b_1\tan\delta_3\sin\psi - a_1\left(\frac{x-\mathfrak{F}}{x}\right)\sin\psi$$
$$\left. + b_1\left(\frac{x-\mathfrak{F}}{x}\right)\cos\psi - \alpha_f\delta_o - \alpha_f\delta_1\sin\psi - \alpha_f\delta_2\cos\psi\right] \qquad (51)$$

To account for the cyclic lift variation, each cyclic lift expression is multiplied by the factor $(1-k)$, the use and derivation of which are explained later.

In addition, the total lift is separated into harmonic components:

$$\frac{dL}{dx} = \frac{dL_o}{dx} + \frac{dL_1}{dx}\sin\psi + \frac{dL_2}{dx}\cos\psi \qquad (52)$$

Equating like parts:

$$\frac{dL_o}{dx} = \frac{\rho}{2}(\Omega R)^2 R c a x^2\left[\Theta + T_w(x-.75) - a_o\tan\delta_3 - \frac{\lambda}{x} - \alpha_f\delta_o\right]$$

$$\frac{dL_1}{dx} = \frac{\rho}{2}(\Omega R)^2 R c a x^2\left[b_1\tan\delta_3 - \left(\frac{x-\mathfrak{F}}{x}\right)a_1 - \alpha_f\delta_1\right](1-k) \qquad (53)$$

$$\frac{dL_2}{dx} = \frac{\rho}{2}(\Omega R)^2 R c a x^2\left[\left(\frac{x-\mathfrak{F}}{x}\right)b_1 + a_1\tan\delta_3 - \alpha_f\delta_2\right](1-k)$$

Substituting the harmonic components into equation 47, integrating radially utilizing the inertial components of equation 49, the following equations in a_1 and b_1 are obtained.

$$\left(\frac{1}{4} - \frac{2}{3}\mathfrak{F}\right)(1-k)a_1 - \left(\frac{1}{4} - \frac{\mathfrak{F}}{3}\right)(1-k)b_1\tan\delta_3$$
$$+ \alpha_f\delta_1\left[\frac{1-x_1^4}{4} - \mathfrak{F}\left(\frac{1-x_1^3}{3}\right)\right](1-k) = \frac{2b_1 I_1\mathfrak{F}}{\rho a c R^4}$$

$$\frac{2\mathfrak{F}}{\gamma}b_1 - \left(\frac{1}{4} - \frac{\mathfrak{F}}{3}\right)(1-k)a_1\tan\delta_3 - \left(\frac{1}{4} - \frac{2}{3}\mathfrak{F}\right)(1-k)b_1 \qquad (54)$$
$$+ \alpha_f\delta_2\left[\frac{1-x_1^4}{4} - \mathfrak{F}\left(\frac{1-x_1^3}{3}\right)\right](1-k) = \frac{2a_1 I_1\mathfrak{F}}{\rho a c R^4} - \frac{2\mathfrak{F}}{\gamma}a_1$$

For convenience the constants in $\mathfrak{F}$ and flap inboard end x_1 are called:

$$P = \frac{1}{4} - \frac{2}{3}\mathfrak{F} \qquad\qquad E = \frac{1-x_1^3}{3}$$

$$H = \frac{1-x_1^4}{4} \qquad\qquad J = \frac{1}{4} - \frac{\mathfrak{F}}{3}$$

Using Kramer's rule and equation 54, the expressions for a_1 and b_1 are obtained, assuming no δ_2 is introduced.

$$a_1 = \frac{-P\alpha_f\delta_1(H - \mathfrak{F}E)}{P^2\left[\frac{2\mathfrak{F}/\gamma}{(1-k)} + J\tan\delta_3\right]^2}$$

$$b_1 = \frac{\alpha_f\delta_1(H - \mathfrak{F}E)\left[\left(\frac{2}{1-k}\right)\mathfrak{F}/\gamma + J\tan\delta_3\right]}{P^2 + \left[\frac{2\mathfrak{F}/\gamma}{1-k} + J\tan\delta_3\right]^2}$$

The partial derivatives are:

$$\frac{\partial a_1}{\partial \delta_1} = \frac{P\alpha_f\delta_1(H - \mathfrak{F}E)}{P^2 + \left[\frac{2}{(1-k)}\mathfrak{F}/\gamma + J\tan\delta_3\right]^2}$$

$$\frac{\partial b_1}{\partial \delta_1} = \frac{\alpha_f(H - \mathfrak{F}E)\left[\frac{2}{(1-k)}\mathfrak{F}/\gamma + J\tan\delta_3\right]}{P^2 + \left[\frac{2}{(1-k)}\mathfrak{F}/\gamma + J\tan\delta_3\right]^2}$$

and similarly if δ_2 were applied but not δ_1:

$$\frac{\partial b_1}{\partial \delta_2} = \frac{P\alpha_f(H - \mathfrak{F}E)}{P^2 + \left[\frac{2}{(1-k)}\mathfrak{F}/\gamma + J\tan\delta_3\right]^2}$$

159

$$\frac{\partial a_1}{\partial f_1} = \frac{-c_j\left(H - \jmath\epsilon\left[\frac{z\, S/\gamma}{(1-k)} + J\tan\delta_j\right]\right)}{P^2 + \left[\frac{z\, S/\gamma}{(1-k)} + J\tan\delta_j\right]^2}$$

The flap-flapping phase angle, $\Delta\psi$, then is:

$$\Delta\psi = \tan^{-1}\frac{\partial b_1/\partial f_1}{\partial a_1/\partial f_1}$$

These are the equations used to generate Figure 84. The important variables are seen to be S/γ, S, and f_3 for constant flap parameters. C_T is introduced through $(1-k)$.

CYCLIC INFLOW VARIATION

The "k" factor introduced in the previous section to account for cyclic inflow variation is now derived.

Data obtained from the K-16 test rig indicated that both the cyclic sensitivity and the phase angle were substantially less than that predicted by the theory of Meyer and Falabella (62). This reduction in control ability could not be attributed to a reduction in flap lift effectiveness alone, because this would alter only the magnitude of the response but not the phase angle. Because the offset flapping hinge increases the natural frequency of the blade, the system is operating below resonance, and the reduction in phase angle implies a reduction in damping.

With the system non-resonant, a cyclic variation in C_L must exist in order to cause the blades to flap. This cyclic variation of C_L implies a cyclic variation of inflow which may be calculated as follows:

For a rotor operating under helicopter forward flight conditions (transition), the elemental thrust obtained from blade element considerations is:

$$\frac{dT}{dr} = \frac{\rho}{2}U^2 C_1 Bc \tag{55}$$

If ϕ is small, $\cos\phi \approx 1.0$, and U^2 can be approximated by:

$$U^2 = (\Omega R)^2\left(x + \mu_1\sin\psi\right)^2$$

Inserting the expression for velocity, this equation becomes:

$$\frac{dT}{dr} = \frac{\rho}{2}\Omega^2 R^2\left(x + \mu_1\sin\psi\right)^2 C_1 Bc \tag{56}$$

From momentum theory the elemental thrust is:

$$\frac{dT}{dr} = 4\pi r\rho\left(V\sin\gamma + v\right)v \tag{57}$$

This equation can also be written:

$$\frac{dT}{dr} = 4\pi r\rho(\Omega R)^2\left[\frac{V\sin\gamma}{\Omega R} + \frac{v}{\Omega R}\right]\frac{v}{\Omega R} \tag{58}$$

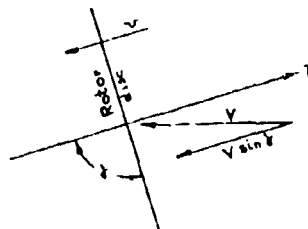Equating the expressions for elemental thrust as obtained from the two theories yields.

$$\frac{8x\,r}{(\Omega R)^2}\left(V\sin\gamma + v\right) = \sigma C_1\left(x + \mu_1\sin x\right)^2 \tag{59}$$

Considering an increment in lift coefficient that results in a corresponding increment in induced velocity:

$$\sigma\Delta C_1\left(x + \mu_1\sin\psi\right)^2 = \left[\frac{8x}{(\Omega R)^2}V\sin\gamma + \frac{8xv}{(\Omega R)^2}\right]\Delta v \tag{60}$$

$$+ \frac{8xv\,\Delta v}{(\Omega R)^2}$$

From the forward flight velocity diagram:

λ_1 is defined as:

$$\lambda_1 = \frac{V\sin\gamma + v}{\Omega R} \tag{61}$$

Substituting this equation and the expression for induced velocity from Gessow and Meyers (67), the previous equation becomes:

$$\sigma\Delta C_1\left(x + \mu_1\sin\psi\right)^2 = 8x\left[\lambda_1 + \frac{C_T}{2\left(\lambda_1^2 + \mu_1^2\right)^{1/2}}\right]\Delta v \tag{62}$$

Considering the velocities normal to, and in the plane of the disc, an expression for inflow angle is obtained:

$$\varphi = \frac{V\sin\gamma + v}{\left(x + \mu_1\sin\psi\right)\Omega R} \tag{63}$$

Upon differentiation this reduces to:

$$\Delta\varphi = \frac{\Delta v}{\left(x + \mu_1\sin\psi\right)\Omega R} \tag{64}$$

Substituting the expression for Δv into equation 62 yields:

$$\sigma\Delta C_1\left(x + \mu_1\sin\psi\right)^2 = \frac{8x}{\Omega R}\left[\lambda_1 + \frac{C_T}{2\left(\lambda^2 + \mu^2\right)^{1/2}}\right]$$
$$\Delta\varphi\left(x + \mu_1\sin\psi\right)\Omega R \tag{65}$$

now $\Delta C_1 = a\Delta\alpha = a\left(\Delta\Theta - \Delta\varphi\right)$ \hfill (66)

replacing ΔC_L by this expression in the previous equation gives:

$$\sigma a\left(\Delta\Theta - \Delta\varphi\right)\left(x + \mu_1\sin\psi\right) = 8x\left[\lambda_1 + \frac{C_T}{2\left(\lambda_1^2 + \mu_1^2\right)^{1/2}}\right]\Delta\varphi \tag{67}$$
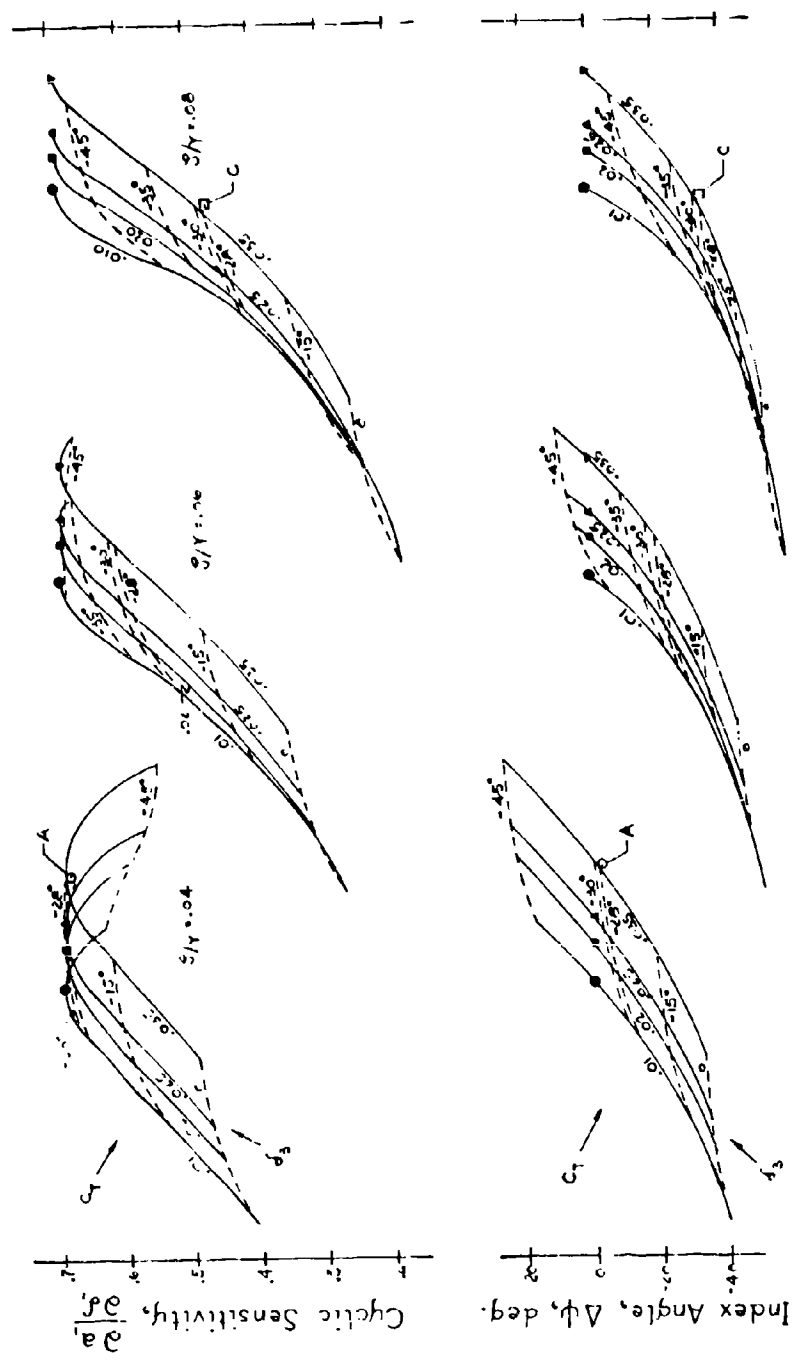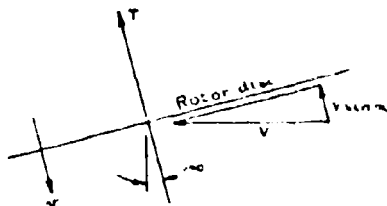
Solving for $\Delta\varphi$ yields:

160

Figure 86

Cyclic Sensitivity and Phase Angle Relationship

$$\Delta \psi = \frac{\Delta \Theta}{1 + \left[\lambda_i + \frac{C_T}{2(\lambda_i^2 + \mu_i^2)^{1/2}}\right] \frac{\theta x}{\sigma a (x + \mu_i \sin \psi)}} \quad (\ )$$

Referring to the sketch, it can be seen that for the propeller condition the flow normal to the rotor disc is $(V \sin \gamma + v)$. Then by definition $\lambda_i = \frac{V \sin \alpha + v}{\Omega R}$

and $\mu_i = \frac{V \cos \alpha}{\Omega R}$.

From the helicopter autorotative velocity diagram

the flow through the rotor disc is $(V \sin \alpha - v)$, and λ is

defined as $\lambda = \frac{V \sin \alpha + v}{\Omega R}$, and $\mu = \frac{V \cos \alpha}{\Omega R}$.

Considering the two diagrams, it is observed that

$$\mu_i = \mu = \frac{V \cos \alpha}{\Omega R}$$

and $\gamma = -\alpha$ which, when substituted into the expression for propeller inflow yields:

$$\lambda_i = \frac{V \sin \alpha - v}{\Omega R}$$

thus:

$$\lambda_i = -\lambda$$

Substituting this expression for λ into the equation for $\Delta \alpha$ yields:

$$\Delta \alpha = \Delta \Theta - \Delta \psi = \Delta \Theta \left[1 - \frac{1}{1 + \left[-\lambda + \frac{C_T}{2(\lambda^2 + \mu^2)^{1/2}}\right] \frac{\theta x}{\sigma a (x + \mu \sin \psi)}} \right]$$

or:

$$\Delta \alpha = \Delta \Theta (1 - k)$$

The expression in brackets, $(1-k)$, accounts for the cyclic inflow variation. The damping force due to flapping velocity is thus reduced by this factor.

It can be shown that the aforementioned factor appears for any cyclic variation, be it flapping, feathering, or flap input. When the equations of Meyer and Falabella (69) are modified to include this term, the agreement with the test data was substantially improved with regard to both controllability and phase angle.

Controllability must, however, be increased to the amount originally estimated, and may be secured by the inclusion of a negative δ_3 hinge. The effect of δ_3 is

shown on Figure 86 for the K-16 airplane.

It is significant to note that from a blade dynamics standpoint, negative δ_3 effectively lowers the

natural frequency towards one/rev, or in other words, tends to remove the hinge offset from the rotor dynamics, and to make the equivalent of a teetering rotor.

It is emphasized that the amount of δ_3 used does not reduce the stability below that of an equivalent zero-offset rotor. Indications are that the stability will be slightly greater than a zero-offset blade.

HUB MOMENT

Rotor controllability depends not only on cyclic sensitivity, but also on the moment resulting from the ensuing blade flapping. This moment is composed of a thrust moment and a centrifugal hub moment due to the flapping hinge offset.

The hub moment is derived in the following in the longitudinal direction, but the same result would be evident in any direction in which the blade was made to flap. The forces acting on a blade element are shown in the following sketch.
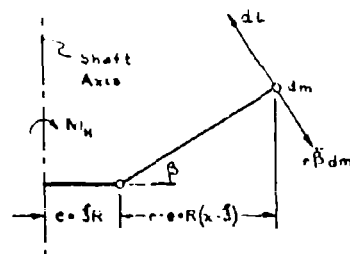
The aerodynamic moment resulting from the loading on the blade and acting at the offset hinge is:

$$dM_A = -dL e$$

The inertia moment per blade is:

$$dM_i = r \ddot{\beta} dm e$$

The average moment in the longitudinal direction is:

$$M_y = -\frac{eb}{2\pi} \int_0^{2\pi} \int_e^R \left[dL - (r-e)\ddot{\beta} dm \right] \cos \psi \, d\psi \, dx \quad (71)$$

Non-dimensionalizing:

$$\bar{e} = \frac{e}{R}, \quad x = \frac{r}{R}$$

then

$$M_y = -\frac{\bar{e} b R}{2\pi} \int_0^{2\pi} \int_{\bar{e}}^1 \left[dL - (x - \bar{e}) R \ddot{\beta} dm \right] \cos \psi \, d\psi \, dx \quad (\ )$$

Now

$$\beta = a_0 - a_1 \cos \psi - b_1 \sin \psi$$
$$\frac{\ddot{\beta}}{\Omega^2} = a_1 \cos \psi + b_1 \sin \psi \quad (7\ )$$

The inertia part of equation 72 is:

$$M_{y_1} = \frac{3bR^2}{2\pi}\int_0^{2\pi}\int_{\zeta}^1 x\,\ddot{\beta}\cos\psi\,dm\,d\psi - \frac{3bR^2}{2\pi}$$

$$\int_0^{2\pi}\int_{\zeta}^1 \ddot{\beta}\cos\psi\,dm\,d\psi \qquad (74)$$

Substituting the expression for $\ddot{\beta}$ (equation 73) into equation 74 and remembering that,

$$\frac{1}{2\pi}\int_0^{2\pi}\sin\psi\cos\psi = 0$$

the following is obtained.

$$M_{y_1} = \frac{\Omega^2 3_0 R^2}{2\pi}\int_0^{2\pi}\int_{\zeta}^1 x a_1 \cos\psi\,dm\,d\psi$$

$$-\frac{\Omega^2 3^2 bR^2}{2\pi}\int_0^{2\pi}\int_{\zeta}^1 a_1 \cos^2\psi\,dm\,d\psi$$

Since $\quad \dfrac{1}{2\pi}\displaystyle\int_0^{2\pi}\cos\psi\,d\psi = 1$

$$M_{y_1} = \Omega^2 \frac{b}{2}R^2 a_1 \, 3 \int_{\zeta}^1 (x-\zeta)\,dm \qquad (7)$$

If $\dfrac{3R^2}{l_1}\displaystyle\int_{\zeta}^1(x-\zeta)\,dm$ is called 3

Then equation 76 becomes.

$$M_{y_1} = \frac{b}{2}\Omega^2 a_1 l_1 \, 3 \qquad ( )$$

This is the principle part of the hub moment and is identical to that given by Meyer and Falabella ( ), but the aerodynamic shear that follows can contribute an appreciable percentage.

For the lift part:

$$M_{y_L} = -\frac{3bR}{2\pi}\int_0^{2\pi}\int_{\zeta}^1 \frac{dL}{dx}\cos\psi\,dx\,d\psi \qquad (7)$$

Following the procedure of the control equations for blade section angle of attack, and assuming small angles for it,

then: $\quad U \approx U_T = \Omega R\left(x + \mu\sin\psi\right)$

and,

$$\frac{dL}{dx} = \frac{c}{2}a_c(\Omega R)^2 R(x+\mu\sin\psi)^2\Big[\theta - \beta\tan\delta_s$$

$$+ T_w(x-.75) + \frac{\lambda}{x+\mu\sin\psi} - \frac{(x-\zeta)(1-k)a_1}{x+\mu\sin\psi}\sin\psi$$

$$+ \frac{(x-\zeta)(1-k)b_1}{x+\mu\sin\psi}\cos\psi - \frac{\mu a_0}{x+\mu\sin\psi}\cos\psi \qquad (79)$$

$$+ \frac{\mu(1-k)a_1}{2(x+\mu\sin\psi)} + \frac{(x-\zeta)(1-k)b_1}{2(x+\mu\sin\psi)}\cos 2\psi$$

$$+ \frac{\mu(1-k)b_1}{x+\mu\sin\psi}\sin\psi\cos\psi$$

$$- \omega_J\left(\dot{s}_0 + \dot{s}_1(1-k)\sin\psi + \dot{s}_2(1-k)\cos\psi\right)\Big]$$

Substituting this expression for dL/dx into equation 78 and integrating azimuthally, the following is obtained.

$$M_{y_L} = -3bR^2\frac{c}{2}a_c(\Omega R)^2\int_{\zeta}^1\left\{a_1\tan\delta_s(1-k)\left[\frac{x^2}{2}+\frac{\mu}{8}\right]dx\right.$$

$$-\mu a_0\frac{\lambda}{2}\,dx + b_1\frac{(x-\zeta)(1-k)}{2}x\,dx \qquad (80)$$

$$+ \frac{\mu^2(1-k)b_1}{8}\,dx$$

$$-\omega_J\dot{s}_2(1-k)\frac{x^2}{2}\,dx - \omega_J\dot{s}_2\frac{(1-k)\mu^2}{8}\,dx\Big\}$$

Radial integration yields

$$M_{y_L} = \frac{b_1 l_1 \Omega^2}{4}\Big[\mu a_0\frac{3-3^3}{2} - a_1\tan\delta_s(1-k)$$

$$\left\{\frac{3-3^4}{3} + \mu^2(3-3^2)\right\}$$

$$-b_1(1-k)\left\{\frac{3}{3}-\frac{3^2}{2}+\frac{3^4}{6}+\frac{\mu^2}{4}(3-3^2)\right\} \qquad (81)$$

$$+\omega_J\dot{s}_2(1-k)3\left\{\frac{1-x^3}{3}+\frac{\mu^2}{4}(1-x_1)\right\}\Big]$$

For convenience the offset and flap constants are defined as

$$A = \frac{1-3^3}{3} \qquad\qquad N = \frac{1}{3}-\frac{3}{2}+\frac{3^6}{6}$$

$$B = 1-3 \qquad\qquad E = \frac{1-x^6}{3}$$

$$D = \frac{1-3^2}{2} \qquad\qquad F = 1-x_1$$

The total hub-moment, aerodynamic and inertia, becomes:

$$M_y = \frac{b}{2} I_1 \gamma \Omega^2 \left[\frac{\gamma}{c} a_o + \frac{3}{2} \left\{ \mu\, a_o D \right. \right.$$

$$- a_1 \tan \delta_3 (1-k)(A + \mu^2 B)$$

$$- b_1 (1-k)\left(N + \frac{\mu^2}{4} B\right) \tag{82}$$

$$\left. \left. + \alpha_{cf} \delta_1 (1-k)\left(E + \frac{\mu^2}{4} \, \digamma\right) \right\} \right]$$

The principle difference between equation 82 and that given by Meyer and Falabella (62) are the terms containing δ_3, flap characteristics α_{cf}, E, F, and the cyclic inflow. The partial derivative with respect to a_1 flapping becomes:

$$\frac{\partial M_y}{\partial a_1} = \frac{b}{2} I_1 \gamma \Omega^2 \left[\frac{\gamma}{c} + \frac{3}{2} \tan \delta_3 (1-k)(A + \mu^2 B) \right]$$

For hover where $\mu = 0$

$$\frac{\partial M_y}{\partial a_1} = \frac{b}{2} I_1 \Omega^2 \left[\gamma + \frac{3\gamma}{2} \tan \delta_3 (1-k) A \right]$$

Equation 82 was used to construct the upper part of Figure . A check of the relative importance of the first and second terms indicates that the second term, because of aerodynamic shear, amounts to 13 percent of the inertia term for the K-16B.

$$\frac{\partial M_x}{\partial a_1} = \frac{\partial M_y}{\partial a_1} + T\left(x_H + \frac{\partial C_{L_w}}{\partial a_1} \frac{S x_{\overline{w}}}{\pi R^2} \right)$$
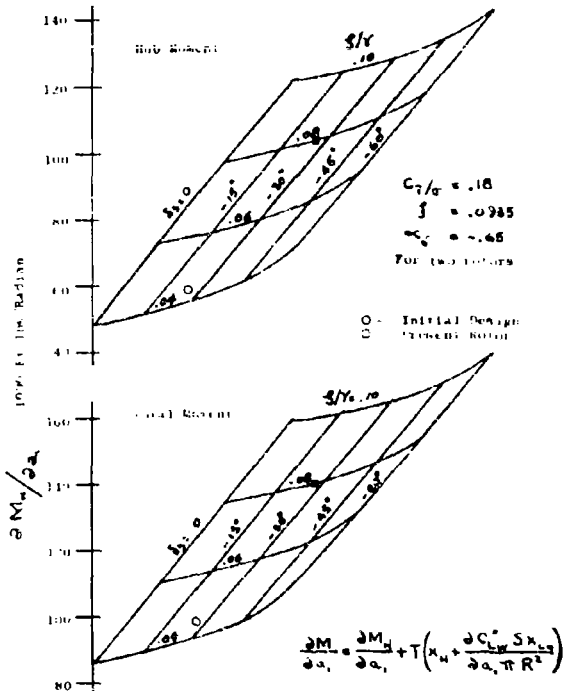
Figure 87

Rotor Control Moment Sensitivity

LONGITUDINAL TRIM AND CONTROL

KAC Report G-113-4(9) presents a graphical method that is amenable to manual solution for trimming an airplane. The following method is based on the same concept but utilizes a computer's capacity for iterative loops. This computer method also allows for several improvements to be made over the manual method, one of which is the inclusion of rotor control equations as an integral part of the trim-

ming process. The procedure begins with a balance of forces, vertical and longitudinal, and determines the velocity at which a particular thrust coefficient furnishes equilibrium. It is then put into moment balance using rotor and elevator, iterating until trim is attained. The sketch defines a number of angles that are pertinent to the solution.

$$\tau'' = \tau + \alpha_w$$

$$\tau' = \tau + \alpha_t + a$$
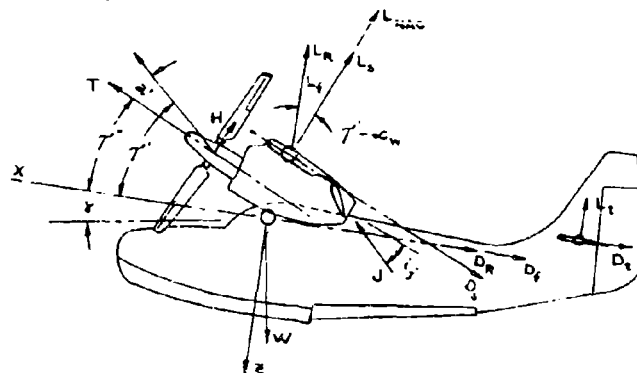
τ — Angle between fuselage and wing

τ' — Angle between relative wind and resultant rotor force

τ'' — Angle between relative wind and wing (For K-16B where $i_w - i_t = 0$)

From the sketch, the longitudinal force balance equation becomes:

$$X = NT\cos\tau' - NT a'\sin\tau' + NJ\cos(\tau'' + i_j)$$
$$-(L_s + L_{NAC})\sin(\tau' - \alpha_w) - (D_s + D_{NAC})\cos(\tau' - \alpha_w)$$
$$-D_R - D_f - D_t - W\sin\gamma \qquad (83)$$

and the Z equation:

$$Z = -NT\sin\tau'' - NT a'\cos\tau' - NJ\sin(\tau'' + i_j)$$
$$-(L_s + L_{NAC})\cos(\tau' - \alpha_w) + (D_s + D_{NAC})\sin(\tau' - \alpha_w)$$
$$+W\cos\gamma - L_R - L_f - L_t \qquad (84)$$

The thrust can be factored out of each equation thus:

$$T = \frac{1}{N(\cos\tau' - a'\sin\tau')}\Big[(L_s + L_{NAC})\sin(\tau' - \alpha_w)$$
$$+(D_s + D_{NAC})\cos(\tau' - \alpha_w) + W\sin\gamma$$
$$-NJ\cos(\tau'' + i_j) + D_R + D_f + D_t + X\Big] \qquad (85)$$

$$T = \frac{1}{N(\sin\tau' + a'\sin\tau')}\Big[-(L_s + L_{NAC})\cos(\tau' - \alpha_w)$$
$$+(D_s + D_{NAC})\sin(\tau' - \alpha_w) + W\cos\gamma$$
$$-NJ\sin(\tau'' + i_j) - L_R - L_f - L_t - Z\Big] \qquad (86)$$

Equating both expressions for T, making $P = \cos\tau' - a'\sin\tau'$, $Q = \sin\tau' + a'\cos\tau'$, and combining $L_s + L_{NAC}$ as L_{SN}, and $D_s + D_{NAC}$ as D_{SN} leads to:

$$(\cos\alpha_w - a'\sin\alpha_w)L_{SN} + (\sin\alpha_w + a'\cos\alpha_w)D_{SN}$$
$$+QNJ\cos(\tau'' + i_j) + PNJ\sin(\tau'' + i_j)$$
$$+Q(W\sin\gamma + D_R + D_f + D_t + D_{NAC}\cos\tau' + X)$$
$$-P(W\cos\gamma - L_R - L_f - L_t - L_{NAC}\cos\tau' - Z) = 0 \qquad (87)$$

Letting $L = \cos\alpha_w - a'\sin\alpha_w$, $M = \sin\alpha_w + a'\cos\alpha_w$, and rearranging for equilibrium, to wit:

$$L_{SN}L + D_{SN}M + QNJ\cos(\tau'' + i_j)$$
$$+Q(D_R + D_f + D_t + D_{NAC}\cos\tau'') + PNJ\sin(\tau'' + i_j)$$
$$+P(L_R + L_f + L_t + L_{NAC}\cos\tau'') = W(P\cos\gamma - Q\sin\gamma) \qquad (88)$$

Placing this equation in coefficient form, the ordinary lift and drag coefficients can be readily estimated:

$$\frac{1}{P\cos\gamma - Q\sin\gamma}\Big[(C_{L_s} + C_{L_{NAC}})q_{res}\, S L + C_{D_s}q_{res} S M$$
$$+QNJ''q'S\cos(\tau'' + i_j) + Q(C_{D_R}q S_R + C_{D_f}q S_f$$
$$+C_{D_t}\frac{q_t}{q}S_t\gamma) + QC_{D_{NAC}}q_{res}S_{NAC}\cos\tau''$$
$$+PNJ''q'S\sin(\tau'' + i_j) + PC_{L_{NAC}}q_{res}S_{NAC}\cos\tau''$$
$$+P(C_{L_R}S_R + C_{L_f}S_f)q + PC_{L_t}\frac{q_t}{q}\gamma S_t\Big] = W \qquad (89)$$

Dividing through by $q''S$ and calling the expression in the brackets X_B:

$$\frac{W}{q''S} = \frac{X_B}{(P\cos\gamma - Q\sin\gamma)q'S}$$

and recalling that from G-113-4: $q'' = \frac{q}{1 - T_C'}$,

or the dynamic pressure at which sustained equilibrium flight at a given weight and T_C' is attained.

Equation 89 contains three separate dynamic pressures which must be reduced to a common basis:

q - the free stream dynamic pressure;
q' - the theoretical dynamic pressure in a fully developed slipstream;
q_{res} - the actual resultant dynamic pressure at the particular point in the slipstream under consideration.

To determine the expressions for q_{res}, λ, α_R, and α_s, in the transition flight regime, reference is made to the next sketch:
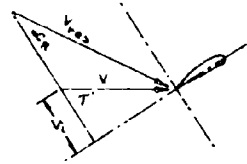
From momentum theory, at the rotor disc:

$$T = 2\rho\pi R^2(v v_i + v^2) \quad \text{where v is the induced velocity, or:}$$

$$v^2 + v v_i - \frac{T}{2\rho\pi R^2} = 0$$

$$v = \frac{-v_i}{2} \pm \frac{v_i}{2}\sqrt{1 + \frac{2T}{\rho\pi R^2 v_i^2}}$$

The total inflow velocity at the rotor disc is therefore:

$$V_{inflow} = -v_i - v_i\left[-\frac{1}{2} + \frac{1}{2}\sqrt{1 + \frac{2C_T}{\left(\frac{v}{\Omega R}\right)^2\cos^2\tau'}}\right]$$

At any point in the slipstream:

$$V_{inflow} = -v_i - 2K_i v_i\left[-\frac{1}{2} + \frac{1}{2}\sqrt{1 + \frac{2C_T}{\left(\frac{v}{\Omega R}\right)^2\cos^2\tau''}}\right] \qquad (90)$$

where $v_i = V\cos\tau'$ and K_i is the ratio of the actual slipstream velocity to the theoretical fully developed slipstream (G-113-4). Referring to the sketch,

$$V_{res}^2 = V^2\cos^2\tau'\left[1 + K_i\left\{-1 + \sqrt{1 + \frac{2C_T}{\left(\frac{v}{\Omega R}\right)^2\cos^2\tau'}}\right\}\right] + V^2\sin^2\tau'$$

165

which upon expansion leads to:

$$V_{res}^2 = V^2\left[1-2k_1\cos\mathcal{T}'(1-k_1)\left(\cos\mathcal{T}'-\sqrt{\cos^2\mathcal{T}'+\frac{2C_T}{\left(\frac{V}{\Omega R}\right)^2\cos^2\mathcal{T}'}}\right)\right.$$
$$\left.+k_1^2\frac{T_c''}{1-T_c''}\right]$$

Again from G-113-4: $C_T = \frac{1}{2}\left(\frac{V}{\Omega R}\right)^2\frac{T_c''}{1-T_c''}$

$$q_{res} = q\left[1-2k_1\cos\mathcal{T}'(1-k_1)\left(\cos\mathcal{T}'-\sqrt{\cos^2\mathcal{T}'+\frac{T_c''}{1-T_c''}}\right)\right.$$
$$\left.+k_1^2\frac{T_c''}{1-T_c''}\right] \tag{91}$$

Referring to equation 90:

$$V_{inflow} = -V\cos\mathcal{T}'\left[1+k_1\left(-1+\sqrt{1+\frac{2C_T}{\left(\frac{V}{\Omega R}\right)^2\cos^2\mathcal{T}'}}\right)\right]$$

$$V_{advance} = V\sin\mathcal{T}'$$

$$\tan\alpha_w = \frac{V_{advance}}{V_{inflow}}$$

$$= \frac{V\sin\mathcal{T}'}{V\cos\mathcal{T}'\left[1+k_1\left(-1+\sqrt{1+\frac{2C_T}{\left(\frac{V}{\Omega R}\right)^2\cos^2\mathcal{T}'}}\right)\right]}$$

$$\tan\alpha_w = \frac{\tan\mathcal{T}'}{1+k_1\left[-1+\sqrt{1+\frac{2C_T}{\left(\frac{V}{\Omega R}\right)^2\cos^2\mathcal{T}'}}\right]} \tag{92}$$

and the inflow ratio, λ, is:

$$\lambda = -\frac{V}{\Omega R}\cos\mathcal{T}'\left[1+k_1\left(-1+\sqrt{1+\frac{2C_T}{\left(\frac{V}{\Omega R}\right)^2\cos^2\mathcal{T}'}}\right)\right] \tag{93}$$

This is the same expression for λ that would be obtained from the equation given by Gessow and Myers (77), namely:

$$\lambda = \frac{-C_T/2}{\sqrt{\lambda^2+\mu^2}}-\frac{V}{\Omega R}\cos\mathcal{T}' \quad \text{assuming } \mu^2 \ll \lambda^2$$

From G-113-4 is also obtained the two additional expressions:

$$q_{res} = q\frac{\sin^2\mathcal{T}'}{\sin^2\alpha_w} \tag{94}$$

and:

$$q'' = \frac{q}{1-T_c''} \tag{95}$$

The component parts of equation 89 are now given in terms of the theoretical slipstream dynamic pressure q'':

$$L_s = NC_{L_s}q_{res}S_s$$
$$= N\left(\Delta C_{L_s}+C_{L_{\alpha_s}}\alpha_w\right)q''\frac{\sin^2\mathcal{T}'}{\sin^2\alpha_w}\left(1-T_c''\right)S_s$$

$$L_{NAC} = NC_{L_{NAC}}q_{res}S_s$$
$$= N\left(\Delta C_{L_N}+C_{L_{\alpha_N}}\alpha_w\right)q''\frac{\sin^2\mathcal{T}'}{\sin^2\alpha_w}\left(1-T_c''\right)S_s$$

$$C_{L_{sN}}'' = N\left[\Delta C_{L_s}+\Delta C_{L_N}+\alpha_w\left(C_{L_{\alpha_s}}+C_{L_{\alpha_N}}\right)\right.$$
$$\left.\frac{\sin^2\mathcal{T}'}{\sin^2\alpha_w}\left(1-T_c''\right)\frac{S_s}{S}\right]$$

Similarly:

$$C_{D_{sN}}'' = N\left(C_{D_{0_s}}+\frac{C_{L_s}^2}{\pi Re}+\frac{f_{NAC}}{S_{NAC}}\right)\frac{\sin^2\mathcal{T}'}{\sin^2\alpha_w}\left(1-T_c''\right)\frac{S_s}{S}$$

$$C_{L_N}'' = \left(\Delta C_{L_N}+C_{L_\alpha}\mathcal{T}''\right)\left(1-T_c''\right)\frac{S_R}{S}$$

$$C_{D_R}'' = \left(C_{D_{0_R}}+\frac{C_{L_R}^2}{\pi Re_R}\right)\left(1-T_c''\right)\frac{S_R}{S}$$

$$C_{L_f}'' = \left(\Delta C_{L_f}+C_{L_{\alpha_f}}\alpha_f\right)\left(1-T_c''\right)\frac{S_f}{S}$$

$$C_{D_f}'' = \left(C_{D_{0_f}}+\frac{C_{L_f}^2}{\pi Re_f}\right)\left(1-T_c''\right)\frac{S_f}{S}$$

$$C_{L_t} = C_{L_{t_\alpha}}\left(\alpha_f+\alpha_{v_t}-k_s\mathcal{T}''+\alpha_{t_s}\frac{\partial\delta e}{\partial\delta_{i_t}}\delta_{i_t}\right)$$

$$C_{L_t}'' = C_{L_t}\frac{q_t S_t}{q S}\left(1-T_c''\right)$$

$$C_{D_t}'' = \left(C_{D_{0_t}}+\frac{C_{L_t}^2}{\pi Re}\right)\frac{q_t S_t}{q S}\left(1-T_c''\right)$$
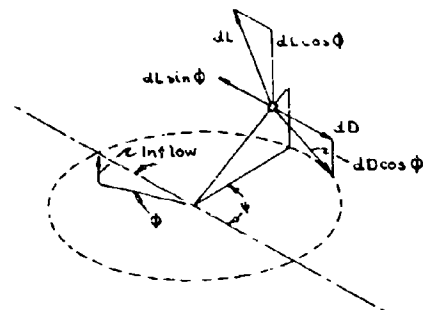
$$J = q''S\left(k_2 T_c''+k_3\right) \quad \therefore \quad J'' = \frac{k_2 T_c''+k_3}{S}$$

Because:

$$\sin\gamma = a_d, \quad \cos\gamma = \sqrt{1-a_x}$$

Inasmuch as $a' \approx \frac{C_H}{C_T}$, it is necessary to determine C_H, which is as follows:

166

The H-force is the average residual blade tangential force:

$$dH = (dD\cos\phi - dL\sin\psi)\sin\psi$$
$$- (dL\cos\phi + dL\sin\phi)\sin\beta\cos\psi \qquad (96)$$

The induced portion is that due to lift:

$$dH_i = -dL\sin\phi\sin\psi - dL\cos\phi\sin\beta\cos\psi$$

Lift is a function of α which is $\Theta + \phi$, ...

$$\Theta = \Theta_{.75} + T_w(x-.75) - \beta\tan\delta_3 - \alpha_d\delta_0 - \alpha_d\delta_1\sin\psi$$

and

$$\phi = \left[\frac{\lambda - (1-\xi)\dot{\beta}/\Omega(1-k) - \mu\beta(1-k)\cos\psi}{x + \mu\sin\psi}\right]$$
$$+ \alpha_d\delta_1\sin\psi(k) + \beta\tan\delta_3(k)$$

$$\alpha = \Theta + \phi$$
$$= \Theta + T_w(x-.75) - a_0\tan\delta_3 + (a_1\cos\psi + b_1\sin\psi)(1-k)\tan\delta_3$$
$$- \alpha_d\delta_0 - \alpha_d\delta_1(1-k)\sin\psi + \frac{\lambda}{x + \mu\sin\psi}$$
$$- \frac{(1-\xi)(\dot{\beta}/\Omega)(1-k)}{x + \mu\sin\psi} - \frac{\mu\beta(1-k)}{x + \mu\sin\psi}\cos\psi$$

Making small-angle assumptions, the total induced H-force is:

$$H_i = -\frac{b}{2\pi}\int_0^{2\pi}\int_e^R \frac{\rho c}{2}\,ac\left[\alpha U_T U_P\sin\psi + \alpha U_T^2\beta\cos\psi\right]d\psi\,dr \qquad (97)$$

Substituting the expressions for α, β, and remembering that $\phi \approx \dfrac{U_P}{U_T}$ and $U_T = \Omega R\left(x + \mu\sin\psi\right)$ where

$$\beta = a_0 - a_1\cos\psi - b_1\sin\psi :$$

$$H_i = \frac{b}{2\pi}\int_e^R\int_0^{2\pi}\frac{(\Omega R)^2 R\rho ac}{2}\left\{\left[\Theta_{.75} + T_w(x-.75) - a_0\tan\delta_3\right.\right.$$
$$+ a_1\tan\delta_3(1-k)\cos\psi + b_1\tan\delta_3(1-k)\sin\psi$$
$$- \alpha_d\delta_0 - \alpha_d\delta_1(1-k)\sin\psi + \frac{\lambda}{x + \mu\sin\psi}$$
$$- \frac{(x-\xi)(1-k)a_1\sin\psi}{x + \mu\sin\psi} + \frac{(x-\xi)(1-k)b_1\cos\psi}{x + \mu\sin\psi}$$
$$- \frac{\mu a_0\cos\psi}{x + \mu\sin\psi} + \frac{\mu(1-k)a_1\cos^2\psi}{x + \mu\sin\psi} \qquad (98)$$
$$\left. + \frac{\mu b_1(1-k)\sin\psi\cos\psi}{x + \mu\sin\psi}\right]\left[\lambda - (x-\xi)(1-k)a_1\sin\psi\right.$$
$$+ (x-\xi)(1-k)b_1\cos\psi - \mu a_0\cos\psi + \mu(1-k)a_1\cos^2\psi$$
$$\left.\left. + \mu b_1(1-k)\sin\psi\cos\psi\right]\left[x + \mu\sin\psi\right]\sin\psi\right.$$

(continued)

$$+ \left[\Theta_{.75} + T_w(x-.75) - a_0\tan\delta_3 + a_1\tan\delta_3(1-k)\cos\psi\right.$$
$$+ b_1\tan\delta_3(1-k)\sin\psi - \alpha_d\delta_0 - \alpha_d\delta_1(1-k)\sin\psi$$
$$+ \frac{\lambda}{x + \mu\sin\psi} - \frac{(x-\xi)(1-k)a_1\sin\psi}{x + \mu\sin\psi}$$
$$+ \frac{(x-\xi)(1-k)b_1\cos\psi}{x + \mu\sin\psi} - \frac{\mu a_0\cos\psi}{x + \mu\sin\psi} + \frac{\mu(1-k)a_1\cos^2\psi}{x + \mu\sin\psi}$$
$$\left. + \frac{\mu(1-k)b_1\sin\psi\cos\psi}{x + \mu\sin\psi}\right](x + \mu\sin\psi)^2$$
$$\left. (a_0 - a_1\cos\psi - b_1\sin\psi)\cos\psi\right\}d\psi\,dx$$

Performing the indicated multiplications, integrating, and non-dimensionalizing results in:

$$\frac{2C_{H_i}}{\sigma a} = \frac{1}{2}\left\{-\lambda\Theta\mu(1-\xi) - T_w\lambda\mu\left(\frac{1-\xi^2}{2}\right) + \frac{3}{4}T_w\lambda\mu(1-\xi)\right. \qquad (99)$$
$$+ \lambda a_0\mu\tan\delta_3(1-\xi) - \lambda b_1\tan\delta_3(1-k)\left(\frac{1-\xi^2}{2}\right)$$
$$+ \lambda\alpha_d\delta_0\mu(1-x_1) + \alpha_d\delta_1\lambda(1-k)\left(\frac{1-x_1^2}{2}\right)$$
$$+ \lambda a_1(1-k)\left(\frac{1}{2} - \xi + \frac{\xi^2}{2}\right) + \Theta_{.75}a_1(1-k)\left(\frac{1}{3} - \frac{\xi}{2} + \frac{\xi^3}{6}\right)$$
$$+ T_w a_1(1-k)\left(\frac{1}{4} - \frac{\xi}{3} + \frac{\xi^4}{12}\right) + \frac{3}{4}T_w(1-k)a_1\left(\frac{1}{3} - \frac{\xi}{2} + \frac{\xi^3}{6}\right)$$
$$- a_0a_1\tan\delta_3(1-k)\left(\frac{1}{3} - \frac{\xi}{2} + \frac{\xi^3}{6}\right) + \frac{3}{4}a_1b_1\tan\delta_3$$
$$(1-k)^2\mu\left(\frac{1}{2} - \xi + \frac{\xi^2}{2}\right) - \alpha_d\delta_0(1-k)a_1\left[\frac{1-x_1^3}{3} - \xi\frac{1-x_1^2}{2}\right]$$
$$+ \lambda a_1(1-k)\left(\frac{1}{2} - \xi + \frac{\xi^2}{2}\right) - \frac{3}{4}\alpha_d\delta_1(1-k)^2\mu a_1$$
$$\left[\frac{1-x_1^2}{2} - \xi(1-x_1)\right] + \frac{\mu a_1^2}{4}(1-k)^2\left(\frac{1}{2} - \xi + \frac{\xi^2}{2}\right)$$
$$- a_1b_1\frac{\mu}{4}\tan\delta_3(1-k)^2\left(\frac{1}{2} - \xi + \frac{\xi^2}{2}\right) - \frac{\mu b_1^2}{4}(1-k)^2$$
$$\left(\frac{1}{2} - \xi + \frac{\xi^2}{2}\right) + \frac{\mu a_0b_1}{4}(1-k)(1-\xi) + \frac{\mu^2}{4}a_0a_1$$
$$\tan\delta_3(1-k)(1-\xi) - \Theta_{.75}\frac{\mu^2}{4}a_1(1-\xi) - \frac{T_w}{8}\mu^2 a_1$$
$$(1-k)(1-\xi^2) + \frac{3}{16}T_w\mu^2 a_1(1-k)(1-\xi) + \frac{\mu^2}{4}a_0a_1$$
$$\tan\delta_3(1-k)(1-\xi) - \frac{\mu}{8}a_1b_1\tan\delta_3(1-k)^2(1-\xi^2)$$
$$+ \frac{\mu^2\alpha_d}{2}\alpha_d\delta_0(1-k)(1-x_1) + \frac{\mu}{4}a_1\alpha_d\delta_1(1-k)^2\left(\frac{1-x_1^2}{2}\right)$$
$$+ \frac{\mu}{4}a_1^2(1-k)^2\left(\frac{1}{2} - \xi + \frac{\xi^2}{2}\right) - \frac{\mu}{8}a_1b_1\tan\delta_3(1-k)^2$$
$$(1-\xi^2) - \frac{\mu b_1^2}{4}(1-k)^2\left(\frac{1}{2} - \xi + \frac{\xi^2}{2}\right) + \frac{\mu^2}{4}a_0b_1(1-k)$$
$$(1-\xi) + \Theta_{.75}a_1\left(\frac{1-\xi^3}{3}\right) + \Theta_{.75}\frac{a_1}{4}\mu^2(1-\xi) + T_w a_1$$
$$\left(\frac{1-\xi^4}{4}\right) - \frac{3}{4}T_w\left(\frac{1-\xi^3}{3}\right)a_1 + T_w a_1\frac{\mu^2}{4}\left(\frac{1-\xi^2}{2}\right)$$

(continued)

167

$$-\frac{3}{4}\,\lambda_w\,a_1\,\mu^2(1-\zeta)-a_o a_1\tan\delta_a\left(\frac{1-\zeta^3}{3}\right)-a_o a_1$$

$$\frac{\mu^2}{4}\tan\delta_a(1-\zeta)-a_o a_1\tan\delta_a(1-k)\left(\frac{1-\zeta^2}{3}\right)+a_1 b_1$$

$$\mu\tan\delta_a(1-k)\left(\frac{1-\zeta^2}{2}\right)-a_o a_1\frac{\mu^2}{4}\tan\delta_a(1-k)(1-\zeta)$$

$$-\alpha_d\,\delta_a\,a_1\left(\frac{1-\lambda^2}{3}\right)-\alpha_d\,\delta_a\,a_1\frac{\mu^2}{4}(1-\lambda_1)-\alpha_d\,\delta_1\frac{\mu}{2}$$

$$a_1(1-k)\left(\frac{1-\lambda^2}{2}\right)+\lambda a_1\left(\frac{1-\zeta^2}{2}\right)-\frac{\mu a_1^2}{4}(1-k)$$

$$\left(\frac{1}{2}-\zeta+\frac{\zeta^2}{2}\right)-a_o b_1(1-k)\left(\frac{1}{3}-\frac{\zeta}{2}+\frac{\zeta^3}{6}\right)+\frac{\mu}{4}b_1^2$$

$$(1-k)\left(\frac{1}{3}-\frac{\zeta}{2}+\frac{\zeta^3}{6}\right)-a_o b_1\frac{\mu^2}{4}(1-k)\left(\frac{3}{2}-2\zeta+\frac{\zeta^2}{2}\right)$$

$$+\mu a_1^2\left(\frac{1-\zeta^2}{2}\right)-a_o b_1\frac{\mu^2}{4}(1-\zeta)+\frac{3}{4}\mu a_1^2(1-k)$$

$$\left(\frac{1-\zeta^2}{2}\right)+\frac{\mu b_1^2}{4}(1-k)\left(\frac{1-\zeta^2}{2}\right)$$

Collecting all the terms, and eliminating all quadruple and triple products of small angles results in:

$$\frac{2C_{M_L}}{\sigma a}=\frac{1}{2}\left\{\frac{2C_T}{\sigma a}\,a_1+(\theta-a_o\tan\delta_a)\left(\frac{1}{3}-\frac{\zeta}{2}+\frac{\zeta^4}{10}\right)(1-k)\,a_1\right.$$

$$-\alpha_d\,\delta_a(1-k)\left[\left(\frac{1}{3}-\frac{\lambda^2}{3}\right)-\zeta\left(\frac{1}{2}-\frac{\lambda^2}{2}\right)\right]a_1$$

$$-(\theta-a_o\tan\delta_a)(1-\zeta)\lambda\mu+\alpha_d\,\delta_a(1-\lambda_1)\lambda\mu$$

$$-a_o\tan\delta_a(1-k)\left(\frac{1-\zeta^3}{3}\right)a_1-\frac{a_o b_1(1-k)}{3}$$

$$-\lambda b_1\tan\delta_a\left(\frac{1-\zeta^2}{2}\right)(1-k)+\frac{T_w}{2}\mu\lambda\left(\frac{1}{2}-\frac{3\zeta}{2}+\zeta^2\right)$$ (100)

$$+\alpha_d\,\delta_1\tan\delta_a\left(\frac{1-\zeta^2}{2}\right)(1-k)+\frac{T_w}{2}\mu\lambda\left(\frac{1}{2}-\frac{3\zeta}{2}+\zeta^2\right)$$

$$\left.+\lambda(1-k)(1-2\zeta+\zeta^2)\,a_1\right\}$$

This is the expression used to determine the induced portion of the H-force to get the a' angle in the trim program. It has been reduced to, and checked with, the simple expression given by Gessow and Myers (79). It is emphasized that the flap terms have a significant effect on the magnitude of the resultant rotor H-force.

The profile portion due to blade drag is small. The second drag term in equation 90 was neglected because it involved the product of two small quantities. Then, for a constant blade profile drag coefficient:

$$H_o=\frac{c\,b_c}{2}\,\mu\left(\Omega R\right)^2 R\,C_{d_o}$$

Non-dimensionalizing:

$$\frac{2H_o}{\sigma a}=\frac{\mu}{2a}\,C_{d_o}$$ (101)

This is added to equation 100 for the total H-force.

The third trim equation, pitching moment, is now developed.

From the diagram the pitching moment is:

$$M=\underset{①}{NTz_h}+\underset{②}{Na'T}+\underset{③}{NM_H}+\underset{④}{M_{w_a}}+\underset{⑤}{M_{w_R}}+\underset{⑥}{NM_{NAC}}$$

$$+\underset{⑦}{M_f}+\underset{⑧}{M_{ta,l}}+\underset{⑨}{NM_{jet}}-\underset{⑩}{M_{fi}}$$ (104)

The several items identified by number are defined as:

Thrust Moment

① & ② $\quad NT(z_u+a'z_h)$

Hub Moment

③ $\quad M_H=\frac{Nb}{2}\,\Omega^2 I_1\,\gamma\left[\frac{T}{4}\,a_1+\frac{\zeta}{2}\left\{\mu a_o D-a_1\tan\delta_a(1-k)\left(N+\frac{\mu^2}{4}B\right)\right.\right.$

$$\left.\left.+\alpha_d\,\delta_a(1-k)\left(E+\frac{\mu^2}{4}F\right)\right\}\right]$$

168
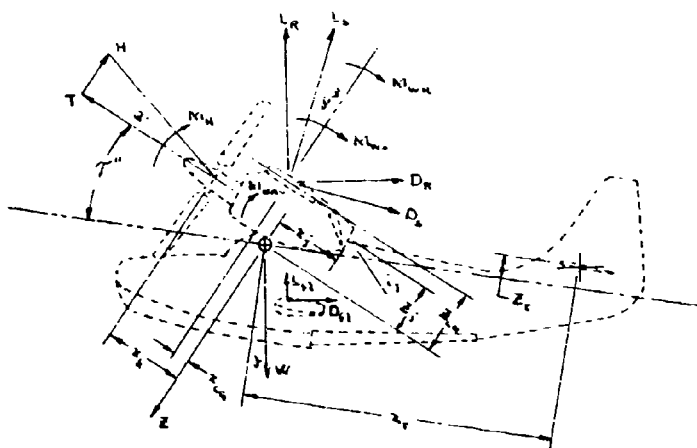
Wing in Slipstream

④ $M_{ws} = \left(\Delta C_{m_{o_g}} + C_{m_{a_c}}\right) \bar{q}''(1 - T_c')\frac{\sin^2 T}{\sin^2 \alpha_w} \bar{c}_s S_s$

$+ L_s\left(x_{cs}\cos\alpha_w - z_{cs}\sin\alpha_w\right) + D_s\left(z_{cs}\cos\alpha_w + x_{cs}\sin\alpha_w\right)$

Wing out of Slipstream

⑤ $M_{wR} = \left(\Delta C_{m_{o_R}} + C_{m_{a_R}}\right)\bar{q}''(1 - T_c')\bar{c}_R S_R + L_R\left(x_{cs}\cos T'\right.$

$\left. - z_{cs}\sin T'\right) + D_R\left(z_{cs}\cos T' + x_{cs}\sin T'\right)$

Nacelles

⑥ $M_{nac} = N\bar{c}_{nac} f_{nac}\bar{q}''(1 - T_c')\frac{\sin^2 T}{\sin^2 \alpha_w}$

Fuselage

⑦ $M_f = \left(C_{m_{o_f}} + C_{m_{a_f}}\alpha_f\right)\bar{q}''(1 - T_c')S_f$

Tail

⑧ $M_t = L_t x_t$

$= C_{L_{a_t}}\left(\alpha_f + \alpha_{o_t} - \delta_{T} \tau' + \alpha_{\delta_e}\frac{\partial\epsilon}{\partial\delta_e}\delta_{i_t}\right)x_t$

Engine Exhaust

⑨ $NM_j = NJ\left(z_j\cos i_j + x_j\sin i_j\right)$

Tip Floats

⑩ $M_{float} = Nf_{float}\lambda_{fl}\bar{q}''(1 - T_c')$

$C_m'' = \frac{1}{\bar{q}''S\bar{c}}\sum\left[① + ② + ③ + ④ + ⑤ + ⑥ + ⑦ + ⑧ + ⑨ + ⑩\right]$

The various moment arms that change with wing tilt are used in tabular form by the program. A center section lift curve slope $C_{L_{a_s}}$ is also used as a function

of wing tilt. In this way, center section stall is accounted for.

CONTROL TO TRIM

A longitudinal control input δ_{i_L} is defined as follows:

$\delta_1 = \delta_{i_L}\cos\psi_o$

$\delta_2 = \delta_{i_L}\sin\psi_o$ are ψ_o is the angle at which the approach

is indexed, and where $\delta = \delta_o + \delta_1\sin\psi + \delta_2\cos\psi$ is the

blade flap input. The flap input is related to the corresponding blade flapping through the following flap control equations. The cyclic sensitivities, or amount of flapping produced per degree of flap deflection, are derived by investigating the conditions leading to a dynamic equilibrium of moments about the flapping hinge. First, the steady thrust equation must be determined:

$$\frac{dT}{dx} = \frac{\rho}{2}caRU_T^2\alpha \tag{103}$$

where α, as given in the subsequent derivation, is

$\alpha = \Theta_{78} + T_w(x - .76) - \left(a_o - a_1\cos\psi - b_1\sin\psi\right)\tan\delta_o$

$- \omega_d\left(\delta_o + \delta_1\sin\psi + \delta_2\cos\psi\right) + \frac{\lambda}{x + \mu\sin\psi}$

$- \frac{(x - \delta)(1-k)}{x + \mu\sin\psi}\left(a_1\sin\psi - b_1\cos\psi\right) - \frac{\mu a_1\cos\psi}{x + \mu\sin\psi}$

$+ \frac{\mu(1-k)a_1\cos^2\psi}{x + \mu\sin\psi} + \frac{\mu(1-k)b_1\sin\psi\cos\psi}{x + \mu\sin\psi}$

$+ k\omega_d\left(\delta_1\sin\psi + \delta_2\cos\psi\right) + k\tan\delta_o\left(-a_1\cos\psi - b_1\sin\psi\right)$

$+ \frac{\gamma z_p}{\Omega R(x + \mu\sin\psi)} + \frac{\gamma\rho(1-k)(a_o - a_1\cos\psi - b_1\sin\psi)}{\Omega R(x + \mu\sin\psi)}$

The last two terms account for pitching velocity, and

$U_T = \Omega R\left(x + \mu\sin\psi\right)$

$U_T^2 = (\Omega R)^2\left(x^2 + 2x\mu\sin\psi + \mu^2\sin^2\psi\right)$

Substituting the expressions for U_T^2 and α into equation 103 and integrating azimuthally, remembering that the average thrust around the azimuth may be expressed as:

$T = \frac{1}{2\pi}\int_0^{2\pi}\int_{\delta or x_1}^{1.0} dT\,d\psi$

$= \frac{\rho}{2}c(\Omega R)^2 Ra\left\{\int_{\delta or x_1}^{1.0}\left[\Theta_{78}x^2 + \frac{\Theta_{78}}{2}\mu^2 + T_w x^3\right.\right.$

$+ T_w\frac{x\mu^2}{2} - \frac{3}{4}T_w x^2 - \frac{3}{8}T_w\mu^2 - a_o\tan\delta_o x^2$

$- \frac{x_o}{2}\tan\delta_o\mu^2 - \frac{\partial\alpha}{\partial\delta}\delta_o x^2 - \frac{\partial\alpha}{\partial\delta}\delta_o\frac{\mu^2}{2}$

$- \frac{\partial\alpha}{\partial\delta}\delta_1(1-k)x\mu + b_1\tan\delta_o(1-k)x\mu + \lambda x$

$- a_1\frac{(1-k)}{2}\mu(x - \delta) + \frac{\mu a_1}{2}(1-k)\lambda + \frac{\gamma z_p}{\Omega R}x$

$+ \frac{\gamma x_p}{\Omega R}a_o(1-k)x - \frac{\gamma x_p b_1}{2\Omega R}(1-k)\mu^2\right]\right\}$ (104)

Integrating with respect to nondimensional radius, and reducing to coefficient form, yields:

$\frac{2C_T}{\sigma a} = \Theta_{78}\left[\left(\frac{1-\delta^3}{3}\right) + \mu^2\left(\frac{1-\delta}{2}\right)\right] + \frac{T_w}{4}\left[\left(\delta^2 - \delta^4\right)\right.$

$\left. - \mu^2\left(\frac{1}{2} - \frac{3\delta}{2} + \delta^2\right)\right] + \lambda_o\left[\frac{\gamma x_p}{\Omega R}(1-k)\left(\frac{1-\delta^2}{2}\right)\right.$

$- \tan\delta_o\left\{\frac{1-\delta^3}{3} + \mu^2\frac{1-\delta}{2}\right\}\right] - \frac{\partial\alpha}{\partial\delta}\delta_o\left[\frac{1-x_1^3}{3}\right.$

$\left. + \mu^2\frac{1-x_1}{2}\right] - \frac{\partial\alpha}{\partial\delta}\delta_1(1-k)\mu\frac{1-x^2}{2} - \lambda\frac{1-\delta^2}{2}$ (105)

$+ \frac{\gamma z_p}{\Omega R}\left(\frac{1-\delta^2}{2}\right) + a_o\left[(1-k)\left\{\mu\frac{1-\delta^2}{4} - \frac{\mu}{2}\left(\frac{1}{2} - \delta + \frac{\delta^2}{2}\right)\right\}\right]$

$+ b_1\left[\tan\delta_o(1-k)\mu\frac{1-\delta^2}{2} - \frac{\gamma x_p}{2\Omega R}\mu^2(1-\delta)\right]$

The aerodynamic moment about the blade flapping hinge may be expressed as:

$$\frac{dM}{dx} = R(x-\xi)\frac{dT}{dx}$$

$$= \frac{e}{2}c(\Omega R)^2 R^2 a\Big[\Theta_{75}(x^2+2x\mu\sin\psi+\mu^2\sin^2\psi)$$

$$(x-\xi)+\zeta_c(x^3+2x^2\mu\sin\psi+x\mu^2\sin^2\psi)(x-\xi)$$

$$-\frac{3}{4}\zeta_w(x^2+2x\mu\sin\psi+\mu^2\sin^2\psi)(x-\xi)$$

$$-a_c\tan\delta_a(x^2+2x\mu\sin\psi+\mu^2\sin^2\psi)(x-\xi)$$

$$-\frac{\partial c}{\partial J}\delta_o(x^2+2x\mu\sin\psi+x\mu^2\sin^2\psi)(x-\xi)$$

$$-\frac{\partial c}{\partial J}\delta_1(1-k)(x^2\sin\psi+2x\mu\sin^2\psi+x\mu^2\sin^3\psi)(x-\xi)$$

$$-\frac{\partial c}{\partial J}\delta_2(1-k)(x^2\cos\psi+x\mu^2\sin^2\psi\cos\psi)(x-\xi) \qquad (106)$$

$$+a_1\tan\delta_a(1-k)(x^2\cos\psi+x\mu^2\sin^2\psi\cos\psi)(x-\xi)$$

$$+b_1\tan\delta_a(1-k)(x^2\sin\psi+2x\mu\sin^2\psi+x\mu^2\sin^3\psi)(x-\xi)$$

$$+\lambda(x+\mu\sin\psi)(x-\xi)-a_1(x-\xi)^2(1-k)(x\sin\psi$$

$$+\mu\sin^2\psi)+b_1(x-\xi)^2(1-k)(x\cos\psi)-\mu a_o(1-k)$$

$$(x-\xi)x\cos\psi+\mu a_o(1-k)(x-\xi)(x\cos^2\psi$$

$$+\mu\sin\psi\cos^2\psi)+\mu b_o(1-k)(x-\xi)(\mu\sin^2\psi\cos\psi)$$

$$+\frac{\gamma x_b}{\Omega R}(x-\xi)(\lambda+\mu\sin\psi)+\frac{\gamma x_b}{\Omega R}a_o(1-k)(x-\xi)$$

$$(x+\mu\sin\psi)-\frac{\gamma x_1}{\Omega R}a_o(1-k)(x-\xi)x\cos\psi$$

$$-\frac{\gamma x_1}{\Omega R}b_1(1-k)(x-\xi)(x\sin\psi+\mu\sin^2\psi)\Big]$$

The steady moment components can be extracted, and integrating with respect to non-dimensional radius yields:

$$\frac{2M}{\gamma I}=\Omega^2\Big\langle\Theta_{75}\Big[\Big(\frac{1}{4}-\frac{\xi}{3}+\frac{\xi^4}{12}\Big)+\frac{\mu^2}{2}\Big(\frac{1}{2}-\xi+\frac{\xi^2}{2}\Big)\Big]$$

$$-a_o\Big[\tan\delta_a\Big\{\Big(\frac{1}{4}-\frac{\xi}{3}+\frac{\xi^4}{12}\Big)+\frac{\mu^2}{2}\Big(\frac{1}{2}-\xi+\frac{\xi^2}{2}\Big)\Big\}$$

$$-\frac{\gamma x_p}{\Omega R}(1-k)\Big(\frac{1}{3}-\frac{\xi}{2}+\frac{\xi^3}{6}\Big)\Big]+a_1\Big[\frac{\mu}{2}(1-k)$$

$$\Big(\frac{1}{3}-\frac{\xi}{2}+\frac{\xi^3}{6}\Big)-(1-k)\frac{\mu}{2}\Big\{\frac{1-\xi^3}{3}-\xi(1-\xi^2)\Big\}\Big]$$

$$+b_1\Big[(1-k)\Big(\frac{1}{3}-\frac{\xi}{2}+\frac{\xi^3}{6}\Big)\tan\delta_a\mu-\frac{\gamma x_b}{\Omega R}\frac{\mu}{2}\Big] \qquad (107)$$

$$\Big(\frac{1}{2}-\xi+\frac{\xi^2}{2}\Big)\Big]-\frac{\partial c}{\partial J}\delta_o\Big[\Big\{\frac{1-\xi^4}{4}-\xi\frac{1-\xi^3}{3}\Big\}$$

$$+\frac{\mu^2}{2}\Big\{\frac{1-\xi^2}{2}-\xi(1-\xi)\Big\}\Big]-\frac{\partial c}{\partial J}\delta_1(1-k)\mu$$

$$\Big[\frac{1-\xi^3}{3}-\xi\frac{1-\xi^2}{2}\Big]+\lambda\Big(\frac{1}{3}-\frac{\xi}{2}+\frac{\xi^3}{6}\Big)$$

$$+\frac{\gamma x_b}{\Omega R}\Big(\frac{1}{3}-\frac{\xi}{2}+\frac{\xi^3}{6}\Big)\Big\rangle$$

$$=\frac{2}{3}a_o(1+\xi)$$

From equation 106 the sine ψ components of moment can be extracted:

$$\Big(\frac{dM}{d\psi}\Big)_{\sin}=\frac{e}{2}b(\Omega R)^2 R^2 a\Big[2\Theta_{75}\mu x(x-\xi)+2T_c\mu x^2$$

$$(x-\xi)-\frac{3}{2}T_w\mu x(x-\xi)-2\gamma_o t\cdot\delta_3\mu x$$

$$(x-\xi)-\frac{2\partial c}{\partial J}\delta_o\mu x(x-\xi)-\frac{\partial c}{\partial J}\delta_1(1-k)$$

$$x^2(x-\xi)-\frac{3\partial c}{4\partial J}\delta_1(1-k)\mu^2(x-\xi)$$

$$+b_1\tan\delta_a(1-k)x^2(x-\xi)+\frac{3x_1}{4}\tan\delta_a(1-k)$$

$$\mu^2(x-\xi)+\lambda\mu(x-\xi)-a_1(1-k)x(x-\xi)^2$$

$$+\frac{\mu a_1}{4}(1-k)\mu(x-\xi)+\frac{\gamma x_b}{\Omega R}a_o(1-k)(x-\xi)\mu$$

$$-\frac{\gamma x_1}{\Omega R}b_1(1-k)x(x-\xi)\Big] \qquad (108)$$

Integrating the previous expression with respect to non-dimensional radius yields the sine component:

$$\frac{2M}{\gamma I}=\Omega^2\Big\langle 2\Theta_{75}\mu\Big(\frac{1}{3}-\frac{\xi}{2}+\frac{\xi^3}{6}\Big)+a_o\Big\{-\Big[\frac{\gamma x_b}{\Omega R}(1-\xi)$$

$$\Big(\frac{1}{2}-\xi+\frac{\xi^2}{2}\Big)-2\tan\delta_a\Big(\frac{1}{3}-\frac{\xi}{2}+\frac{\xi^3}{6}\Big)\Big]\Big\}$$

$$+a_1\Big\{\frac{\mu}{4}\mu(1-k)\Big(\frac{1}{2}-\xi+\frac{\xi^2}{2}\Big)-(1-k)\Big(\frac{1}{4}-\frac{2\xi}{3} \qquad (109)$$

$$+\frac{\xi^2}{2}-\frac{\xi^4}{12}\Big)\Big\}+b_1\Big\{\tan\delta_a(1-k)\Big[\Big(\frac{1}{4}-\frac{\xi}{3}+\frac{\xi^4}{12}\Big)$$

$$+\frac{3\mu^2}{4}\Big(\frac{1}{2}-\xi+\frac{\xi^2}{2}\Big)\Big]-\frac{\gamma x_b}{\Omega R}(1-k)\Big(\frac{1}{3}-\frac{\xi}{2}+\frac{\xi^3}{6}\Big)\Big\}$$

$$-\frac{2\partial c}{\partial J}\delta_o\mu\Big\{\frac{1-\xi^3}{3}-\xi\frac{1-\xi^2}{2}\Big\}-\frac{\partial c}{\partial J}\delta_1\Big\{(1-k)$$

$$\Big[\frac{1-\xi^4}{4}-\xi\Big(\frac{1-\xi^3}{3}\Big)+\frac{3\mu^2}{4}\Big(\frac{1-\xi^2}{2}+\xi(1-x_1)\Big)\Big]\Big\}$$

$$+\frac{T_w\mu\xi}{12}+\lambda\mu\Big(\frac{1}{2}-\xi+\frac{\xi^2}{2}\Big)+\frac{\gamma x_b}{\Omega R}\mu\Big(\frac{1}{2}-\xi+\frac{\xi^2}{2}\Big)\Big\rangle$$

The cosine ψ components of moment can be extracted from equation 106:

$$\Big(\frac{dM}{d\psi}\Big)_{\cos}=\frac{e}{2}c(\Omega R)^2 R^2 a\Big[-\frac{\partial c}{\partial J}\delta_2(1-k)x^2(x-\xi)$$

$$-\frac{\partial c}{4\partial J}\delta_2(1-k)\mu^2(x-\xi)+a_1\tan\delta_a(1-k)x^2$$

$$(x-\xi)+a_1\frac{\tan\delta_a}{4}(1-k)\mu^2(x-\xi)+b_1x(x-\xi)^2$$

$$(1-k)-\mu a_o(1-k)x(x-\xi)+\frac{\mu^2 b_1}{4}(1-k)(x-\xi) \qquad (110)$$

$$-\frac{\gamma x_1}{\Omega R}b_1(1-k)x(x-\xi)\Big]$$

Integrating the previous expression with respect to non-dimensional radius yields:

$$\frac{2M}{\lambda I} = \Omega^2 \left\langle -\mu a_0 (1-k)\left(\frac{1}{3} - \frac{S}{2} + \frac{S^2}{6}\right) + a_1 (1-k)\left\{ \tan\delta_b \right.\right.$$

$$\left[\left(\frac{1}{4} - \frac{S}{3} + \frac{S^2}{12}\right) + \frac{\mu^2}{4}\left(\frac{1}{2} - S + \frac{S^2}{2}\right)\right] - \frac{q\lambda_h}{\Omega R}$$

$$\left(\frac{1}{3} - \frac{S}{2} + \frac{S^2}{6}\right) + b_1 \left\{(1-k)\left(\frac{1}{4} - \frac{2S}{3} + \frac{S^2}{2} - \frac{S^4}{12}\right)\right.$$ (111)

$$\left. + \frac{\mu^2}{4}(1-k)\mu\left(\frac{1}{2} - S + \frac{S^2}{2}\right)\right\} - \frac{\partial\alpha}{\partial J} \dot{a}_2 (1-k)$$

$$\left.\left\{\left[\frac{1-x_1^4}{4} - S\frac{1-x_1^3}{3}\right] + \frac{\mu^2}{4}\left[\frac{1-x_1^2}{2} - S(1-x_1)\right]\right\}\right\rangle$$

The inertia moment about the flapping hinge may be expressed by:

$$\frac{2M_I}{\lambda I \Omega^2} = \frac{2}{\gamma}\left[a_0(1+S) - a_1\left(S - \frac{I_{\gamma a}\tan\delta_b}{I_1}\right)\cos\psi \right.$$

$$\left. - b_1\left(S - \frac{I_{\gamma a}\tan\delta_b}{I_1}\right)\sin\psi\right]$$ (112)

Because of the pitching velocity, a Coriolis acceleration is experienced, causing an extra inertia force that must be included in the moment about the blade flapping hinge. Thus:

$$\Delta M_i = 2q\Omega I(1+S)\sin\psi$$

or:

$$\frac{\Delta 2M_i}{I\Omega^2\gamma} = \frac{4q}{\gamma\Omega}(1+S)\sin\psi$$

Equating the aerodynamic and inertia moments about the flapping hinge, and incorporating the following redefinitions of the offset constants:

$A = \left(\frac{1-S^3}{3}\right)$ $H = \frac{1-x_1^4}{4}$

$B = (1-S)$ $J = \frac{1}{4} - \frac{S}{3}$

$C = -\frac{1}{4} + \frac{3}{4}S - \frac{S^2}{2}$ $L = \frac{1}{2} - S + \frac{S^2}{2}$

$D = \frac{1-S^2}{2}$ $M = -\frac{1}{24} + \frac{S}{4} - \frac{3S^3}{6}$

$E = \frac{1-x_1^3}{3}$ $P = \frac{1}{4} - \frac{2S}{3} + \frac{S^2}{2}$

$F = 1 - x_1$ $N = \frac{1}{3} - \frac{S}{2} + \frac{S^3}{6}$

$G = \frac{1-x_1^2}{2}$ $Q = \frac{S}{2} - S^2 + \frac{S^3}{2}$

yields the sine component:

$$\frac{4q}{I\Omega}(1+S) - b_1\left(S - \frac{I_{\gamma a}\tan\delta_b}{I_1}\right)\frac{2}{\gamma} = 2\Theta\mu N + a_0\left\{\mu \right.$$

$$\left[\frac{q\lambda_h}{\Omega R}(1-k)L - 2\tan\delta_b N\right]\right\} + a_1\left\{\frac{\mu^2}{4}(1-k)L - (1-k)P\right\}$$

$$+ b_1\left\{\tan\delta_b(1-k)\left[J + \frac{3\mu^2}{4}L\right] - \frac{q\lambda_h}{\Omega R}(1-k)N\right\}$$ (113)

$$- \frac{\partial\alpha}{\partial J} \dot{a}_1\left\{(1-k)\left[(H - SE) + \frac{3\mu^2}{4}(G - SF)\right]\right\} + \frac{I_{\gamma a}\mu}{12}S$$

$$+ \lambda\mu L + \frac{q\lambda_h}{\Omega R}\mu L - \frac{2\partial\alpha}{\partial J}\dot{\zeta}_2\mu(E - Su)$$

and the cosine component, assuming $\dot{a}_1 = 0$:

$$-a_1\left(S - \frac{I_{\gamma a}\tan\delta_b}{I_1}\right)\frac{2}{\gamma} = -\mu a_0(1-k)N + a_1(1-k)\left\{\tan\delta_b \right.$$

$$\left[J + \frac{\mu^2}{4}L\right]\right\} - \frac{q\lambda_h}{\Omega R}N + b_1\left\{(1-k)P + \frac{\mu^2}{4}(1-k)L\right\}$$

$$- \frac{\partial\alpha}{\partial J}\dot{\zeta}_2(1-k)\left\{(H - SE) + \frac{\mu^2}{4}(G - SF)\right\} + a_1\left\{\frac{2}{\gamma}\right.$$

$$\left(\frac{I_{\gamma a}\tan\delta_b}{I_1}\right) + \tan\delta_b(1-k)\left[J + \frac{\mu^2}{4}L\right]\right\} = \mu a_0(1-k)N$$ (114)

$$+ \frac{q\lambda_h}{\Omega R}N - b_1\left\{(1-k)P + \frac{\mu^2}{4}(1-k)L\right\} + \frac{\partial\alpha}{\partial J}\dot{\zeta}_2(1-k)$$

$$\left\{(H - SE) + \frac{\mu^2}{4}(G - SF)\right\}$$

The foregoing control equations are evaluated by a matrix inversion procedure as an integral part of the trim program. They are also separately evaluated for arbitrary values of μ, λ, and C_T. Some of the results are presented in Figure 41.

In summary, the whole trimming procedure can be outlined as:

For a particular C_T, an initial estimate of γ' is used, together with initial values of q'. The dynamic pressure (q) is calculated for the given weight, or required C_T, from the force equilibrium equations. Then, C_T, μ, λ, and k are calculated, as well as C_H from the C_H equation. The control equations are entered, and a'_{1_L} and a' are determined. The angle γ' is adjusted by the a', and this loop repeated until Δa is within tolerance. The moment equation is then used with the estimated a_1, and the whole process is repeated with the new a_1 until C_M is either zero or the specified value.
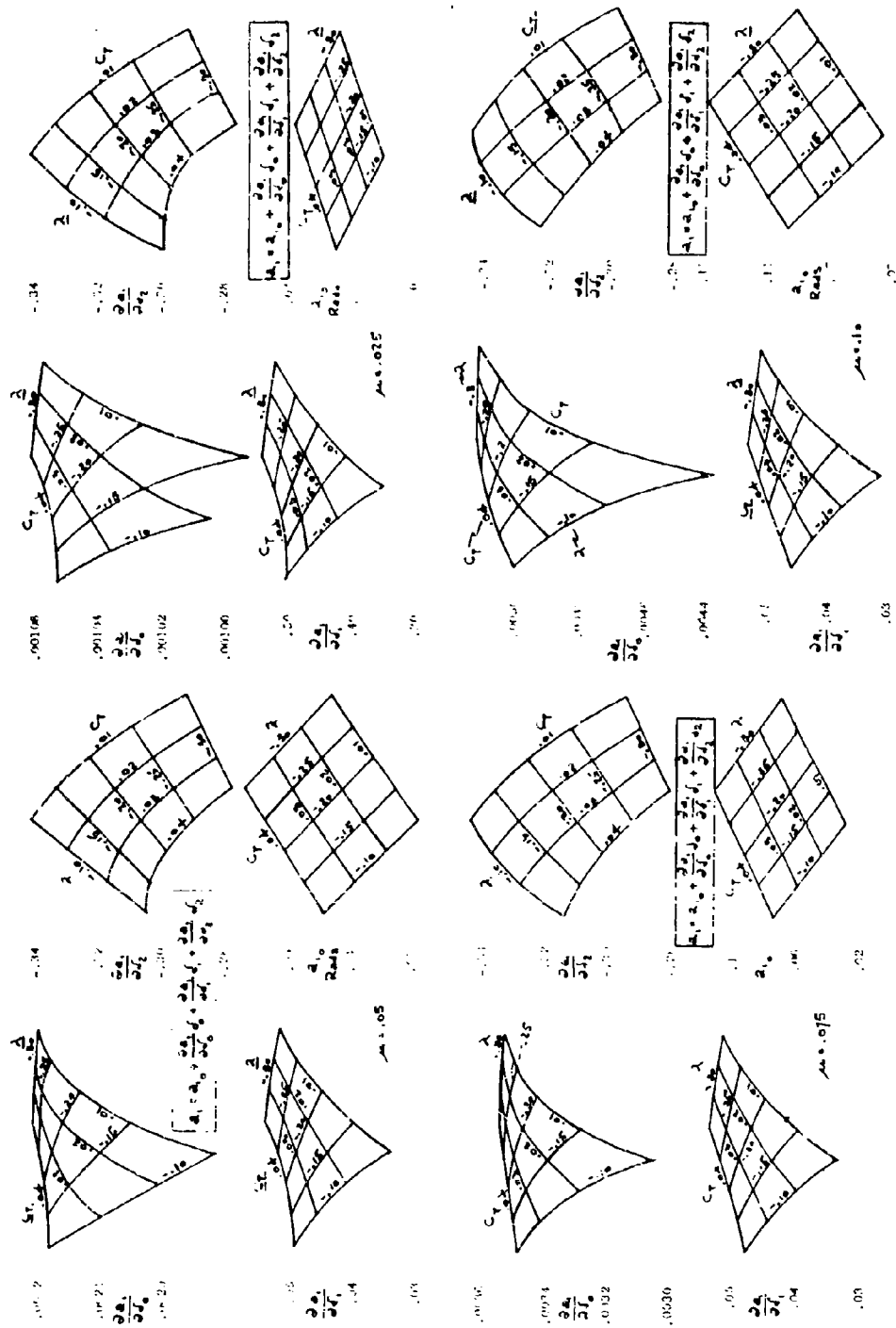
Figure 88
Rotor Control Sensitivity

172

APPENDIX E
K-16B STABILITY AND CONTROL

To assure satisfactory handling qualities, pilots' opinions that are statistically significant and amenable to design must be correlated in terms of basic dynamic characteristics of the aircraft. One such item for hovering flight, proposed in 1956 in KAC Report G-90 (1), is angular acceleration. This appears to be a reasonable criterion because angular accelerations of the aircraft produce proportional translational accelerations at the pilot's seat - and translational acceleration is one of the important items of sensory information used by the pilot in flight. This proposal was suggested by the results of helicopter flight testing conducted by the NACA (TN 2459, 1952)(64), and reinforced by the Bureau of Naval Weapons (A.D.Crim, 1956)(65).

Angular acceleration is proportional to the ratio of control moment-of-inertia. It was shown in KAC Report G-90 that for geometrically similar aircraft, moment of inertia is proportional to the square of the gross weight, and control moment proportional to the gross weight to the 3/2 power. It can be deduced that angular acceleration is proportional to the ratio of control moment to the moment of inertia, or the reciprocal of the square root of gross weight. The results of this analysis (ibid) indicate that for geometrically similar aircraft the angular acceleration is proportional to the reciprocal of the square root of the gross weight, and that the accelerations felt at the pilot's seat remain constant regardless of gross weight because, also, the distance to the pilot's seat is proportional to the square of the gross weight. This demonstrates that angular acceleration is one good universal parameter for control comparison of geometrically similar aircraft.

Of course, the initial accelerations produced by control inputs are not the only criteria determining good handling qualities of a hovering and low-speed aircraft. The basic damping characteristics of the configuration itself enters into the determination of pilot opinion. Salmirs and Tapscott have amply demonstrated this (NACA TN D-58)(66). They presented boundaries for acceptable handling qualities in terms of initial angular acceleration per inch of stick deflection versus the angular velocity of damping derivatives about the three axes. These boundaries were obtained using a variable stability H-5 helicopter, and were extended by Tapscott to helicopters of greater weight (IAS Paper 60-51)(67).

However, VTOL aircraft, having wings and engines and nacelles outboard of the centerline, are geometrically quite dissimilar to a helicopter like the H-5. The analysis of KAC Report G-90 showed that moments of inertia are proportional to the square of the gross weights only for geometrically similar aircraft. This same conclusion is also implied by A'Harrah and Kwiatkowski (IAS Paper 61-62) (68) inasmuch as dissimilar aircraft will have different values of the speed derivative. To apply the boundaries obtained from the variable-stability helicopter to VTOL aircraft it may be more nearly correct to alter the boundaries as follows:

$$\frac{M}{I_V} = \frac{M}{I_H} \frac{\left(\frac{W_V}{W_H}\right)^{3/2}}{\frac{I_V}{I_H}}$$

where the "V" refers to the VTOL and the "H" to the helicopter.

This was done for the K-16B and the results are shown in Figure 89. This figure is a reproduction of the criteria charts in Tapscott's IAS Paper (67).

The boundaries changed considerably except for the case where the ratio of gross weight to moment of inertia was nearly the same in both cases - in pitch. Referring to the rolling mode of Figure 89, the K-16B exceeds the control sensitivity required for acceptable rolling control for an acceptable natural damping derivative. (In the K-16B this can be readily investigated because rotor control sensitivity can be varied in flight and, with stability augmentation, the damping derivative can be altered. The same comment applies to the other two modes). According to Tapscott's criteria, the natural

characteristics in yaw are unacceptable (Figure 89).

Initial Acceleration per Inch of Stick, Rad sec
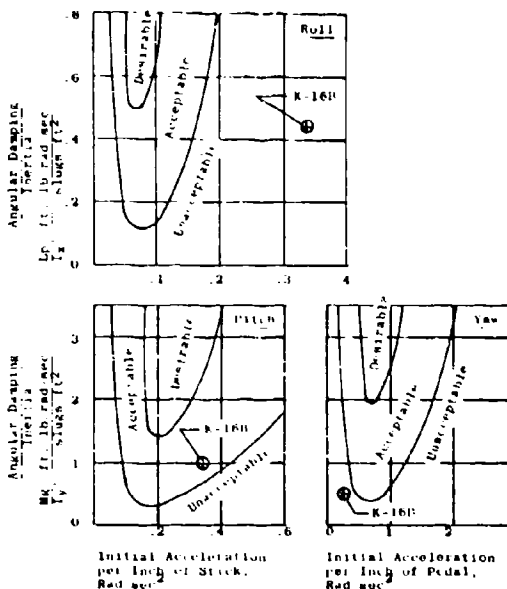
Initial Acceleration per Inch of Pedal, Rad sec

Figure 89
Handling Qualities Boundaries from Tapscott

Although Tapscott's work represents a good start in determining good handling qualities criteria, more needs to be done to broaden them to V/STOL aircraft. The addition of more data to establish reasonable criteria was a prime purpose of the X-16B program and explains the degree of flexibility incorporated into the aircraft systems.

The choice of damping as one of the criteria was a wise one, for the basic stability characteristics of the aircraft certainly affect the pilot's opinion of adequate aircraft control. Here again, however, more enters into the determination of the aircraft damping characteristics than the angular velocity damping. This was discussed by A'Harrah, et al, in IAS Paper 61-62 (68) which shows that the static stability derivatives also enter into the determination of the aircraft damping ratio, as well as do the speed stability derivatives. The characteristics developed by A'Harrah give a good indication of the aircraft's damping characteristics, which can be measured in flight, namely the time to half or double the amplitude of the oscillation. If the damping characteristics are specified in this form, satisfaction with this phase of handling qualities will be assured because it deals directly with the entire aircraft - not just one factor. The criteria charts developed by A'Harrah are reproduced in Figure 90, upon which are spotted the K-16B characteristics.

Results obtained during handling qualities flight tests of basically unstable aircraft, such as VTOL's and helicopters, must be correlated in terms such as the foregoing to eliminate the effect of geometric dissimilarities. The characteristics of the K-16B can be so varied that sufficient flight test data can be obtained to determine satisfactory damping and control sensitivities boundaries.

The boundaries established by A'Harrah were determined using a VTOL simulator. Pilots' opinions of simulations of aircraft cannot be expected to be the same as those of the aircraft itself, for no simulator presents
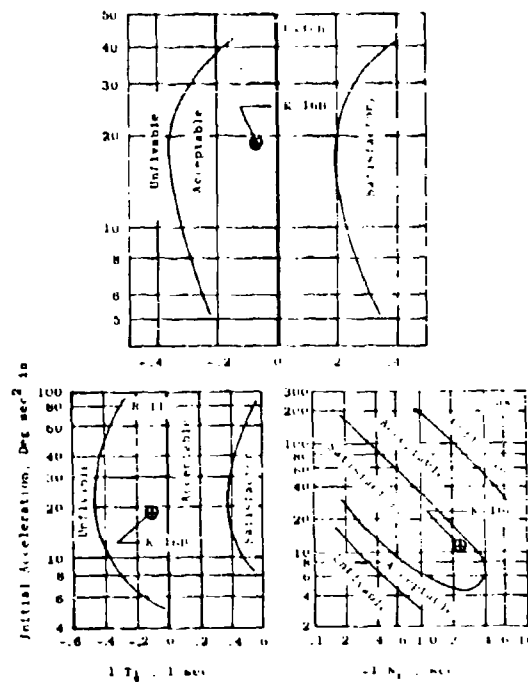
173

Figure 90
Handling Qualities Boundaries from Simulation

a perfect simulation. For example, the angular and translational accelerations may not be duplicated. Nevertheless, a simulator can be useful in comparing simulations of different aircraft on a relative basis. It is only when these results are transferred to an absolute scale that erroneous conclusions may be drawn.

There are, of course, other factors that can be expected to influence pilots' opinions of satisfactory control effectiveness. Among these are the relationship between translational and angular acceleration as a function of speed. This relationship is apparent to the pilot in the ease with which he can hover over a spot while in gusty air. Ideally, he would wish small control movements to cause translation with minimum rotation. The helicopter approaches this. If substantial rotation had to precede any translation, the resulting time lag would induce a tendency on the part of the pilot to overcontrol. This is objectionable. There is, then, some relationship between translational acceleration and corresponding angular acceleration that determines good handling qualities of a hovering aircraft. This effect should deteriorate with speed to the angular type of the standard airplane. This relationship must also be defined in the establishment of good control effectiveness criteria.

It is of point that the helicopter-type cyclic control of the K 16B will result in inherent translational acceleration capabilities with minimum angular acceleration.

A summary of the performance of the K-16B is presented in Table VII and the accompanying SAC charts, Figure 91. The performance was calculated using standard performance analysis methods, and uses the data from both the 1/8-scale model wind tunnel tests at DTMB and the full-scale tests at ARC. The analysis assumes the product improvements of the propulsive rotor as presented earlier in this report.

For usefulness in a flying qualities research program the airplane should have a certain minimum performance enabling it to explore all regimes in which a VTOL aircraft might be expected to perform. Every effort was made to assure such performance for the K-16B.

For vertical flight of the K-16B the resultant force weight ratio (F/W) at the normal gross weight of 9300 lb is 1.06, which leads to a hovering ceiling of 2400 feet. This is equivalent to a 400 fpm vertical rate of climb, which should be adequate for a control and stability evaluation in vertical flight. Vertical climb performance with T58-GE8 engines is shown in Figure 91.

In forward flight at military power from both engines the rate of climb is 6000 fpm and the service ceiling is 36,000 feet. At normal rated power the rate of climb is 3960 fpm, and the service ceiling is 23,000 feet.

Inasmuch as the hovering requirement calls for two T58-GE8 engines, cruising can be accomplished most efficiently by operating one engine nearer to normal power rather than both engines at partial power. If this is done, with presently installed tankage the range is approximately 200 n. miles.

From a hover the K-16B is capable of converting to a speed of 60 knots, the flaps-up stalling speed, in 12 seconds in a total distance of 850 feet (Figure 92). This calculated result presumes that the pilot will continually tilt the wing at its maximum rate (5.4 deg/sec) and keep the hull level using longitudinal control. Perhaps a more realistic transition was that performed by a pilot during the simulator studies of the airplane. This is also plotted on Figure 92. In this case the pilot initially accelerated more slowly by "keeping" the tilt

Summary of Performance
(Standard Conditions)

|	
Normal Gross Weight	9300
Maximum Speed (MRP)	
Sea Level	211 kts
10,000 feet	215 kts
Maximum Rate of Climb - SL (MRP)	6000 FPM
Maximum Rate of Climb - SL (NRP)	3960 FPM
Vertical Rate of Climb - SL	400 FPM
Service Ceiling (MRP)	36,000 ft
Service Ceiling (NRP)	23,000 ft
Hover Ceiling	2,400 ft
Range - SL - (760# fuel)	
Single Engine	190 n. mi
Two Engine	130 n. mi
Speed for Maximum Range	
Single Engine	130 kts
Two Engine	140 kts
Maximum Endurance (760# fuel)	
Single Engine	1.95 hrs
Two Engine	1.25 hrs
Speed for Maximum Endurance	
Single Engine	93 kts
Two Engine	79 kts
Hover Endurance (780# fuel)	0.52 hrs
*12,000# Gross Weight STOL Operation Distance over 50 foot obstacle (zero wind - 300 runway)	514 ft
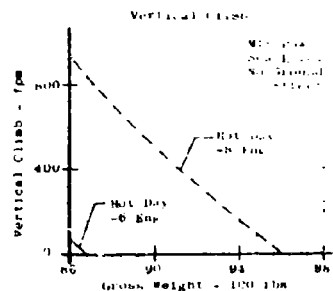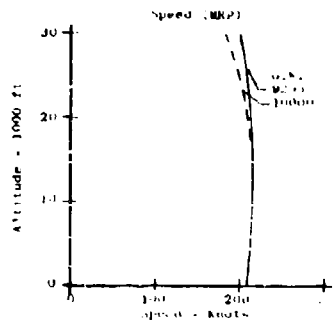
*Landing gear weight restriction
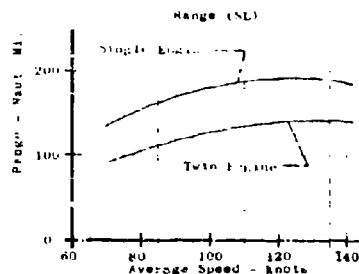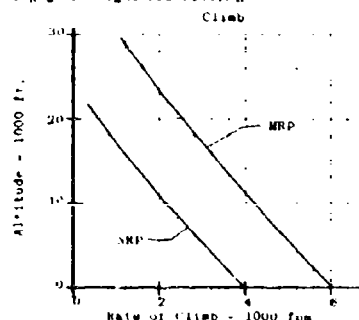
Figure
SAC Charts

button. The return transition to hover from the simulator studies is also shown on the same figure. The total distance travelled in slowing down from 100 knots was 650 feet.

A time history of the K-16B descent following a single engine failure during hover is shown in Figure 93. The descent was calculated by a step-by-step analysis using the data of NACA TN 3307 (69). For this, it was assumed that the remaining engine shares its military power equally between the rotors. During the descent, the fuselage attitude is maintained level by longitudinal control. The rates of wing tilt (65 degrees in 3 seconds, and in 12 seconds) correspond to the design emergency rate and the normal rate. At airspeeds above 80 knots, altitude can be maintained on one engine. Though it is possible for the wing to be cranked down using battery supply, with a total power loss at 350 feet recovery would be the same as that with a freely falling safe.

Figure 94 shows the STOL characteristics of the ship at 12,000 lb gross weight, which is a limiting condition of the JRF-5 landing gear at 6 fps sinking speed. The curves were calculated at constant wing tilt angles with the exception of the point marked "varied tilt". Although the airplane left the ground in shorter distances as the wing tilt was set at higher angles, the air drag was so large at these angles that more distance was covered

in the climbout. The minimum distance appeared to occur at a tilt angle of 19 degrees.

Most of the calculations were made for a wing flap angle (δ_{f_W}) of 20 degrees because the available data indicated that this angle yielded the highest maximum lift-drag ratio. With the 40 degree flap deflection, however, the greater lift resulted in so much shorter ground run (85 feet shorter) that the 50 foot altitude was cleared in 42 feet less.

Another type of take-off was completed by assuming that the wing tilt drive was activated at the beginning of the take-off run until a 19 degree tilt angle was attained. In this way, the large net thrusting force available with low wing tilt could be utilized. But some lifting force was also lost and the ground run was shortened by only 25 feet. For this case a rate of wing tilt of 4.1 deg/sec was assumed.

Another possible type of take-off is for the pilot to nose the airplane down as soon as the elevator will have some effect, and accelerate without climbing until the speed for best angle of climb is attained. However, a cursory examination indicated that so much ground would be covered in accelerating at zero climb that it could not be recovered by the greater climb angle.
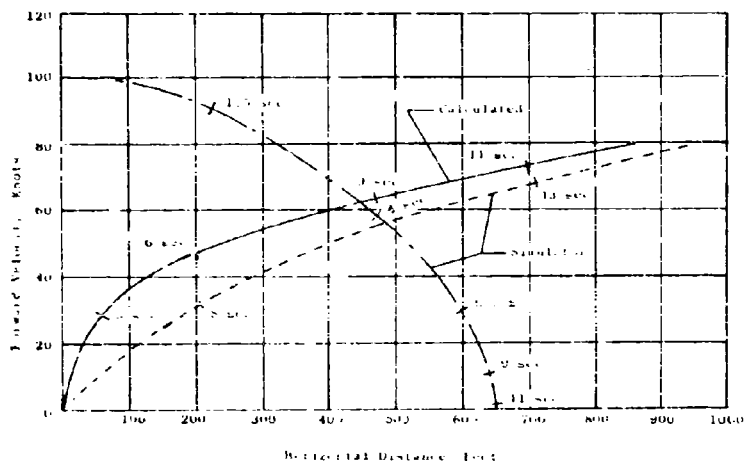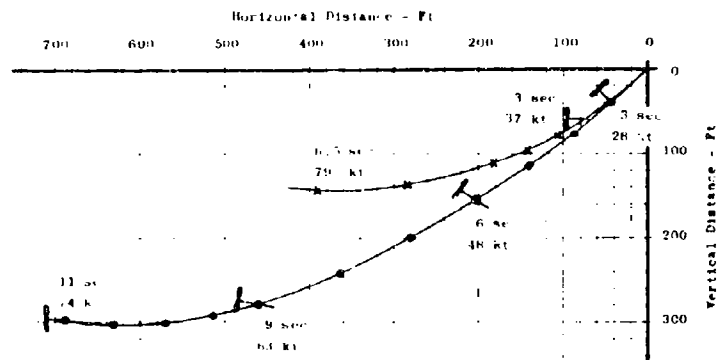

Figure 94
Transition Acceleration and Deceleration

176

Single engine power failure
Fuselage maintained horizontal
Rate of wing attitude change $\begin{cases} 65^\circ/12 \text{ sec} & \bullet \\ 65^\circ/1 \text{ sec} & x \end{cases}$
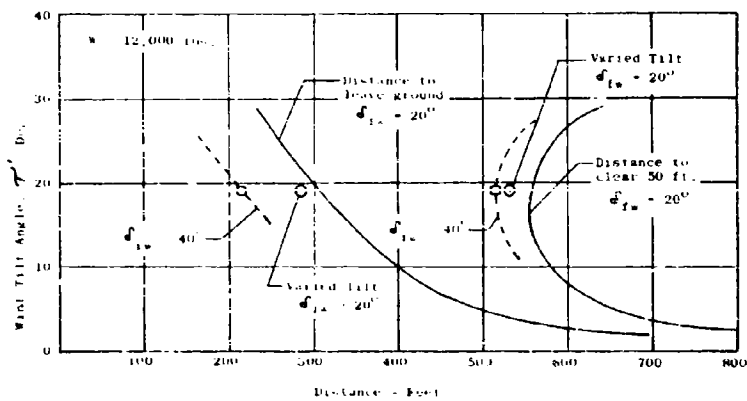
Figure 93
Time History - Single Engine Recovery

Figure 94
K for STOL Take-Off

177

KAMAN *Aircraft Corporation*

BLOOMFIELD, CONNECTICUT